

MÖSSBAUER STUDIES OF IRON MINERALS  
UNDER PRESSURES OF UP TO 200 KILOBARS

by

<sup>Francis</sup>  
(FRANK) E. HUGGINS

B.A., Oxford University  
1970

SUBMITTED IN PARTIAL FULFILLMENT  
OF THE REQUIREMENTS FOR THE  
DEGREE OF DOCTOR OF  
PHILOSOPHY

at the

MASSACHUSETTS INSTITUTE OF  
TECHNOLOGY

August, 1974  
(2 February, 1975)

Signature of Author \_\_\_\_\_

Department of Earth and Planetary Sciences, August 12, 1974

Certified by \_\_\_\_\_

\_\_\_\_\_  
Thesis Supervisor

Accepted by \_\_\_\_\_

\_\_\_\_\_  
Chairman, Departmental Committee on Graduate Students

~~WITHDRAWN~~  
NOV FROM  
MIT LIBRARIES  
Indoren

MÖSSBAUER STUDIES OF IRON MINERALS  
UNDER PRESSURES OF UP TO 200 KILOBARS

BY

Frank E. Huggins

Submitted to the Department of Earth and Planetary Sciences  
on August 12, 1974 in partial fulfillment of  
the requirements for the Degree of Doctor of Philosophy

ABSTRACT

For the most part, iron minerals only show small changes in Mössbauer parameters with pressure, which suggest that the electronic structures of iron silicates and oxides are not greatly different at 200 kb than at zero pressure. The high incompressibility of silicates precluded the observation of large effects, but the trends suggest that for volume changes comparable to those occurring in more compressible phases, similar electronic effects will be observed. At room temperature and at pressures less than 180 kb, pressure-induced reduction is nowhere near as large nor as common in silicates and oxides as it is in organometallic compounds. Except for  $\text{Fe}^{3+}$  in tetrahedral sites in silicates, the isomer shift trends correlate well with expected site compressibilities. The ferric quadrupole splitting trends with pressure are generally larger than predictions based on compression at constant distortion. The ferrous quadrupole splitting trends with pressure may be interpreted using Ingalls' (1964) model and arise from either changes in the splitting of the lower 3d orbital levels with pressure if the site distortion is small, or from changes in the crystal structure if the site distortion is large. The quadrupole splitting of the ferrous mineral as a function of temperature is needed to interpret the quadrupole splitting trend with pressure. Changes in the magnetic characters of silicates and oxides at pressures up to 200 kb are small. Silicates remain paramagnetic, while oxides show a very small decrease in magnetic field strength. The combination of isomer shift and quadrupole splitting changes with pressure suggest that there is a slight but significant increase in covalent character of the iron-oxygen bonds over 200 kb, mostly in the upper 3d levels, which is responsible for the increase in conductivity and the shift to lower energy and broadening of the absorption edge with pressure observed in a number of ferrous phases.

The experimental technique for obtaining Mössbauer spectra at high pressures has been examined in the course of this study and improved so

that unnecessary complications caused by thick absorber phenomena can be greatly reduced. The synthesis of mineral phases was required to boost the  $^{57}\text{Fe}$  content if the iron concentration in the mineral was below 20 wt % iron per structural site. Significant but incomplete results were obtained in the course of such syntheses on the effect of substituting aluminum by iron in muscovite using the Mössbauer effect to monitor oxidation states. The general question of control of oxidation states in minerals was also considered and the analysis suggests that crystallographic details play a role in determining the oxidation state at a given oxygen fugacity and temperature.

Since the compressibility of individual sites appears to be an important parameter in determining the extent of electronic effects, some discussion of the ways of estimating site compressibilities is appended.

THESIS SUPERVISOR: Roger G. Burns  
TITLE: Professor of Mineralogy and Geochemistry

TABLE OF CONTENTS

TITLE PAGE	1
ABSTRACT	2
TABLE OF CONTENTS	4
INDEX OF FIGURES IN THE TEXT	8
INDEX OF TABLES IN THE TEXT	11
ACKNOWLEDGMENTS	13
Chapter 1: INTRODUCTION	14
1.1 General Aim of the Study. . . . .	14
1.2 The Role of Iron in Studies of the Earth. . . . .	15
1.3 Techniques Used to Study Electronic Properties of Cations in Minerals. . . . .	18
Chapter 2: PREVIOUS WORK AND ITS APPLICATIONS TO EARTH SCIENCES	20
2.1 Introduction. . . . .	20
2.2 Theory of the Electronic Structure of Solids. . . . .	20
2.3 High Pressure Results . . . . .	27
2.3.1 Effect of pressure on electrical con- ductivity. . . . .	27
2.3.2 High pressure absorption spectral measurements . . . . .	30
2.3.3 Previous high pressure Mössbauer results. . . . .	34
(a) Spin-state transitions. . . . .	34
(b) Pressure-induced reduction. . . . .	37
(c) Effect of pressure on hyperfine magnetic splittings . . . . .	48
(d) Effect of pressure on the Mössbauer isomer shift. . . . .	49
(e) Variation of quadrupole splitting with pressure . . . . .	50
2.4 Summary of Previous Results . . . . .	52
2.5 Delineation of Areas of Investigation in this Study . . . . .	54
Chapter 3: EXPERIMENTAL DETAILS	59
3.1 Introduction. . . . .	59
3.2 Mössbauer Spectroscopy: Theory and Practice. . . . .	59
3.2.1 The Mössbauer effect . . . . .	59
3.2.2 Parameters from a <sup>57</sup> Fe Mössbauer spectrum. . . . .	62



3.2.3	Practice of Mössbauer spectroscopy of iron minerals . . . . .	67
3.2.4	Mössbauer bibliography . . . . .	72
3.3	High Pressure Mössbauer Experimentation . . . . .	72
3.3.1	The high pressure cell . . . . .	72
3.3.2	Sample preparation . . . . .	73
3.3.3	Pressure calibration . . . . .	79
3.3.4	Adjustments to the Mössbauer apparatus . . . . .	82
3.3.5	Experimentation difficulties . . . . .	82
3.3.6	High temperature additions to the high pressure cell. . . . .	93
3.3.7	High pressure Mössbauer studies with the diamond cell . . . . .	93
3.4	Synthesis Experiments . . . . .	102
3.4.1	Introduction . . . . .	102
3.4.2	Synthesis techniques . . . . .	102
3.4.3	Synthesis of micas . . . . .	107
	(a) Ferriphlogopites . . . . .	110
	(b) Ferrimuscovites . . . . .	116
	(c) Other mica syntheses . . . . .	117
3.4.4	Synthesis of garnets . . . . .	117
	(a) Aluminum-iron garnets . . . . .	118
	(b) Chromium-iron garnets . . . . .	118
	(c) Titanium-iron garnets . . . . .	123
	(d) Other garnet syntheses . . . . .	123
3.4.5	Synthesis of potassium iron feldspar . . . . .	123
3.4.6	Synthesis of magnetite . . . . .	124
3.4.7	Sources of other samples . . . . .	124
Chapter 4:	MÖSSBAUER RESULTS AND DISCUSSION . . . . .	128
4.1	Introduction . . . . .	128
4.2	Mössbauer Results . . . . .	130
4.2.1	Garnets . . . . .	130
	(a) $\text{Ca}_3\text{AlFeSi}_3\text{O}_{12}$ . . . . .	131
	(b) FeCr garnet . . . . .	131
	(c) $\text{Ca}_3\text{TiFe}_2\text{Si}_2\text{O}_{12}$ . . . . .	144
	(d) CaZrFe garnet, $\text{Ca}_{2.5}\text{Zr}_{2.5}\text{Fe}_3\text{O}_{12}$ . . . . .	148
	(e) Almandine . . . . .	152
4.2.2	Micas . . . . .	156
	(a) Ferriphlogopite, $\text{KMg}_3\text{FeSi}_3\text{O}_{10}(\text{OH})_2$ . . . . .	156
	(b) Ferriphlogopite, $\text{KMg}_3(\text{Fe,Al})\text{Si}_3\text{O}_{10}(\text{OH})_2$ . . . . .	160
	(c) Muscovite, $\text{K}(\text{Al}_{0.8}\text{Mg}_{0.1}\text{Fe}_{0.1}^{3+})_2\text{Al}_{0.8}\text{Si}_{3.2}\text{O}_{10}(\text{OH})_2$ . . . . .	160
4.2.3	Other mineral phases . . . . .	166
	(a) Fayalite . . . . .	166
	(b) Iron microcline . . . . .	170
	(c) Hematite . . . . .	174
	(d) Magnetite . . . . .	180
	(e) Orthoferrosilite . . . . .	184
4.2.4	Relative f# experiments . . . . .	184
	(a) Fayalite and iron microcline . . . . .	188

	(b) Fayalite and acmite . . . . .	188
	(c) Other experiments . . . . .	191
4.3	Discussion of Results . . . . .	191
4.3.1	Isomer shift changes with pressure . . . . .	194
4.3.2	Quadrupole splitting trends with pressure. . . . .	208
4.3.3	Ferric quadrupole splitting trends . . . . .	209
4.3.4	Ferrous quadrupole splitting trends. . . . .	218
4.3.5	Changes in Fe <sup>2+</sup> /Fe <sup>3+</sup> ratio with pressure . . . . .	236
4.3.6	Changes in magnetism of oxides and silicates with pressure. . . . .	243
4.3.7	Pressure-induced changes in isomer shifts and quadrupole splittings and their relation to the covalency of ferrous-ligand bonds . . . . .	245
Chapter 5:	DISCUSSION AND SPECULATION OF TOPICS OF IMPORTANCE FOR EARTH SCIENCES ARISING FROM THIS STUDY . . . . .	250
5.1	Speculations on the Pressure-induced Electron Transfer Transition in Ferric Silicates . . . . .	250
5.2	Covalency Changes in the Earth. . . . .	258
5.3	Discussion of the Effect of Pressure and Temperature on Ferrous Crystal-field Stabili- zation Energies . . . . .	265
Chapter 6:	CONCLUSIONS AND SUGGESTIONS FOR FUTURE WORK . . . . .	283
6.1	Conclusions and Summary of High Pressure Mössbauer Results . . . . .	283
6.2	Suggestions for Future Work . . . . .	286
6.2.1	High pressure Mössbauer experiments. . . . .	286
6.2.2	Related experiments. . . . .	287
6.2.3	Unrelated topic. . . . .	288
REFERENCES		289
APPENDICES		309
Appendix A1:	RESULTS FROM SYNTHESIS EXPERIMENTS . . . . .	310
A1.1	The Substitution of Octahedral Aluminum by Ferric Iron in Muscovite. . . . .	310
A1.2	Calculation of the Formula of the Garnet Formed in Synthesis Experiment #41. . . . .	321
A1.3	Control of Oxidation State in Oxides and Silicate Minerals . . . . .	324
Appendix A1:	REFERENCES . . . . .	336
Appendix A2:	SITE COMPRESSIBILITIES . . . . .	339
A2.1	Considerations on the Compressibilities of Individual Polyhedral Sites Within a Crystal Structure . . . . .	339
Appendix A2:	REFERENCES . . . . .	346

Appendix A3: COMPUTER ROUTINES	347
A3.1 Modification of Stone's Original Program . . . . .	347
A3.1.1 Calculation of iron Mössbauer parametric data from the fit. . . . .	347
(a) Modifying read in of initial estimates and number of peaks . . . . .	348
(b) Calculation of Mössbauer parameters and print out of such data. . . . .	349
A3.1.2 Calculation of conversion parameters from iron foil spectra . . . . .	351
A3.1.3 Other changes. . . . .	353
A3.2 Calculation of $F_{val}$ for Ferrous Minerals as a Function of Temperature, T, and the Lower Level Splittings, $\Delta_1$ and $\Delta_2$ . . . . .	355
Appendix A3: REFERENCES. . . . .	357
VITA	358

INDEX OF FIGURES IN THE TEXT

(Page numbers refer to figure captions, the figures will be found on the page immediately following.)

FIGURE		PAGE
2.1	High spin and low spin configurations for ferrous iron in a slightly distorted site. . . . .	24
2.2	The effect of pressure on ferric chloride . . . . .	28
2.3	Schematic configuration diagram for pressure-induced reduction . . . . .	43
3.1	Basic Mössbauer experimentation . . . . .	63
3.2	Mössbauer experiment. . . . .	68
3.3	Diagram of high pressure anvil used in this study . . . . .	74
3.4	Pressure distribution on the sample in the high pressure cell at low pressures and at high pressures . . . . .	76
3.5	Calibration curve used to convert Heise gauge reading to pressure on the sample . . . . .	80
3.6	Difference between regular geometry and high pressure geometry for Mössbauer experimentation. . . . .	83
3.7	Mössbauer spectrum of a blank boron pellet in the high pressure cell at about 25 kb . . . . .	87
3.8	Mössbauer spectra of synthetic ferriphlogopite (SE #15) . . .	89
3.9	Mössbauer spectra of a mechanical mixture of fayalite and iron microcline . . . . .	91
3.10	Diagram showing heating device for high pressure Mössbauer experiments at temperatures up to 100 °C. . . . .	94
3.11	Schematic diagram showing the gasketing technique used in the diamond cell. . . . .	97
3.12	Mössbauer spectrum of hematite in the diamond cell. . . . .	99
3.13	Capsule configurations used in the synthesis experiments . . . . .	108
4.1	Mössbauer spectra of FeAl garnet. . . . .	133
	(a) at 0 kb and at 57 kb . . . . .	133
	(b) in regular geometry and high pressure geometry . . . . .	135
4.2	Mössbauer spectra of FeCr garnet. . . . .	139
	(a) in regular geometry and at 98 kb . . . . .	139
	(b) at 180 kb and at 110 kb (88 °C). . . . .	141
4.3	Mössbauer spectra of the garnet, $\text{Ca}_3\text{LiFe}_2\text{Si}_2\text{O}_{12}$ . . . . .	146
4.4	Mössbauer spectra of CaZrFe garnet and CaThZrFe garnet. . . . .	150
4.5	Mössbauer spectra of almandine, GN1A. . . . .	154
4.6	Mössbauer spectra of ferriphlogopite, SE #16. . . . .	158
4.7	Mössbauer spectra of ferriphlogopite, SE #15. . . . .	162
4.8	Mössbauer spectrum of muscovite, SE #20 . . . . .	164
4.9	Mössbauer spectra of fayalite, Rockport . . . . .	168

FIGURE		PAGE
4.10	Mössbauer spectra of iron microcline. . . . .	172
4.11	Energy level diagram for phases giving rise to magnetically split Mössbauer spectra and schematic Mössbauer spectrum of hematite. . . . .	176
4.12	Mössbauer spectra of hematite . . . . .	178
4.13	Mössbauer spectrum of magnetite . . . . .	182
4.14	Mössbauer spectra of orthoferrosilite . . . . .	186
4.15	Mössbauer spectra of a mechanical mixture of fayalite and iron microcline. . . . .	189
4.16	Mössbauer spectra of a mechanical mixture of fayalite and acmite . . . . .	192
4.17	Summary of isomer shift trends with pressure for ferrous phases. . . . .	198
4.18	Summary of isomer shift trends with pressure for ferric phases . . . . .	200
4.19	Initial isomer shift trends with pressure for the various iron cation and coordination combinations . . . . .	202
4.20	The 3d levels in tetrahedral, cubic and octahedral coordinations . . . . .	210
4.21	Summary of quadrupole splitting trends with pressure for ferric phases. . . . .	212
4.22	Summary of quadrupole splitting trends with pressure for ferrous phases . . . . .	219
	(a) for almandine, fayalite and $Fe^{2+}$ in mica . . . . .	219
	(b) for M1 and M2 sites in orthoferrosilite. . . . .	221
4.23	Two aspects of Ingalls' model for the quadrupole splitting of ferrous phases . . . . .	225
	(a) The effect of distortion at constant temperature. . . . .	225
	(b) The effect of temperature at constant distortion . . . . .	227
4.24	The relationship between Mössbauer absorption and iron concentration in the Mössbauer sample. . . . .	240
5.1	Predicted change of molar volume with pressure for a ferric phase undergoing the pressure-induced charge transfer transition. . . . .	253
5.2	Expected changes with depth of radius ratio, bulk modulus, bond covalency and volume due to various electronic transitions. . . . .	261
5.3	Example of the interrelationship of CFSE, $\Delta_o$ and the five 3d levels for ferrous iron in an octahedral site. . . . .	266
5.4	Five 3d levels, CFSE and $\Delta_c$ for ferrous iron in almandine . . . . .	270
5.5	CFSE as a function of temperature . . . . .	279

FIGURE	PAGE
A1.1.1 Plot of octahedral divalent cations against octahedral ferric iron for muscovite analyses. . . . .	311
A1.1.2 The octahedral site and 3d energy levels in muscovite. . . . .	317
A1.3.1 Schematic diagram showing the expected inter-relationship between oxygen fugacity, bond length, coordination and oxidation state of iron . . . . .	330
A1.3.2 Schematic diagram showing the expected inter-relationship between oxygen fugacity, bond length, coordination and oxidation state of titanium . . . . .	333

INDEX OF TABLES IN THE TEXT

TABLE		PAGE
2.1	The parameters, A and B, for many of the compounds studied by Drickamer and co-workers. . . . .	40
2.2	Phases of mineralogical interest studied by the high pressure Mössbauer technique. . . . .	56
3.1	Glossary of symbols used in section 3.4 and Appendix A1. . . . .	103
3.2	Chemical forms of the elements used in "oxide" mixes in the course of this study. . . . .	106
3.3	Synthesis of micas: Experimental details. . . . .	111
	(a) Ferriphlogopites. . . . .	111
	(b) Ferrimuscovites . . . . .	113
	(c) Other micas . . . . .	115
3.4	Synthesis of garnets: Experimental details. . . . .	119
	(a) Aluminum-iron garnets . . . . .	119
	(b) Chromium-iron garnets . . . . .	120
	(c) Titanium-iron garnets . . . . .	121
	(d) Other garnet syntheses. . . . .	122
3.5	Synthesis of iron feldspar, $\text{KFeSi}_3\text{O}_8$ : Experimental details . . . . .	125
3.6	Synthesis of magnetite: Experimental details. . . . .	126
3.7	Composition of samples containing iron of natural isotopic abundance which were used in this study . . . . .	127
4.1	Mössbauer data for $\text{Ca}_3\text{AlFeSi}_3\text{O}_{12}$ as a function of pressure. . . . .	132
4.2	Mössbauer data for $\text{Ca}_3\text{CrFeSi}_3\text{O}_{12}$ as a function of pressure. . . . .	138
4.3	Mössbauer data for $\text{Ca}_3\text{TiFe}_2\text{Si}_2\text{O}_{12}$ . . . . .	145
4.4	Mössbauer data for $\text{Ca}_{2.5}\text{Zr}_{2.5}\text{Fe}_3\text{O}_{12}$ and for $\text{Ca}_{2.5}\text{Th}_{0.5}\text{Zr}_2\text{Fe}_3\text{O}_{12}$ . . . . .	149
4.5	Mössbauer data for almandine, GN1A, as a function of pressure. . . . .	153
4.6	Mössbauer data for $\text{KMg}_3\text{FeSi}_3\text{O}_{10}(\text{OH})_2$ as a function of pressure. . . . .	157
4.7	Mössbauer data for $\text{KMg}_3(\text{FeAl})\text{Si}_3\text{O}_{10}(\text{OH})_2$ as a function of pressure . . . . .	161
4.8	Mössbauer data for fayalite (Rockport, MA) as a function of pressure . . . . .	167
4.9	Mössbauer data for iron microcline as a function of pressure. . . . .	171
4.10	Mössbauer data for hematite as a function of pressure. . . . .	175

TABLE		PAGE
4.11	Mössbauer data for magnetite. . . . .	181
4.12	Mössbauer data for orthoferrosilite from Manchuria as a function of pressure . . . . .	185
4.13	Range of isomer shift values for different ox- idation states of iron coordinated by oxygens. . . . .	196
4.14	Compilation of Fe <sup>3+</sup> (IV) isomer shift data. . . . .	206
4.15	Values of lower energy level splittings calculated from the temperature dependence of the quadrupole splitting for ferrous phases of mineralogical interest. . . . .	230
5.1	Effect of changes in pressure, temperature, coor- dination number, spin multiplicity and cation oxidation state on radius ratio, covalency of metal-oxygen bonds and bulk modulus . . . . .	260
5.2	Estimated changes over 100 kb in the splittings of lower 3d levels, $\Delta_1$ and $\Delta_2$ , for some ferrous minerals. . . . .	275
A1.3.1	Examples of multivalent elements in oxides and silicates . . . . .	325
A2.1.1	Polyhedral compressibilities for andradite, Ca <sub>3</sub> Fe <sub>2</sub> Si <sub>3</sub> O <sub>12</sub> . . . . .	344



### ACKNOWLEDGMENTS

I am especially fortunate to have had Professor Roger Burns as my advisor, not only for this thesis, but also for the duration of my stay at M.I.T. His advice and assistance on both professional and personal levels have been most valuable, for which I am extremely grateful.

I would also like to thank Professor Jack Tossell and Dr. David Vaughan for assistance with experimental details in the early stages of this thesis. Rateb Abu-Eid, Rudi Hon and Dr. Earle Whipple also receive my thanks for useful discussions which contributed to the directions and ideas of this thesis.

Last, but not least, I am indebted to Michelle Huggins, whose skills with a typewriter have added greatly to the presentation of this thesis and who has been most understanding with the demands made of our married life by this thesis.

## Chapter 1

### INTRODUCTION

#### 1.1 General Aim of the Study

Our understanding of the Earth's interior has increased greatly during the last twenty years and will continue to do so as further interest is focussed in this direction. Beginning with the investigations of Birch (1952), which were among the earliest studies to integrate geophysical and geological data through use of solid state theory, subsequent studies and developments have enabled current models of the Earth's interior, especially the mantle, to be relatively precise (see, for example, Press (1970); Ringwood (1970); Anderson et al. (1971); Ahrens (1972, 1973)). As might be expected with models based for the most part on data obtained by indirect means, a number of uncertainties and some inconsistencies still remain to be refined or resolved.

In view of recent developments in solid state physics concerning the variety of electronic phenomena occurring in materials under extreme pressures (see, for example, Babb and Robertson (1963); Drickamer (1965); Drickamer et al. (1970); Drickamer and Frank (1973)), it appeared likely that similar techniques applied to minerals might be useful for furthering our understanding of phenomena within the Earth.

The present study was initiated with this broad goal in mind. However, due to restrictions of time and techniques, this study does not attempt to investigate all possible applications of pressure-induced electronic changes to Earth Sciences. Instead, it concerns itself primarily with the changes

in electronic properties of iron-containing minerals under pressures of up to 200 kb by using Mössbauer spectroscopy to monitor such changes. But, as will be indicated in this and the following chapters, such studies of the behavior of iron in minerals are of considerable interest due to their potential importance for Earth Sciences.

### 1.2 The Role of Iron in Studies of the Earth

The behavior of iron, probably more than any other element, is critical to our understanding and interpretation of geochemical and geophysical data related to the Earth's interior. By weight, iron is the most abundant element in the Earth (Mason, 1966) and it is the fourth most abundant element in the silicate portion of the Earth (Mason, 1966; Ringwood, 1966a). The importance of iron goes beyond its abundance, however, since a number of its properties are unique among the elements of major occurrence. The properties which make iron such an important element include:

- (a) It is the only major element exhibiting variable valence, since it exists in the Earth in at least three oxidation states, Fe(III), Fe(II) and Fe(0). Thus iron plays a major role in determining the partial pressure of volatiles (especially  $p_{O_2}$ ,  $p_{H_2}$ ,  $p_{H_2O}$ ,  $p_{CO_2}$ ,  $p_{CO}$ ) and controlling other redox reactions within the Earth.
- (b) It is the most abundant element whose oxides have  $\bar{m} \neq 20$  ( $\bar{m}$  - mean atomic weight). This fact introduces complications in the interpretation of seismic velocity-depth profiles for density and mineralogic correlation.
- (c) The electrical and magnetic properties of mineral phases within

the Earth are for the most part determined by iron. Without this property of iron, electrical and magnetic studies of the Earth would be insignificant compared to their actual importance.

- (d) Mg/Fe solid solution in silicate phases of major occurrence affects many properties of the Earth. For example, the depth of the olivine-spinel transition, which is mainly responsible for the 400 km discontinuity (Ringwood, 1970) in the Earth, is not only determined by the Mg:Fe ratio, but is also blurred by such solid solution over a range of depth.
- (e) Iron is the major element responsible for electronic absorption features (and color) of the common silicates. These features arise in two ways: firstly, due to crystal field  $d \leftrightarrow d$  transitions within the incomplete 3d subshell of the iron cations and, secondly, due to charge transfer or electron transfer either between two adjacent metal cations of different valence (metal-metal charge transfer) or between metal cations and their surrounding oxygen anions or ligands (metal $\rightarrow$ ligand or ligand $\rightarrow$ metal charge transfer). Burns (1970) has described the occurrence of these processes for the common silicates.
- (f) Iron cations are the only major cations capable of existing in two or more spin states within the Earth (Fyfe, 1960). Iron is a transition element and has an incomplete 3d shell of electrons. The spin state is determined by how the d electrons (6 for Fe(II); 5 for Fe(III)) distribute themselves over the five 3d orbitals. The high spin state has the least number of paired

spins whereas the low spin state has as many paired spins as possible; there are intermediate spin states as well in certain situations. The size and properties of the different spin states are quite different and such changes in spin state would seriously change the role of iron in minerals. Strens (1969), Burns (1969a), Gaffney (1972) and Gaffney and Anderson (1973) discuss the implications of such transitions.

Four of these six properties, (a), (c), (e) and (f), are due directly to the electronic behavior of iron. Thus data on the electronic properties of iron in minerals as a function of pressure would help elucidate the role of this critical element for Earth studies. Studies which are directly related to these properties are radiative transfer studies of the Earth (very dependent on spin, valence and charge transfer properties of iron), seismic discontinuity studies (some discontinuities in the lower mantle are probably caused by spin state changes in ferrous cations), studies of reduction-oxidation equilibria of magmas and of the core/mantle boundary (controlled by valence state properties of iron), investigations of the  $\text{Fe}^{2+}/\text{Mg}$  distribution between different sites in minerals and its effect on geophysical and geochemical properties of major mantle phases (dependent on the electronic energy levels in ferrous cations), and studies of the Earth's electrical and magnetic properties.

Furthermore, it has been predicted and shown (Drickamer, 1965) that as pressure is increased, ionic substances (which include silicates) become increasingly covalent and may even approach metallic behavior at extremely high pressures. This trend is due to increasing the orbital overlap of

cation and anion as the volume of the solid decreases with increasing pressure and has been virtually ignored in interpretation of the properties of the Earth. Unless the silicate contains iron, the only experiments which may be performed on it to measure this trend are electrical conductivity studies. The presence of iron enables other techniques such as Mössbauer spectroscopy and electronic absorption spectroscopy to be used to study this trend.

### 1.3 Techniques Used to Study Electronic Properties of Cations in Minerals

The two techniques, Mössbauer spectroscopy and electronic absorption spectroscopy, have been used most to investigate the electronic properties of iron mineral phases. Although the two techniques are quite different in theory and operation, both can give information on the oxidation state, spin state and also crystallographic coordination of iron cations in minerals. In a sense, the techniques complement each other since electronic absorption spectroscopy measures the energy of radiation-induced electronic transitions directly, but is less specific for identifying the absorbing species (the technique is not restricted to iron alone) whereas Mössbauer spectroscopy is highly specific for identifying the role of iron cations, but does not measure electronic transition energies. Instead, Mössbauer spectroscopy gives important information on the relative covalent character of the iron-ligand bonds, on site distortions, and on magnetic interactions between iron cations, if present. Of the two techniques, electronic absorption spectroscopy is more suited to high pressure work, since it requires less deviation from experimental techniques at atmospheric pressure. However, the Mössbauer results are easier to interpret, for the

most part, in the absence of auxillary crystallographic data as a function of pressure, since the technique is much more specific for a given cation species, and when set-up, the Mössbauer technique is less fraught with experimental difficulties.

As the high pressure Mössbauer technique was extensively used in this study, a brief description of the theory and technical procedures relating to Mössbauer spectroscopy is given in chapter 3. For further details on electronic absorption spectroscopy, Schmidtke (1968) and Lever (1968) should be consulted for theory and applications, Burns (1970) for mineralogical applications and Babb and Robertson (1963) and Bell and Mao (1972) for high pressure techniques and applications.

## Chapter 2

### PREVIOUS WORK AND ITS APPLICATIONS TO EARTH SCIENCES

#### 2.1 Introduction

Previous investigations of the electronic properties of iron phases under high pressures have relied on Mössbauer spectroscopy, absorption spectroscopy and electrical conductivity measurements. Electrical conductivity involves a bulk measurement of the solid, rather than individual iron cations in the solid. However, the iron cations in a silicate framework do appear to affect the electrical conductivity drastically compared to the other major cations ( $\text{Mg}^{2+}$ ,  $\text{Ca}^{2+}$ ,  $\text{Si}^{4+}$ ,  $\text{Al}^{3+}$ ) found in mantle silicates, so that conductivity measurements are quite sensitive to iron cations (Bradley et al., 1964). The other two techniques, as discussed in section 1.3, give information directly on the iron atoms in the silicate. For this reason, two extreme groups of theories have arisen in order to interpret the electronic structure of iron-containing solids. These are, firstly, theories based on the band theory of solids which attempt to consider the bulk solid as a whole, and, secondly, theories related to localized metal atoms which just consider the iron cation for example, and its immediate neighboring anions or ligands.

#### 2.2 Theory of the Electronic Structure of Solids

Band theory attempts to describe the electronic structure of a solid as continuous bands of closely spaced electronic energy levels running through the solid. The energy bands meet certain boundary and periodic



conditions determined by the symmetry and size of a reciprocal unit cell of structure or Brillouin zone. The bands are separated by gaps of forbidden energies. If the uppermost band containing electrons, or the valence band, is only partially filled, the solid will generally have metallic properties; whereas if it is completely filled, the solid will be a metal, semimetal, semiconductor or insulator depending on the size of the energy gap between the valence band and the lowest unfilled band or the conduction band. Most silicates, which do not contain iron or other transition elements, have large band gaps (on the order of 6-10 eV) and are insulators (Shankland, 1969). The addition of iron transforms the electrical conducting properties towards those of a semiconductor and the effective band gap is reduced to about 3 eV. Band theory has been quite successful in interpreting the transport properties of solids, especially electrical conductivity. However, for complex structures like silicates, band theory has only been applied in a qualitative manner.

The effective band gap in silicates corresponds to the energy of the first metal-ligand charge transfer absorption band in the localized theories, which will invariably be a ligand $\rightarrow$ iron feature if the silicate contains appreciable iron, or ligand $\rightarrow$ titanium if there is appreciable titanium present (Loeffler et al., 1974). Since titanium is of minor importance in mantle phases compared to iron, only ligand $\rightarrow$ iron bands will be discussed. Molecular orbital theory is best suited to describe these features which involve the excitation of an electron from ligand orbital to a metal orbital. In fact, considerable advances have been made recently in treating cation sites in mineral structures using a computational molecular orbital theory known

as the SCF-X<sub>α</sub> scattered wave cluster method (Tossell et al., 1973, 1974). Not only can this theory predict charge transfer energies reasonably well, but it can also be used to interpret electron (ESCA) and X-ray spectral data, which come from excitation of electrons between energy levels not involved in bonding and deeper into the electronic structure of the atom. The drawback with this approach, however, is that it idealizes the system quite severely, so that it is not very accurate for the energies of the electronic levels which are mostly localized on the iron atom. For this reason, crystal-field theory in the extended form of ligand-field theory is most useful for treating the iron electron levels.

Unlike molecular orbital theory, which constructs "molecular" electronic energy levels appropriate to a given coordination site as a whole by combining iron atomic electronic levels with ligand atomic electronic levels, crystal-field theory only considers the five 3d iron electronic orbital levels and how they are perturbed by the surrounding electrostatic environment of the ligands. Ligand-field theory goes one step further and introduces some details of how the iron 3d orbitals and ligand orbitals interact, but still it is essentially concerned only with the cation orbitals.

The application of crystal-field theory to transition metal geochemistry and silicate mineralogy has been quite profitable, finding use in the interpretation of the crystal chemistry of transition metals in minerals, the behavior of transition elements in various geologic situations and so on (see Burns (1970) for comprehensive review). In a regular site such as octahedral or tetrahedral, the five 3d orbitals are split into one

group of two orbitals and one group of three orbitals, separated by the energy known as the crystal-field splitting parameter,  $\Delta$ . In a distorted site, these degeneracies are often lifted, but the concept of  $\Delta$  remains since the splittings due to distortion are generally smaller than the original splitting. Depending on the symmetry of the site and the splittings of the five 3d orbitals, some transition elements may be stabilized in one site, but destabilized in another. The concept of the crystal-field stabilization energy, CFSE, was introduced as a measure of the stabilization of transition elements in a site. CFSE is defined as:

$$\text{CFSE} = \sum_i (E_o - E_{ji}) \quad 2.1$$

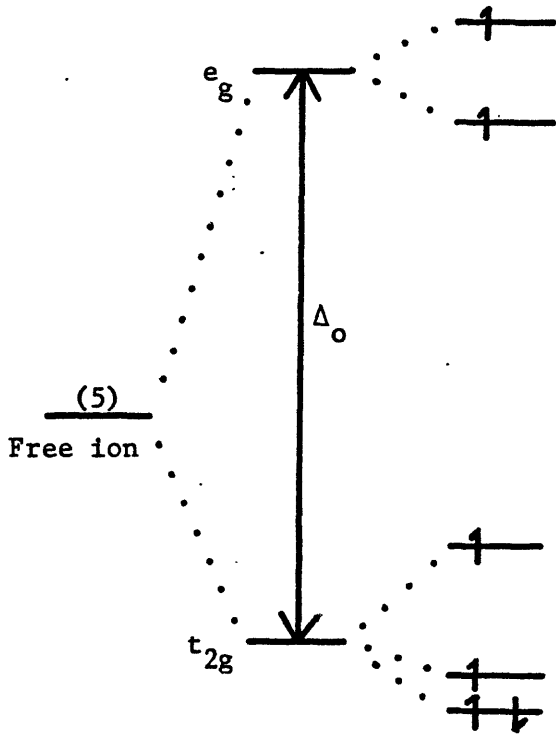
$$\text{where } E_o = \sum_{j=1}^5 E_j / 5 \quad 2.2$$

where  $E_{ji}$  is the energy of the orbital level occupied by the  $i^{\text{th}}$  3d electron,  $E_j$  is the energy of the  $j^{\text{th}}$  level, and  $E_o$  is known as the baricentre of energy. The filling of the five 3d orbital levels is determined by the rule of maximum multiplicity for the first transition series elements in silicates. That is, as many levels as possible are occupied by just one electron before the doubling or pairing of electrons is permitted (figure 2.1). Since as many spins as possible are unpaired, this is known as the high spin state. However, in some minerals such as pyrite, for example, the crystal-field splitting parameter exceeds the pairing energy,  $P$ , so that the pairing of electrons is energetically favorable before all of the levels are occupied singly (figure 2.1), yielding the low spin state. Each spin state for a given cation has a different ionic radius and

Figure 2.1

The high spin and low spin configurations for ferrous iron in a slightly distorted octahedral site. The relative magnitudes of the octahedral crystal-field splitting energy,  $\Delta_o$ , and the pairing energy,  $P$ , determine the spin state.

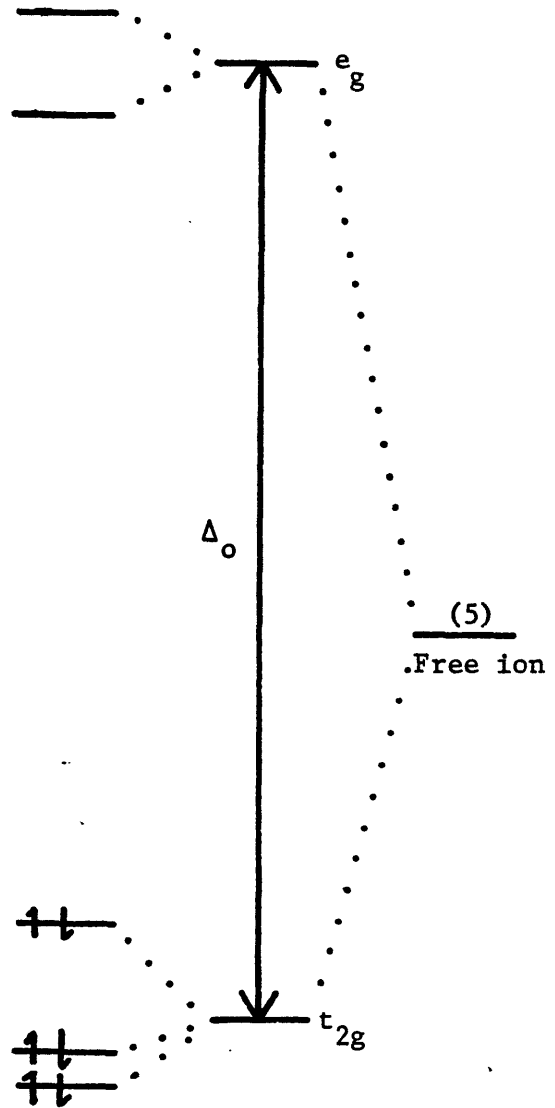
The diagram also shows schematically how the energy degeneracy of the five 3d levels in the free ion is lifted when the ion is surrounded by an octahedral ligand environment.



High spin ferrous iron

$$\Delta_o < P$$

e.g.  $\text{Fe}^{2+}$  in silicates



Low spin ferrous iron

$$\Delta_o > P$$

e.g.  $\text{Fe}^{2+}$  in  $\text{FeS}_2$

properties, so that if a high spin  $\rightarrow$  low spin transition should occur in a given compound, it can be expected to undergo substantial changes in physical properties.

Although the energies,  $\Delta$  and CFSE, are small compared to the total lattice energy of a solid, they can be estimated from spectral measurements fairly accurately so that their influence on the behavior of transition elements in mineral structures and crystal chemistry is reasonably well understood on the basis of crystal-field theory.

Ligand-field theory extends crystal-field theory by considering the ligands as more than point charges and, in particular, attempts to describe the interaction of ligand electrons with cation electrons. This is equivalent to describing the covalency of the metal-ligand bonding which crystal-field theory ignores because it treats the bonding as purely electrostatic or ionic. Two parameters, known as Racah parameters B and C, have been introduced into ligand-field theory to describe the degree of covalency of the metal-ligand bond. The Racah parameters describe the interelectronic repulsions among the 3d electrons of a given cation. The interelectron repulsions are largest in the free ion since the 3d electrons are most closely drawn in towards the nucleus and have their smallest spatial extent in the free ion. Therefore, the Racah parameters are also largest in the free ion. With increasing covalency, the 3d electron clouds expand and mingle with the ligand electron clouds so that the interelectronic repulsions among the 3d electrons of the cation decrease. Therefore, the Racah parameters generally decrease with increasing covalency.

Both crystal-field theory and ligand-field theory were developed to

interpret the absorption spectra due to transition metal cations in solids or liquids and the values of  $\Delta$ , CFSE and the Racah parameters, B and C, can be estimated from such spectra. Molecular orbital theory was developed for a better and more detailed understanding of the metal-ligand bonding. It is also most useful for interpreting charge-transfer features between metal and ligands which occur in the absorption spectra and higher energy spectra of solids. There is a further charge transfer feature often found in absorption spectra of solids arising from electron transfer between two adjacent cations in the structure. This is known as metal-metal charge transfer and commonly occurs between two oxidation states of the same cation (e.g.,  $\text{Fe}^{2+} \rightarrow \text{Fe}^{3+}$ ) although not exclusively by any means. None of the theories discussed here can adequately describe this phenomenon.

This brief description of the electronic theories of solids should suffice for this study as much more detailed accounts can be found in the literature. Band theory is treated by Kittel (1966). Ligand-field and crystal-field theories are treated by Figgis (1968) and by Cotton (1971). Molecular-orbital theory is treated in a traditional manner by Cotton (1971) whereas the SCF- $X_{\alpha}$  computational technique is best summarized by Johnson (1973). For information on metal-metal charge transfer the papers by Allen and Hush (1967) and Hush (1967) should be consulted.

## 2.3 High Pressure Results

### 2.3.1 Effect of pressure on electrical conductivity

The measurement of electrical conductivity is one of the easiest to make at very high pressures and many such measurements have been made on a variety of materials from metals to insulators. Generally with increasing

pressure the electrical conductivity of semimetals and semiconductors increases quite rapidly and metallic-like conduction is the rule for these phases above 200 kb (Drickamer, 1965). For example, the elements iodine and selenium, which are insulators at ambient conditions, behave like metals at high pressure and many semiconductors and insulators based on the diamond structure, such as silicon, germanium and ZnS, exhibit metallic-like electrical conduction at pressures in excess of about 100-200 kb. The changes in conductivity with pressure can almost always be correlated with changes in the gap between the conduction and valence bands. As the conductivity increases, the band gap decreases and vice versa. In the band model, it is predicted that as the interatomic distance decreases, the bands get broader and increasingly overlap, which is equivalent to predicting that as pressure is increased, the solid becomes increasingly metallic-like. This is entirely consistent with the general behavior of these phases with pressure. However, the fine details must be determined by the band structure of the individual phase. For more ionic crystals such as the thallos halides which crystallize in the CsCl structure, the band gap also decreases rapidly (Drickamer, 1965), suggesting that ionic insulators will also become metallic at very high pressures. However, since the original band gap is larger at zero pressure than in the semimetals and semiconductors, then it is necessary to go to higher pressures before the metallic-like state is reached.

Electrical conductivity experiments on silicates as a function of pressure have been carried out by Bradley et al. (1964, 1973), by Mao (1973) and by Duba et al. (1974). Bradley et al. (1964) investigated the



conductivity of olivine as a function of temperature, pressure, Fe/Mg ratio and ferric content and found that at constant pressure and composition the conductivity,  $\sigma$ , of all olivines increased on heating according to the equation:

$$\sigma = \sigma_0 e^{-E/kT} \quad 2.3$$

where  $\sigma_0$  and E are functions of composition:  $\sigma_0$  increases markedly with Fe<sup>3+</sup> content while E, the activation energy for conduction, decreases with increasing pressure and with increasing Fe<sup>2+</sup> content except when the Fe<sup>2+</sup> content is less than 1%. Similar conductivity experiments (Bradley et al., 1973) on nickel and manganese orthosilicates have shown a similar pressure trend for both conductivity and activation energy as for ferrous iron. The consensus of data indicates that M<sup>3+</sup> and vacancy formation is responsible for the conductivity of iron, manganese and nickel orthosilicates. Similar conclusions have been reached by Duba (1972), Duba and Nicholls (1973) and Duba et al. (1973) in a sequence of different conductivity measurements correlated with the oxidation state of iron in olivines in various ways. Therefore, the electrical conductivity should be sensitive to factors controlling the oxidation state of iron.

Results obtained by Mao (1973), not only for olivines but also for other ferrous phases, show very similar electrical conductivity trends over a much wider range of pressure to those found by Bradley et al. (1964). In addition, spectroscopic measurements and observations made on samples under pressure show a considerable broadening and shift to lower energy of the ferrous-ligand charge transfer band. This phenomenon suggests that the

decrease in activation energy with pressure for electrical conduction observed by Bradley et al. (1964) results from a decrease in the effective band gap with pressure associated with broadening of the conduction band. The augmentation of electrical conductivity with pressure of  $(\text{Mg,Fe})_2\text{SiO}_4$  polymorphs and  $(\text{Mg,Fe})\text{O}$  lead Mao (1973) to suggest that the inversion of electrical conductivity data to give temperature profiles for the Earth must result in temperatures that are quite inaccurate, since such inversion studies do not allow for the substantial increase in  $\sigma$  with pressure.

### 2.3.2 High pressure absorption spectral measurements

In addition to the absorption spectral results on the pressure shift of the charge transfer edge in ferrous silicates reported by Mao (1973), Pitt and Tozer (1970a) and Balchan and Drickamer (1959), which are probably best interpreted by means of band theory, there are a number of pressure-induced effects in high pressure absorption spectral studies which are more readily interpreted using ligand-field theory.

The crystal-field splitting parameter,  $\Delta$ , is predicted to increase with pressure because of the following relationship:

$$\Delta \propto r^{-5} \quad \text{or} \quad \Delta \propto V^{-5/3} \quad 2.4$$

or

$$\ln \Delta \propto -5/3 \ln V \quad 2.5$$

where  $r$  is the metal-ligand bond length and  $V$  is the volume of the site.

Thus with pressure:

$$\frac{d\Delta}{\Delta dP} = \frac{-5}{3V} \frac{dV}{dP} \quad 2.6$$

$$\frac{d\Delta}{dP} = \frac{+5\Delta}{3K} \quad 2.7$$

where  $K$  is the bulk modulus of the site. This equation would appear to be very easy to test. However, reliable values for  $\Delta$  at high pressure are difficult to obtain since usually the mineral site is distorted and also  $K$  for a given mineral site can only be measured by means of crystal structure analysis as a function of pressure. Nevertheless, by taking high symmetry oxides such as  $MgO$  or  $Al_2O_3$  and doping them with small concentrations of transition elements, these problems are circumvented, since the distortion of the site will be minimized. Also,  $K_{site} = K_{bulk}$  can therefore be estimated from PV systematics for the solid. Such results have been summarized by Drickamer (1965). For  $Al_2O_3$  the  $r^{-5}$  dependence of  $\Delta$  holds very well for  $Ti^{3+}$ ,  $V^{3+}$ ,  $Cr^{3+}$ ,  $Ni^{3+}$  and  $Ni^{2+}$ . For  $MgO$ ,  $\Delta$  increases slightly faster than  $r^{-5}$  for all ions investigated which include  $Ti^{3+}$ ,  $Ni^{2+}$ ,  $Cr^{3+}$  and  $Co^{2+}$ . This is attributed to the fact that the local compressibility around these ions may be slightly greater than the bulk compressibility of  $MgO$ . A similar approach has been undertaken by Shankland et al. (1974) for ferrous iron in mineral structures, which shows that the ferrous crystal-field bands do shift to higher energy with pressure. These investigators also found that the energy,  $E$ , of bands about  $10,000 \text{ cm}^{-1}$ , which can be related to  $\Delta$ , increases with pressure according to the equation:

$$\frac{dE}{dP} \approx 1.3 \frac{E}{K} \quad 2.8$$

where  $K$  is the bulk modulus of the solid. Whether this result has any quantitative relevance to how the crystal-field splitting parameter varies

with pressure is dubious, because of the many assumptions which must be made to interrelate equations 2.7 and 2.8.<sup>1</sup>

The Racah parameter, B, has also been measured as a function of pressure for some simple Cr<sup>3+</sup>, Ni<sup>2+</sup> and Mn<sup>2+</sup> containing systems. These measurements are summarized by Drickamer (1965) and show that the Racah parameters for different ions all decrease with pressure. For example, the value of B for Cr<sup>3+</sup> in Al<sub>2</sub>O<sub>3</sub> changes from 630 cm<sup>-1</sup> to 610 cm<sup>-1</sup> over about 100 kb. However, this is a relatively small change compared to the change from the free ion value of about 920 cm<sup>-1</sup> (Lever, 1968) to the value for Cr<sup>3+</sup> in Al<sub>2</sub>O<sub>3</sub>. Decreases in the value of B with pressure arise from a decrease in the interelectronic repulsions among the 3d electrons due to an increase in covalency as described above. Therefore, the decrease in B with pressure indicates a slight but significant increase in covalency with pressure.

Some very limited data can be obtained on crystallographic effects as a function of pressure from the changes in separation of crystal-field bands split by distortions of the crystal. However, these effects can at best only be qualitatively related to specific atomic motions even when the symmetry of the site is very high.

The intensity of spectral bands in iron minerals will be affected by pressure, but exactly how is a difficult quantum-mechanical problem, so

---

<sup>1</sup>These results, however, indicate that  $\Delta$  does probably increase with pressure, and so ferrous crystal-field stabilization energies can also be expected to increase with pressure, unless there is drastic reduction in site distortion with pressure, offsetting the increase in  $\Delta$  with pressure.

that results on this topic are sketchy. On the whole, metal-ligand charge transfer bands appear to increase much more rapidly in intensity with pressure than crystal-field bands (Mao, 1973; Abu-Eid, 1974). Accompanied by a shift to lower energy, the charge transfer bands begin to dominate the spectra of ferrous minerals at high pressure. This has important consequences, not only for the color of the mineral, but also for the transfer of heat by radiation through mantle silicates. Mao (1973) suggests that the pressure-induced shift and increase in intensity of the first metal-ligand charge transfer band (or absorption edge) in ferrous containing silicates will considerably reduce the importance of radiative heat transfer in the mantle. This is in accord with Pitt and Tozer (1970b) but in contrast to Clark's (1957a) evaluation on the basis of the zero pressure spectrum. Both Mao (1973) and Pitt and Tozer (1970b) suggest that phonon conduction would appear to be a more viable heat transfer mechanism than radiative transfer. Heat convection in the upper mantle may be an even more efficient heat transfer mechanism than any of these mechanisms and must also be considered when temperature profiles for the Earth are determined (Pitt and Tozer, 1970b).

Optical absorption measurements of iron minerals as a function of pressure have yielded information on the change of covalency of metal-ligand bonds with pressure and on the transport of heat within the Earth. In principle, such measurements can give information on site compressibilities, the change in site distortion with pressure and the value of CFSE as a function of pressure. In combination with electrical conductivity measurements, optical absorption studies as a function of pressure indicate

that ferrous silicates become increasingly conducting at high pressures but remain semiconductors as the effective bond gap shifts very roughly about 1 ev in about 200 kb. Almost all such investigations have been carried out on ferrous silicates, whereas most high pressure Mössbauer studies reviewed in the next section have investigated the electronic structure of ferric phases. Therefore, comparison between the results of absorption spectra and Mössbauer measurements at high pressures are only qualitative at this stage.

### 2.3.3 Previous high pressure Mössbauer results

Although the theory of Mössbauer spectroscopy is outlined in the next chapter, the results of previous high pressure Mössbauer studies which are relevant to the present study will be discussed here. For further background, the reader may consult section 3.2 on Mössbauer theory.

Until the start of this thesis, all the work of interest had come from the laboratory of Professor H.G. Drickamer at the University of Illinois, Urbana, where investigations were concentrated on electronic transitions such as spin-state transitions and pressure-induced reduction in chemical compounds. In the course of such studies, results have been presented on how other Mössbauer parameters such as isomer shift, quadrupole splitting and magnetic hyperfine splittings change with pressure. However, relatively few fundamental interpretations have been made of such data.

#### 2.3.3 (a) Spin state transitions

At high pressures, spin-state transitions in both ferric and ferrous iron should occur, which completely changes the character and behavior of these cations in minerals (Fyfe, 1960; Burns, 1969a;

Strens, 1969; Gaffney, 1972). Such transitions should occur in the Earth at depths in excess of 1,000 km, so that the observation by static high pressure techniques of such transitions in silicates containing octahedral iron cations is not possible at the present time. However, dynamic shock experiments may be able to induce such transitions. Theoretical, but inconclusive, attempts have been made to fit Hugoniot data obtained in shock experiments to hypothetical phases containing low-spin iron cations (Gaffney and Anderson, 1973).

A number of high pressure Mössbauer experiments have found spin-state changes in iron compounds of no direct mineralogical interest. The high spin to low spin transition in  $\text{Fe}^{2+}$  has been observed in  $\text{MnS}_2$  doped with about 2% ferrous iron (Bargeron et al., 1971). Up to about 40 kb, only about 10% of the ferrous iron is in the low spin state, but at higher pressures the transition from high spin to low spin gradually takes place so that at about 125 kb the transition is essentially complete and the ferrous iron is all in the low spin state. As is well known, pyrite,  $\text{FeS}_2$ , is completely low spin at ambient conditions, so that locating the ferrous cation in the larger  $\text{MnS}_2$  framework is equivalent to applying a negative pressure, which can be eliminated by then applying pressure. Similar transitions have been observed in ferrous organometallic complexes (Fisher and Drickamer, 1971).

The reverse transition from low spin to high spin has also been observed in iron with increasing pressure. This is surprising because ionic radii of high spin states are generally larger than those of the low spin states (Shannon and Prewitt, 1969). However, in certain low spin ferrous

cyanides and organometallic complexes where there is extensive  $\pi$  bonding between ligand and cation, it appears that it is possible to partially eliminate spin-pairing with increasing pressure. This change in spin state occurs by changing the electron occupation of ligand orbitals due to relative energy shifts of orbital levels and to changes in the configuration interaction between different ligand states (Drickamer and Frank, 1973). Because of the extremely covalent and backbonding nature of cation-ligand bonds in compounds exhibiting these reverse transitions, it is unlikely that low spin to high spin transitions occur in minerals which do not exhibit this kind of bonding.

The low spin state has been suggested for the silicate minerals deerite and gillespite. It was suggested that deerite might contain low spin ferrous iron on the basis of its low magnetic susceptibility, density and metallic-like lustre (Carmichael et al., 1966). However, subsequent Mössbauer experiments (Bancroft et al., 1968) and further magnetic susceptibility considerations (Strens, personal communication) showed that the mineral contained only high spin iron. Gillespite,  $\text{BaFeSi}_4\text{O}_{10}$ , contains ferrous iron in a square planar site and, based on an obvious color change, was reported to undergo a high spin  $\rightarrow$  low spin transition at 26 kb (Strens, 1966) since the geometry of the site is highly favorable for such a transition. Unpublished results obtained by Vaughan and Tossell on the Mössbauer spectra of gillespite as a function of pressure were inconclusive but did show that a definite change was taking place. Subsequently, Hazen and Abu-Eid (1974) have shown that the transition is, in fact, a displacive phase transition and that the square planar site about ferrous iron becomes



a distorted tetrahedral site above 26 kb. Therefore, at the present time, no direct evidence exists for spin-pairing in ferrous iron in silicates. For this reason, spin-state transitions were not expected to be observed in a study of iron-containing silicates at pressures up to 200 kb and no effort was directed towards this phenomenon in this study.

### 2.3.3 (b) Pressure-induced reduction

Pressure-induced reduction is the process whereby ferrous iron is formed from ferric iron as the result of pressure per se. It has been observed in a wide range of compounds from ionic ferric fluorides to complex ferric organometallic phases. This transition is easily recognized by Mössbauer spectroscopy, since ferrous and ferric Mössbauer absorptions are quite different. Recently, Mössbauer results have been correlated with high pressure absorption spectral measurements (Frank and Drickamer, 1972; Hara et al., 1974) so that the phenomenon is now well established by these techniques.

The pressure-induced reduction of ferric phases is, for the most part, reversible, although usually with hysteresis (figure 2.2). For most of the phases studied, the pressure dependence of the conversion of ferric to ferrous is of the form (Lewis and Drickamer, 1968b):

$$K = \frac{C(\text{II})}{C(\text{III})} = AP^B \quad 2.9$$

where A and B are constants; K is the equilibrium constant; C(II) and C(III) are the fractions of ferrous and ferric sites; and P is the pressure in kb. Table 2.1 is a summary of some data on this conversion. Notable exceptions, which Drickamer and his co-workers investigated and

Figure 2.2

The effect of pressure on ferric chloride,  $\text{FeCl}_3$  (after Lewis and Drickamer, 1968b). Note the pressure-induced appearance of peaks due to ferrous iron and also the reversible nature of the phenomenon with some hysteresis on releasing the pressure.

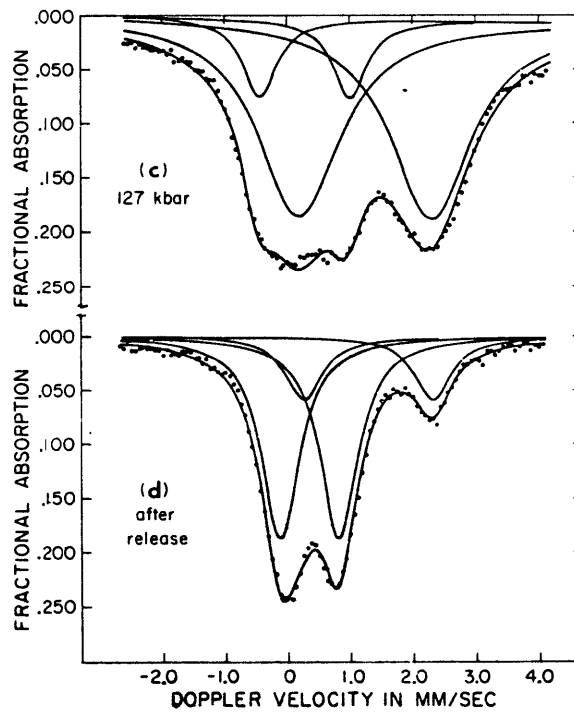
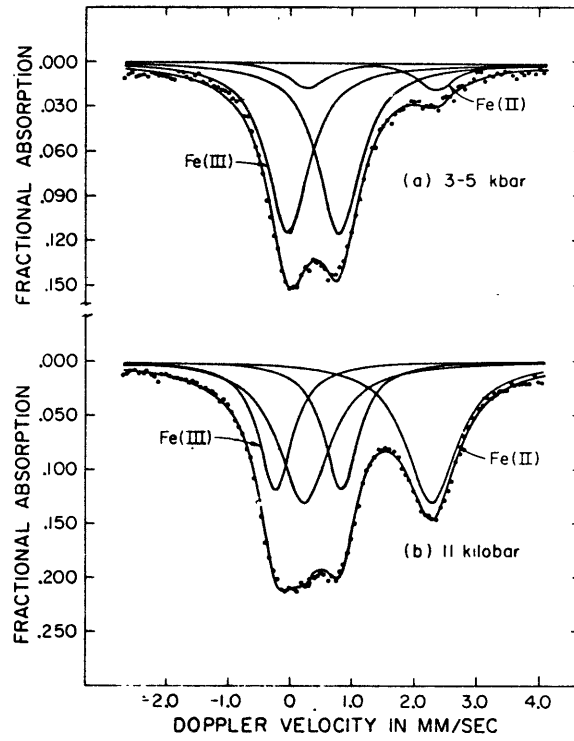


Table 2.1

THE PARAMETERS, A AND B, WHICH DESCRIBE THE REACTION:

$$C(\text{II})/C(\text{III}) = K = AP^B$$

FOR MANY OF THE COMPOUNDS STUDIED BY DRICKAMER AND CO-WORKERS  
(Measurements at room temperature, unless otherwise indicated.)

COMPOUND	A	B	Ref*
Phosphate glass (High Fe <sup>2+</sup> content)	0.130	0.192	1
FeCl <sub>3</sub> ·6NH <sub>3</sub> (P > 25 kb)	0.460	0.270	2
Sr Ferric oxalate	0.115	0.301	3
Phosphate glass (Low Fe <sup>2+</sup> content)	0.049	0.312	1
Ferric citrate	0.112	0.350	4
FeBr <sub>3</sub>	0.076	0.526	5
FePO <sub>4</sub>	0.079	0.457	1
KFeCl <sub>4</sub>	0.091	0.497	5
Ferric oxalate	0.041	0.510	3
Fe(NCS) <sub>3</sub> ·6H <sub>2</sub> O	0.136	0.528	3
FeCl <sub>3</sub>	0.265	0.564	5
K <sub>3</sub> Fe(NCS) <sub>6</sub>	0.024	0.692	3
FeF <sub>3</sub> ·3H <sub>2</sub> O	0.027	0.950	2
FeF <sub>3</sub> ·3H <sub>2</sub> O (excess H <sub>2</sub> O)	0.072	0.950	2
FeCl <sub>3</sub> ·3H <sub>2</sub> O	0.063	0.950	2
Ferric acetate (418 °K)	0.022	0.986	4
Hemin	5.5 x 10 <sup>-3</sup>	1.53	6
Fe(AHA) <sub>3</sub>	1.3 x 10 <sup>-3</sup>	1.66	7

Table 2.1  
(Continued)

COMPOUND	A	B	Ref <sup>*</sup>
Ferrichrome	$3.1 \times 10^{-4}$	1.67	7
Fe(SHA) <sub>3</sub>	$3.7 \times 10^{-5}$	1.86	7
K <sub>3</sub> Fe(CN) <sub>6</sub>	0.0011	2.06	4
Ferric acetylacetonate	$1.2 \times 10^{-5}$	2.23	3
Fe(BHA) <sub>3</sub>	$8.1 \times 10^{-7}$	2.54	7
Ferric acetate (382 °K)	$2.2 \times 10^{-7}$	3.05	4
FeCl <sub>3</sub> ·6NH <sub>3</sub> (P < 25 kb)	$2.4 \times 10^{-6}$	4.06	2
Ferric β-diketone complexes	$\sim 10^{-6} - 10^{-2}$	2.80 - 0.98	8

\*References:

- |                                     |                                    |
|-------------------------------------|------------------------------------|
| (1) Lewis and Drickamer, (1968a)    | (5) Lewis and Drickamer, (1968b)   |
| (2) Holzapfel and Drickamer, (1969) | (6) Champion and Drickamer, (1967) |
| (3) Drickamer et al., (1970)        | (7) Grenoble and Drickamer, (1971) |
| (4) Drickamer et al., (1969b)       | (8) Frank and Drickamer, (1972)    |

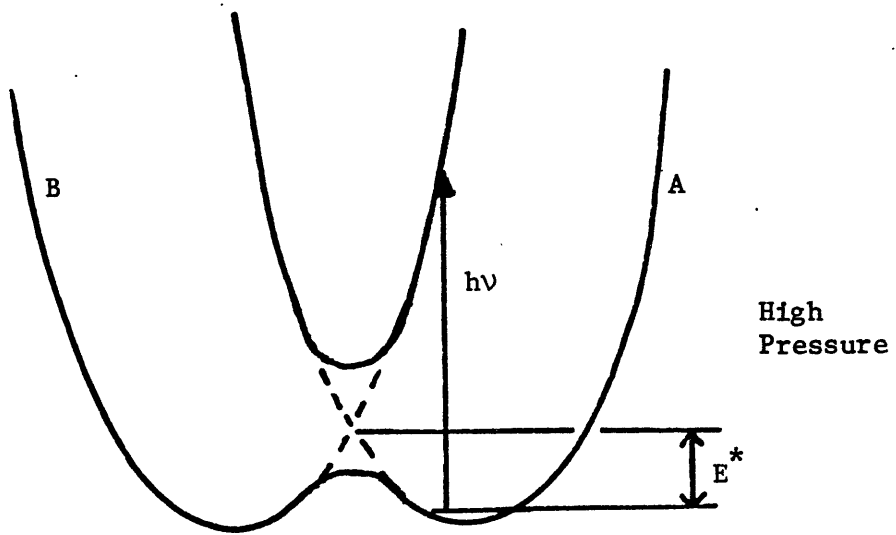
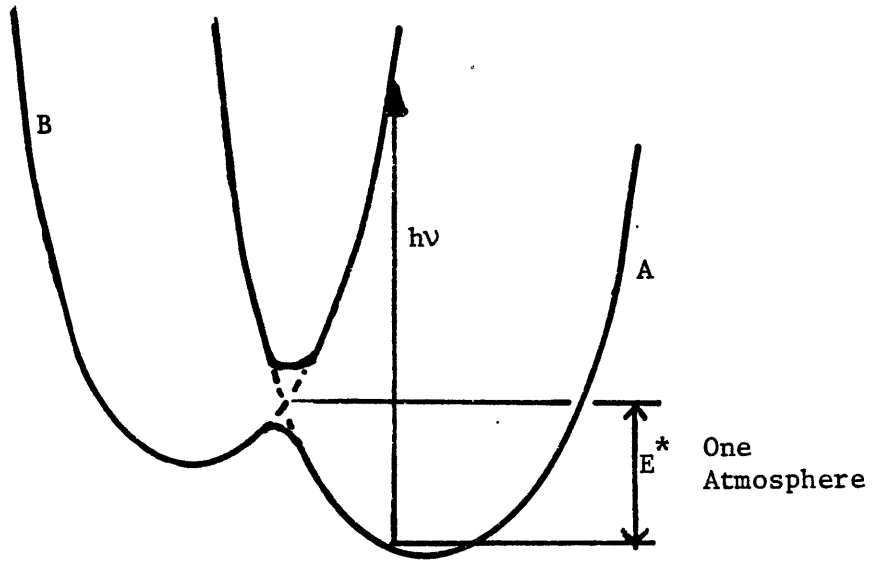
failed to show pressure-induced reduction, are a ferric containing silicate glass (Lewis and Drickamer, 1968a), and hematite (Vaughan and Drickamer, 1967a). Certain ferric fluorides were originally reported not to show pressure-induced reduction (Champion et al., 1967) but were later shown to exhibit the phenomenon to a small degree (Christoe and Drickamer, 1970; Holzapfel and Drickamer, 1969). Vaughan and Tossell (unreported results) also found no conclusive evidence for reduction in acmite,  $\text{NaFeSi}_2\text{O}_6$  or andradite,  $\text{Ca}_3\text{Fe}_2\text{Si}_3\text{O}_{12}$ . However, the phase magnesioriebeckite,  $\text{Na}_2\text{Mg}_3\text{Fe}_2^{3+}\text{Si}_8\text{O}_{22}(\text{OH})_2$ , did exhibit pressure-induced reduction (Burns et al., 1972b). In this amphibole, the  $\text{Fe}^{2+}$ /total iron ratio changed from 1/3 to close to 1/2 over 200 kb, indicating that the ferric cations were being reduced to ferrous cations. The results indicated that the pressure-induced reduction phenomenon does occur in minerals, but that the effect is probably not very large. In order to understand why the effect is probably small in minerals requires a more detailed examination of the data and mechanisms postulated for this process.

The formation of ferrous cations at the expense of ferric cations as a result of pressure involves the transfer of an electron from the ligand environment to the central cation. Increasing pressure tends to shift the energy of one set of orbitals with respect to another, which may frequently lead to a new ground state for the system. As pressure is increased, the ferrous cation and a positive hole on the ligands must become more stable relative to the ferric cation and regular ligands, so that reduction occurs. This is shown schematically in figure 2.3. The charge transfer process is believed to occur thermally, which means that it is not subject to selection

Figure 2.3

Schematic configuration diagram for pressure-induced reduction (after Drickamer et al., 1972). Potential energy curve A represents ferric iron and regular ligands, while potential energy curve B represents ferrous iron and the electron deficient ligands which becomes increasingly stable with increasing pressure relative to curve A.

Optical transitions occur vertically on such a diagram and need an energy,  $h\nu$ , to reach the new electronic state, whereas thermal transitions only need exceed an energy,  $E^*$ , to achieve the same result.





rules and other restrictions that govern optical charge transfer processes. Optical transitions must occur vertically in figure 2.3 in accordance with the Franck-Condon principle. Thermal transitions, on the other hand, are slow and can take advantage of atomic rearrangements and relaxed selection rules. For this reason, thermal transitions usually occur at much lower energy than optical transitions (Drickamer et al., 1972).

From a thermodynamic point of view, in order for reduction to occur with increasing pressure, the volume increase due to the formation of the larger ferrous cation must be more than compensated for by the decrease in volume due to the formation of a positive hole on the ligands. Therefore, as long as the volume of the system as a whole decreases on reduction, the reduction will be favored by increasing pressure (Drickamer et al., 1969a).

It would appear from the details of the mechanism that reduction should occur most readily in those compounds containing ligands with electron donating properties or ligands which are capable of extensive positive charge delocalization. Such a systematic study of the ligands' influence on the reduction has been recently carried out by Frank and Drickamer (1972). Twelve differently substituted  $\beta$ -diketone ferric chelates were synthesized and grouped according to the electron donating ability of the ligands. The results of the investigation were somewhat inconclusive as the electron donating ability of different chelating ligands behaved differently under pressure. Nevertheless, a number of conclusions could be reached showing how the ligands affect the reduction. Generally it was found for these chelates that the constant A in equation 2.9 is a measure of the electron donor property. Other factors being equal, large values of

A correlated with good electron donating ability.

The two phosphate glasses listed in table 2.1 indicate a further complexity. The presence of ferrous cations influences the reduction of ferric to ferrous giving rise to quite different values of A and B for the two phosphate glasses, which differ only in ferrous content. Since silicates commonly contain both ferrous and ferric cations, this complexity should be of interest to mineralogically related studies.

Table 2.1 also indicates that the value of B generally rises with increasing complexity and size of the ligands and thus decreasing  $\text{Fe}^{3+}$  atom % in the phase. Now, B is a measure of the pressure range over which reduction occurs since large values of B correlate with a small pressure range for reduction and vice versa. The range of pressure for the reduction is a result of the interaction between iron centers (Slichter and Drickamer, 1972) and B is a measure of such interaction. Little interaction between iron centers correlates with a small pressure range for reduction and a large value of B; and, conversely, large interaction between iron centers correlates with a large pressure range for reduction and a small value of B. Small interaction between iron cations and large values of B are to be expected for molecular solids, whereas ionic solids should give rise to large interactions and small values of B.

Other important factors which ought to affect the reduction but which have not been fully investigated are (i) the role of coordination of the ferric cation and (ii) the compressibility of the site or phase. The coordination of ferric cations should be important for two reasons: firstly, the more ligands coordinated directly to the cation, the easier it should

be for positive charge delocalization to take place; and, secondly, cations in sites which can accommodate both ferrous and ferric ions should reduce more easily than those cations which are in sites large enough for ferric cations, but uncomfortably small for ferrous cations. This may be the underlying reason why the ferric-containing silicate glass did not reduce: the ferric cations are in tetrahedral sites and radius ratio criteria do not favor the formation of ferrous cations in such sites. The phosphate glasses, by way of contrast, do contain octahedrally coordinated ferric cations and reduce quite readily. Similarly, octahedrally coordinated ferric cations in  $\text{FeCl}_3$  reduce more easily than tetrahedrally coordinated ferric cations in  $\text{KFeCl}_4$  despite the lower atom %  $\text{Fe}^{3+}$  content in the latter which would be the basis for predicting a reduction trend opposite to that observed.

The second uninvestigated parameter, the role of compressibility, should affect the reduction significantly for the following reason: since reduction depends on the relative energies of the normal and reduced states, the less compressible the compound, the greater the pressure that must be applied to reduce the difference in relative energy so that appreciable thermal charge transfer may take place. Therefore, compounds which are highly incompressible will show little reduction. This factor, along with high atom %  $\text{Fe}^{3+}$  content is probably responsible for the reduction of  $\text{Fe}^{3+}$  cations not being observed in hematite, acmite and andradite.

In addition, the poor electron donating ability of oxygen anions in silicates relative to other ligands around the ferric cation will also inhibit the reduction phenomena. Fluoride anions are also very poor

electron donating ligands and therefore do not show large degrees of reduction. The poor electron donating ability may also be reflected in the degree of covalency of the ferric cation bonds. Ionic bonding, for the most part, should give rise to little reduction whereas covalent bonding should give rise to considerably more reduction. For this reason, some theoretical analysis has been attempted (Drickamer et al., 1972) in relating the thermal charge transfer phenomenon to the position and breadth of the optical charge transfer peak which is a measure of the difference in energy of the reduced state relative to the ground state. In increasingly covalent systems, such bands occur at lower and lower energies suggesting that the reduction phenomena occurs easiest in covalent systems.

For most systems, the conversion to the ferrous state increases with increasing temperature indicating that the enthalpy for the electron transfer is endothermic. Typical  $\Delta H$  values range from -5 to +20 Kcal/mole (Drickamer et al., 1970). The temperature dependence of this electronic transition in silicates would be of great significance for studies of the Earth's interior, since it raises the question of whether ferric cations are stable in the Earth's mantle (Tossell et al., 1972).

### 2.3.3 (c) Effect of pressure on hyperfine magnetic splittings

Relatively little work has been carried out on the effect of pressure on the magnetic behavior of phases using Mössbauer techniques. The magnetic hyperfine splitting parameter,  $H_0$ , is reduced by only 1% in hematite (Vaughan and Drickamer, 1967a) whereas the magnetic splittings in iron sulphides are eliminated by the application of 50 kb (Kasper and Drickamer, 1968; Vaughan and Tossell, 1973). This distinction suggests

a fundamental difference in bonding and electronic behavior between sulphides and oxides, but nothing has really been made of it. By careful choosing of composition and conditions, large pressure-induced magnetic effects can be produced and monitored by Mössbauer spectroscopy. Two such studies should be mentioned since attempts have been made to theoretically analyze the results. These are, firstly, a study of Pd<sup>57</sup>Co alloys (Cohen and Drickamer, 1973) and, secondly, a study of CoO containing a small amount of ferrous iron (Syassen and Holzapfel, 1973).

### 2.3.3 (d) Effect of pressure on the Mössbauer isomer shift

The isomer shift is a primary parameter obtainable from a Mössbauer spectrum (see section 3.2). It is a measure of the s electron density at the iron nucleus and can be related to the degree of covalency of the iron-ligand bond. As a function of pressure, the isomer shifts of most iron compounds show a decrease with pressure (Champion et al., 1967; Drickamer and Frank, 1973). This decrease may be interpreted as an increase in covalency of the iron-ligand bond. On the average, Fe(II) compounds show a larger effect than Fe(III) compounds which may be related to predicted differences in site compressibility or to a larger change of covalency for Fe(II) with pressure. Other effects (Erickson, 1967) may also contribute to the isomer shift, so that each case should be analyzed individually.

Some data exist for the minerals ilmenite, pyrite and hematite. Ilmenite, FeTiO<sub>3</sub>, shows a decrease in isomer shift from 1.04 to 0.94 mm/sec over 150 kb (Vaughan and Drickamer, 1967a); pyrite, FeS<sub>2</sub>, which contains low spin Fe(II), shows a decrease in isomer shift from 0.30 to 0.15 mm/sec

over 200 kb (Vaughan and Drickamer, 1967b); hematite, on the other hand, shows a very small decrease in isomer shift over 200 kb, which may almost entirely be explained by the second-order Doppler effect, or change in the mean square velocity of the nucleus in its site with pressure (Vaughan and Drickamer, 1967a). For ferric iron in tetrahedral sites in silicate glass, a significant increase in isomer shift over 100 kb is observed (Lewis and Drickamer, 1968a). This result is atypical compared to the behavior of other phases which are of mineralogical interest or are fairly ionic in nature. For example, all isomer shift trends reported by Champion et al. (1967), for a number of ionic inorganic iron phases, show significant decreases with pressure.

Despite the large body of data on the isomer shift trends with pressure, to date very little use has been made of it. Frank and Drickamer (1972) were able to correlate the isomer shift change with pressure with the degree of pressure-induced reduction occurring in iron  $\beta$ -diketone complexes over the range 60-160 kb. Besides this correlation, however, no other systematic interpretation of isomer shift data has been presented.

### 2.3.3 (e) Variation of quadrupole splitting with pressure

The quadrupole splitting is another primary parameter obtainable from a Mössbauer spectrum (see section 3.2). The quadrupole splitting depends on the symmetry of the charge distribution about the nucleus and hence on the symmetry of the site. It is, therefore, a parameter which can be related to crystallographic details. For ferric phases, the quadrupole splitting depends only on the position of the charged ions in the crystal structure and pressure-induced changes in the quadrupole

splitting of ferric phases arise from changes in the crystal structure with pressure. For ferrous phases, the quadrupole splitting depends largely on the electronic structure of the iron cation in addition to a smaller contribution from the crystal structure. The electronic structure contribution results from the asymmetric occupation of the five 3d orbital levels by the six 3d electrons. The order of filling the 3d levels and their relative energies are determined by the site symmetry. The relative energies of the levels determine the temperature dependence of the high-spin ferrous quadrupole splitting due to the Boltzmann distribution of the sixth electron over these 3d levels. The pressure dependence of ferrous quadrupole splittings comes from pressure-induced changes in both the crystal structure and the relative energies of the 3d levels.

Ferric quadrupole splittings generally increase with pressure most probably because of bulk compression of the structure, which should increase the quadrupole splitting, even if there is no change in the structural distortions. Ferrous quadrupole splittings show more variable behavior with pressure, presumably because of their dependence on two factors, which tend to act oppositely to each other. The ferric quadrupole splittings with pressure can be generalized, but the ferrous case must be treated on an individual basis.

One of the more important results for this parameter is the pressure trend of the quadrupole splitting of hematite which shows a decrease from +0.37 mm/sec at ambient conditions, to zero mm/sec at about 30 kb and to -0.38 mm/sec at about 200 kb (Vaughan and Drickamer, 1967a). This result has been interpreted as arising from a small movement of the ferric cation

toward the center of symmetry of the oxygen octahedra in hematite accompanied by a Morin transition.

Other than hematite, all quadrupole splitting trends with pressure have only been used qualitatively, if at all, to indicate whether or not the structure is becoming increasingly distorted at high pressure relative to zero pressure.

#### 2.4 Summary of Previous Results

The three techniques, electrical conductivity measurements, absorption spectroscopy and Mössbauer spectroscopy, have been used to elucidate the electronic structure and related properties of iron phases under pressure.

The most general result is that the electrical conductivity of iron minerals can be expected to increase quite significantly with pressure, accompanied by a decrease in the effective band gap as indicated by absorption spectral measurements on the shift of the charge transfer absorption edge. Furthermore, trends of both the Racah parameter,  $B$ , and the Mössbauer isomer shift indicate that metal-ligand bonds become increasingly covalent with increasing pressure. Both absorption spectral measurements and Mössbauer quadrupole splitting data can be used to indicate, in a qualitative manner for the most part, crystallographic changes with pressure. Pressure-induced electronic transitions such as the charge transfer reduction phenomenon and spin-state transitions can also be monitored as a function of pressure using both absorption and Mössbauer spectral techniques.

Most of the evidence available at present suggests that spin-pairing transitions in iron silicates and oxides will not occur at pressures below



200 kb, while pressure-induced reduction may only occur to a small extent in ferric silicate minerals. It is quite possible that compositional conditions could be optimized so that pressure-induced reduction occurs to a much larger extent in silicates. Pressure-induced magnetic transitions have been observed in sulphides, but not in oxide phases; again, a compositional investigation for oxides could result in large and significant effects as a function of pressure.

These pressure-induced changes in the electronic structure and properties of minerals have been applied to questions of the thermal and electrical transport properties of minerals and the Earth. At the present time, interpretations of such properties would appear to be in a state of change, due to the recently encountered phenomena reported by Mao (1973). The incomplete data on the effect of pressure on the absorption spectral parameters,  $\Delta$  and CFSE, may be applied to interpretations of the order/disorder of magnesium and ferrous iron between different sites in minerals, and have been related to compressibility data. More work is needed on these important interrelationships, not only in the sense of more data being obtained but also in the direction of obtaining more complete and reliable estimates of these parameters, rather than relying on very approximate estimates from the energies of bands in the optical absorption spectrum. The results and conclusions of the high pressure Mössbauer technique have been least applied to Earth Sciences, although its potential applications have been summarized by Burns et al. (1972a). In particular, it would appear that much more detailed interpretations of the primary Mössbauer parameters, the isomer shift and quadrupole splitting, as a

function of pressure are possible. Pressure-induced reduction and its effect on mineral properties, in particular, should be a most profitable area for study, since its potential application to Earth Sciences could well be most significant.

## 2.5 Delineation of Areas of Investigation in this Study

As discussed in the last section, of the three techniques which have been mostly used to investigate the electronic properties of iron-containing materials as a function of pressure, the Mössbauer effect has been the least applied to Earth Sciences. For this reason, this study and some earlier work carried out by Vaughan and Tossell here at M.I.T. represent the first serious attempts to apply this high pressure technique to problems in Earth Sciences. It was felt, therefore, that initial studies should represent a survey of the field. By looking at common silicate, oxide and sulphide minerals, containing both ferrous and ferric iron, as well as magnetic and non-magnetic minerals, all of the likely possible electronic phenomena, which are expected to be encountered, would indeed be covered.

The intention of this study is to examine a variety of mineral phases to cover as thoroughly as possible the different kinds of minerals and pressure-induced electronic phenomena. Since Vaughan and Tossell have investigated a number of sulphides, the present study is restricted to oxide and silicate minerals. Due to its potential importance for Earth Sciences, some considerable emphasis is placed on the observation of pressure-induced reduction in ferric silicates, and, based on the conclusions in section

2.3.3 (b), a variety of ferric-containing minerals should be investigated to optimize the compositional conditions. For this and other reasons, the synthesis of phases containing ferric iron is necessary so that the role of coordination and solid solution effects on the pressure-induced reduction phenomenon can be investigated. Such syntheses are reported in the next chapter.

A more detailed understanding of the Mössbauer parameters, isomer shift and quadrupole splitting, is necessary to fully utilize information on the pressure dependence of these parameters. A range of minerals should be investigated so that the trends of isomer shifts and quadrupole splittings with pressure can be subdivided according to valence state and coordination number of the iron cation.

Table 2.2 lists, firstly, all phases which have been previously studied by the high pressure Mössbauer technique and are of direct mineralogical interest and, secondly, those phases which are studied in the present investigation. As can be seen from the list, all common coordination number and valence state combinations for iron in minerals will have been studied, with the exception of ferrous iron in tetrahedral sites. The latter is probably of little consequence in high pressure phases likely to be encountered in the mantle. These twenty or so phases should be sufficient to be able to survey all possible high pressure electronic phenomena in minerals, which can be monitored by Mössbauer spectroscopy.

Table 2.2

## PHASES OF MINERALOGICAL INTEREST STUDIED BY THE HIGH PRESSURE MÖSSBAUER TECHNIQUE

PHASE	COMPOSITION	IRON VALENCE STATE	COORDINATION NUMBER	MAGNETIC	REFERENCE
Iron metal	Fe	0	12	Yes	1
Hematite	Fe <sub>2</sub> O <sub>3</sub>	3	6	Yes	2
Wüstite	FeO	2	6	Yes	2
Ilmenite	FeTiO <sub>3</sub>	2	6		2
Pyrite	FeS <sub>2</sub>	2	6		3
Ferric silicate glass		3	4		4
Magnesioriebeckite	Na <sub>2</sub> Mg <sub>3</sub> Fe <sub>2</sub> Si <sub>8</sub> O <sub>22</sub> (OH) <sub>2</sub>	3 (2)	6 (6)		5
Acmite	NaFeSi <sub>2</sub> O <sub>6</sub>	3	6		6
Andradite	Ca <sub>3</sub> Fe <sub>2</sub> Si <sub>3</sub> O <sub>12</sub>	3 (2)	6 (8)		6
Gillespite	BaFeSi <sub>4</sub> O <sub>10</sub>	2	4 (s.p.)		6
Fayalite	Fe <sub>2</sub> SiO <sub>4</sub>	2	6		6
Troilite	FeS	2	6	Yes	7
Chalcopyrite	CuFeS <sub>2</sub>	3	4	Yes	8

Table 2.2  
(Continued)

PHASE	COMPOSITION	IRON VALENCE STATE	COORDINATION NUMBER	MAGNETIC	REFERENCE
Pyrrhotite	$\text{Fe}_{1-x}\text{S}$	2	6	Yes	8
Garnet	$\text{Ca}_3\text{FeAlSi}_3\text{O}_{12}$	3	6		9
Garnet	$\text{Ca}_3\text{FeCrSi}_3\text{O}_{12}$	3	6		9
Garnet	$\text{Ca}_3\text{TiFe}_2\text{Si}_2\text{O}_{12}$	3	6,4		9
Garnet	$\text{Cu}_{2.5}\text{Zr}_{2.5}\text{Fe}_3\text{O}_{12}$	3	4		9
Ferriphlogopite	$\text{KMg}_3\text{FeSi}_3\text{O}_{10}(\text{OH})_2$	3 (2)	4 (6)		9
Ferriphlogopite	$\text{KMg}_3(\text{Fe,Al})\text{Si}_3\text{O}_{10}(\text{OH})_2$	3 (2)	4 (6)		9
Muscovite	$\text{K}(\text{Al,Fe,Mg})_2\text{AlSi}_3\text{O}_{10}(\text{OH})_2$	3,2	6,6		9
Ferrimicrocline	$\text{KFeSi}_3\text{O}_8$	3	4		9
Almandine	$(\text{Fe,Mg})_3\text{Al}_2\text{Si}_3\text{O}_{12}$	2	8		9
Fayalite	$\text{Fe}_2\text{SiO}_4$	2	6		9
Orthoferrosilite	$(\text{Fe,Mg})\text{SiO}_3$	2	6		9
Hematite	$\text{Fe}_2\text{O}_3$	3	6	Yes	9
Magnetite	$\text{Fe}_3\text{O}_4$	2,3	6,4	Yes	9

Table 2.2  
(Continued)

References:

- |                                    |  |
|------------------------------------|--|
| (1) Pipkorn et al., (1964)         | (6) Vaughan and Tossell, (unpublished) |
| (2) Vaughan and Drickamer, (1967a) | (7) Kaspar and Drickamer, (1968)       |
| (3) Vaughan and Drickamer, (1967b) | (8) Vaughan and Tossell, (1973)        |
| (4) Lewis and Drickamer, (1968a)   | (9) This Work                          |
| (5) Burns et al., (1972b)          |  |

## Chapter 3

### EXPERIMENTAL DETAILS

#### 3.1 Introduction

This chapter describes the theory and practice of Mössbauer spectroscopy, the high pressure modifications to normal Mössbauer techniques and the results of synthesis experiments, which were carried out in the course of this study. It outlines the experimental work of this study, while the results of the high pressure Mössbauer experiments are described and discussed in detail in the following two chapters. A discussion of conclusions relating to the hydrothermal synthesis experiments is presented in Appendix A1.

#### 3.2 Mössbauer Spectroscopy: Theory and Practice

##### 3.2.1 The Mössbauer effect

The Mössbauer effect, which was only discovered as recently as 1957 (Mössbauer, 1958), is the name given to the phenomenon of recoilless fluorescence and resonant absorption of  $\gamma$ -rays. Although it is a nuclear property, the phenomenon is sensitive to the chemical and bonding environment around nuclei exhibiting this effect because the  $\gamma$ -ray energy is perturbed slightly. The Doppler effect is used to perturb the incident  $\gamma$ -ray energy in order to establish resonance between nuclei in differing chemical environments. To obtain resonance, however, the  $\gamma$ -ray must be absorbed and emitted without recoil. The probability of the recoilless process occurring is great only when the nucleus is in a solid since the

recoil energy may be dissipated by phonon scattering throughout whole crystallites without the nuclei in question experiencing recoil. The probability of the recoilless process,  $f$ , is given by (Wertheim, 1964):

$$f = e^{-4\pi\langle x^2 \rangle / \lambda^2} \quad 3.1$$

where  $\lambda$  is the  $\gamma$ -ray wavelength and  $\langle x^2 \rangle$  is the component of the mean square vibrational amplitude of the nucleus emitting or absorbing the  $\gamma$ -ray in the direction of the  $\gamma$ -ray flux. Using the Debye model for the solid state, it can be shown (Wertheim, 1964) that:

$$f = \exp \left[ - \frac{6E_R}{k\theta_D} \left( \frac{1}{4} + \left( \frac{T}{\theta_D} \right)^2 \int_0^{\theta_D/T} \frac{x dx}{e^x - 1} \right) \right] \quad 3.2$$

where  $E_R$  is the recoil energy of the free nucleus which approximately equals  $E_\gamma^2/2Mc^2$ ;  $M$  is the nuclide mass;  $E_\gamma$  is the  $\gamma$ -ray energy; and  $c$  is the velocity of light; where  $T$  is temperature;  $\theta_D$  is the Debye temperature for the solid;  $k$  is Boltzmann's constant; and  $x$  equals  $h\omega/2\pi k\theta_D$ , where  $h$  is Planck's constant; and  $\omega$  is the phonon frequency. At low temperatures equation 3.2 reduces to:

$$T \ll \theta_D: \quad f = \exp \left[ - \frac{E_R}{k\theta_D} \left( \frac{3}{2} + \frac{\pi^2 T^2}{\theta_D^2} \right) \right] \quad 3.3$$

Although equations 3.2 and 3.3 are strictly valid only for monatomic solids, they do demonstrate that the recoil-free fraction,  $f$ , is sensitive to the phonon spectrum of the solid and show how the recoil-free fraction depends on  $E_\gamma$ ,  $M$ ,  $\theta_D$  and  $T$ . Both increasing  $T$  and  $E_\gamma$  decrease  $f$  whereas increasing  $\theta_D$  and  $M$  increase  $f$ .



Therefore, for a nuclide to give rise to the Mössbauer effect it must satisfy all of the following conditions: firstly, the nuclide should be heavy (the Mössbauer effect has not been observed in elements lighter than potassium); secondly, the  $\gamma$ -ray energy involved in the Mössbauer effect should be small (200 keV represents an upper limit); and thirdly, the ratio of  $\theta_D:T$  should be favorable (the lower the temperature the better). In addition, a fourth condition must hold: the uncertainty in energy of the Mössbauer  $\gamma$ -ray (i.e., its width) should be small compared to chemical effects, so that information is not obscured due to the diffuse nature of the absorption. This factor is determined directly by the mean lifetime of the excited state involved in the Mössbauer transition according to the Heisenberg uncertainty principle (Bancroft, 1974):

$$\Gamma_H \tau = h/2\pi \quad 3.4$$

where  $\Gamma_H$  is the Heisenberg uncertainty, which in this case is the full width at half height of the absorption;  $\tau$  is the mean lifetime of the excited state; and  $h$  is Planck's constant.

Of the 60 or so nuclides exhibiting an observable Mössbauer effect,  $^{57}\text{Fe}$  combines the four conditions discussed in the last paragraph in such a way as to be the most convenient Mössbauer isotope to use, and the majority of Mössbauer studies have been performed with this isotope. Experiments may be performed routinely at room temperature and can be performed at temperatures of up to 1000 °K. Only  $^{57}\text{Fe}$  of the stable isotopes of iron exhibits an observable Mössbauer effect and iron Mössbauer studies relate to this isotope which only constitutes 2.2% of natural isotopic

abundance of iron. The energy levels involved in the  $^{57}\text{Fe}$  Mössbauer effect and the basic experimentation are described in figure 3.1. The energy spectrum is produced by means of the Doppler effect of the moving radioactive  $^{57}\text{Co}$  source which perturbs the energy of the  $\gamma$ -rays emitted by the source. Doppler velocities of the order of 1 cm/sec (approximately  $10^{-10}$  times the  $\gamma$ -ray energy) are sufficient to obtain complete resonance with  $^{57}\text{Fe}$  in any chemical environment. The recoil energy for an unbound  $^{57}\text{Fe}$  nucleus is approximately  $10^{-4}$  times the  $\gamma$ -ray energy, so that there is no chance of interference from non-recoil-free phenomena. The experimental line width is usually of the order of 0.3 mm/sec (theoretical line width according to equation 3.4 is 0.1 mm/sec) which permits reasonable resolution of chemical effects.

### 3.2.2 Parameters from a $^{57}\text{Fe}$ Mössbauer spectrum

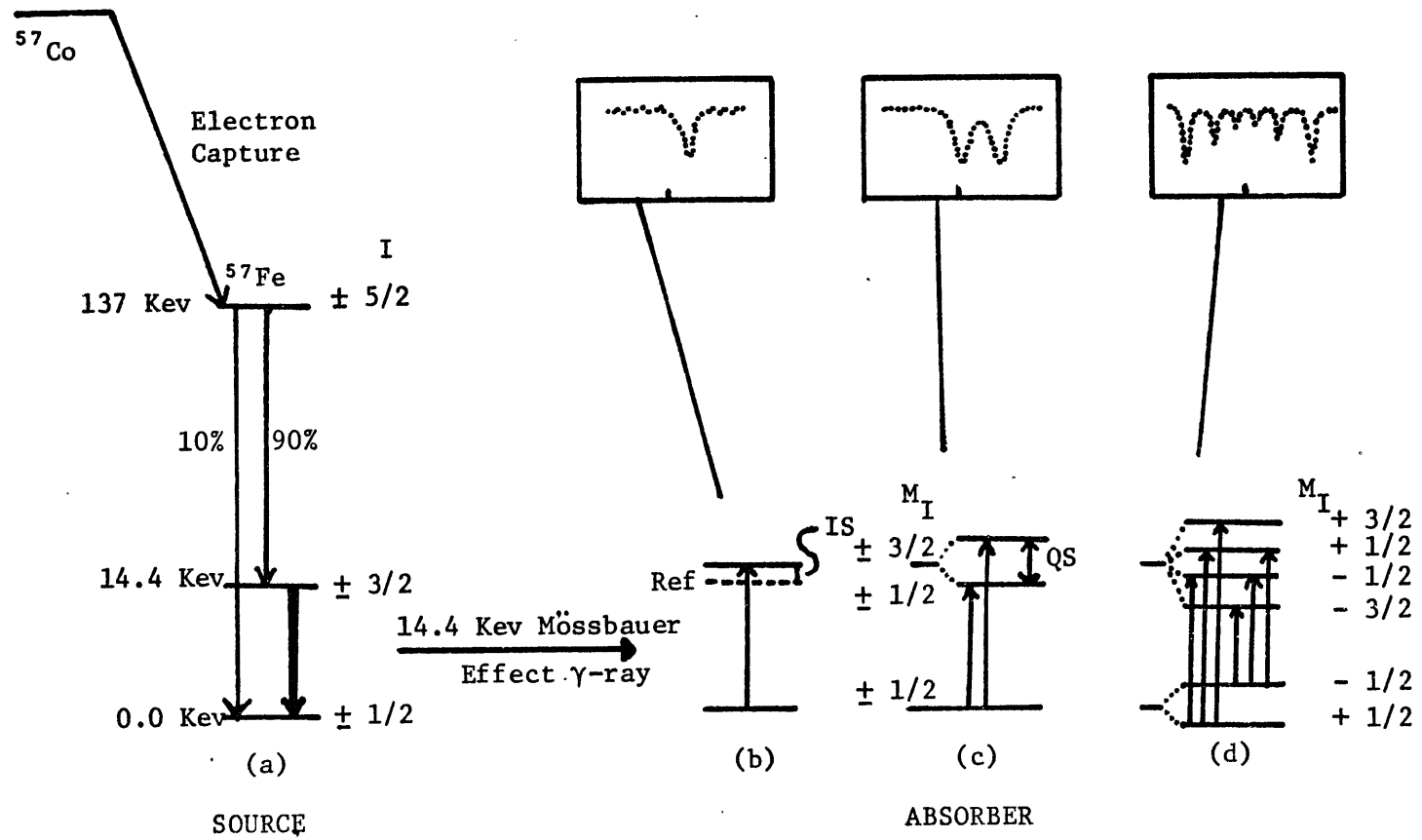
The two principal parameters obtained from a  $^{57}\text{Fe}$  Mössbauer spectrum are the isomer shift (IS) and the quadrupole splitting (QS). These are described in figure 3.1. The isomer shift is the center of energy of the components in the spectrum of one type of iron species and is a measure of the difference in chemical environments about  $^{57}\text{Fe}$  nuclei. Values are generally quoted relative to some standard (iron metal foil at room temperature is used in this study). Variations in the value of isomer shift arise from differences in the electron density at the nucleus, according to the equation:

$$\text{IS} = \frac{4\pi}{5} Z e^2 R^2 \left( \frac{\delta R}{R} \right) \left[ |\psi(0)|_{\text{abs}}^2 - |\psi(0)|_{\text{ref}}^2 \right] \quad 3.5$$

where  $\delta R = R_{\text{ex}} - R_{\text{gd}}$  is the difference in radii of excited and ground states;

Figure 3.1

Basic Mössbauer experimentation. (a) Production of  $^{57}\text{Fe}$   $\gamma$ -rays by electron capture by  $^{57}\text{Co}$  source. The source is oscillating to give rise to the Doppler shift and a range in energy about 14.4 keV. (b) Absorption of  $\gamma$ -rays by  $^{57}\text{Fe}$  in sample absorber at energy, IS, relative to some standard, where IS is the isomer shift. (c) Splitting of energy levels by QS, the quadrupole splitting. (d) Effect of magnetic field on the energy levels is to remove all remaining degeneracies and to give rise to a six-peak spectrum.



and  $|\psi(0)|^2$  is the electron density at the nucleus, for the absorber or reference material. Only s electrons have a non-zero probability of being at the nucleus and chemical effects are observed due to the interaction of the iron 3s electrons and the bonding electrons. Since  $\delta R$  is negative (Walker et al., 1961), decreasing isomer shift values reflect increasing s electron density at the nucleus.

The  $^{57}\text{Fe}$  quadrupole splitting is obtained from a Mössbauer spectrum as the energy separation of the spectral components of the quadrupole doublet for one species of iron atom. The quadrupole splitting arises from an asymmetric charge distribution about the  $^{57}\text{Fe}$  nucleus, which produces an electric field gradient (EFG) at the nucleus. The interaction of the EFG with the nuclear quadrupole moment of the excited state partially lifts the degeneracy of the energy levels of the excited state, resulting in a quadrupole split spectrum (figure 3.1 (c)). The general equation describing the interaction of the EFG and the nuclear quadrupole moment,  $Q$ , is (Wertheim, 1964):

$$QS = \frac{eQV_{zz}}{2}(1 + \eta^2/3)^{1/2} \quad 3.6$$

where  $\eta = (V_{xx} - V_{yy})/V_{zz}$  is the asymmetry parameter and  $V_{xx}$ ,  $V_{yy}$ ,  $V_{zz}$  are principal components of the diagonalized EFG tensor. In general, there will be two contributions to the components of the EFG tensor, one describing the asymmetric nature of the ligands and the other describing the contribution due to a non-spherical distribution of electrons over the five 3d orbitals:

$$V_{ii} = (1 - R)V_{ii}^{val} + (1 - \gamma_{\infty})V_{ii}^{lat} \quad 3.7$$

where  $R$  and  $\gamma_{\infty}$  are antishielding factors which attempt to describe and allow for polarization of the inner electrons by the valence and lattice contributions to the EFG respectively.

More complete descriptions of both parameters, isomer shift and quadrupole splitting, are presented in Chapter 4 when the pressure dependence of these parameters are interpreted. From the values of these two parameters, different chemical and bonding properties of iron cations in silicates including valence state, spin state and crystallographic coordination are easily determined. Ferrous-ferric ratios can also be estimated from the areas under absorption peaks in the spectrum, if certain assumptions are made concerning the values of the recoil-free fractions for the different iron species.

The interaction of the nuclear magnetic dipole moment with a magnetic field lifts the remaining degeneracies of the nuclear state (figure 3.1 (d)). Selection rules permit six transitions between the split levels. The transitions between nuclear states are polarized and the relative intensities of the six peaks are determined by the angle between the magnetic field vector and the direction of the  $\gamma$ -rays (Wertheim, 1964; Grant, 1967). In a magnetic solid, which is randomly oriented, these transitions characteristically have intensities 3:2:1:1:2:3. More complicated spectra result when both an EFG and a magnetic field are present and, depending on the angle between the directions of the principal axes of the EFG and the magnetic field, the spectra can be simple or extremely difficult to interpret. Some of the simpler cases are discussed by

Wertheim (1964). The magnetic field may result from the coupling of the magnetic moments of iron atoms within the solid or may be applied externally; its strength,  $H_0$ , is measured as the energy separation of the lowest and highest energy peaks.

A number of other parameters or quantities can be extracted from Mössbauer spectra or series of spectra. These parameters, along with those mentioned above, are summarized by Herber (1967) but are not of great interest for Mössbauer studies of minerals.

### 3.2.3 Practice of Mössbauer spectroscopy of iron minerals

Virtually all Mössbauer work on minerals has concerned iron because  $^{57}\text{Fe}$  is the most convenient Mössbauer isotope with which to work and iron is a major element in Earth Sciences. Normally, as long as the mineral contains in excess of about 1 wt % of iron (Bancroft, 1974) and the amount of material available contains 10 mg of iron or more, spectra can be routinely obtained. For spectra at ambient conditions, the sample is generally ground with sugar and sprinkled into a disc-holder of area about 4 sq. cm. The mineral sample is diluted in sugar so that the packed disc contains between 3 and 5 mg of iron per sq. cm., which appears to be the optimum concentration to avoid thick absorber phenomenon and yet produce good counting statistics (Bowen et al., 1969; Whipple, 1973). Sugar serves to randomize the orientation of the mineral with respect to the  $\gamma$ -ray flux direction so that orientation effects are minimized (Bowen et al., 1969).

The equipment used for recording Mössbauer spectra is shown schematically in figure 3.2. Two spectra may be recorded simultaneously and the

Figure 3.2

Mössbauer experiment. (a) Hydraulics for high pressure Mössbauer studies. (b) The basic experiment of emission, absorption and detection of  $\gamma$ -rays (shown in more detail in figure 3.6). (c) Electronics for performing and recording Mössbauer spectra. (d) Computation of results.

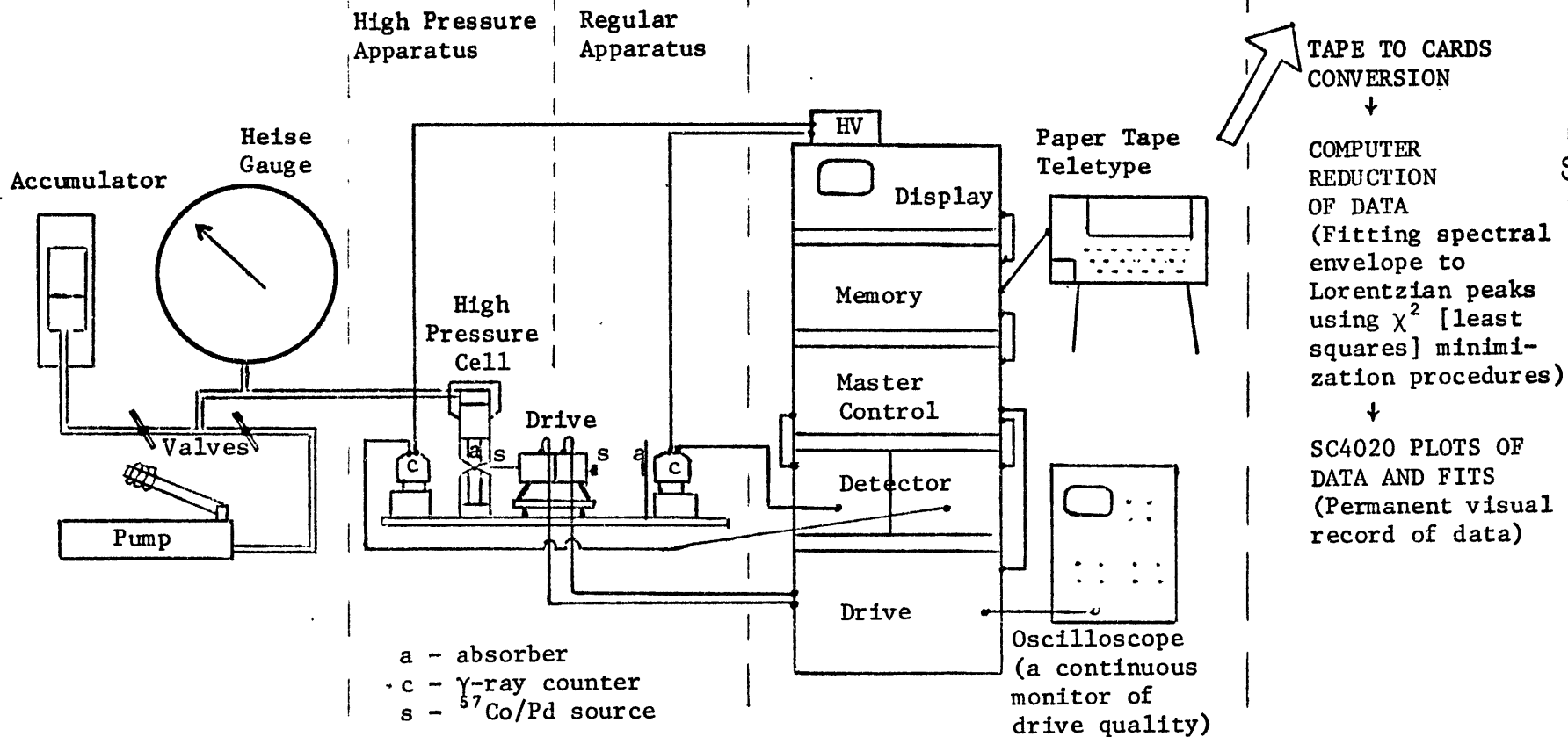


(a) HYDRAULICS

(b) EXPERIMENT

(c) ELECTRONICS

(d) COMPUTATION



sawtooth drive mechanism oscillates both  $\gamma$ -ray sources. The absorption of  $\gamma$ -rays by each sample is measured electronically, using gated counters operating at 1600 volts, into 512 channels of a multichannel analyzer supplied by Nuclear Data. The drive system and interrelated electronics were supplied by Austin Science Associates, who were responsible for designing and building the complete system. Besides a continuous visual oscilloscope record of the spectra, individual spectra could be stored permanently on paper tape at the end of a run by using the Teletype readout. This output was convenient for computer reduction of the Mössbauer data.

Computer fitting of the data was based on the program written by A.J. Stone for the analysis of absorption spectral envelopes into component peaks. For Mössbauer spectra, a typical resonant absorption phenomenon, the line shape for the component peaks is Lorentzian and the intensity of absorption,  $I_{\text{abs}}$ , shows a dependence on energy,  $E$ , of the form (Bancroft, 1974):

$$I_{\text{abs}}(E) = \frac{\Gamma_{\text{ex}}}{2\pi} \left[ \frac{I_{\text{t}}}{(E-E_{\text{t}})^2 + (\Gamma_{\text{ex}}/2)^2} \right] \quad 3.8$$

where  $\Gamma_{\text{ex}}$  is the experimental full width at half peak height; and  $E_{\text{t}}$  is the nuclear transition energy at the resonant or maximum absorption. To fully describe a Lorentzian peak, the position in energy or Doppler velocity, the width at either the maximum intensity,  $I_{\text{t}}$ , or the area under the peak must be known. Therefore, each peak is fitted in the computer program to three variables. In addition, four more variables are used to describe the baseline, so that in order to fit  $N$  peaks to an observed envelope,  $3N + 4$  parameters are available in the computer program. The program fits

these parameters to the envelope by an iterative method until a convergence test is satisfied. The least squares parameter,  $\chi^2$ , is used as the statistical fit criterion. In order to make convergence more rapid, constraints may be placed on the behavior of sets of parameters in the fitting procedure. For example, peak widths and areas may be held constant for peaks constituting a quadrupole doublet for a particular stage in the fitting procedure, and then allowed to vary independently at a later stage in the procedure.

Performing this program on the M.I.T. IBM 370 computer enables the fitted spectra to be displayed on Stromberg-Carlson 4020 output and the spectra reproduced in this thesis have been obtained in this manner. Certain additions to Stone's original program have been made in the course of this thesis and these are discussed in Appendix A3.1. Further details of Stone's program may be found in Stone (1967) and Bancroft (1974).

Calibration of the Doppler velocity energy scale was achieved by standardizing spectra to a spectrum of iron foil of thickness 0.001" taken at about the same time and at the same velocity settings of the drive. Usually, the velocity setting of the drive was sufficient to allow all six peaks of the iron foil spectrum to be observed. The mean position of the six iron foil peaks defines zero Doppler velocity, while the slope of a plot of iron foil peak positions (in channels) against standard Doppler velocities for these peak positions (in mm/sec) gives the increment of velocity per channel. The iron foil spectrum also served as a reference spectrum for checking the performance of the Mössbauer equipment, since the intensities of peaks and spacings between peaks should be symmetrical about

the center of the spectrum.

### 3.2.4 Mössbauer bibliography

More complete descriptions of the theory and practice of Mössbauer spectroscopy may be found in the literature. The theory of the Mössbauer effect has been presented many times; among the best treatments are, in my opinion, Wertheim (1964), Danon (1968), Greenwood (1970) and Bancroft (1974). The practice of Mössbauer spectroscopy is best presented by Bancroft (1974), while Kalvius and Kankeleit (1972) in detail and Wertheim (1964) more generally present good reviews of instrumentation. The applications of the Mössbauer effect have ranged from tests of Einstein's theory of relativity to investigations of haemoglobin and to archaeological investigations of pottery; however, for mineralogical application there appears to be only two publications (Maddock, 1972; Bancroft, 1974) which have attempted to cover the breadth of such studies. High pressure Mössbauer studies of iron have been reviewed by Drickamer and Frank (1973), Drickamer et al. (1970), while Holzapfel (1970) has discussed iron and other elements. Some of the results of such studies have been described in Chapter 2. The high pressure techniques and necessary modifications of standard practices are described in the next sections.

## 3.3 High Pressure Mössbauer Experimentation

### 3.3.1 The high pressure cell

The cell design duplicates that described by Debrunner et al. (1966) and consists of a pair of unsupported Bridgeman anvils made of tungsten carbide. The anvil flats have a diameter of 0.08" and are supported by a 9° taper on a rod of tungsten carbide of 0.70" in diameter.

The anvils are enclosed in steel jackets of 1.75" diameter. Figure 3.3 shows details of the anvils and the lead collimators.

The anvils were work-hardened before use by applying 75-90 kb pressure to a pyrophyllite disc of the same dimensions of the sample disc (see below) for a few minutes. The anvil flats were then re-ground to the dimensions given above.

Pressure in the cell is applied uniaxially by a ram of 1.50" diameter connected hydraulically to an oil pump and a Heise gauge, which is the primary measure of the pressure applied to the sample. The hydraulics are shown schematically in figure 3.2.

### 3.3.2 Sample preparation

Because of the known pressure distribution in a uniaxial anvil arrangement (figure 3.4), the Mössbauer sample was restricted to the central maximum region of low pressure gradient and the technique for doing this is now described.

A hole of 0.08" diameter was drilled in the center of a pyrophyllite disc of 0.50" diameter and thickness 0.015". This hole was filled with a boron/lithium hydroxide mixture and the whole disc was compacted by applying a pressure of 12 kb for a few minutes. A second hole of 0.02" diameter was drilled in the center of the B/LiOH filled hole and filled with the sample diluted in amorphous boron. The whole disc was again compacted, this time at a pressure of 18 kb for a few minutes. The remaining pyrophyllite annulus around the B/LiOH/sample pellet was carefully chipped away leaving the central cylindrical pellet with dimensions 0.08" diameter x 0.015" thickness and the sample contained in the central region of 0.02"

Figure 3.3

Diagram of the high pressure anvil used in this study. Also shown are the lead collimators which restrict the passage of  $\gamma$ -rays between the source and detector to the sample pellet.

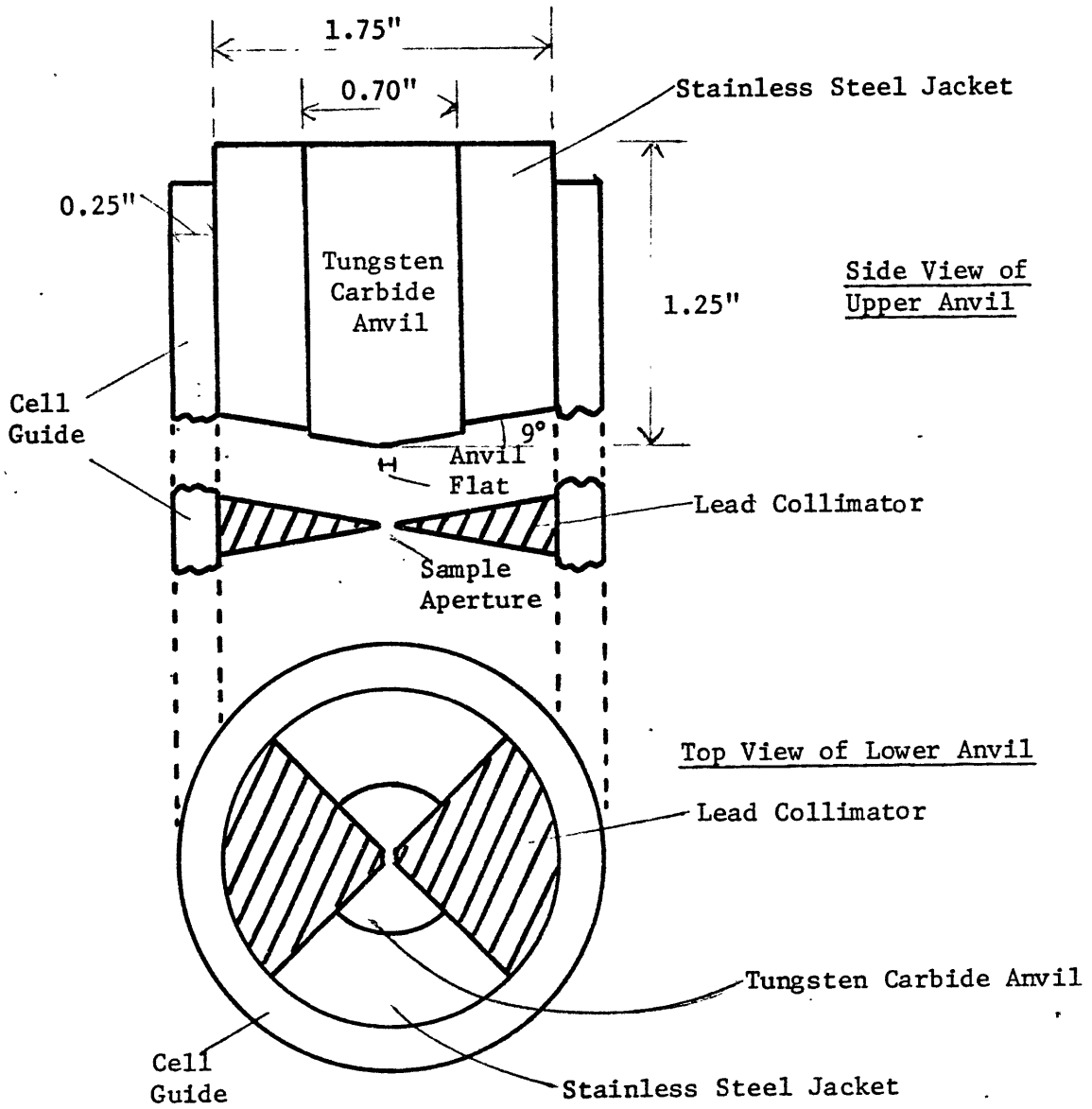
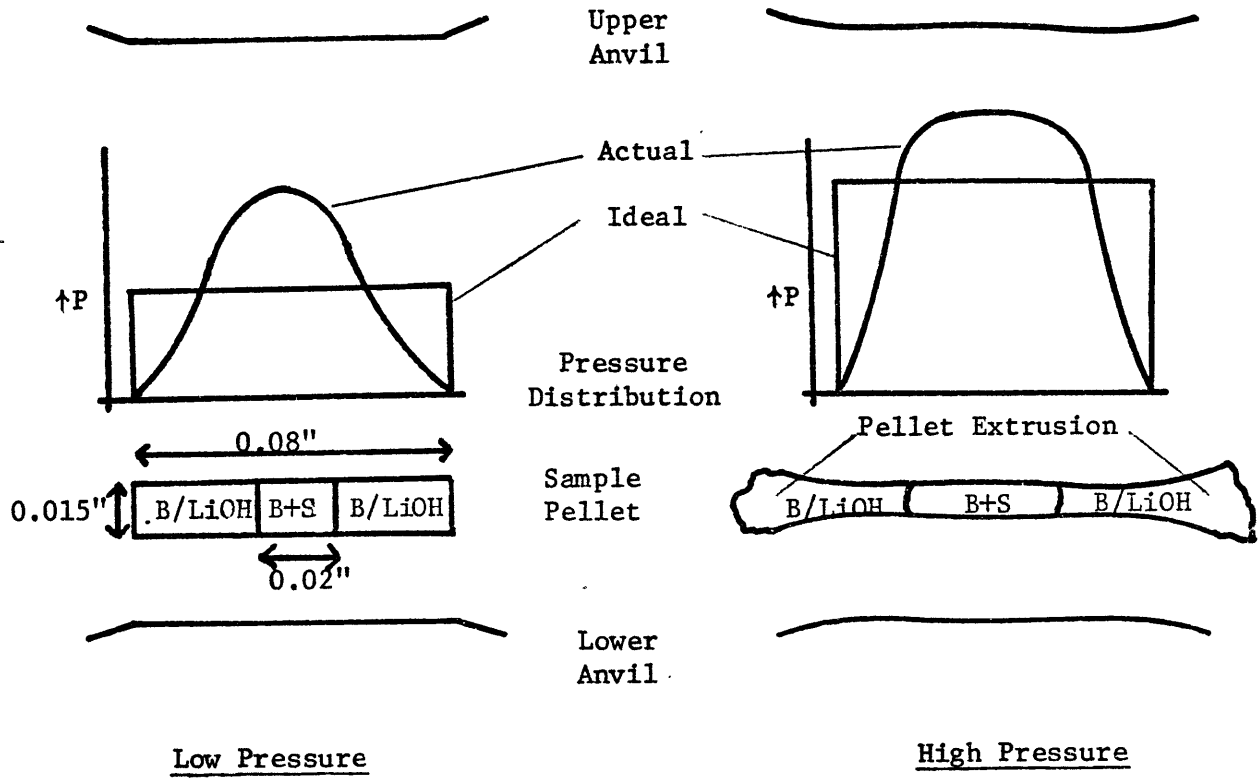


Figure 3.4

Pressure distribution on the sample in the high pressure cell at low pressures and at high pressures. Note the deformation of the anvils and extrusion of sample at high pressure. A scale drawing of the sample pellet is also shown.





B + S - Boron + Sample Mixture

diameter (figure 3.4). By use of a binocular microscope, the sample was placed exactly at the center of the anvil flat.

It was discovered in the course of this study that the dilution of the sample in boron was extremely critical in terms of spectrum quality and Mössbauer peak width. Most of the samples used in high pressure Mössbauer studies are prepared from  $\text{Fe}_2\text{O}_3$  containing 90%  $^{57}\text{Fe}$ , a 40 times increase over natural abundance, so that counting times can be short due to a large signal-to-noise ratio. However, by increasing the  $^{57}\text{Fe}$  content of the samples, considerable care had to be taken to ensure that the results did not suffer from the effects of thick absorber phenomena, which causes the spectral absorption to be not linearly proportional to the concentration of  $^{57}\text{Fe}$  in the sample.

The best results were obtained with a sample:boron ratio such that  $^{57}\text{Fe}$  constituted about 1/2-1% by weight of the sample mix and where the collimation of the  $\gamma$ -ray flux was as narrow as practical (approximately 0.04"). It is recommended that  $\text{Fe}_2\text{O}_3$  containing 20%  $^{57}\text{Fe}$  be used for synthesizing samples with iron oxide contents exceeding 10 wt % as this concentration of  $^{57}\text{Fe}$  will lead to more manageable dilutions. For samples with iron oxide contents in excess of about 40-50 wt %, iron of normal isotopic abundance can be used, either for synthesis or in naturally occurring minerals.

The minimum recommended dilution ratio of sample:boron is 1:2, since compaction of the sample pellet becomes more difficult as the amount of boron in the pellet decreases.

### 3.3.3 Pressure calibration

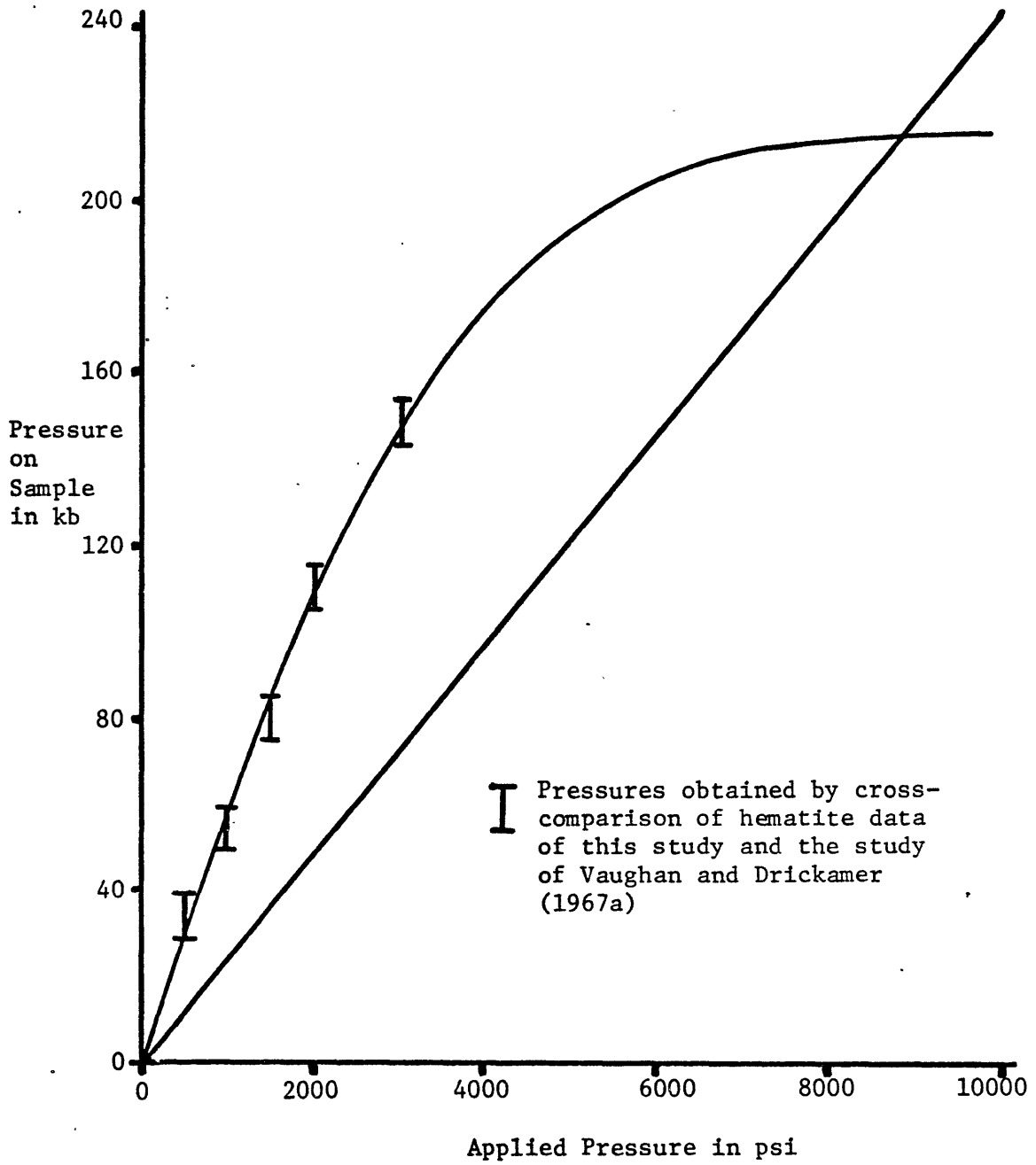
Since the cell design was identical to that described by Debrunner et al. (1966) and since extremely accurate pressure calibration is not required because most of the results are qualitative, it is only necessary to show that the published calibration curve of Debrunner et al. (1966) is, in fact, consistent with our apparatus, allowing for the difference in ram area of a factor of nine. This was achieved by running a sample of hematite and relating the effective quadrupole splitting to pressure on the sample by means of the reported data of Vaughan and Drickamer (1967a). Satisfactory agreement was found, so that the calibration curve published by Debrunner et al. (1966) was used for our apparatus. This calibration curve was originally obtained based on the pressure shift of XRD peaks of aluminum powder in a pellet similar to that described above. The curve of Debrunner et al. (1966) is reproduced in figure 3.5 with the scale appropriate for the Heise gauge used in the present study. The points plotted are pressures obtained by means of interrelating the two sets of data on hematite. The straight line is obtained by calculation, assuming pressure over the whole flat is uniform and using the formula:

$$pA = F = Pa \qquad 3.9$$

where  $a$  is the flat area;  $A$  is the ram area;  $p$  is the applied pressure (Heise);  $P$  is the pressure on the sample pellet; and  $F$  is the force which is conserved. At high pressures ( $P > 150$  kb), the calibration curve bends over as elastic or plastic deformation effects become serious in the anvils (figure 3.4). This limits pressures to a maximum of about 220 kb,

Figure 3.5

Calibration curve used to convert Heise gauge reading to pressure on the sample. The plotted points are pressures obtained by the comparison of hematite data. The straight line is obtained by calculation assuming pressure over whole anvil flat is uniform.



regardless of the applied pressure. Other factors, however, usually ensured that pressures in excess of 200 kb were rarely attained and that 150-180 kb was usually the routinely obtained maximum.

#### 3.3.4 Adjustments to the Mössbauer apparatus

The actual Mössbauer apparatus only required very slight modification to take spectra of samples under high pressures. In order to achieve as large a flux of  $\gamma$ -rays as possible through the small sample volume, the  $\gamma$ -ray source had to get within 2 cm of the sample. For this reason, the source was shaped like a screwdriver so that it would fit between the tapers of the anvils and the end of the screwdriver was either made of palladium and impregnated with radioactive  $^{57}\text{Co}$  or a thin foil of Pd impregnated with  $^{57}\text{Co}$  stuck on the end of the screwdriver-shaped rod. Figure 3.6 shows the difference between the normal geometry experiment and the high pressure geometry. Note that the normal geometry sample presents a thin aspect to the  $\gamma$ -ray flux whereas the high pressure sample does not.

#### 3.3.5 Experimentation difficulties

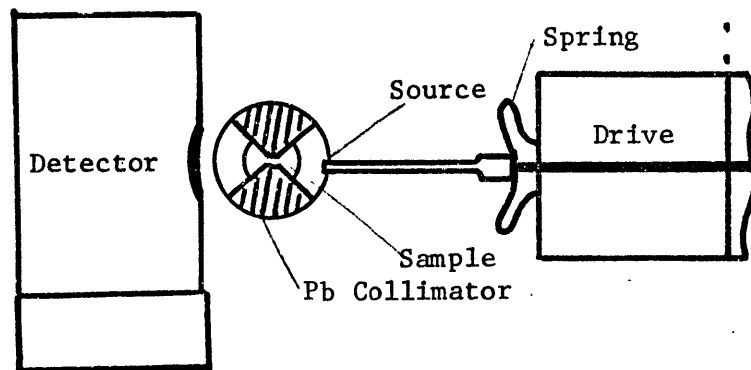
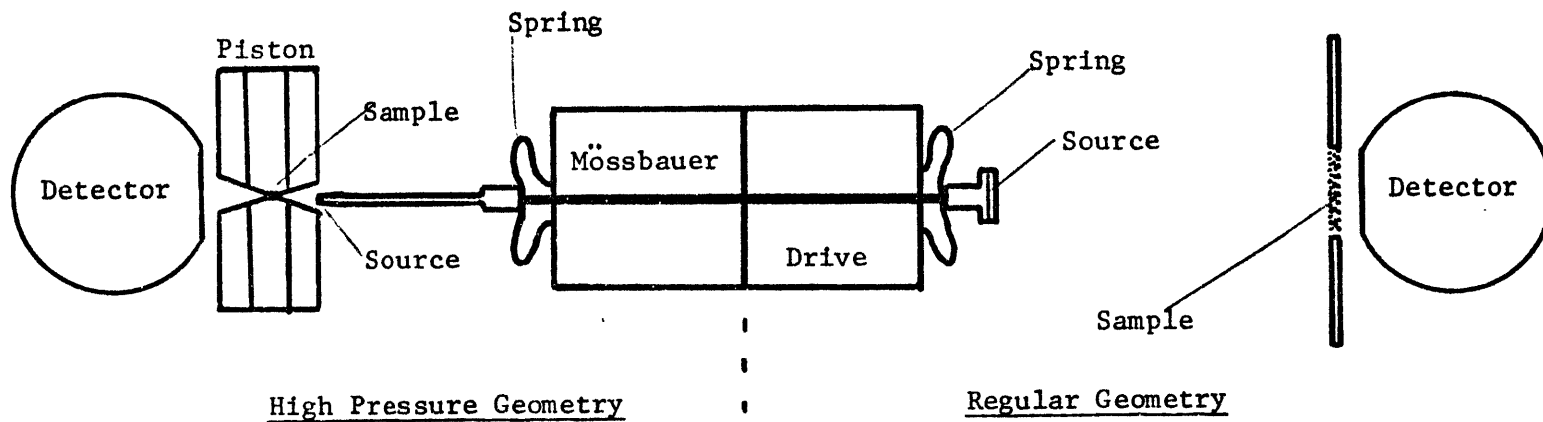
Since the area of the source had to be small, only a 10 millicurie source could be used (compared to a 100 millicurie source for normal use). Also, the severe restriction of the small area of the sample aperture in the high pressure cell meant that count rates were very low. Compensating this slow count rate was the enrichment of  $^{57}\text{Fe}$  in the samples, but even so, experiments at the very highest pressures could take up to 14 days to accumulate enough counts (approximately 20,000 counts/channel) so that the fitting statistics were not too bad.

Also complicating matters was the phenomenon encountered with some of

Figure 3.6

Difference between regular geometry and high pressure geometry for Mössbauer experimentation. Note the difference in sample aspect and size and also in the  $^{57}\text{Co}$  sources for the two experiments.

From Side, Lead Collimators Removed



From Above, Upper Piston Removed



the enriched synthetic samples of spectral line broadening by up to 3 times as pressure was increased. This phenomenon was most severe in the range 0-50 kb. Natural samples, on the other hand, showed at most only a slight increase (30%) in width, so that broadening with pressure can not be an intrinsic phenomenon. Similarly, the postulation that the application of pressure distorts the cation sites slightly to give rise to a highly broadened absorption can also be rejected. The only conclusion that may be made is that the broadening phenomenon is a thick absorber property; indeed, increasing the dilution appeared to prevent the broadening. On comparing results of the natural fayalite reported in this study with the results of Vaughan and Tossell (unreported data) on synthetic enriched fayalite, the broadening does not appear to influence peak positions, so that isomer shift and quadrupole splitting data obtained from samples which do broaden appreciably with pressure are probably unaffected. The broadening also affected the peak shape, since fits with Lorentzian line shapes (a good approximation, normally) resulted in unnaturally curved baselines and usually did not fit well at maxima and minima in the spectra.

A further complication was found when a blank boron pellet was placed in the cell so that comparison between an actual spectral baseline and the computer fit baselines could be made. The baseline was not only curved in the opposite sense to that found in most computer fits of broadened spectra but was also an order of magnitude less curved. For this reason, the fits reported in this thesis for broadened spectra are those in which the baseline is constrained straight as this is a good approximation to the actual curvature. Constraining the baseline to be straight did not in any way

significantly affect the statistics of the fitting procedure. On the other hand, most natural samples, even when fitted with no constraints, had baseline curvatures comparable to the curvature of the blank.

The blank run, however, also exposed another minor complication. The boron was found to contain a small percentage of iron, as shown by the absorption just above zero mm/sec in figure 3.7. This is attributed to impurity within the amorphous boron as the parameters for this absorption are similar to those found by Wäppling et al. (1972) for iron in metallic boron-iron alloys containing about 1% iron. For natural samples, this added absorption could occasionally be observed and allowed for in the computer-fitting procedure. In the synthetic enriched samples, which were generally much stronger absorbers, this impurity was ignored in the fitting as the line-shape approximation probably introduced a larger error.

Although the positions of well separated peaks are believed to be unaffected by the complications listed above, uncertainties and errors in peak parameters must increase as the peaks increasingly overlap. This affects area data of overlapping peaks in particular, especially in the case of thick absorbers, which do not have a linear relationship between sample concentration or effective Mössbauer thickness and peak area. It was often found that on going from a normal geometry experiment (a thin absorber) at 1 bar to a high pressure experiment geometry (a thick absorber) at 1 bar that the ratio of absorption of overlapping peaks relative to that of resolved peaks was much less in the high pressure experiment than in the normal geometry experiment. Examples of this phenomenon are shown in figures 3.8 and 3.9. The effect was most conspicuous for experiments with

Figure 3.7

Mössbauer spectrum of a blank boron pellet in the high pressure cell at about 25 kb. Note the negative curvature of the baseline and the small absorption at 0.25 mm/sec, indicating that the boron contains some iron impurity. (For technical information regarding this plot and subsequent plots of Mössbauer data in this chapter, see section 4.1.)

93127 500. 200. 300. 400. 500.  
BROWN KELLEY AT 25 KB 19/11/73

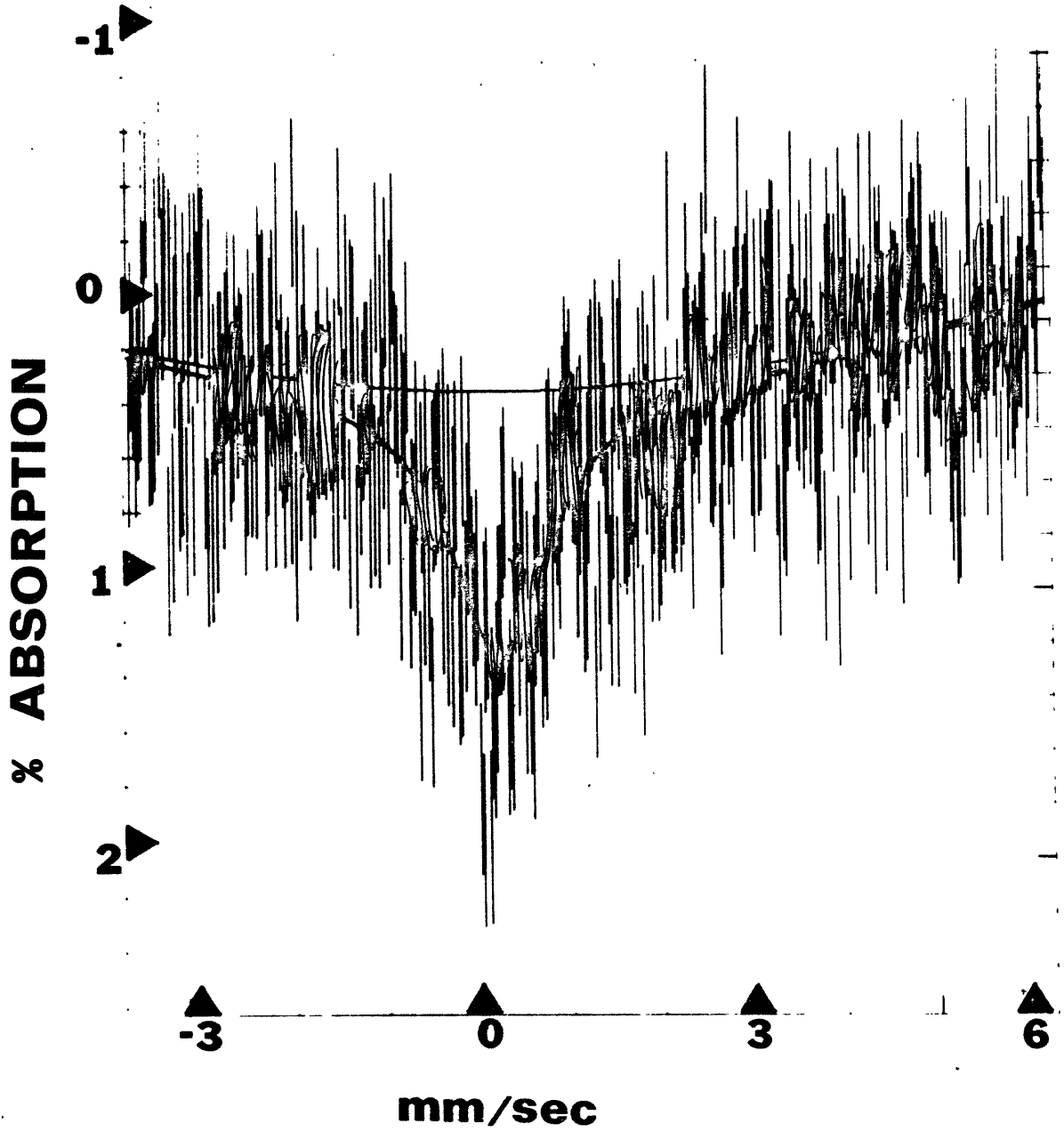


Figure 3.8

Mössbauer spectra of synthetic ( $^{57}\text{Fe}$  enriched) ferriphlogopite (SE #15) in the regular geometry (left) and high pressure geometry (right). The largest peak in the regular geometry spectrum is closer to the sum of the two smaller peaks than in the high pressure geometry spectrum.

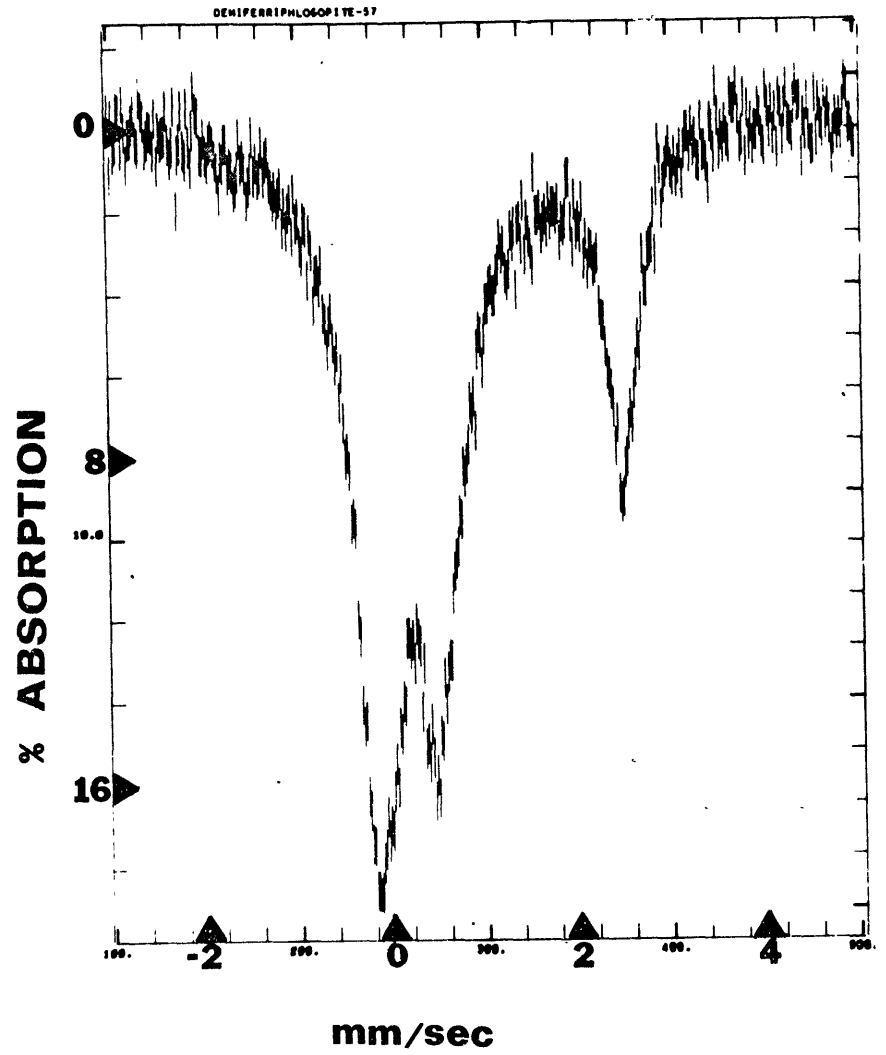
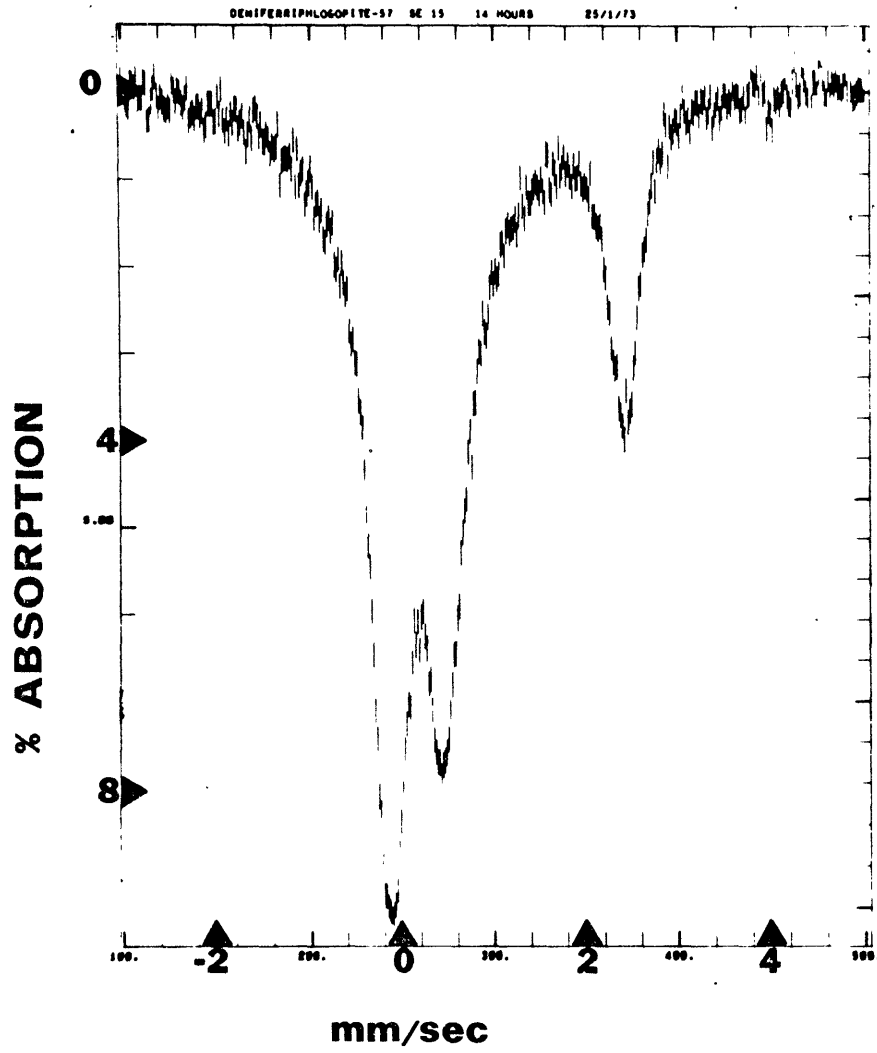
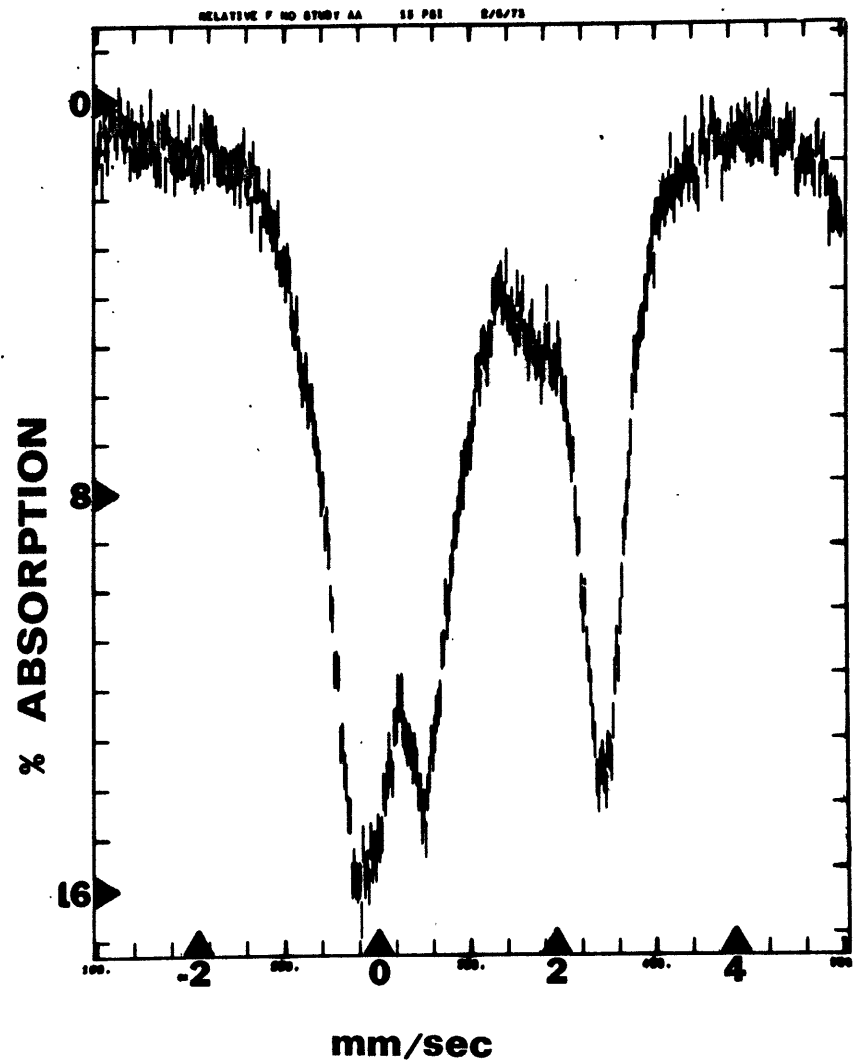
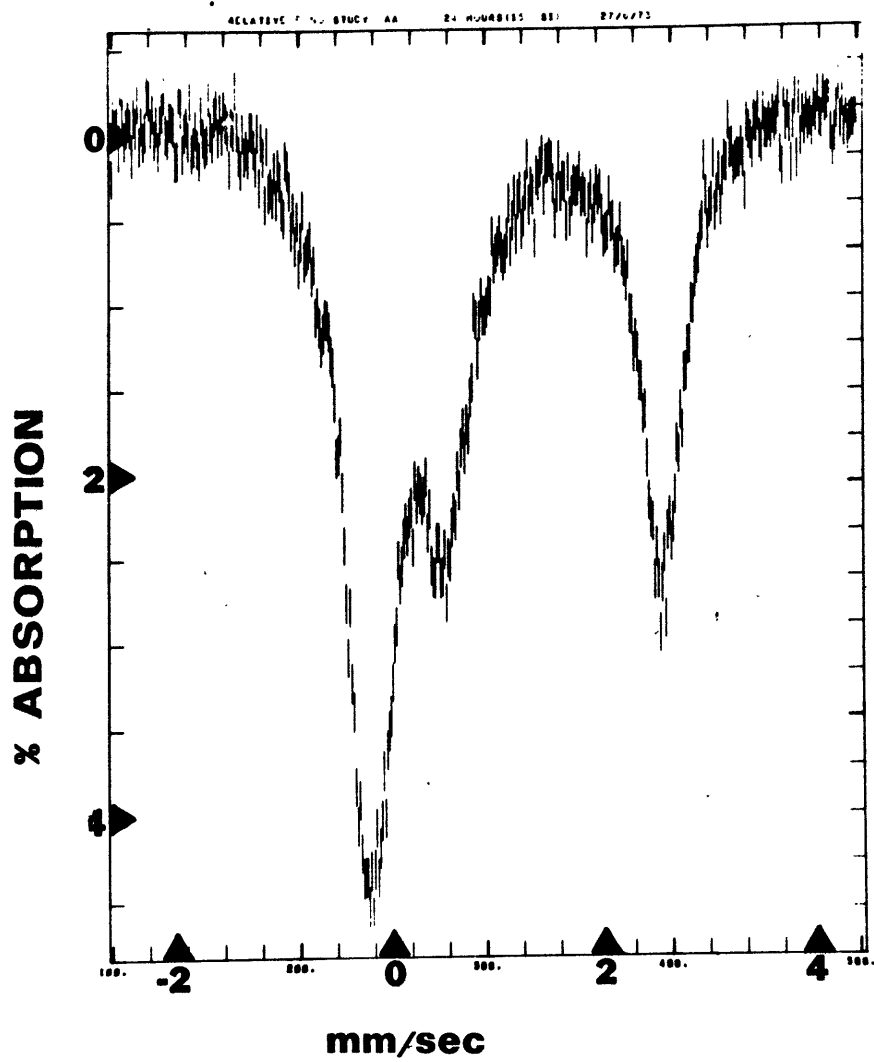


Figure 3.9

Mössbauer spectra of a mechanical mixture of fayalite and iron microcline (both  $^{57}\text{Fe}$  enriched) in the regular geometry (left) and the high pressure geometry (right). The largest peak in the regular geometry spectrum is much closer to the sum of the two smaller peaks than in the high pressure geometry spectrum.





mechanical mixtures of two phases (figure 3.9). However, once at pressure the relative areas did not change greatly suggesting that the change in geometry was most significant. For this reason, area measurements involving resolved and overlapping peaks must be regarded with caution.

Appropriate dilution of the samples in the high pressure geometry may have avoided many of the above mentioned complications. Unfortunately, the experiments carried out on natural minerals, which were the important results for realizing these effects, were among the last to be carried out in this study, so that most of the earlier results obtained with synthetic enriched phases do suffer from these problems.

### 3.3.6 High temperature additions to the high pressure cell

For one of the high pressure runs on iron-chromium garnet, a simple heating jacket was positioned around the high pressure cell in order that temperatures up to 100 °C could be obtained.

The heating jacket consisted of a four-foot long Electrothermal heating tape wound around the outside of the cell guide connected to a small Variac voltage regulator. Temperature was measured by means of a thermocouple connected to a Therm-O-Meter direct-reading temperature meter. Insulation between the exterior of the press and the heating units was provided by asbestos pads. The set-up is shown schematically in figure 3.10.

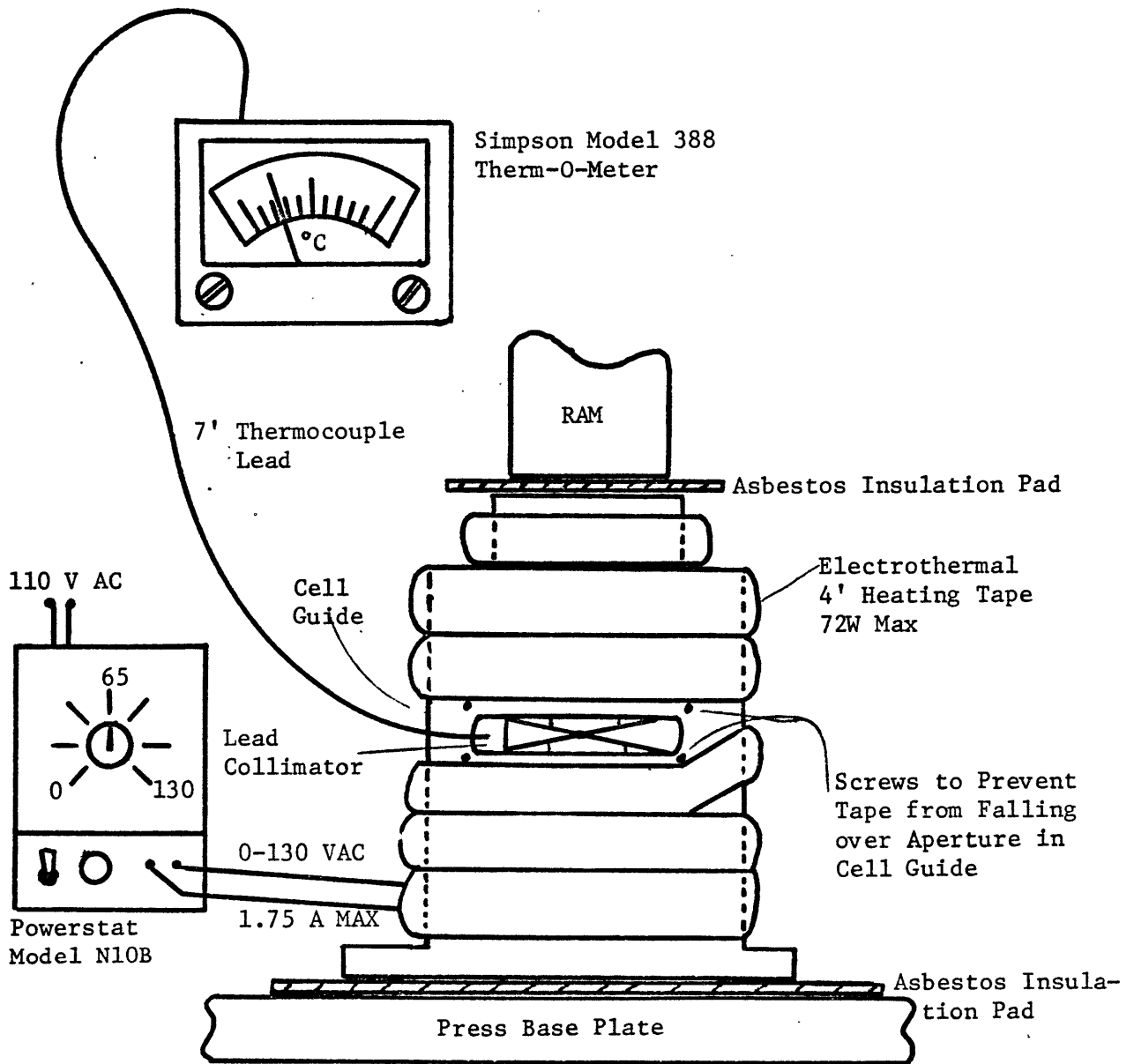
Due to the large thermal capacity of the press and inadequate insulation, maximum temperatures of only about 100 °C could be obtained. By improving these factors, the range could probably be extended 50 °C.

### 3.3.7 High pressure Mössbauer studies with the diamond cell

The diamond cell (Bassett, 1974) is fast becoming the premier

Figure 3.10

Diagram showing heating device for high pressure Mössbauer experiments at temperatures up to 100 °C.



cell for simple high pressure studies. The advantages of the diamond cell are many: it is extremely small and adaptable to many kinds of experiments; it can reach 300 kb without anvil support; the observation of the sample is possible under high pressure; and it is relatively cheap. The main disadvantage is: the sample studied is very small ( $\sim 10 \mu\text{g}$ ).

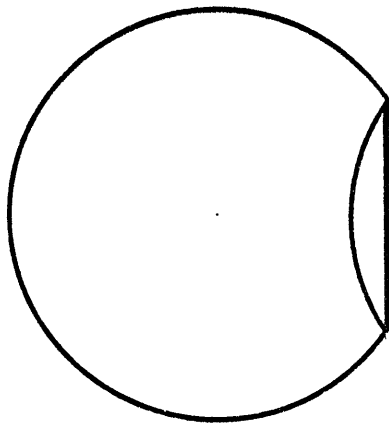
Discussion with Professor W.A. Bassett of the University of Rochester indicated that Mössbauer studies of  $^{57}\text{Fe}$  enriched samples under pressure in the diamond cell should be possible and the following attempt was made.

The important and necessary step that was taken was to place the sample in a gasket made of material impervious to the  $\gamma$ -rays, so that  $\gamma$ -rays which did not go through the sample hole would be greatly reduced in intensity relative to those that did go through the sample aperture in the gasket. The gasket was made of nickel of thickness 0.25 mm and dimensions 10 mm x 10 mm. A central hole in the gasket of diameter approximately 0.1 mm was drilled and filled with  $^{57}\text{Fe}_2\text{O}_3$ . The gasket was loaded into the cell between the diamond anvils and the cell placed between the  $\gamma$ -ray source and the detector as shown in figure 3.11.

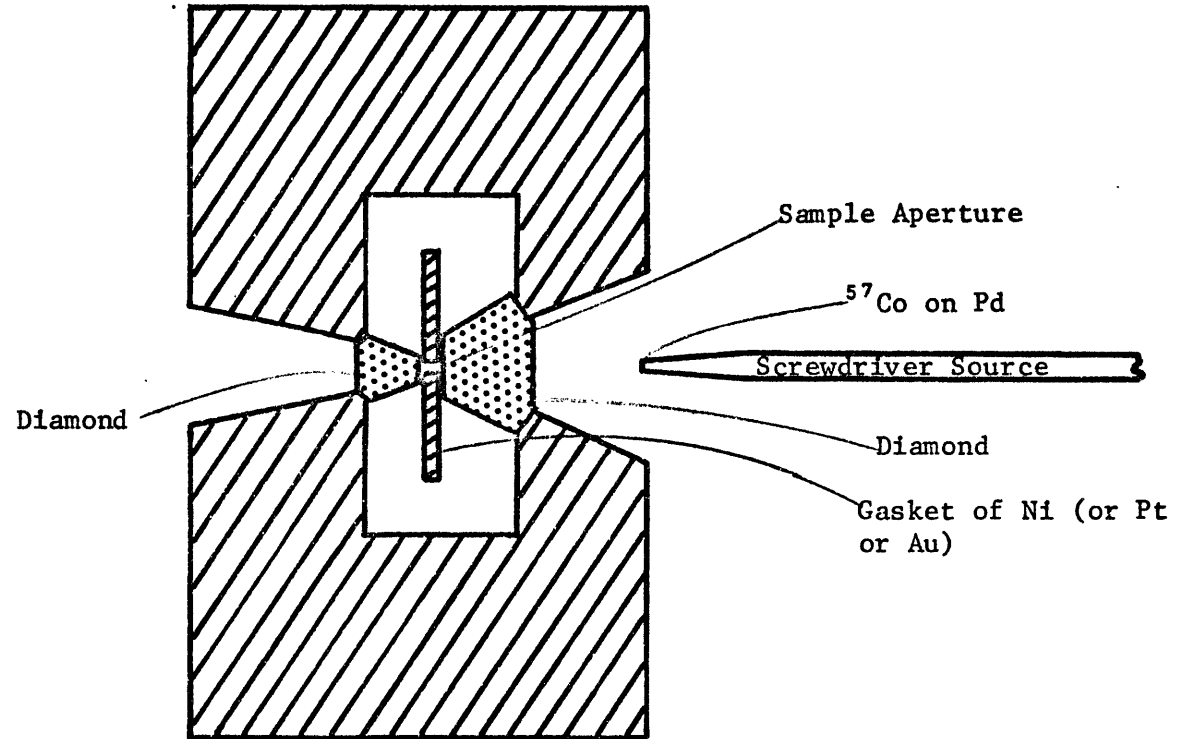
After one week, the hematite spectrum appeared as shown in figure 3.12. The inner four peaks of this magnetic spectrum are shown and are of about equal intensity. Although the absorption effect is small, the equal intensity of the peaks indicates thick absorber phenomena for that portion of the  $\gamma$ -ray flux which went through the sample. Thus, a very large percentage of the  $\gamma$ -rays reaching the detector must not go through the sample in order to account for the low absorption effect. If gold or platinum were to be used instead of nickel, only about 7% of the 14.4 keV radiation

Figure 3.11

Schematic diagram showing the gasketing technique used in the diamond cell. Also indicated is the geometry for this kind of high pressure Mössbauer experiment, which involves directing the  $\gamma$ -rays through the diamonds.



Detector

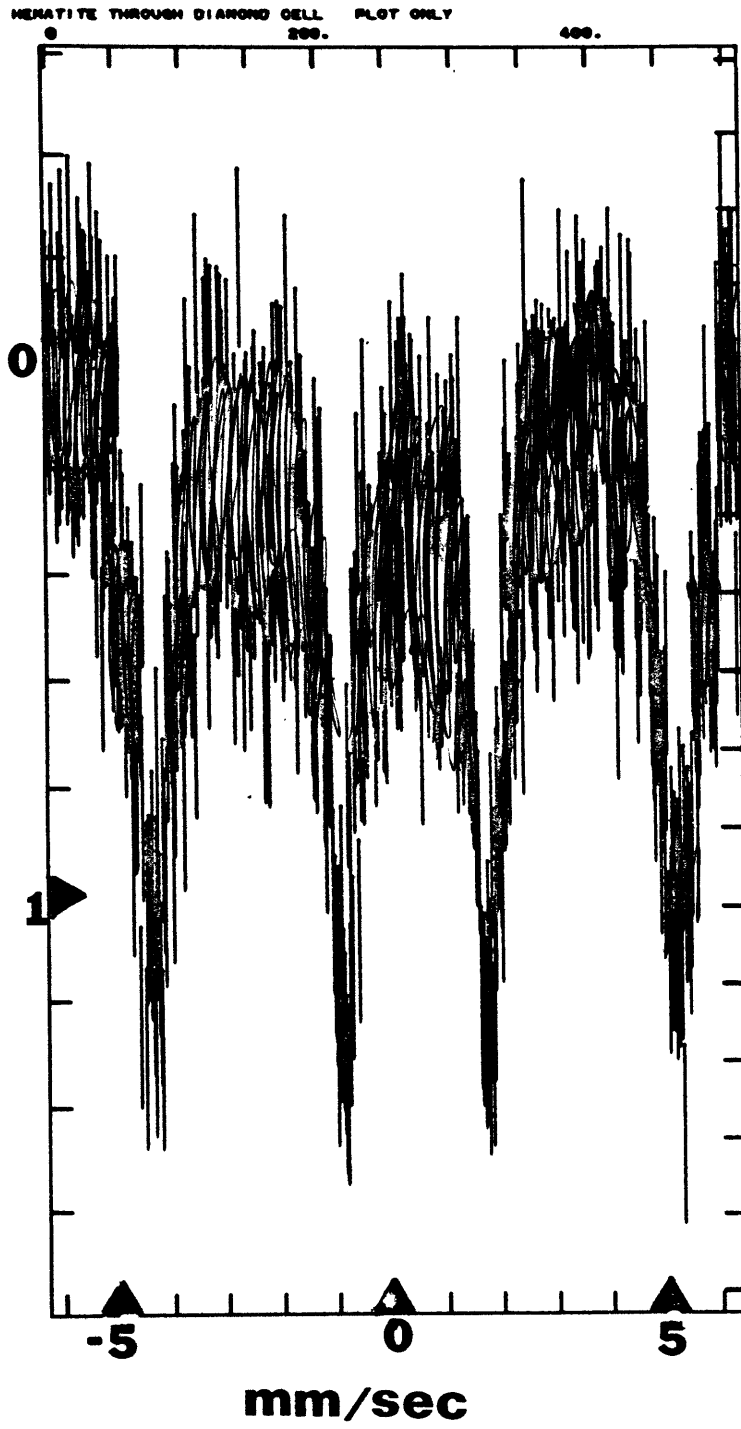


Diamond Cell  
(simplified)

Figure 3.12

Mössbauer spectrum of the inner four peaks of hematite obtained in the diamond cell set-up shown in figure 3.11.

**% ABSORPTION**





transmitted through the nickel would reach the detector. This would cut the count rate to 7%, but the hematite peaks would have exactly the same absolute absorption, which would then represent a 15% absorption instead of just over 1% absorption and improve the statistics for the same counting time.

Other improvements, other than avoiding thick absorber phenomena, for improving the spectrum quality would be:

1. to collimate the  $\gamma$ -ray beam;
2. to design a small window, highly efficient  $\gamma$ -ray detector; and
3. to make the sample aperture as large as possible.

The advantages the diamond cell version for high pressure Mössbauer experiments are:

1. the cell is easier to work with;
2. hydrostatic experiments can be performed using liquid in the gasket aperture, thus avoiding possible shear effects;
3. the length of time for the experiment is uniform and does not depend on pressure; and
4. the simultaneous application of high temperature should be easier as well as much more extended in range.

Disadvantages of the diamond cell are:

1. the sample is much smaller;
2. pressure is harder to measure on a primary basis; and
3. experiments at low pressure take much longer than in the other cell.

### 3.4 Synthesis Experiments

#### 3.4.1 Introduction

The need for synthesis of phases has already been indicated. On one hand, some compositional control is useful. On the other hand, as large a Mössbauer absorption as is practical is required which necessitates synthesis of certain phases starting with hematite enriched in  $^{57}\text{Fe}$ , the Mössbauer isotope of iron. Due to the cost of  $^{57}\text{Fe}_2\text{O}_3$ , the synthesis experiments were carried out in two stages; the first stage was the execution of dummy syntheses using  $\text{Fe}_2\text{O}_3$  with natural isotopic abundance until the required phase was obtained. The second stage was to duplicate the conditions of the most successful synthesis of the phase, but to use  $^{57}\text{Fe}_2\text{O}_3$  in the starting mix. Other methods of enriching mineral phases in  $^{57}\text{Fe}$ , such as ion diffusion, were not attempted because of the lack of data on such techniques.

During the synthesis work, a number of interesting results and problems were encountered, which were unrelated to the task of synthesizing phases containing  $^{57}\text{Fe}$ . Such findings are discussed in detail in Appendix A1 and are mentioned only in passing in this chapter.

A glossary of symbols used in this chapter and Appendix A1 is given in table 3.1.

#### 3.4.2 Synthesis techniques

Hydrothermal techniques similar to those described by Huebner (1971) were used for all of the synthesis experiments reported here. Where possible, the conditions to synthesize phases were obtained from established stability fields for the phases as reported in the literature.

Table 3.1

GLOSSARY OF SYMBOLS USED IN SECTION 3.4 AND APPENDIX A1

CC:	Capsule configuration; numbers in this column in tables 3.3-3.6 refer to diagrams in figure 3.13
P:	Pressure in kilobars
T:	Temperature in degrees centigrade
t:	Time in hours
SE#:	Synthesis experiment number
XRD:	X-ray diffraction; phases listed in tables 3.3-3.6 appeared in the X-ray diffraction pattern of the synthesis run product
Möss:	Mössbauer spectrum; in tables 3.3-3.6 interpretation of the Mössbauer spectrum of the run product is summarized
Opt:	Optical microscope observations of the run product; although such observations were routinely made, only additional pertinent data are listed in tables 3.3-3.6
Spa:	Absorption spectrum; results obtained from an absorption spectrum of the run product
Spr:	Reflectance spectrum; results obtained from a diffuse reflectance spectrum of the run product
N:	Synthesis experiments of iron-containing phases starting with $\text{Fe}_2\text{O}_3$ of normal isotopic abundance
E:	Synthesis experiments of iron-containing phases starting with $\text{Fe}_2\text{O}_3$ enriched in $^{57}\text{Fe}$ isotope

Table 3.1  
(continued)

Buffer symbols (in order of decreasing  $fO_2$  buffering ability)

HM:	Hematite-magnetite
NNO:	Nickel-nickel oxide
QFM:	Quartz-fayalite-magnetite
MW:	Magnetite-wüstite (above 600 °C)
IM:	Iron metal-magnetite (below 600 °C)
IW:	Iron metal-wüstite (above 600 °C)
IQF:	Iron metal-quartz-fayalite

However, since the investigation of stability fields was not the prime motivation of this study, normal precautions and calibrations associated with the art of hydrothermal synthesis were not carried out. These factors included: no accurate calibrations of the thermocouples used in this study, disregard for the exactness of the bomb-furnace distance and initial content of buffers (e.g., using Fe alone rather than Fe+FeO for the IW buffer) and ignoring temperature and pressure variations of the order of 10 °C or 1,000 psi during a run. These details, crucial for the establishment of stability fields and calculation of thermodynamic data, need not be of any concern for synthesis alone. For this reason, the temperatures and pressures quoted in the tables of syntheses are accurate only to  $\pm 10$  °C and  $\pm 0.1$  kb respectively.

The starting materials were "oxide" mixes, where the description "oxide" includes silicate glasses and hydroxides. The chemical form for each element used in this study is listed in table 3.2.

After being dried for a few hours at 250-400 °C and subsequently allowed to cool in a dessicator, the chemicals were weighed out in stoichiometric amounts corresponding to the desired formula so that 50 mg of the desired phase were obtained. After grinding the "oxide" mix under acetone for about 20-30 minutes, it was packed in a precious metal capsule of medium size (2 mm diameter) and about 2 cm long. The capsule was sealed at both ends by arc-welding. If sufficient H<sub>2</sub>O could not be generated from the chemicals in the "oxide" mix, demineralized H<sub>2</sub>O was added so that approximately 5 mg of H<sub>2</sub>O would be present in the sealed capsule during the synthesis run.

Table 3.2

CHEMICAL FORMS OF THE ELEMENTS USED IN "OXIDE"  
MIXES IN THE COURSE OF THIS STUDY

Mg:	MgO
Al:	" $\gamma$ -Al <sub>2</sub> O <sub>3</sub> " an amorphous-like form of alumina formed by heating AlCl <sub>3</sub> ·6H <sub>2</sub> O
Si:	SiO <sub>2</sub> glass and/or K <sub>2</sub> Si <sub>2</sub> O <sub>5</sub> glass
K:	K <sub>2</sub> Si <sub>2</sub> O <sub>5</sub> glass, prepared according to the method of Schairer and Bowen (1955)
Ca:	Ca(OH) <sub>2</sub> , or CaO formed by thermal decomposition of Ca(OH) <sub>2</sub>
Ti:	TiO <sub>2</sub> , rutile
Cr:	Amorphous Cr <sub>2</sub> O <sub>3</sub> or ammonium dichromate
Fe:	Hematite, Fe <sub>2</sub> O <sub>3</sub> or <sup>57</sup> Fe <sub>2</sub> O <sub>3</sub>

The precious metal capsules used in this study were either gold or silver-palladium ( $\text{Ag}_{80}\text{Pd}_{20}$ ) alloy. Platinum was not used because of the alloying properties of iron and platinum (Huebner, 1971). The stability field of the mineral to be synthesized usually determined the buffer to be used, which in turn determined the capsule configuration to be used. The capsule configurations used in this study are shown in figure 3.13.

Identification of the run product and final buffer composition was primarily achieved by means of standard X-ray diffraction techniques. Mössbauer spectroscopy, optical microscopy and occasionally diffuse reflectance or absorption spectroscopy were also used for verification purposes. Indeed, the importance of Mössbauer spectroscopy for the investigation of the product of iron-containing mineral synthesis runs can not be over-emphasized, since crystallographic and valence state complications, otherwise vaguely suspected and usually ignored, are clearly shown. This finding agrees with those of other recent Mössbauer studies of synthesized iron-containing minerals and is especially critical for hydroxyl-containing phases such as amphiboles and micas (Semet, 1973; Ernst and Wai, 1970; Virgo, 1972; Wones and Burns, unpublished).

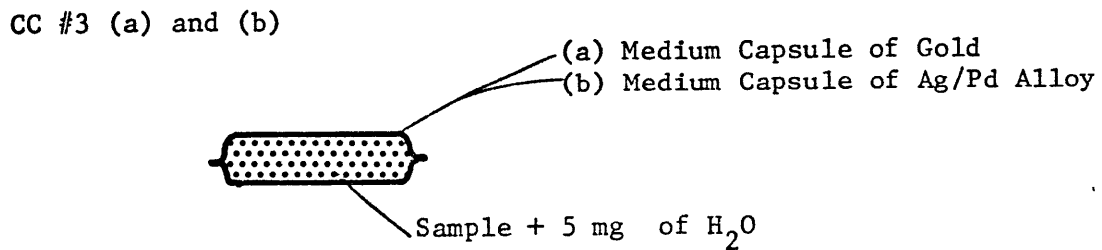
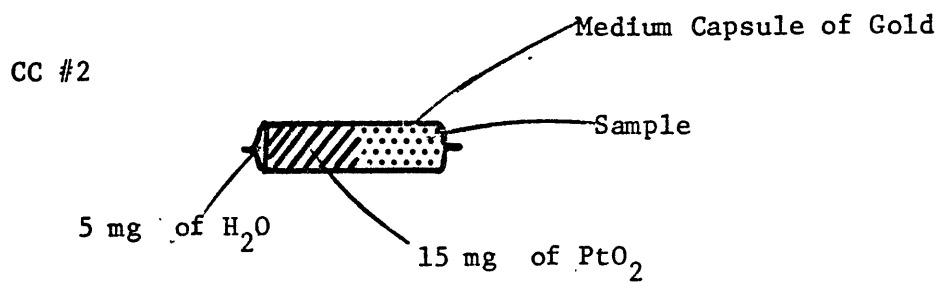
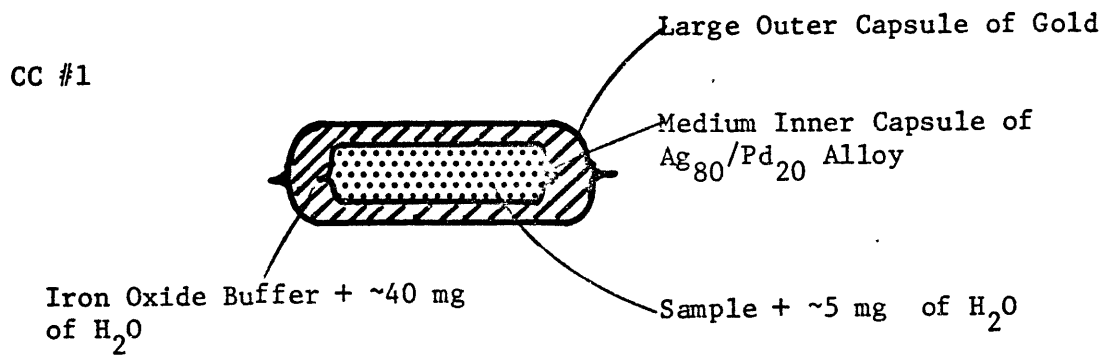
#### 3.4.3 Synthesis of micas

Synthetic micas which were prepared for high pressure Mössbauer experiments included ferriphlogopites,  $\text{KMg}_3(\text{Fe}^{3+}, \text{Al})\text{Si}_3\text{O}_{10}(\text{OH})_2$  and ferrimuscovites,  $\text{K}(\text{Al}, \text{Fe}^{3+})_2\text{AlSi}_3\text{O}_{10}(\text{OH})_2$ . Ferrous-containing micas were not synthesized intentionally; however, most mica phases synthesized contained some ferrous iron, so that data on the Mössbauer parameters of ferrous cations in micas as a function of pressure were also obtained.

Figure 3.13

Capsule configurations used in the synthesis experiments. (a) CC #1: external  $f_{O_2}$  buffer. Both capsules sealed. Oxygen fugacity of sample determined by external iron oxide- $H_2O$  buffer and P, T conditions. (b) CC #2: internal  $f_{O_2}$  buffer. Capsule sealed. Oxygen fugacity determined by  $PtO_2$  decomposition. (c) CC #3 "unbuffered": 3(a): gold tubing used.  $f_{O_2}$  indeterminate - sample isolated from bomb. 3(b): Ag/Pd alloy tubing used.  $f_{O_2}$  determined by the bomb since  $H_2$  permeates through Ag/Pd. Oxygen fugacity of bomb is close to NNO. Capsules sealed.

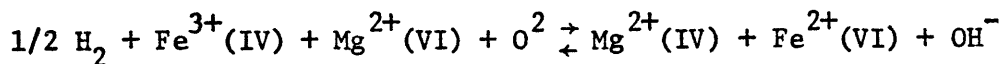




### 3.4.3 (a) Ferriphlogopites, $\text{KMg}_3(\text{Fe}^{3+}, \text{Al})\text{Si}_3\text{O}_{10}(\text{OH})_2$

No stability fields are reported in the literature for these phases, which contain tetrahedral ferric iron. However, a number of syntheses of  $\text{KMg}_3\text{Fe}^{3+}\text{Si}_3\text{O}_{10}(\text{OH})_2$  have been reported (Hazen and Wones, 1972; Annersten et al., 1971; Wise and Eugster, 1964) and these data were used as a starting point. The successful ferriphlogopite syntheses in this study are listed in table 3.3(a).

In almost all runs, Mössbauer spectroscopy showed that the product contained some  $\text{Fe}^{2+}$  (VI) and, in one case, a mica with a 25%  $\text{Fe}^{2+}/(\text{Fe}^{3+} + \text{Fe}^{2+})$  ratio was obtained. The XRD patterns and optical observations indicated that mica was the only phase present above the 5% level, and Mössbauer spectra showed that no unreacted iron oxide phases were present. Since the ferriphlogopite starting materials were weighed out to yield micas with exact chemical composition, the occurrence of some ferrous iron in the octahedral layer is somewhat mystifying. Two possible explanations can be offered: firstly, MgO is difficult to dry completely so that the weighed out material may not represent 100% MgO, thus enabling some ferrous iron to be produced to fill the vacancies in the octahedral layers, along with other changes to preserve electrical neutrality in the mica structure; or, secondly, the coupled reaction:



takes place, which involves locating some of the magnesium in the tetrahedral layer and concomitant redox reactions of  $\text{Fe}^{3+}$  to  $\text{Fe}^{2+}$  and  $\text{O}^{2-}$  to  $\text{OH}^-$ . Seifert and Schreyer (1971) have documented mica syntheses where

Table 3.3

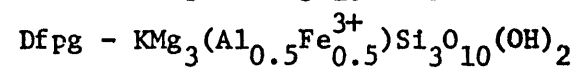
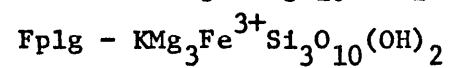
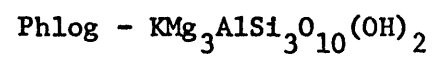
## SYNTHESIS OF MICAS: EXPERIMENTAL DETAILS

## (a) Ferriphlogopites

Both XRD and OPT showed mica to be the only phase present.

SE#	PHASE	CC	P	T	BUFFER	t	RESULTS AND COMMENTS
14	Phlog	3a	2.0	627	--	286	XRD: Mica - used as reference X-ray pattern Color: White
1	N-Fplg	3a	2.0	675	--	48	XRD: Mica Color: Pink Möss: Fe <sup>3+</sup> (IV) doublet + 5% Fe <sup>2+</sup> (VI)
16	E-Fplg	3a	2.0	627	--	286	XRD: Mica Color: Pink Möss: Fe <sup>3+</sup> (IV) doublet + 10% Fe <sup>2+</sup> (VI)
23	E-Fplg	3a	2.0	679	--	72	XRD: Mica Color: Pink Möss: Fe <sup>3+</sup> (IV) doublet + 15% Fe <sup>2+</sup> (VI)
12	N-Dfpg	3a	2.0	630	--	110	XRD: Mica Color: Pale pink Opt: $\bar{n} \approx 1.590$
15	E-Dfpg	3a	2.0	627	--	286	XRD: Mica Color: Pale pink Möss: Fe <sup>3+</sup> (IV) doublet + 25% Fe <sup>2+</sup> (VI) Spr: Typical Fe <sup>3+</sup> (IV) features + trace of Fe <sup>2+</sup> (VI)

Table 3.3 (a)  
(continued)



XRD Comparison: ASTM 10-492, 19-493, Hazen (1972)

XRD Comparison: ASTM 17-520, Hazen (1972)

XRD Comparison: Average of Phlog and Fplg data

Table 3.3  
(continued)

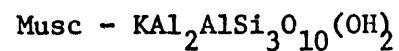
(b) Ferrimuscovites

XRD always showed that synthesis was never 100% successful.

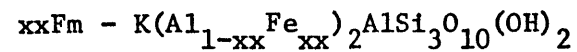
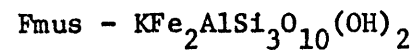
SE#	PHASE	CC	P	T	BUFFER	t	RESULTS AND COMMENTS
17	Musc	3a	2.0	627	--	165	XRD: Feldspar + corundum - see Yoder and Eugster (1955) for explanation
13	N-Fmus	3a	2.0	437	--	280	XRD: Hematite + feldspar + mica - mica possibly annite - $d_{001}$ much larger than muscovite
2	N-50Fm	3a	2.0	675	--	72	XRD: Hematite + feldspar + mica Möss: Hematite
11	N-50Fm	3a	2.0	437	--	280	XRD: Hematite + feldspar + mica
18	N-10Fm	3a	2.0	627	--	165	XRD: Mica + feldspar Color: Pale purple Spr: Featureless
38	N-10Fm	2	2.0	606	PtO <sub>2</sub>	25	XRD: Mica + trace feldspar Color: Off white Möss: Fe <sup>3+</sup> > 90%
39	N-10Fm	2	2.0	608	PtO <sub>2</sub>	68	XRD: Mica + trace feldspar Color: Off white
55	N-25Fm	2	2.0	600	PtO <sub>2</sub>	42	XRD: Mica + minor feldspar Color: Blue-grey Möss: ~25% Fe <sup>2+</sup>

Table 3.3 (b)  
(continued)

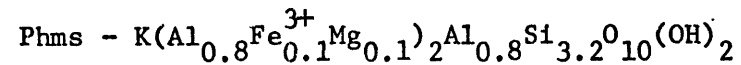
SE#	PHASE	CC	P	T	BUFFER	t	RESULTS AND COMMENTS
58	E-20Fm	2	2.0	600	PtO <sub>2</sub>	24	XRD: Mica + feldspar + magnetite Möss: Magnetite + Fe <sup>3+</sup> doublet. Incomplete synthesis.
19	N-Phms	3a	2.0	627	--	165	XRD: Mica + minor feldspar Color: Pale purple Möss: 30% Fe <sup>2+</sup> Spr: Featureless
20	E-Phms	3a	2.0	617	--	130	XRD: Mica + minor feldspar Color: Pale purple Möss: 50% Fe <sup>2+</sup>



XRD Comparison: ASTM 7-32 (2M<sub>1</sub>), 7-25 (1M, 1Md)



XRD Comparison: Muscovite 1M pattern

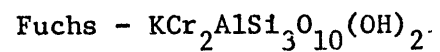
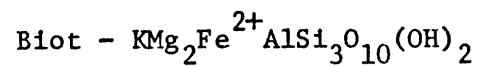
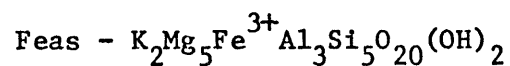


XRD Comparison: Muscovite 1Md pattern

Table 3.3  
(continued)

(c) Other micas

SE#	PHASE	CC	P	T	BUFFER	t	RESULTS AND COMMENTS
21	N-Feas	3a	2.0	679	--	72	XRD: Mica Color: Blue Möss: 30% Fe <sup>2+</sup> (VI) Spr: Minimum at blue end of visible
25	E-Feas	3a	2.0	647	--	70	XRD: Mica Color: Blue Möss: 30% Fe <sup>2+</sup> (VI)
54	N-Feas	2	2.0	600	PtO <sub>2</sub>	42	XRD: Mica Color: Blue
22	N-Biot	3a	2.0	451	--	285	XRD: Mica Color: Blue
59	Fuchs	3a	2.0	549	--	138	XRD: Cr <sub>2</sub> O <sub>3</sub> + feldspar + trace of mica

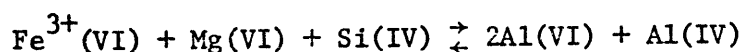


XRD Comparison: ASTM 10-492, 10-493

$Mg^{2+}$  in tetrahedral coordination is required. In their study, micas were synthesized with almost 10% of the tetrahedral sites filled by  $Mg^{2+}$ . In the present study, the second explanation for the presence of  $Fe^{2+}(VI)$  requires, at most, only 4% of the available tetrahedral sites to be filled by  $Mg^{2+}$ . In either case, the deviation from the expected stoichiometry and structure is not large. In fact, the presence of  $Fe^{2+}(VI)$  in these micas was useful because it permitted the delineation of Mössbauer parameters for  $Fe^{2+}(VI)$  in micas as a function of pressure. Attempts to fit  $Fe^{3+}(VI)$  in the Mössbauer spectra of these micas were not successful and it was concluded that  $Fe^{3+}(VI)$  was either absent or negligible (< 5% total Fe). Although cell parameters were not calculated for these micas, the intensities and d-spacings of the peaks in the XRD patterns were in very close agreement with those found in the ASTM card file and in the literature for synthetic phases of similar compositions.

#### 3.4.3 (b) Ferrimuscovites, $K(Al,Fe^{3+})_2AlSi_3O_{10}(OH)_2$

Unlike the trioctahedral micas, synthesis studies of the substitution of  $Fe^{3+}$  for octahedral  $Al^{3+}$  in dioctahedral micas are very limited and only three literature references could be found pertaining to this problem. Both Lindqvist (1966) and Crowley and Roy (1964) indicated an upper limit of approximately 30% substitution of " $Fe^{3+}$ " for  $Al(VI)$  in muscovite, whereas Wise and Eugster (1964) were more concerned with the join muscovite-phengite and showed that the phase celadonite,  $KMgFe^{3+}Si_4O_{10}(OH)_2$ , could be formed from muscovite by means of the coupled substitution:





The present study, which had the advantage of using Mössbauer spectroscopy as a routine analytical tool, also ran into problems in the course of synthesizing these micas. Some potassium feldspar was always found in the synthesis products along with the mica, but not  $\text{Al}_2\text{O}_3$  or  $\text{Fe}_2\text{O}_3$  phases, and most of the phases contained large contents of ferrous iron (up to 50%  $\text{Fe}^{2+}/(\text{Fe}^{2+} + \text{Fe}^{3+})$ ). The complications of this system in the light of the limited experimental work performed here are discussed in more detail in Appendix A1.1. Syntheses along the joins muscovite-ferrimuscovite and muscovite-celadonite were attempted and are listed in table 3.3(b).

Although a number of problems remain to be solved concerning the substitution of  $\text{Fe}^{3+}$  for  $\text{Al}^{3+}$  in muscovite, the available evidence strongly suggests that the ferric iron is located in the octahedral sites of these micas. The color and reflectance spectra of these micas are consistent with  $\text{Fe}^{3+}(\text{VI})$  and not  $\text{Fe}^{3+}(\text{IV})$ . Also, the parameters of the ferric peaks in the Mössbauer spectrum are similar to other  $\text{Fe}^{3+}(\text{VI})$  species.

#### 3.4.3 (c) Other mica syntheses

A number of other iron-containing micas were synthesized in the course of this study. For completeness, these syntheses are listed in table 3.3(c) but the products were not used for high pressure experiments because of difficulties over controlling the iron oxidation state and time limitations. These syntheses were attempted in order to try and prepare  $\text{Fe}^{3+}_4(\text{OH})_2$  and  $\text{Fe}^{3+}_6$  coordinations in trioctahedral micas. Synthesis of the mica fuchsite was also attempted.

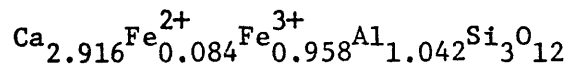
#### 3.4.4 Synthesis of garnets

Syntheses of garnets are well documented in the literature.

Although some of the phases synthesized in this study do not correspond with any synthesized previously, earlier hydrothermal garnet synthesis studies which were informative for this study include Christophe-Michel-Levy (1956) and Coes (1955) for andradite-grossular compositions, Jagitsch (1956) for andradite and uvarovite compositions, Yoder (1950) and Roy and Roy (1957) for grossular and Hsu (1968) for almandine. In addition, Huckenholz and Yoder (1971) and Huckenholz (1969) have presented partial details of the stability fields of andradite and of titanium andradite garnets respectively; these studies did not use standard hydrothermal synthesis techniques however.

#### 3.4.4 (a) Aluminum-iron garnets

Synthesis of a garnet of approximate composition  $\text{Ca}_3\text{FeAlSi}_3\text{O}_{12}$  was straightforward except for a complication posed by about 2.7 wt %  $\text{CaCO}_3$  being present in the calcium hydroxide used in the synthesis which caused some deviation from the required formula. The actual formula of the garnet (SE #41) synthesized is discussed in detail in Appendix A1.2 and approximates:



The small amounts of  $\text{CaCO}_3$  and  $\text{CaSiO}_3$  also present in the run-product can be ignored. The details of the syntheses are given in table 3.4(a).

#### 3.4.4 (b) Chromium-iron garnets

Some syntheses of  $\text{Cr}^{3+}$ -containing garnets were initially attempted using amorphous  $\text{Cr}_2\text{O}_3$  in the starting mix, SE #29 and SE #43, but due presumably to kinetic factors, crystalline  $\text{Cr}_2\text{O}_3$  was always

Table 3.4

## SYNTHESIS OF GARNETS: EXPERIMENTAL DETAILS

## (a) Aluminum-iron garnets

SE#	PHASE	CC	P	T	BUFFER	t	RESULTS AND COMMENTS
27	N-Gran	2	1.0	675	PtO <sub>2</sub>	45	XRD: Garnet (a = 11.95 Å) Möss: Minor hematite + Fe <sup>3+</sup> (VI) doublet
41	E-Gran	2	1.0	676	PtO <sub>2</sub>	45	XRD: Garnet (a = 11.94 Å) + CaCO <sub>3</sub> + CaSiO <sub>3</sub> Color: Orange-red Möss: 92% Fe <sup>3+</sup> (VI) + 8% Fe <sup>2+</sup> (VIII)

Gran - Ca<sub>3</sub>AlFeSi<sub>3</sub>O<sub>12</sub>

XRD Comparison: ASTM 10-288, 3-826

Table 3.4  
(continued)

(b) Chromium-iron garnets

SE#	PHASE	CC	P	T	BUFFER	t	RESULTS AND COMMENTS
43	Uvar	3a	1.0	675	* --	240	XRD: $\text{Cr}_2\text{O}_3 + \text{CaSiO}_3$
48	Uvar	3b	1.0	675	--	115	XRD: Garnet (a = 12.00 Å) Color: Bright green Spa: $\text{Cr}^{3+}$ (VI) peaks
29	N-Uvar	1	1.0	672	* HM	70	XRD: Garnet (a = 12.05 Å), $\text{Cr}_2\text{O}_3$ , $\text{CaSiO}_3$
49	N-Uvar	1	1.1	666	HM	96	XRD: Garnet (a = 12.00 Å) hematite + cristobalite
51	N-Uvar	3b	1.0	703	--	141	XRD: Garnet (a = 12.03 Å) Color: Drab green Möss: $\text{Fe}^{3+}$ doublet
53	E-Uvar	3b	1.0	714	--	120	XRD: Garnet (a = 12.03 Å) Color: Drab green Möss: $\text{Fe}^{3+}$ doublet

- 120 -

Uvar -  $\text{Ca}_3\text{Cr}_2\text{Si}_3\text{O}_{12}$

XRD Comparison: ASTM 11-696

Uvar -  $\text{Ca}_3\text{FeCrSi}_3\text{O}_{12}$

\* Starting mix contained amorphous  $\text{Cr}_2\text{O}_3$ ; all others contained ammonium dichromate.

Table 3.4  
(continued)

(c) Titanium-iron garnets -- all unsuccessful

SE#	PHASE	CC	P	T	BUFFER	t	RESULTS AND COMMENTS
28	N-Tian	2	1.0	665	PtO <sub>2</sub>	46	XRD: Garnet + magnetite
50	N-Tian	1	1.0	673	HM	96	XRD: Garnet (a = 12.07 Å) + magnetite + perovskite Möss: Fe <sup>3+</sup> doublet + magnetite
52	N-Tian	3b	0.5	790	--	138	XRD: Garnet + perovskite + magnetite

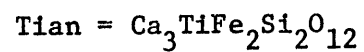
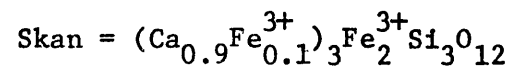
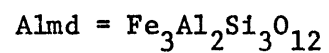
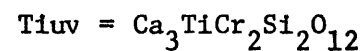
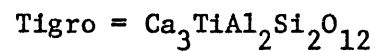


Table 3.4  
(continued)

(d) Other garnet syntheses -- all unsuccessful

SE#	PHASE	CC	P	T	BUFFER	t	RESULTS AND COMMENTS
44	Tigro	3b	1.0	675	--	240	XRD: Perovskite + anorthite + grossular + gehlenite (?)
45	Tiuv	3b	1.0	675	--	240	XRD: Sphene + CaSiO <sub>3</sub> + perovskite + Cr <sub>2</sub> O <sub>3</sub>
57	N-Almd	1	2.0	652	IW	66	XRD: Fe <sub>2</sub> SiO <sub>4</sub> + other phases, no garnet
60	N-Skan	3b	1.0	655	--	96	XRD: Andradite + Fe <sub>3</sub> O <sub>4</sub> + SiO <sub>2</sub> Möss: Fe <sup>3+</sup> doublet + magnetite

122



found in the run-product. Thus, alternative sources of  $\text{Cr}^{3+}$  were sought. Ammonium dichromate was found suitable and was subsequently used for all other chromium garnet syntheses. The details of the syntheses are given in table 3.4(b).

#### 3.4.4 (c) Titanium-iron garnets

Since titanium-containing garnets often contain  $\text{Fe}^{3+}$  in tetrahedral coordination, much emphasis was placed on the synthesis of a garnet of composition  $\text{Ca}_3\text{TiFe}_2\text{Si}_2\text{O}_{12}$ . Both Ito and Frondel (1967) and Huckenholz (1969) have recorded the synthesis of such a phase in air, starting from gels and glasses respectively, but requiring much higher temperatures than were available to this investigation. The attempts to synthesize this phase using hydrothermal techniques were unsuccessful and are listed in table 3.4(c).

#### 3.4.4 (d) Other garnet syntheses

In the course of this study, garnets of other compositions were attempted. None was successful. For completeness, these are listed in table 3.4(d).

#### 3.4.5 Synthesis of potassium iron feldspar

The synthesis of the feldspar,  $\text{KFeSi}_3\text{O}_8$ , was quite straightforward. In his study of the stability field of ferriannite, Wones (1963) had established part of the stability field of  $\text{KFeSi}_3\text{O}_8$  by showing that ferriannite breaks down to iron feldspar, iron oxides and water at high oxygen fugacities. Thus, by maintaining high oxygen fugacities ( $f\text{O}_2 \geq \text{HM}$ ), the synthesis was easily achieved and no trace of ferrous iron was found. The only impurity in the product was occasional traces of unreacted  $\text{Fe}_2\text{O}_3$ .

Synthesis details are given in table 3.5.

One unusual point of these syntheses was that the XRD pattern varied slightly with different buffers. The feldspar synthesized under HM conditions had intensities matching exactly those listed on ASTM card #16-153 whereas feldspars synthesized with  $\text{PtO}_2$  as an internal buffer had peaks in the correct positions, but of differing intensity. The reason for this is not clear, unless iron-silicon ordering in the tetrahedral sites is a function of oxygen fugacity.

#### 3.4.6 Synthesis of magnetite

Magnetites synthesized in this study were obtained by holding hematite at the oxygen fugacity determined by the iron-nickel alloy bomb (approximately NNO) for a long period of time. The syntheses were 100% successful and details are given in table 3.6.

#### 3.4.7 Sources of other samples

In the latter part of this thesis, it was realized that certain natural minerals could be studied at high pressure since the requirement of enrichment of iron in the  $^{57}\text{Fe}$  isotope was not necessary if the iron content was large enough. Samples of natural iron minerals which were studied include: fayalite, from Rockport, Massachusetts; almandine, from Washington Camp Mine, Arizona; and orthoferrosilite, from Manchuria. In addition, two synthetic garnets donated by Dr. J. Ito of Harvard were used. The compositions and references for these five samples are given in table 3.7.

In addition, Dr. D.J. Vaughan made available two  $^{57}\text{Fe}$  enriched samples which he had prepared. These were acmite,  $\text{NaFeSi}_2\text{O}_6$  and fayalite,  $\text{Fe}_2\text{SiO}_4$ .



Table 3.5

SYNTHESIS OF IRON FELDSPAR,  $\text{KFeSi}_3\text{O}_8$ : EXPERIMENTAL DETAILS

SE#	PHASE	CC	P	T	BUFFER	t	RESULTS AND COMMENTS
26	N-Kffs	2	1.7	647	$\text{Ag}_2\text{O}$	70	XRD: Mica, ferriannite Opt: Black glass, oxygen fugacity too low
20	SE #26P	2	0.6	596	$\text{PtO}_2$	23	XRD: Feldspar Opt: Red powder
33	N-Kffs	2	1.0	602	$\text{PtO}_2$	23	XRD: Microcline Möss: $\text{Fe}^{3+}$ (IV) doublet only
34	N-Kffs	1	1.1	602	HM	90	XRD: Microcline Möss: $\text{Fe}^{3+}$ (IV) doublet only
36	E-Kffs	2	0.6	618	$\text{PtO}_2$	23	XRD: Microcline Möss: $\text{Fe}^{3+}$ (IV) + 10% $\text{Fe}_2\text{O}_3$ - incomplete synthesis
37	SE #36P	2	1.0	602	$\text{PtO}_2$	28	XRD: Microcline Möss: $\text{Fe}^{3+}$ (IV) + 2% $\text{Fe}_2\text{O}_3$

Kffs =  $\text{KFeSiO}_8$  SE #xxP - Product of SE #xx used as starting material

XRD Comparison: ASTM 16-153

Table 3.6

## SYNTHESIS OF MAGNETITE: EXPERIMENTAL DETAILS

SE#	PHASE	CC	P	T	BUFFER	t	RESULTS AND COMMENTS
31	N-Magn	3b	2.0	666	--	257	XRD: 100% Magnetite Möss: Characteristic magnetite pattern only
35	E-Magn	3b	1.0	675	--	375	XRD: 100% Magnetite Möss: Characteristic magnetite pattern only

Magn =  $\text{Fe}_3\text{O}_4$

XRD Comparison: ASTM 19-629

Table 3.7

COMPOSITION OF SAMPLES CONTAINING IRON OF NATURAL ISOTOPIC ABUNDANCE WHICH WERE USED IN THIS STUDY

PHASE	COMPOSITION	Wt % Fe	REF
Fayalite	$(\text{Fe}_{0.97}\text{Mn}_{0.03})_2\text{SiO}_4$	54	1
Almandine	$(\text{Fe}_{0.76}\text{Mg}_{0.18}\text{Mn}_{0.05})_3\text{Al}_2\text{Si}_3\text{O}_{12}$	34	2
Orthoferrosilite	$(\text{Fe}_{0.87}\text{Mg}_{0.13})\text{SiO}_3$	38	3
Garnet	$\text{Ca}_3\text{TiFe}_2\text{Si}_2\text{O}_{12}$	21	4
Garnet	$\text{Ca}_{2.5}\text{Zr}_{2.5}\text{Fe}_3\text{O}_{12}$	24	4

- (1) Analysis reported in Burns and Huggins (1972)
- (2) EMP analysis reported by Whipple (1973)
- (3) Analysis reported in table 3, Deer et al. (1963)
- (4) Synthesized at conditions given in Ito and Frondel (1967)

## Chapter 4

### RESULTS AND DISCUSSION

#### 4.1 Introduction

This chapter is bipartite; the first half presents the results of the Mössbauer experiments performed on the samples while under pressure and the second half discusses and interprets these results. The results are presented according to mineral phase, whereas the discussion of the results is presented according to Mössbauer parameter.

All data reported in section 4.2 are tabulated as a function of pressure in kilobars (kb). The Mössbauer parameters, isomer shift, quadrupole splitting and widths, are given in mm/sec, relative to iron foil calibration runs. The percentages listed in these tables refer to the ratio of the area for that absorption to the total area under the absorption envelope. The term "regular" in these tables refers to results obtained from samples when they were run in the normal geometry as opposed to the high pressure geometry (figure 3.6).

The pressures listed in tables in section 4.2 are probably accurate to only about  $\pm 10\%$ , based on the estimated accuracy of the calibration curve. However, as these Mössbauer data are used only in a qualitative manner for the most part, this uncertainty is not very serious. The errors in the Mössbauer parameters, isomer shift and quadrupole splitting, are determined by uncertainties in the calibration and in the computer-fitted peak positions. The iron foil calibration curve introduces an error of less than  $\pm 0.01$  mm/sec in converting from channels to mm/sec and the major error

in the Mössbauer data results from uncertainty in the peak positions. For isolated peaks these computer calculated uncertainties are also generally less than  $\pm 0.01$  mm/sec, so that the total uncertainty in the position of such peaks is probably only about  $\pm 0.01$  mm/sec. However, as the peaks increasingly overlap, the uncertainties in the positions of the overlapping peaks increase, and larger errors can be expected for such data. The runs which are particularly poor in this respect include the ferriphlogopites and the mixture of iron microcline and fayalite. Other than these phases, all other phases have spectra in which the overlapping of peaks is not too serious and a general error of  $\pm 0.02$  mm/sec may be regarded as representative for the rest of the Mössbauer data as a function of pressure. It should be noted that running a suite of spectra as a function of pressure does minimize any calibration uncertainties, since the set-up is not altered in any way during a given high pressure run.

Relative area data are subject to large errors and no reliable estimate can be made of the error in these data. Such data, especially involving small and large peaks, could be subject to an error of up to about 50% of the small peaks' area because of thick absorber phenomena and the poor statistics of such peaks. Relative area data should only be regarded as indicative. No attempt was made to use such data in anything other than a qualitative manner in this study.

The Mössbauer spectra shown in the figures in this chapter are all fitted spectra, unlike most of those shown in the previous chapter, which were basically just plots of the raw spectral data. The data are plotted as % absorption (left hand vertical scale) against energy or relative

velocity of the source with respect to the absorber (horizontal scale). From left to right in these plots, each of the 510 channels represents a small increase in relative velocity over the previous channel. The channel number scale is given as the upper horizontal scale and occasionally appears as the lower scale as well, if the iron foil calibration parameters had not been specified in the computing procedure. The error bars shown for all points in these plots are  $\pm 2$  standard deviations long, where the standard deviation of a given datum point is defined as the square root of the baseline count. The component peaks have been given a Lorentzian shape and are shown as continuous lines in these plots. The lowest continuous line is the fitted envelope to the data and represents the sum of the individual peak amplitudes as a function of energy. The highest continuous line in these plots is the computer fitted baseline. Ideally, due to the oscillatory motion of the source, this line should be symmetrically curved about zero velocity (lower in the center than at the ends), but was often constrained to be horizontal in these spectra as the ideal curvature should be small.

## 4.2 Mössbauer Results

### 4.2.1 Garnets

A number of garnet phases were studied which include the following synthetic phases,  $\text{Ca}_3\text{AlFeSi}_3\text{O}_{12}$  (SE #41),  $\text{Ca}_3\text{CrFeSi}_3\text{O}_{12}$  (SE #53),  $\text{Ca}_3\text{TiFe}_2\text{Si}_2\text{O}_{12}$  and  $\text{Ca}_{2.5}\text{Zr}_{2.5}\text{Fe}_3\text{O}_{12}$  and a natural almandine,  $(\text{Fe,Mg})_3\text{Al}_2\text{Si}_3\text{O}_{12}$ .

#### 4.2.1 (a) $\text{Ca}_3\text{AlFeSi}_3\text{O}_{12}$

This phase contained about 10% of the iron as  $\text{Fe}^{2+}$  in the eight-coordinate sites in addition to ferric in the octahedral sites (see Appendix A1.2 for details), so that results were obtained for two kinds of iron cations. Two separate high pressure runs of this sample were carried out. The Mössbauer spectra were fitted to four peaks as shown in figure 4.1a and Mössbauer parameters are tabulated as a function of pressure in table 4.1. The agreement between the two runs is satisfactory, except perhaps for the isomer shift value for the ferrous peaks. However, since the  $\text{Fe}^{2+}$  absorption is small and one of the ferrous peaks is located very close to the ferric peaks, some scatter can be expected. Of the two runs, the second is superior in quality since the increase in width is not so great and the spectral percent absorption is much larger. Both runs, however, appear to indicate that the high pressure spectra are those of thick absorbers, not only from the width, but also from the jump in ferrous/total iron ratio on changing the geometry (figure 4.1b).

The isomer shifts of both  $\text{Fe}^{3+}$  (VI) and  $\text{Fe}^{2+}$  (VIII) decrease with pressure, while the quadrupole splittings increase initially with pressure and then decrease slightly as pressure is further increased. The ferric quadrupole splitting shows a larger change with pressure.

#### 4.2.1 (b) FeCr garnet

To compare and contrast the behavior of ferric iron in a variety of octahedral environments, yet in the same structure, the FeCr garnet (SE #53) was synthesized so that it could be compared with the synthetic FeAl garnet (SE #41) and andradite (Vaughan and Tossell,

Table 4.1

MÖSSBAUER DATA FOR  $\text{Ca}_3\text{AlFeSi}_3\text{O}_{12}$ , AS A FUNCTION OF PRESSURE.

(The garnet contains approximately 3% almandine component.)

PRESSURE		$\text{Fe}^{3+}$ (VI)				$\text{Fe}^{2+}$ (VIII)			
		IS	QS	WDTH	%	IS	QS	WDTH	%
REGULAR	1 bar	0.40	0.60	0.40	92	1.27	3.60	0.32	8
HIGH	0 kb	0.41	0.60	0.42	90	1.29	3.60	0.29	10
PRESSURE	107 kb	0.37	0.73	1.02	88	1.29	3.61	0.41	12
Run 1	175 kb	0.37	0.73	1.00	88	1.28	3.60	0.31	12
REGULAR	1 bar	0.39	0.59	0.37	92	1.25	3.56	0.32	8
HIGH	0 kb	0.39	0.62	0.53	88	1.25	3.59	0.29	12
PRESSURE	57 kb	0.37	0.78	0.85	87	1.22	3.64	0.32	13
Run 2	108 kb	0.36	0.76	0.86	87	1.23	3.62	0.36	13
	145 kb	0.37	0.76	0.82	87	1.23	3.62	0.34	13
	177 kb	0.36	0.76	0.87	87	1.23	3.61	0.36	13

All fits reported at that stage in the computer fitting where the half-widths and areas for each peak of the individual doublets are held equal. The baseline is constrained to be straight.



Figure 4.1

Mössbauer spectra of FeAl garnet.

Figure 4.1a. Fitted Mössbauer spectra of FeAl garnet at 0 kb (left) and 57 kb (right). The large central peaks are assigned to  $\text{Fe}^{3+}$  (VI); the small outer peaks are assigned to  $\text{Fe}^{2+}$  (VIII).

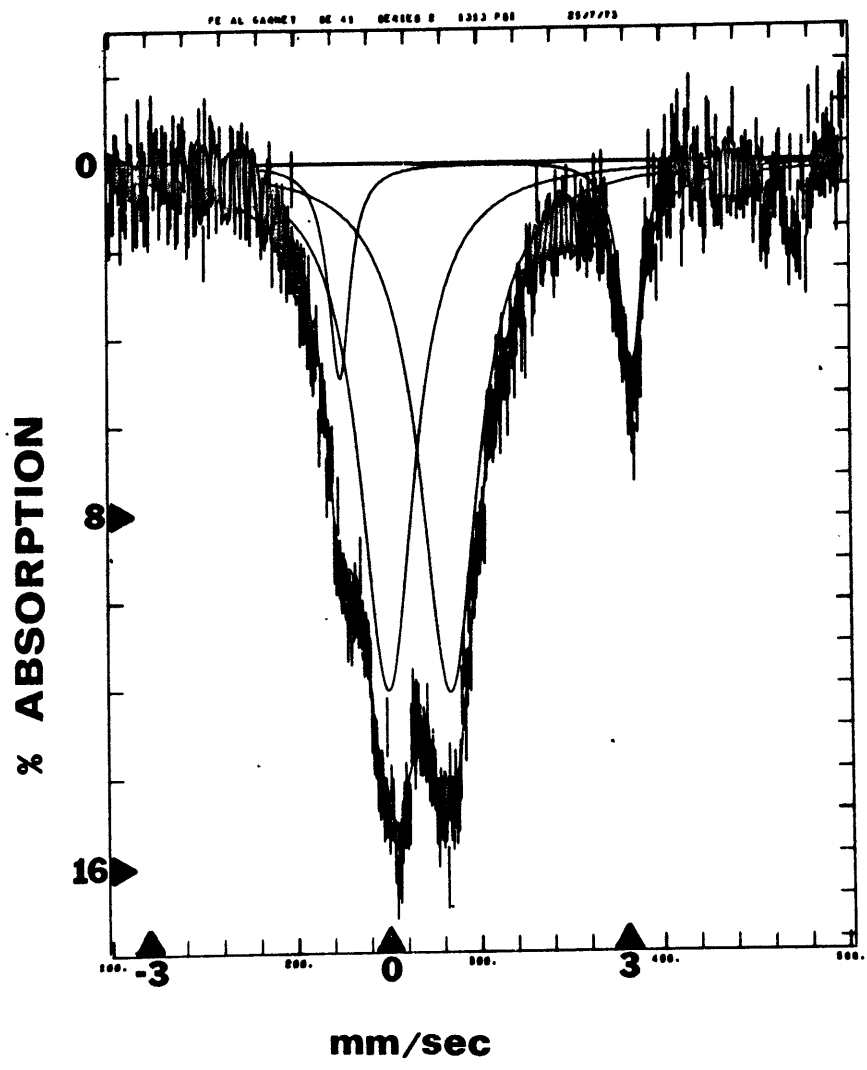
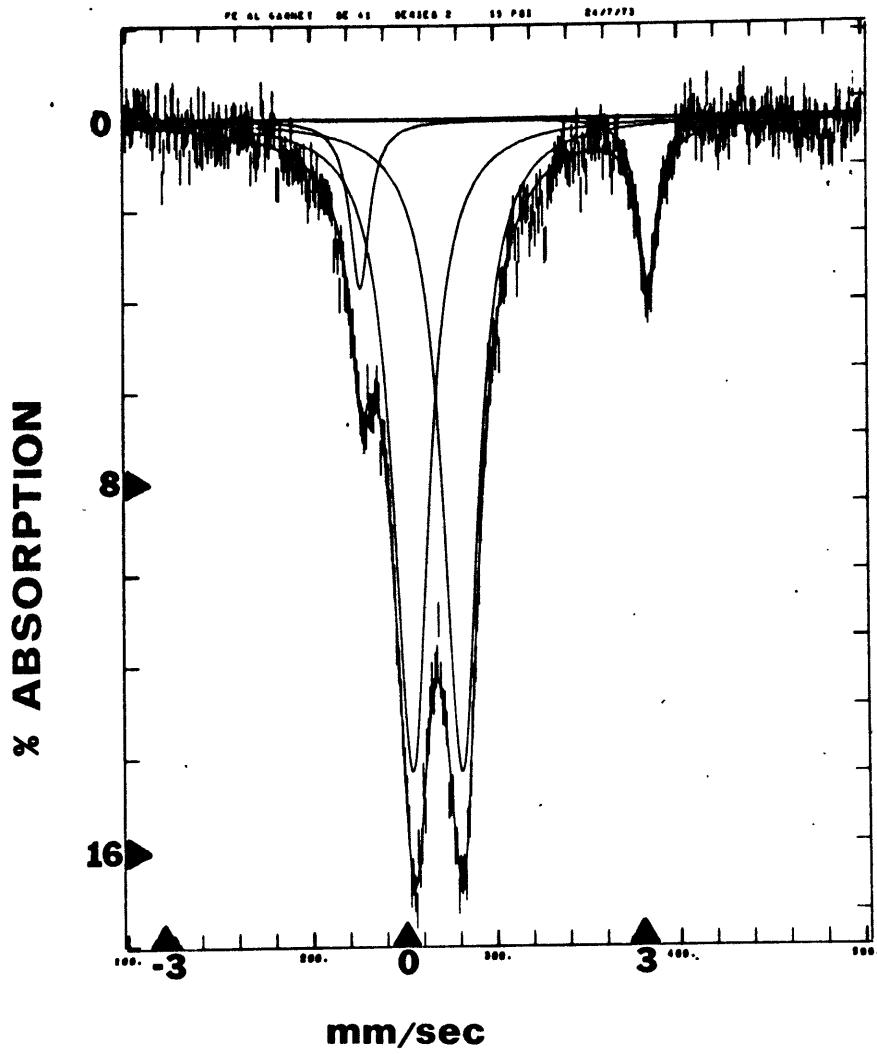
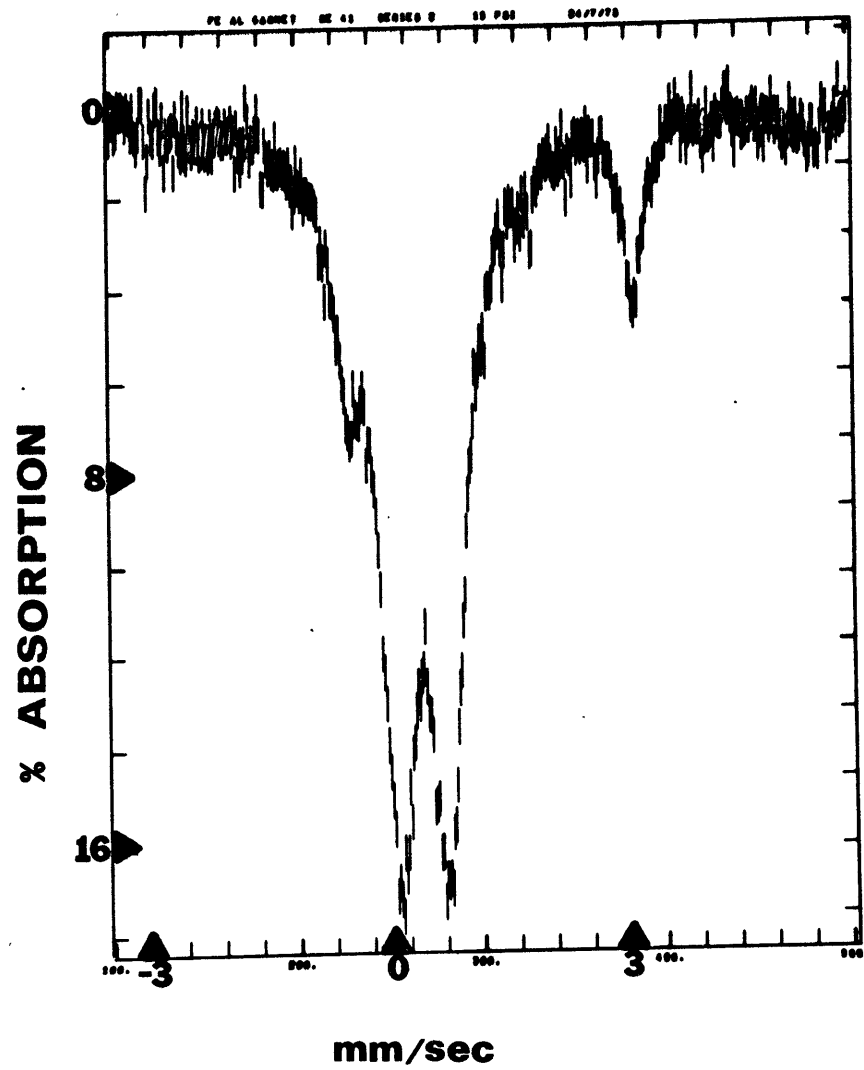
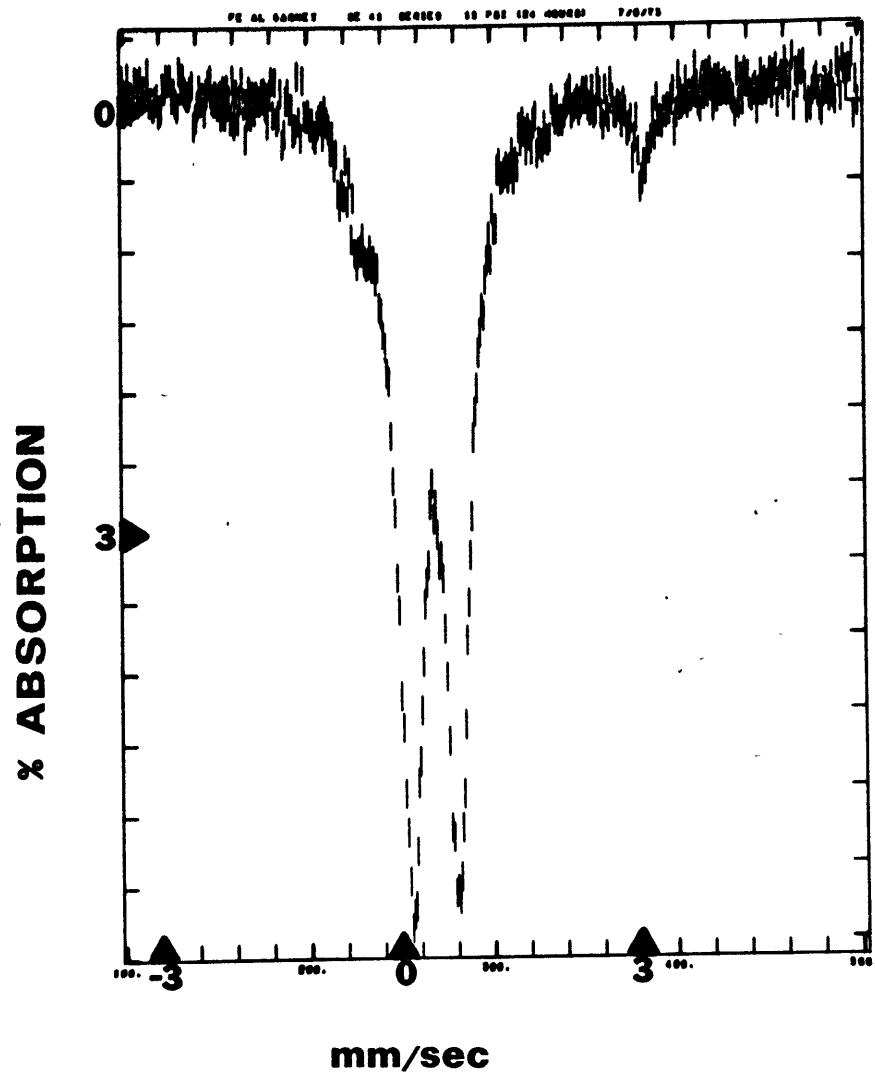


Figure 4.1  
(continued)

Figure 4.1b. Mössbauer spectra of FeAl garnet at zero pressure, showing the difference between the regular geometry spectrum (left) and high pressure geometry spectrum (right). The augmentation of the small peaks on changing the geometry is due to thick absorber effects.



unpublished results). Based on ionic radii considerations, the octahedral sites in this garnet are expected to be about the same size as those in andradite but somewhat larger than those in FeAl garnet. In this way, it was hoped that the effect of site size could be assessed for the pressure-induced reduction phenomenon. Both andradite (Vaughan and Tossell, unpublished) and FeAl garnet (subsection 4.2.1 (a)) showed no signs of pressure-induced reduction, although broadening of the ferric peaks due to the thick absorber phenomena could possibly have obscured any emerging ferrous features in these two samples.

Two separate high pressure runs were made with this sample; the second run went up to 150 kb at room temperature whereas the first run went up to about 100 kb at room temperature and then the pressure was kept constant while the temperature was raised first to 57 °C and then to 88 °C using the set-up described in section 3.3.6. The variation of the Mössbauer parameters with pressure for both runs is described in table 4.2 and four spectra are shown in figure 4.2a,b. Of the two runs, the second run, which averaged baselines of 50,000 counts/channel, is statistically much more reliable than the first run which averaged baselines of 20,000 counts/channel. In both runs, a small peak emerged at about +1.7 to +2.2 mm/sec when the pressure reached about 100 kb. This peak appeared to increase in intensity when the pressure was increased further to 180 kb, and also when the temperature was raised to 90 °C. In addition, increasing asymmetry of the ferric absorption was found, indicating that the low velocity half of this emerging absorption is located under the low velocity ferric peak. Again, the isomer shift and quadrupole splitting values for this small

Table 4.2

MOSSBAUER DATA FOR  $\text{Ca}_3\text{FeCrSi}_3\text{O}_{12}$  AS A FUNCTION OF PRESSURE

PRESSURE	TEMP	$\text{Fe}^{3+}$ (VI)			$\text{Fe}^{2+}$ (VI)			$\text{Fe}^{2+}$ PEAK POSITION <sup>1</sup>	
		IS	QS	%	IS	QS	%		
Regular 1 bar	25 °C	0.39	0.58	100		--		--	
High Pressure Run 1	0 kb	25	0.39	0.59	100		--	--	
	50 kb	25	0.36	0.72			trace <sup>2</sup>	--	
	98 kb	25	0.36	0.68			trace <sup>2</sup>	--	
	107 kb	57	0.35	0.67	80	0.87	2.26	20	2.00
	107 kb	88	0.32	0.65	83	0.68	2.04	17	1.70
	130 kb	25	0.33	0.69			trace <sup>2</sup>		--
High Pressure Run 2	0 kb	25	0.39	0.59	100		--		--
	95 kb	25	0.36	0.74	90	0.84	2.41	10	2.04
	180 kb	25	0.34	0.74	83	0.86	2.57	17	2.15

<sup>1</sup>Position of the high energy peak which can be observed visually.

<sup>2</sup>Small peak was apparent visually, but could not be fitted accurately (peak amounts to less than 10%).

All fits reported at that stage in the computer fitting where the halfwidths and areas for each peak of the individual doublets are held equal. The baseline is constrained to be straight.

Figure 4.2

Mössbauer spectra of FeCr garnet.

Figure 4.2a. Fitted Mössbauer spectra of FeCr garnet in the regular geometry (left) and at 98 kb at room temperature (right). The fitted peaks are assigned to  $\text{Fe}^{3+}$  (VI). The regular geometry spectrum indicates the presence of very small amounts (< 2%) of  $\text{Fe}^{2+}$  (VIII) and possibly  $\text{Fe}^{2+}$  (VI) by the non-random fluctuations in the data at about 3.0 and 2.0 mm/sec respectively. The high pressure spectrum shows a trace of an emerging peak at about 2.0 mm/sec.

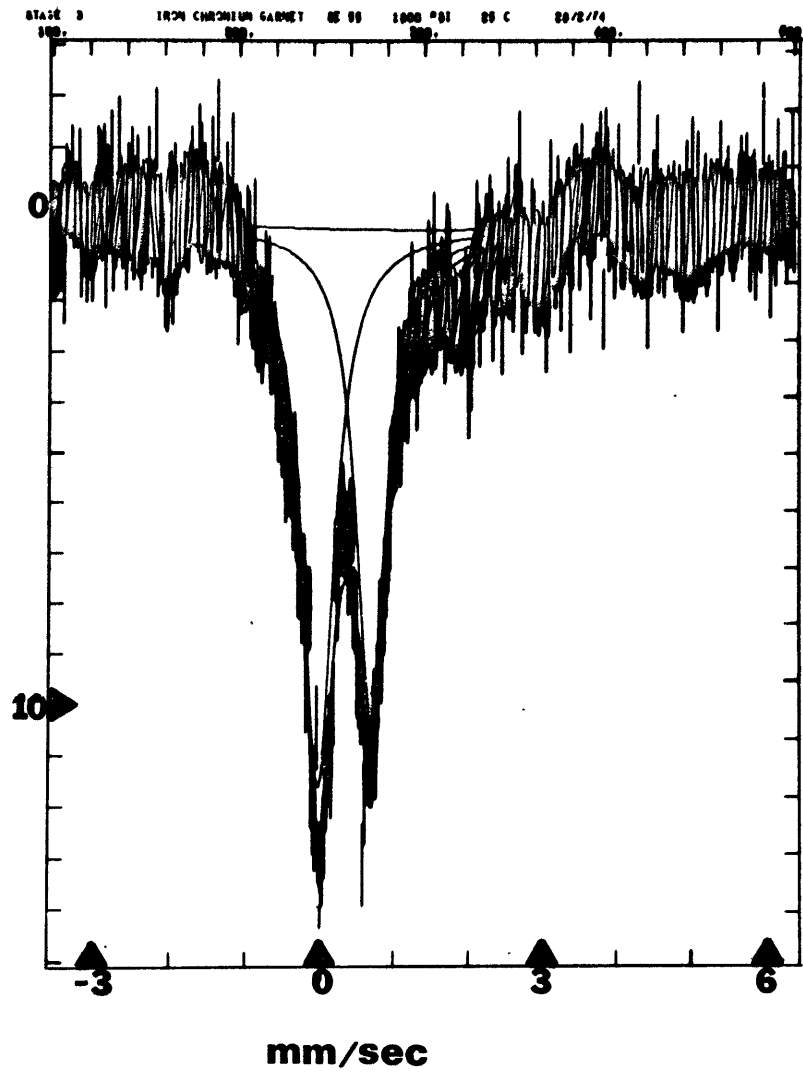
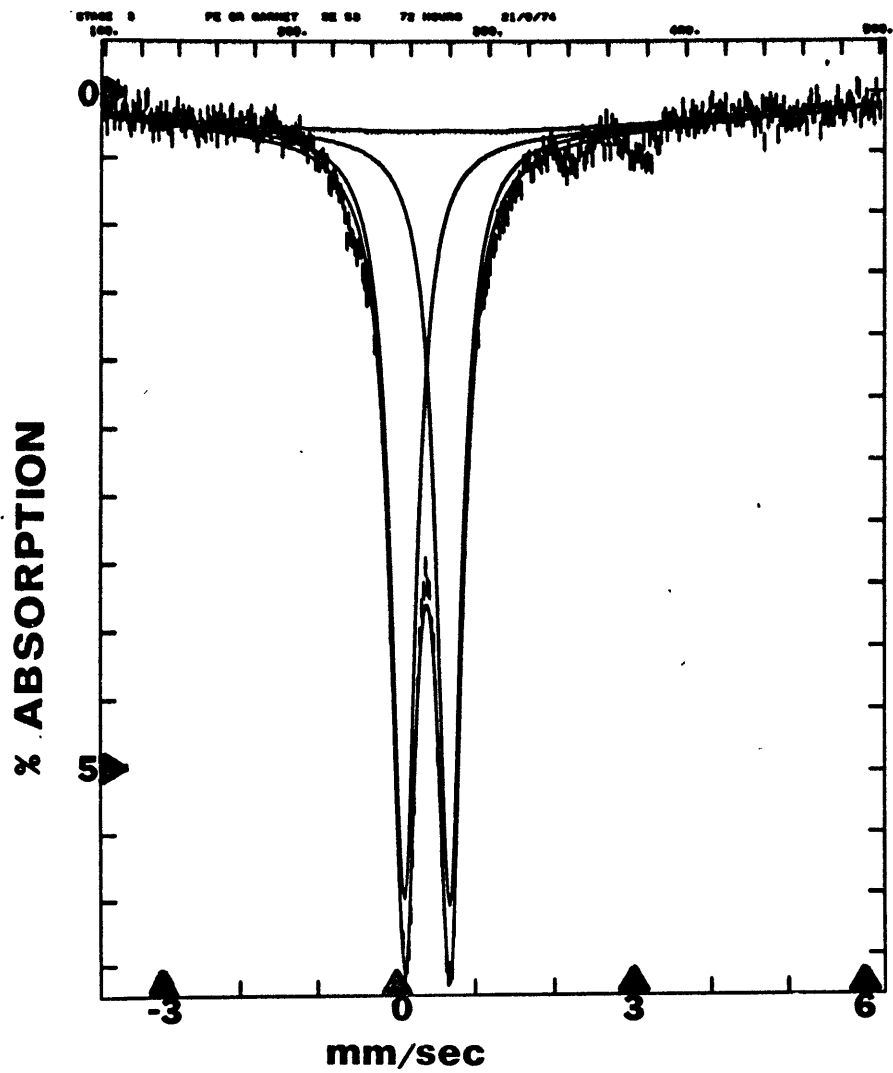
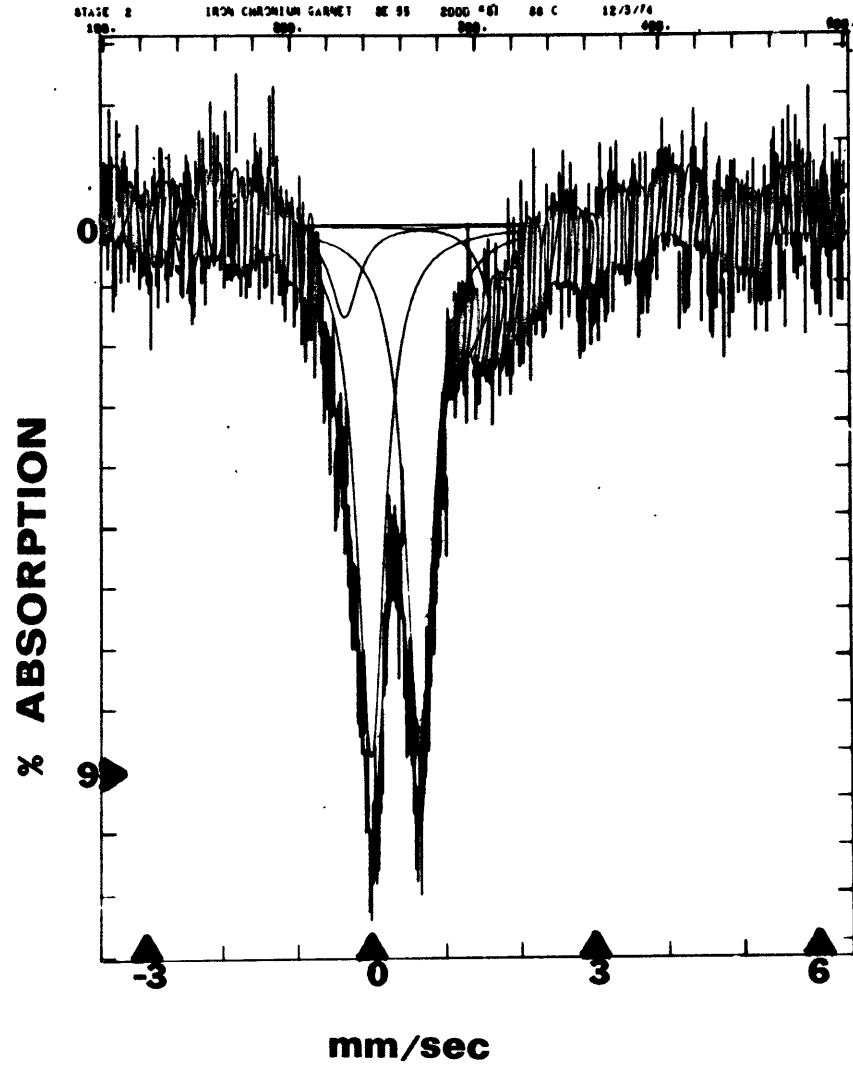
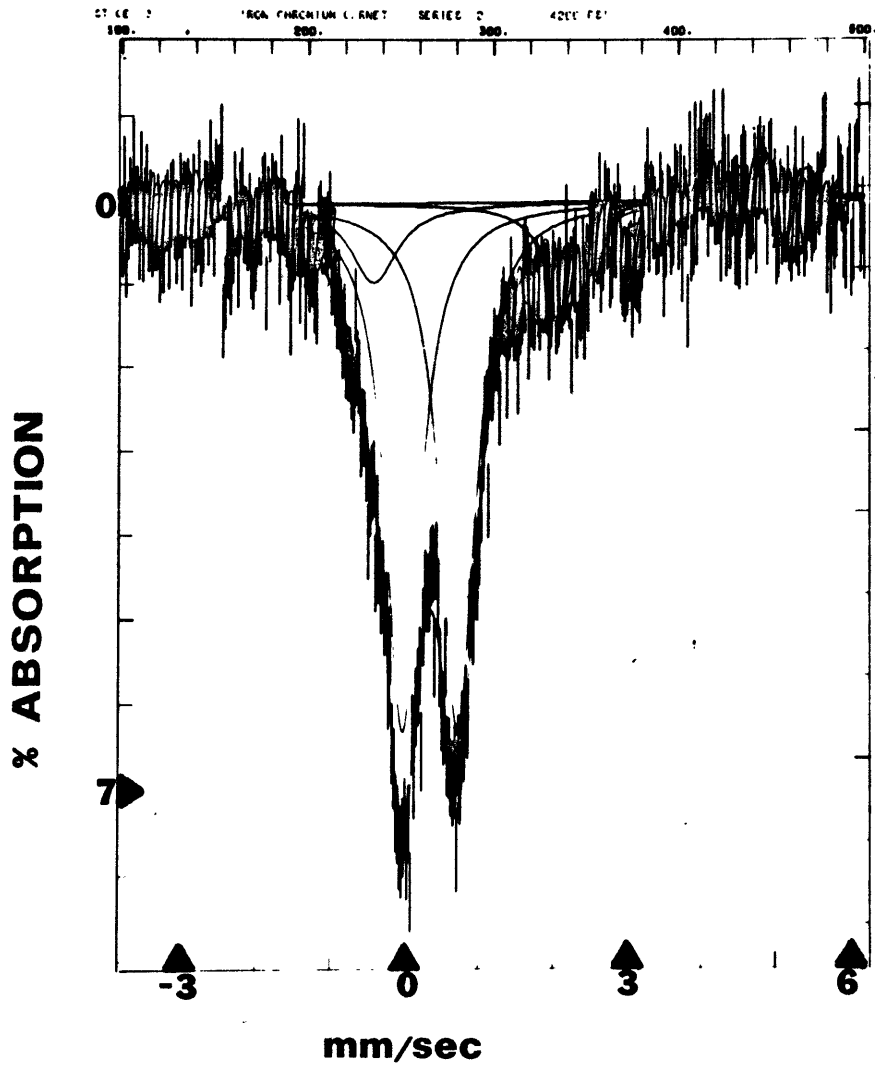




Figure 4.2  
(continued)

Figure 4.2b. Fitted Mössbauer spectra of FeCr garnet at 180 kb and 25 °C (left) and 107 kb and 88 °C (right). Both spectra show a substantial increase in the absorption at about 2.0 mm/sec compared to that in the spectrum of the sample at 98 kb shown in Figure 4.2a.



$\text{Fe}^{2+}$  absorption must also be regarded with a healthy degree of skepticism since the low energy peak of this doublet is located under the ferric absorption and is subject to large errors. Nevertheless, the parameters do appear to be consistent with  $\text{Fe}^{2+}$  rather than  $\text{Fe}^{3+}$ , since for the observed peak to originate from ferric iron, a further peak should have been observed visually at about -1.5 to -1.0 mm/sec. The parameters are not  $\text{Fe}^{2+}$  (VIII) since the high energy peak for this absorption occurs at about +3.1 mm/sec and is relatively insensitive to pressure (see subsection 4.2.1 (e)). The most likely candidate for giving rise to this absorption is ferrous iron in octahedral sites caused by pressure-induced reduction of the original ferric iron. The parameters and temperature dependence of the position of the absorption peak suggest that the ferrous cation is in a very small, very regular octahedral site, which is exactly the description of this octahedral site in garnet (Novak and Gibbs, 1971).

This sample, therefore, appears to show incipient pressure-induced reduction, whereas the other ferric containing garnets did not. In addition to increasing pressure, increasing temperature appears to augment the amount of ferrous found by the pressure-induced reduction process. Further discussion of these points is presented in section 4.3.5.

It should be pointed out that divalent cations can exist in the octahedral sites in garnets. Previous investigations into the range of cation substitutions in synthetic garnets have shown that  $\text{Co}^{2+}$ ,  $\text{Ni}^{2+}$ ,  $\text{Mg}^{2+}$ ,  $\text{Mn}^{2+}$  and  $\text{Fe}^{2+}$  can be found in the octahedral sites (Geller et al., 1962; Ito, 1967). According to Novak and Gibbs (1971), fairly large cations (up to ionic radii of 0.85 Å) can be accommodated in the octahedral sites of

calcium silicate garnets, so that there appears to be no structural problem accommodating  $M^{2+}$  cations in the octahedral sites in garnets. The problem, of course, is in the charge balance. For natural silicate garnets elemental abundances conspire so that very large trivalent cations, which might charge balance  $M^{2+}$  cations in the garnet octahedral sites by going into the eight-coordinate sites, are uncommon, and therefore garnets containing octahedral  $M^{2+}$  are extremely rare in nature. On the other hand, the charge transfer phenomenon is a completely different charge balancing phenomenon and does not depend on elemental abundances, so that  $M^{2+}$  in the octahedral site of garnet at very high pressures and temperatures could be extensive.

#### 4.2.1 (c) $Ca_3TiFe_2Si_2O_{12}$

This synthetic garnet was reported to contain both tetrahedral and octahedral ferric cations in about the same proportions (Burns, 1972). The present study agreed with this observation, and fitting the spectra to four peaks was sufficient. However, there would appear to be two alternative ways to fit the spectra of Ti containing garnets and these are indicated in table 4.3. The inner-outer configuration was used by Burns (1972) for this sample whereas Whipple (1973) used the sequential configuration in different Ti-rich garnets. Data for fits of both kinds are reported for this sample.

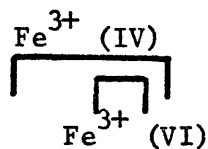
This sample represents about the lower limit of natural iron content for reasonable high pressure spectral data (about 10 wt % Fe per structural site). The higher pressure spectra at about 100 kb and 150 kb were statistically so poor that no computer fits of the data were achieved. Two spectra are shown in figure 4.3.

Table 4.3

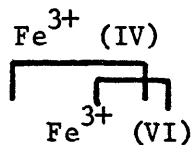
MÖSSBAUER DATA FOR  $\text{Ca}_3\text{TiFe}_2\text{Si}_2\text{O}_{12}$

	PRESSURE	$\text{Fe}^{3+}$ (IV)			$\text{Fe}^{3+}$ (VI)			WDTH
		IS	QS	%	IS	QS	%	
Fit 1	Regular	0.23	1.20	51	0.37	0.67	49	0.36
	0 kb	0.24	1.20	50	0.36	0.66	50	0.45
	55 kb	0.24	1.24	52	0.33	0.57	48	0.39
Fit 2	Regular	0.17	1.08	51	0.43	0.79	49	0.36
	0 kb	0.16	1.05	49	0.43	0.81	51	0.45
	55 kb	0.12	1.01	53	0.46	0.83	47	0.39

FIT 1 inner-outer:



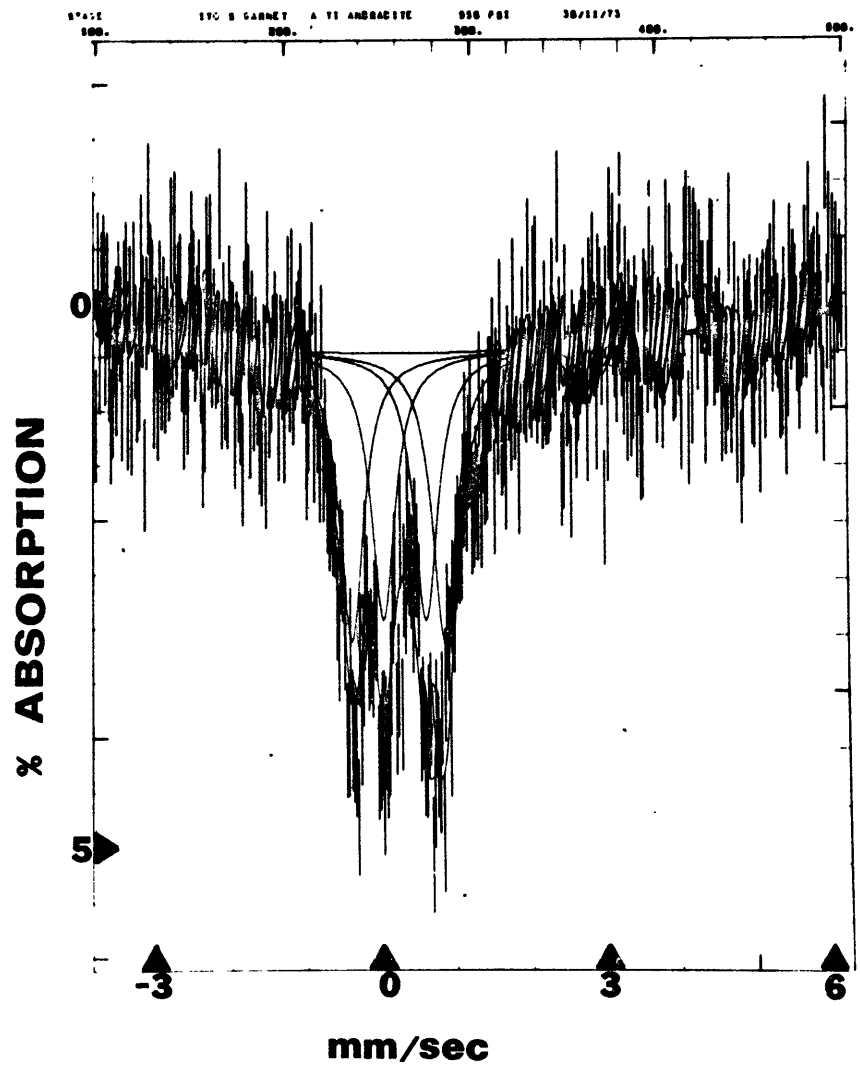
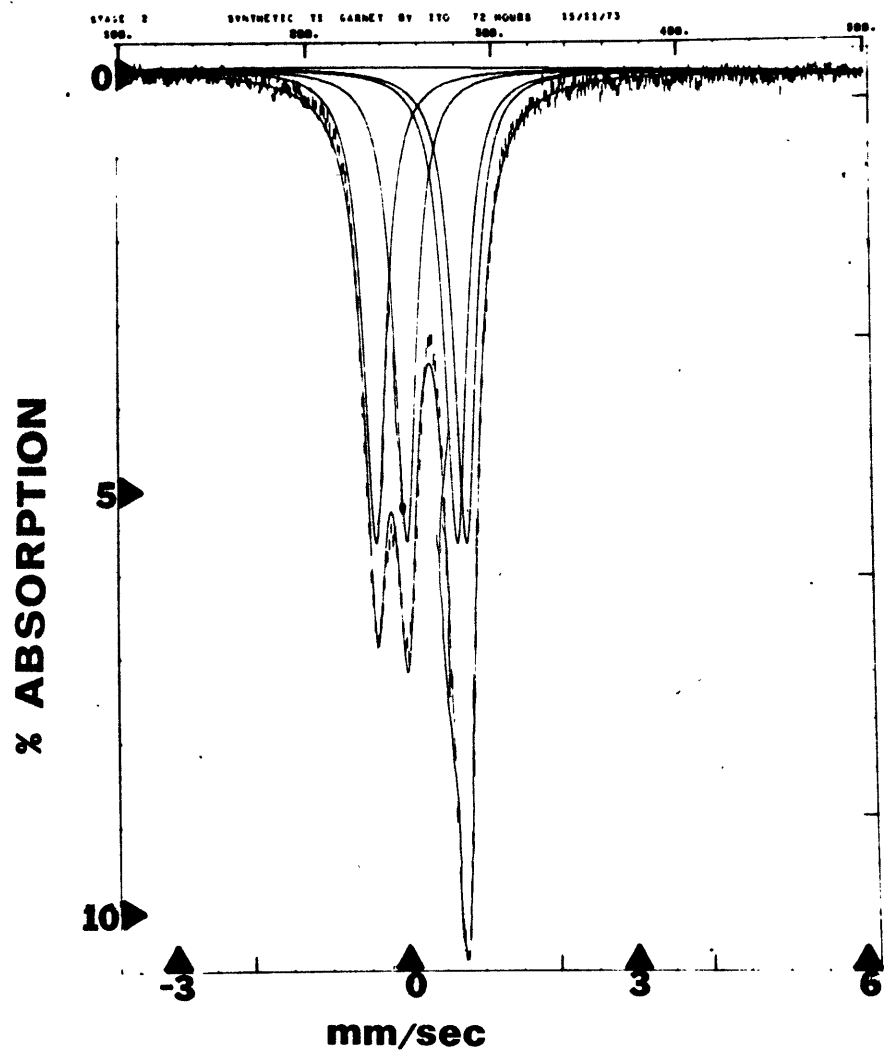
FIT 2 sequential:



All fits reported at that stage in the computer fitting where the half-widths are constrained equal for all four peaks and areas are held equal in pairs. The baseline is constrained straight.

Figure 4.3

Fitted Mössbauer spectra of the garnet,  $\text{Ca}_3\text{TiFe}_2\text{Si}_2\text{O}_{12}$ , in the regular geometry (left) and at 55 kb (right). The assignment of the peaks is discussed in the text and in table 4.3. The high pressure spectrum represents the worst quality data for which fits are reported.



The inner-outer configuration for computer fitting of the data is, in fact, favored by the limited data. Not only are the values for  $\text{Fe}^{3+}$  (VI) more consistent in this configuration, but also the pressure trend to 50 kb for both sites is similar to those in other garnets only when this configuration is used in the computer fitting. The sequential configuration, used by Whipple (1973) in fitting schorlomite and melanite spectra, is not necessarily wrong; as will be shown in due course, the isomer shift of tetrahedral ferric in garnets appears to have a considerable range of value depending on composition and either fit could be appropriate.

4.2.1 (d) CaZrFe garnet,  $\text{Ca}_{2.5}\text{Zr}_{2.5}\text{Fe}_3\text{O}_{12}$

This garnet was synthesized by Dr. Jun Ito of Harvard University and was reported in Ito and Frondel (1967). The garnet has a cell parameter of 12.65 Å. The Mössbauer spectrum of this garnet is shown in figure 4.4. The two large peaks are  $\text{Fe}^{3+}$  (IV). However, there is a considerable amount of hematite (approximately 45%) also revealed in the spectrum. The origin of this material is not clear. It probably represents unreacted starting mix; however, it may mean that the composition of the garnet is not exactly that given in the formula. Nevertheless, since the large ferric doublet definitely appears to arise from ferric iron in the tetrahedral sites in garnet, the high pressure run was carried out.

The high pressure run was of much better quality than that for the  $\text{Ca}_3\text{TiFe}_2\text{Si}_2\text{O}_6$  (it contains three times more iron per site). Isomer shift and quadrupole splitting data for  $\text{Fe}^{3+}$  (IV) are reported in table 4.4. The isomer shift showed virtually no change up to 100 kb, while the quadrupole splitting also did not change very much with pressure.



Table 4.4

MÖSSBAUER DATA FOR  $\text{Ca}_{2.5}\text{Zr}_{2.5}\text{Fe}_3\text{O}_{12}$  AS A FUNCTION OF PRESSURE.

MÖSSBAUER DATA FOR  $\text{Ca}_{2.5}\text{Th}_{0.5}\text{Zr}_2\text{Fe}_3\text{O}_{12}$

Hematite constituted about 50% of the iron absorption in both samples.

$\text{Ca}_{2.5}\text{Zr}_{2.5}\text{Fe}_3\text{O}_{12}$ :

PRESSURE		$\text{Fe}^{3+}$ (IV)		
		IS	QS	WDTH
High	0 kb	0.15	1.03	0.64
Pressure	50 kb	0.14	1.00	0.63
Run	107 kb	0.14	1.05	0.72

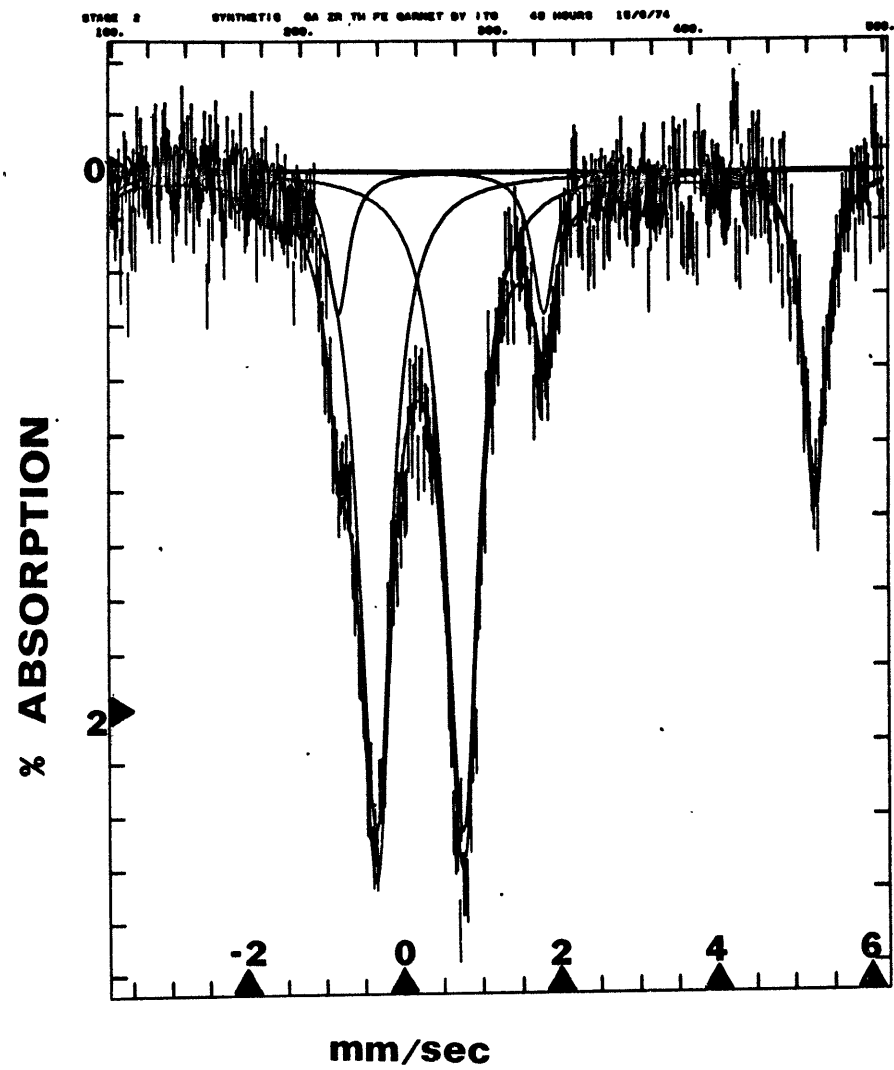
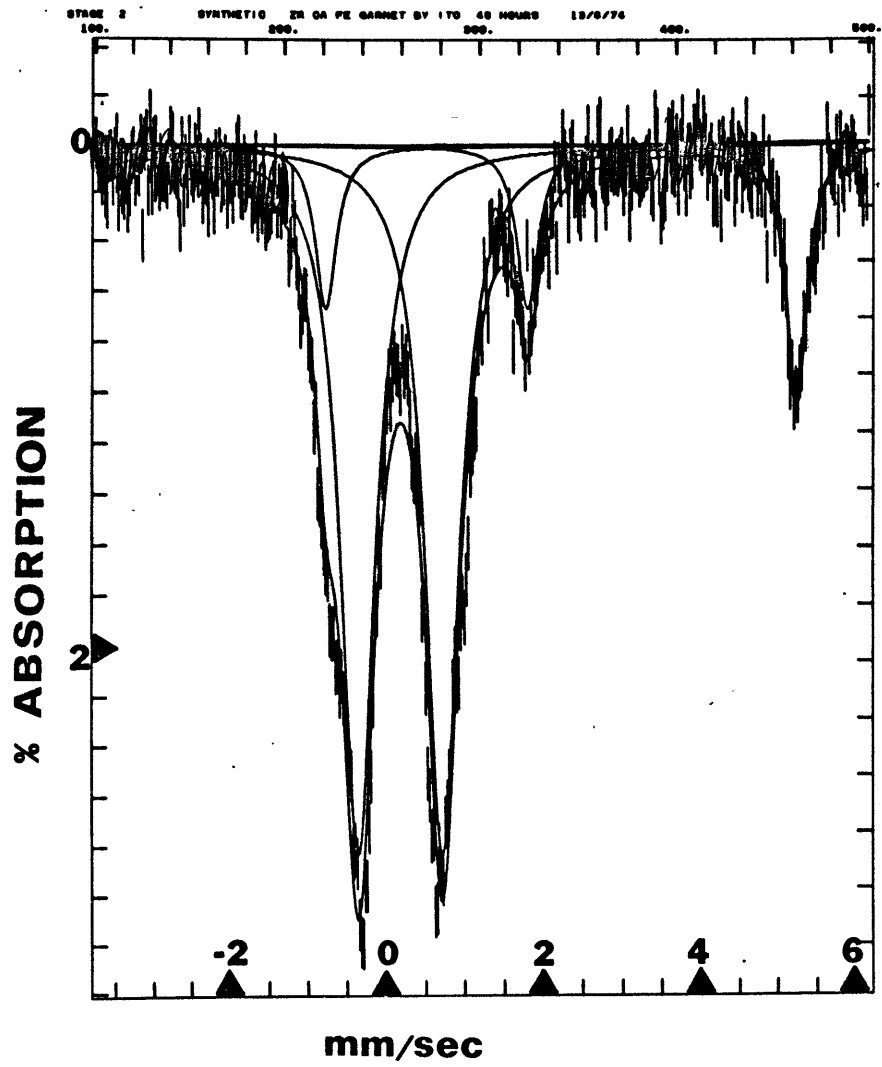
$\text{Ca}_{2.5}\text{Th}_{0.5}\text{Fe}_3\text{O}_{12}$ :

PRESSURE		$\text{Fe}^{3+}$ (IV)		
		IS	QS	WDTH
Regular	1 bar	0.21	1.10	0.50

All fits reported at that stage in the computer fitting where the four observed hematite peaks are all constrained in width, but equal in area by pairs, and where the ferric (IV) peaks are constrained equal in area and width. Baseline is constrained straight only for the high pressure runs.

Figure 4.4

Fitted Mössbauer spectra of CaZrFe garnet (left) and CaThZrFe garnet (right) at 0 kb. The large central peaks are assigned to  $\text{Fe}^{3+}$  (IV) and the three smaller peaks are due to hematite.



Another of Ito's samples, the composition of which was  $\text{Ca}_{2.5}\text{Th}_{0.5}\text{Zr}_2\text{Fe}_3\text{O}_{12}$ , was run only at room pressure for comparison purposes. The Mössbauer data for this phase is also reported in table 4.4 and the spectrum is shown in figure 4.4. It too contained approximately 50% of the iron as hematite. The Mössbauer parameters are consistent with ferric iron in tetrahedral sites; however, the isomer shift is  $\sim 0.06$  mm/sec more positive than for the CaZrFe garnet. This fact suggests that the isomer shift for  $\text{Fe}^{3+}$  (IV) must be very sensitive to bonding differences.

#### 4.2:1 (e) Almandine

The almandine sample used in this study is the same as the garnet GN1A investigated by Whipple (1973). The almandine,  $(\text{Fe},\text{Mg},\text{Mn})_3\text{Al}_2\text{Si}_3\text{O}_{12}$ , was shown by Whipple, using electron microprobe analysis, to have Fe:Mg:Mn ratios of 75:18:5, which gives this almandine a composition similar to that used by Lyubutin and Dodokin (1971b) in their Mössbauer study of almandine.

In the high pressure spectra, two almandine peaks and a third peak to allow for the iron-containing boron were fitted. Although fitting the B(Fe) peak did not significantly change the Mössbauer parameters of the almandine, it did result in consistent widths for the almandine peaks and reasonable chi-square values for the fit. The data are tabulated in table 4.5 and two spectra are shown in figure 4.5.

The isomer shift of the almandine decreased a large amount over the first 50 kb, but showed only a slight decrease on increasing the pressure further. The quadrupole splitting showed only a very slight continuous increase up to 150 kb.

Table 4.5

MÖSSBAUER DATA FOR ALMANDINE, GNIA, AS A FUNCTION OF PRESSURE.

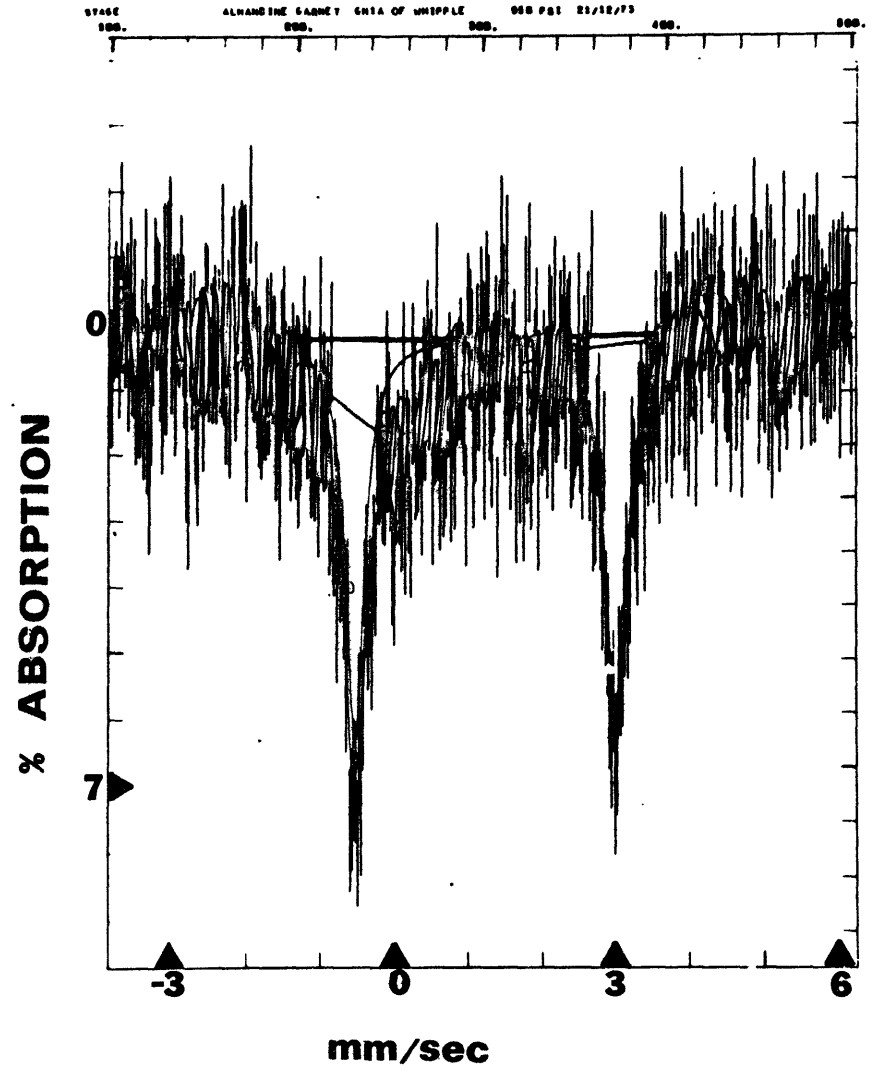
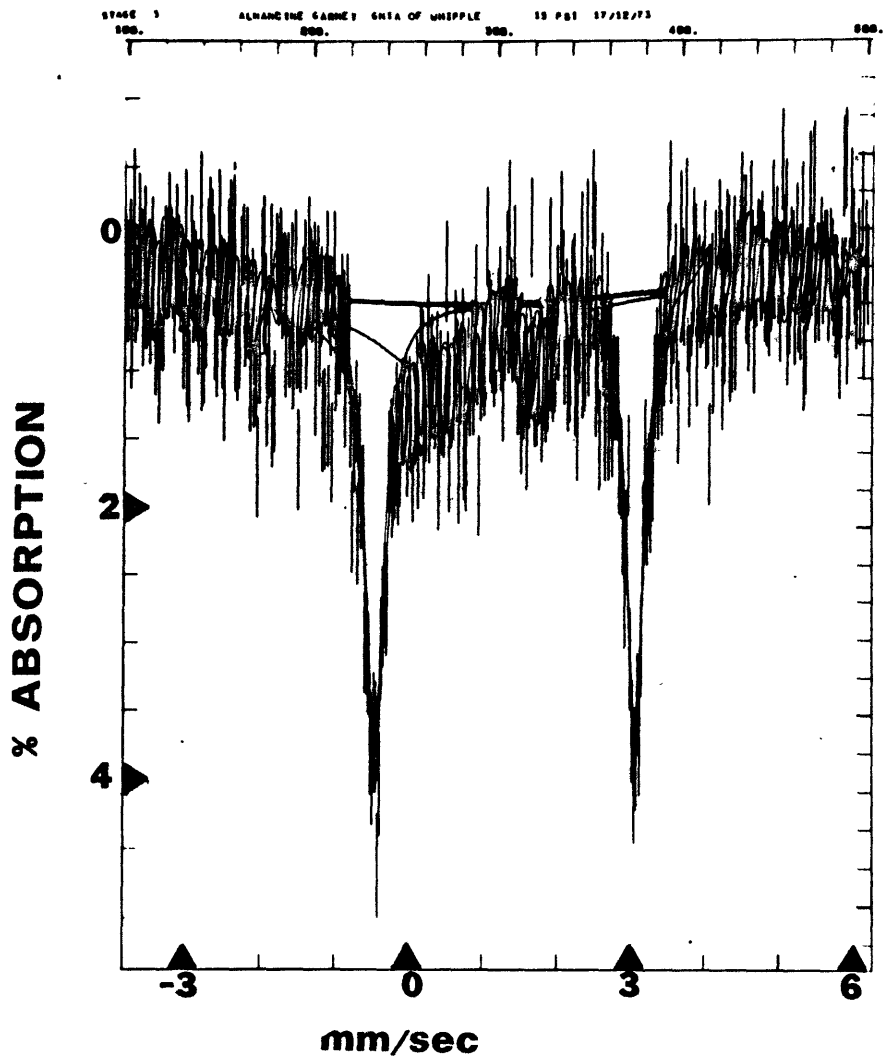
PRESSURE		Fe <sup>2+</sup> (VIII)		
		IS	QS	WDTH
<sup>1</sup> REGULAR	1 bar	1.29	3.54	0.28
HIGH PRESSURE	0 kb	1.31	3.51	0.28
	55 kb	1.25	3.53	0.34
	100 kb	1.24	3.55	0.38
	150 kb	1.24	3.55	0.36

<sup>1</sup>Data from Whipple (1973)

A third peak was fitted to allow for the small absorption of B(Fe). All fits reported at that stage in the computer fitting where the two almandine peaks were held equal in both area and width.

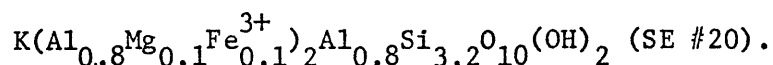
Figure 4.5

Fitted Mössbauer spectra of almandine, GN1A, at 0 kb (left) and at 55 kb (right). A broad peak is fitted to allow for the absorption of the iron-containing boron.



#### 4.2.2 Micas

The spectra of three synthetic micas were investigated as a function of pressure in the course of this study. Two of the specimens were based on the trioctahedral mica structure. These are the ferriphlogopites:  $\text{KMg}_3\text{FeSi}_3\text{O}_{10}(\text{OH})_2$  (SE #16), and  $\text{KMg}_3(\text{Fe,Al})\text{Si}_3\text{O}_{12}(\text{OH})_2$  (SE #15). The other mica was a dioctahedral mica of composition:



All three micas contained varying amounts of octahedral ferrous iron (see discussion in sections 3.4.3 (a), 3.4.3 (b) and Appendix A1.1) so that the Mössbauer parameters of octahedral ferrous iron in a mica structure were also obtained as a function of pressure.

##### 4.2.2 (a) Ferriphlogopite, $\text{KMg}_3\text{FeSi}_3\text{O}_{10}(\text{OH})_2$

This ferriphlogopite sample, SE #16, contained about 12% ferrous iron in octahedral coordination so that results were obtained for both ferrous (VI) and ferric (IV) absorptions.

The high pressure Mössbauer data are reported in table 4.6 and two representative spectra are shown in figure 4.6. The isomer shift of  $\text{Fe}^{3+}$  (IV) increases, while that of  $\text{Fe}^{2+}$  (VI) decreases with pressure. Quadrupole splitting trends for both cations show increases with pressure. The  $\text{Fe}^{2+}/\text{Fe}^{3+}$  ratio also increases quite markedly with pressure; although some of this increase can be attributed to the larger relative increase in width of  $\text{Fe}^{2+}$  (VI) with pressure, there is an increase in peak amplitude as well which can be noticed on visually examining the spectra. The increase in width with pressure suggests thick absorber phenomena.



Table 4.6

MÖSSBAUER DATA FOR  $\text{KMg}_3\text{FeSi}_3\text{O}_{10}(\text{OH})_2$   
AS A FUNCTION OF PRESSURE

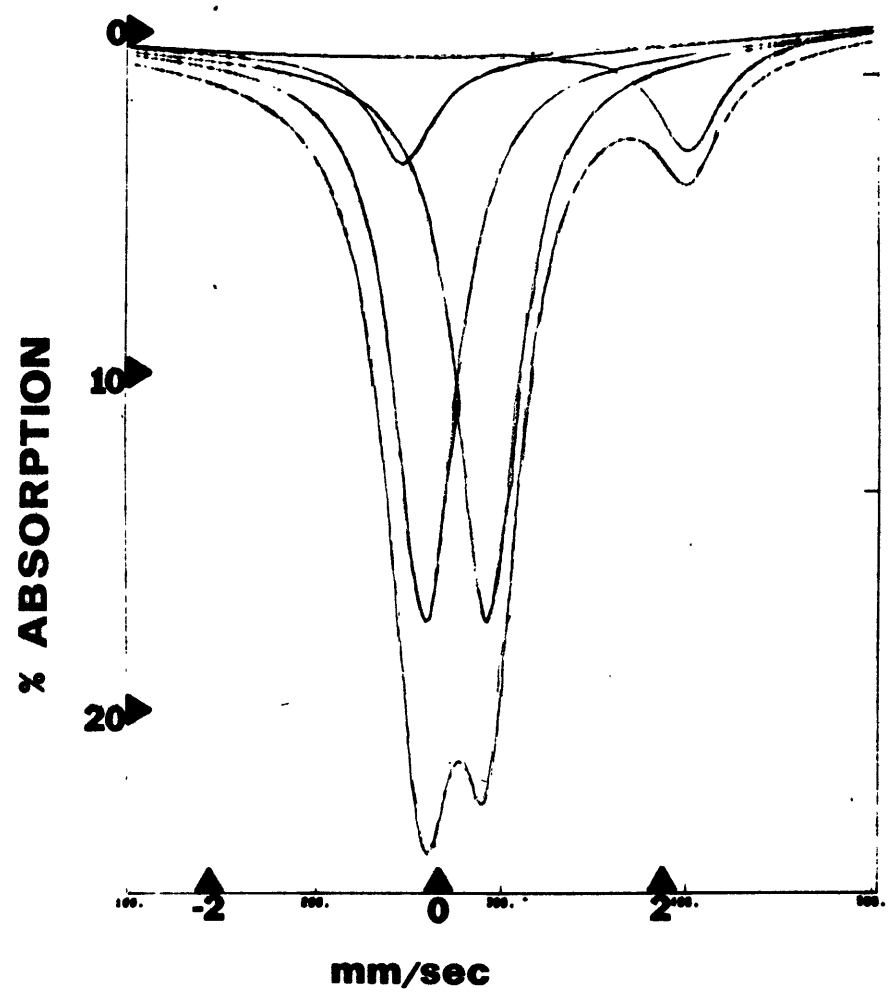
PRESSURE		$\text{Fe}^{3+}$ (IV)				$\text{Fe}^{2+}$ (VI)			
		IS	QS	WDTH	%	IS	QS	WDTH	%
Regular	1 bar	0.19	0.57	0.57	88	1.00	2.63	0.33	12
High Pressure Run	0 kb	0.18	0.54	0.68	87	1.00	2.62	0.50	13
	57 kb	0.21	0.64	0.79	83	0.93	2.65	0.53	17
	107 kb	0.22	0.67	0.94	86	0.94	2.69	0.46	14
	175 kb	0.25	0.66	0.92	78	0.92	2.72	0.58	22

All fits reported at that stage in the computer fitting where the widths and areas of the peaks were held equal in pairs.

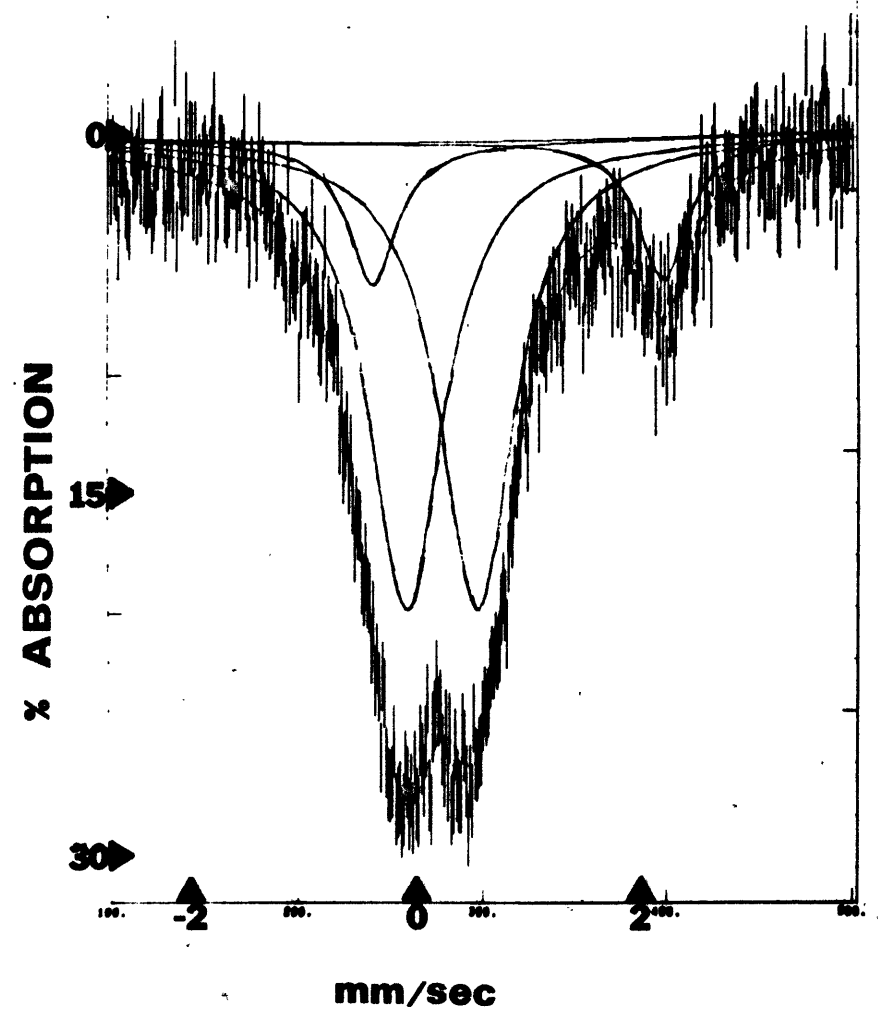
Figure 4.6

Fitted Mössbauer spectra of ferriphlogopite (SE #16) at 0 kb (left) and 57 kb (right). The large central peaks are assigned to  $\text{Fe}^{3+}$  (IV); the smaller peaks are assigned to  $\text{Fe}^{2+}$  (VI).

57-FERRIPHLOGOPITE HI P 15 PSI 31/10/72



57-FERRIPHLOGOPITE HI P 1000 PSI 1/11/72



4.2.2 (b) Ferriphlogopite,  $\text{KMg}_3(\text{Fe,Al})\text{Si}_3\text{O}_{10}(\text{OH})_2$

This ferriphlogopite, SE #15, contained about 25% of the iron as  $\text{Fe}^{2+}$  (VI) although the intention was to synthesize the composition,  $\text{KMg}_3\text{Fe}_{0.5}\text{Al}_{0.5}\text{Si}_3\text{O}_{10}(\text{OH})_2$ . This amount of ferrous iron is almost exactly the same absolute quantity of  $\text{Fe}^{2+}$  (VI) as found for the previous ferriphlogopite (SE #16).

The high pressure Mössbauer data are reported in table 4.7; two spectra are shown in figure 4.7. Qualitatively, the trends of the Mössbauer parameters and the general behavior with pressure are similar to those of the other ferriphlogopite. The isomer shift appears to show a larger increase with pressure and a maximum between 50 and 100 kb. These data should be regarded with caution, since the overlap of the low velocity peaks is considerable, which could give rise to large errors in the positions of these two peaks.

4.2.2 (c) Muscovite,  $\text{K}(\text{Al}_{0.8}\text{Mg}_{0.1}\text{Fe}_{0.1}^{3+})_2\text{Al}_{0.8}\text{Si}_{3.2}\text{O}_{10}(\text{OH})_2$

This synthetic dioctahedral mica was found to contain almost 50% of the octahedral iron in the ferrous state. A high pressure run was attempted with this phase, but the spectra were found in retrospect to be of very poor quality. The main reason for the poor data was that the Mössbauer spectrometer was in poor adjustment at this particular time. As the run was not repeated, no high pressure data are presented for this phase.

The regular geometry run, which was carried out at a later time, is shown in figure 4.8. The isomer shift and quadrupole splitting for octahedral ferric absorption are 0.40 mm/sec and 0.76 mm/sec respectively.

Table 4.7

MÖSSBAUER DATA FOR  $\text{KMg}_3(\text{FeAl})\text{Si}_3\text{O}_{10}(\text{OH})_2$   
AS A FUNCTION OF PRESSURE

PRESSURE		$\text{Fe}^{3+}$ (IV)				$\text{Fe}^{2+}$ (VI)			
		IS	QS	WDTH	%	IS	QS	WDTH	%
Regular	1 bar	0.22	0.56	0.54	72	1.10	2.61	0.36	28
High Pressure Run	53 kb	0.34	0.63	1.02	67	1.06	2.73	0.55	33
	109 kb	0.34	0.68	0.96	64	1.03	2.69	0.59	36
	176 kb	0.29	0.69	0.78	60	0.98	2.72	0.70	40

All fits reported at that stage in the computer fitting where the widths and areas of the peaks were held equal in pairs.

Figure 4.7

Fitted Mössbauer spectra of ferriphlogopite (SE #15) in the regular geometry (left) and at 176 kb (right). The larger peaks are assigned to  $\text{Fe}^{3+}$  (IV); the smaller peaks are assigned to  $\text{Fe}^{2+}$  (VI).

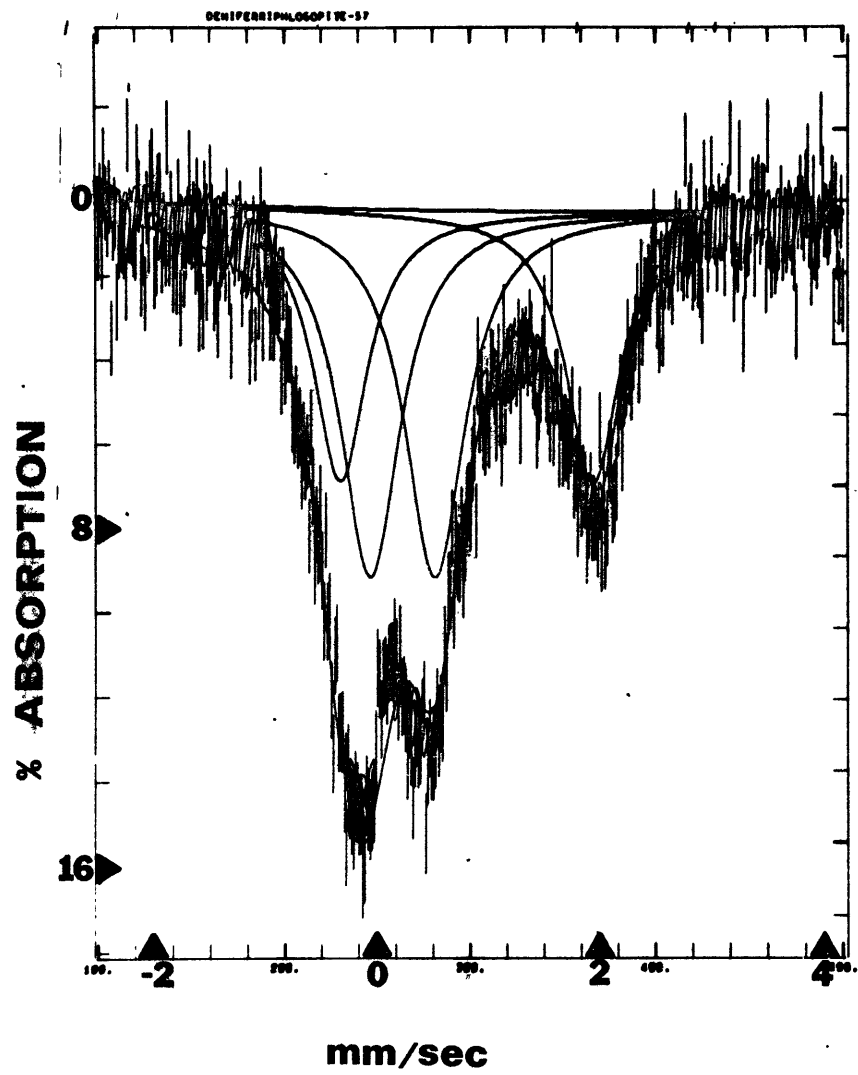
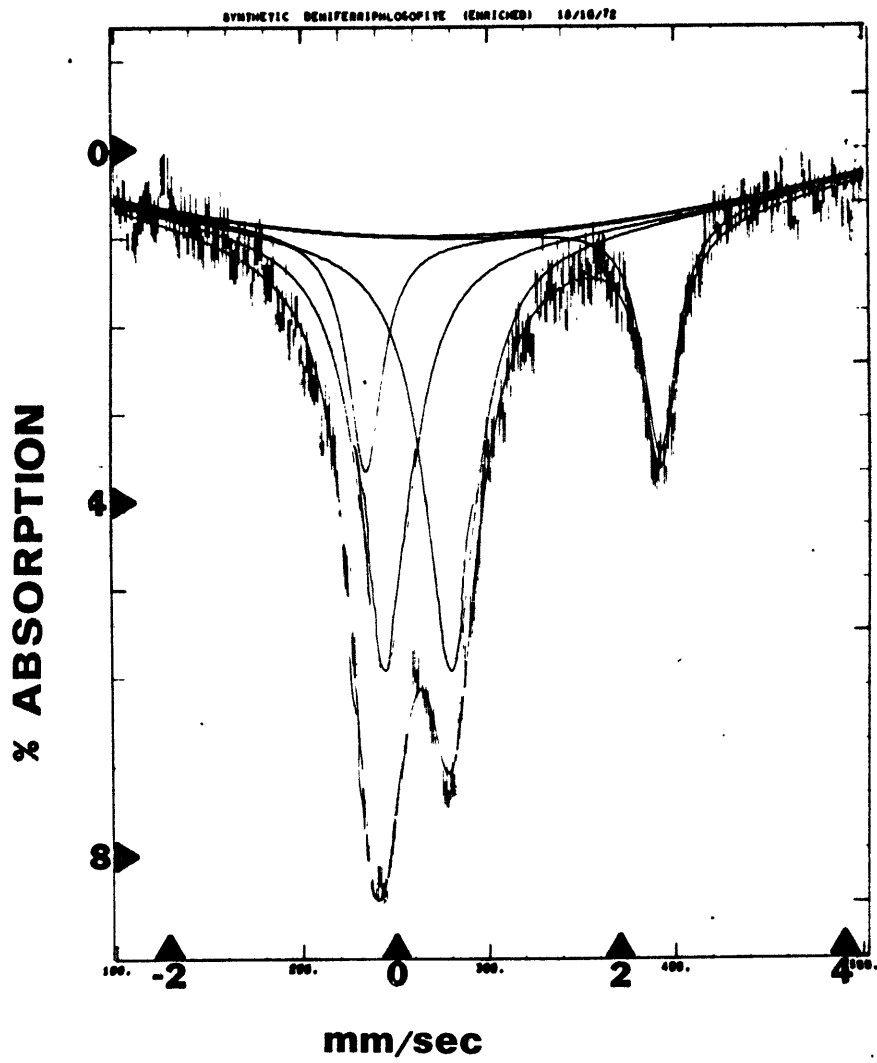
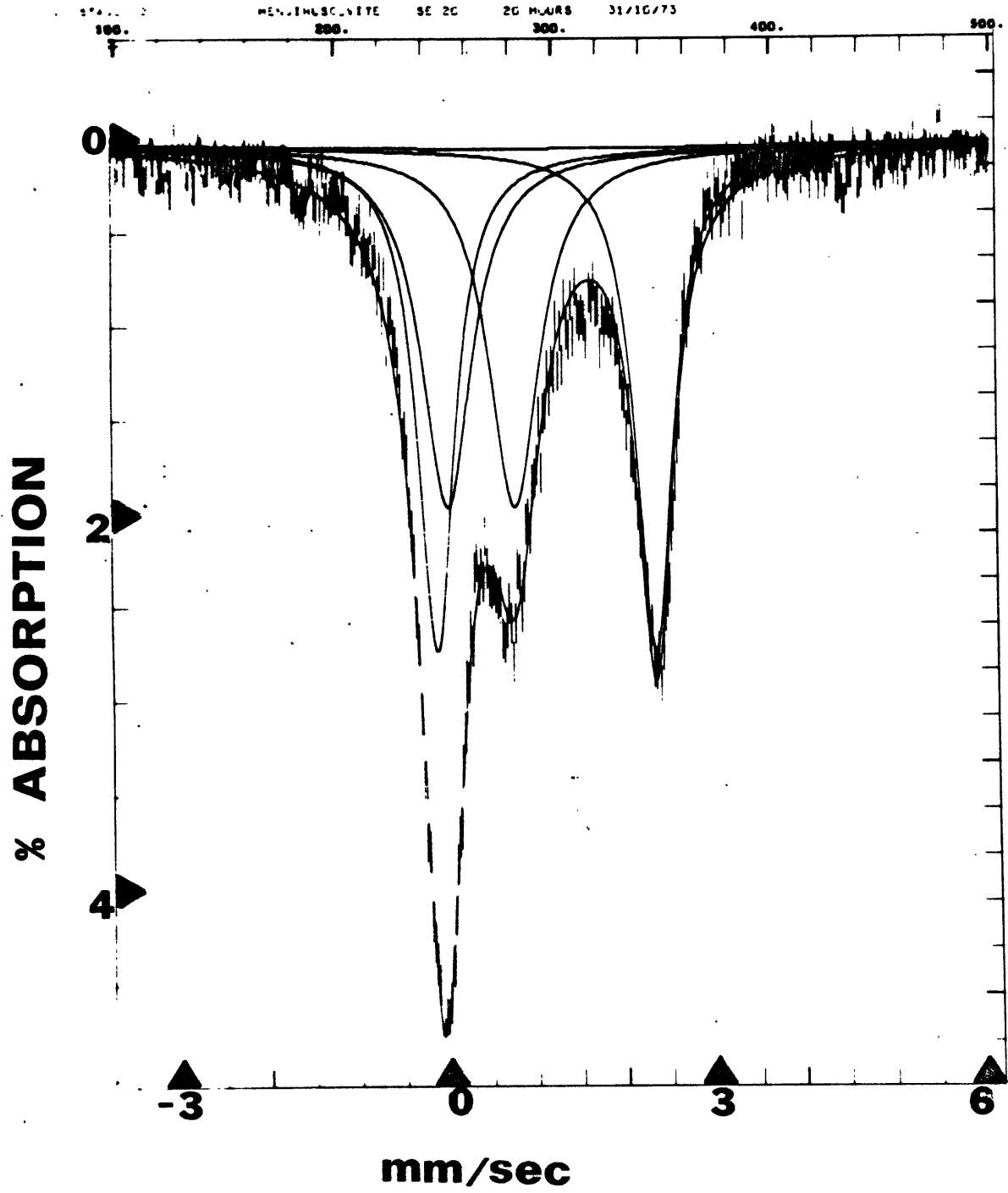


Figure 4.8

Fitted Mössbauer spectrum of muscovite (SE #20) in the regular geometry. The outer, narrower peaks are assigned to  $\text{Fe}^{2+}$  (VI); the inner, broader peaks are assigned to  $\text{Fe}^{3+}$  (VI).





The isomer shift and quadrupole splitting for the octahedral ferrous absorption are 1.12 mm/sec and 2.45 mm/sec respectively. The  $\text{Fe}^{2+}/(\text{Fe}^{2+} + \text{Fe}^{3+})$  ratio is 0.495. The widths of the ferric absorption and ferrous absorption are broad, having values of 0.69 mm/sec and 0.50 mm/sec respectively.

#### 4.2.3 Other mineral phases

This section describes results for fayalite, magnetite, hematite, iron microcline and orthoferrosilite, which were investigated as a function of pressure in the course of this study.

##### 4.2.3 (a) Fayalite

A natural sample of fayalite was used in the high pressure run. The fayalite spectrum was fitted to two peaks although in theory four might have been expected since the structure contains two distinct octahedral sites in which the ferrous cations are located. In agreement with many other investigations of fayalite (Virgo and Hafner, 1972; Bancroft et al., 1967; Eibschutz and Ganiel, 1967), the spectrum of fayalite at room temperature shows no resolution of the two components.

Similarly, at high pressure there was no observable increase in the resolution of the spectral components, so that the spectra were only fitted to two peaks. There was a 33% increase in width, however, which may be taken as evidence for a slight change in the resolution, although visually no resolution was observed. A third peak, to allow for the iron impurity in the boron, was also fitted. Data are presented in table 4.8 and two spectra are shown in figure 4.9.

Vaughan and Tossell (unpublished) investigated the Mössbauer spectrum of a fayalite synthesized from a 90%  $^{57}\text{Fe}$  containing mix as a function of

Table 4.8

MÖSSBAUER DATA FOR FAYALITE (ROCKPORT, MA)  
AS A FUNCTION OF PRESSURE.

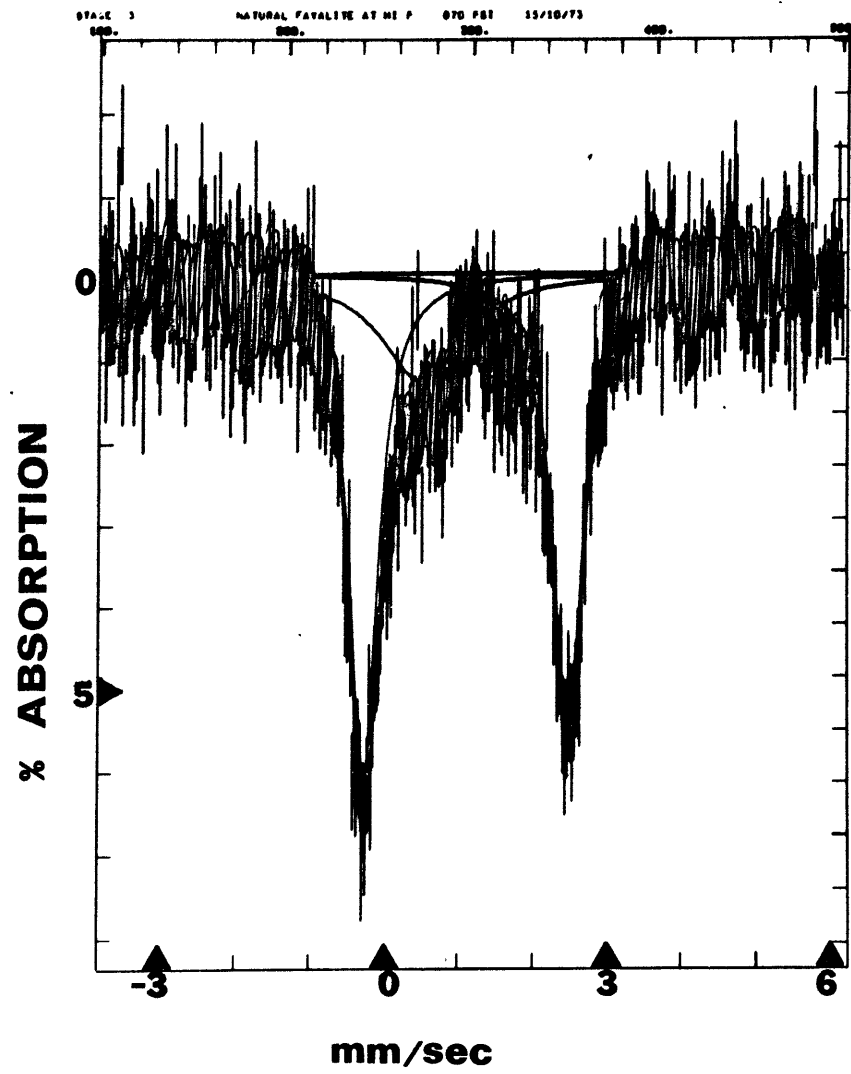
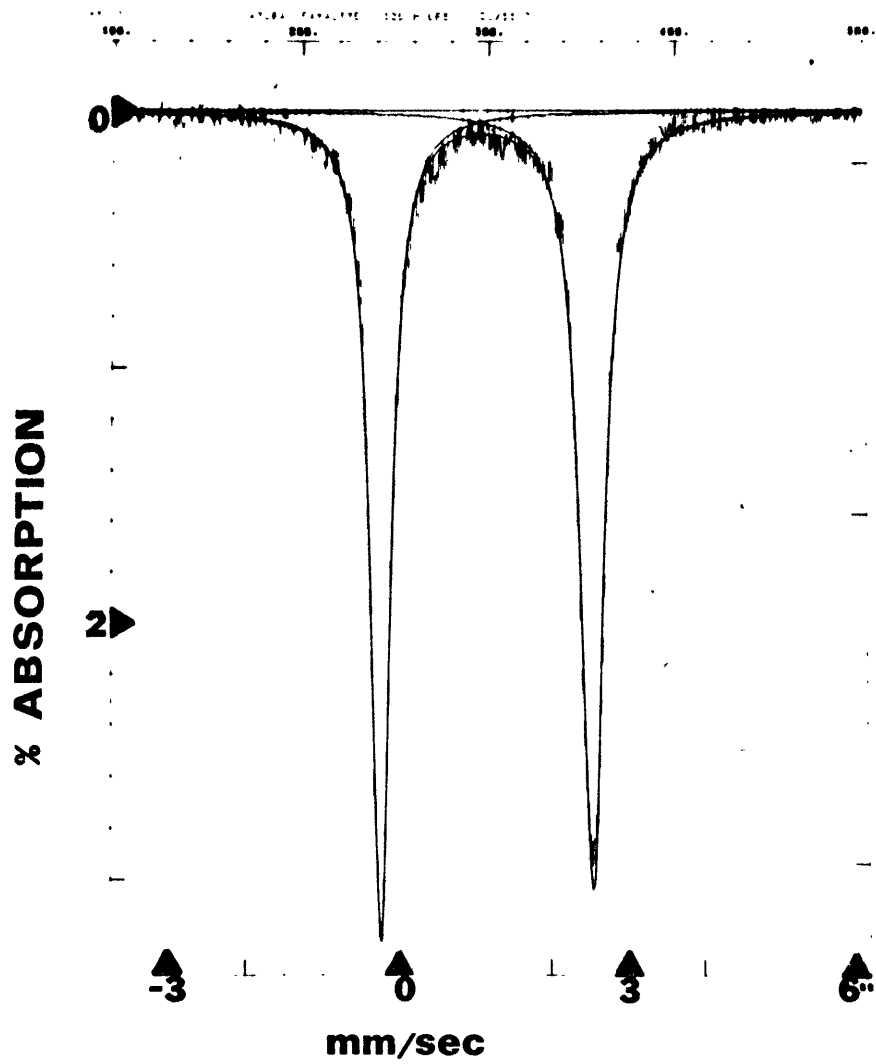
PRESSURE		Fe <sup>2+</sup> (VI)			
		IS	QS	WDTHS <sup>1</sup>	
REGULAR	1 bar	1.16	2.78	0.31	0.37
HIGH	0 kb	1.14	2.82	0.35	0.38
PRESSURE	50 kb	1.10	2.75	0.46	0.48
RUN	105 kb	1.06	2.78	0.38	0.46
	151 kb	1.07	2.73	0.50	0.48

<sup>1</sup>The low energy peak's width is on the left.

A third peak was fitted to allow for the small absorption of B(Fe). All fits reported at that stage in the computer fitting where the two fayalite peaks were held equal in area only.

Figure 4.9

Fitted Mössbauer spectra of fayalite, from Rockport, MA, in the regular geometry (left) and at 50 kb (right). A broad peak is fitted in the high pressure spectrum to allow for the absorption of the iron-containing boron.



pressure. Their sample pellet contained approximately ten times the  $^{57}\text{Fe}$  that was present in the sample pellet of natural fayalite. The computer fits of their samples showed highly curved baselines and much larger widths (approximately three times the natural fayalite line width), obviously indicating thick absorber behavior. Unfortunately, the calibration iron-foil data for the synthetic fayalite Mössbauer runs are not available so that it is not possible to quantitatively compare isomer shift and quadrupole splitting trends. From the peak positions in channel numbers alone, however, qualitatively the isomer shift and quadrupole splitting for the synthetic fayalite decrease with increasing pressure, similar to the results reported here.

#### 4.2.3 (b) Iron microcline

Iron microcline was run twice in the high pressure press and results for both runs are reported here. Data are presented in table 4.9 and two spectra are shown in figure 4.10.

Judging from the large increase in width with pressure both runs appear to suffer from thick absorber effects, although the second run does not show so large an increase and provides better quality data. The agreement between the two runs in terms of isomer shift and quadrupole splitting values is very good and any difference is within experimental error ( $\pm 0.02$  mm/sec). The quadrupole splitting shows a very large increase in the first 50 kb, exceeding even that reported by Lewis and Drickamer (1968a) for  $\text{Fe}^{3+}$  silicate glass. The isomer shift also shows a large increase with increasing pressure.

There was also some hematite, presumably unreacted from the synthesis,

Table 4.9

MÖSSBAUER DATA FOR IRON MICROCLINE AS A FUNCTION OF PRESSURE.

PRESSURE		IS	QS	Fe <sup>3+</sup> (IV) WDTHS <sup>1</sup>		Fe <sub>2</sub> O <sub>3</sub> <sup>2</sup> %
REGULAR	1 bar	0.21	0.60	0.45	0.45	5.2
HIGH	0 kb	0.23	0.65	0.60	0.60	---
PRESSURE	104 kb	0.29	1.50	1.16	1.38	---
Run 1	176 kb	0.30	1.57	1.24	1.42	---
	205 kb	0.29	1.53	1.12	1.32	---
HIGH	0 kb	0.22	0.65	0.59	0.57	8.8
PRESSURE	25 kb	0.26	1.31	0.91	1.10	9.4
Run 2	60 kb	0.29	1.49	0.94	1.11	8.0
	90 kb	0.30	1.52	0.96	1.15	9.6
	110 kb	0.31	1.52	0.98	1.07	9.0
	145 kb	0.31	1.52	0.98	1.15	7.0
	175 kb	0.30	1.53	1.01	1.17	7.4

<sup>1</sup>The low energy peak's width is on the left.

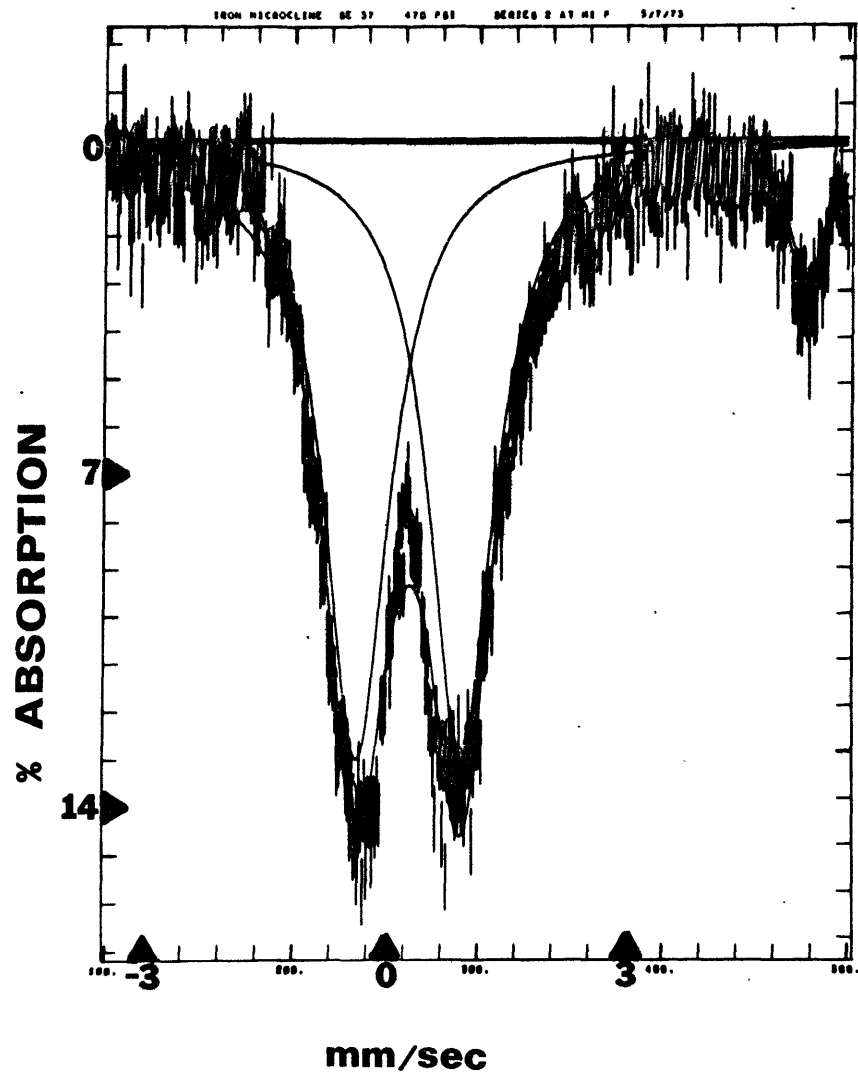
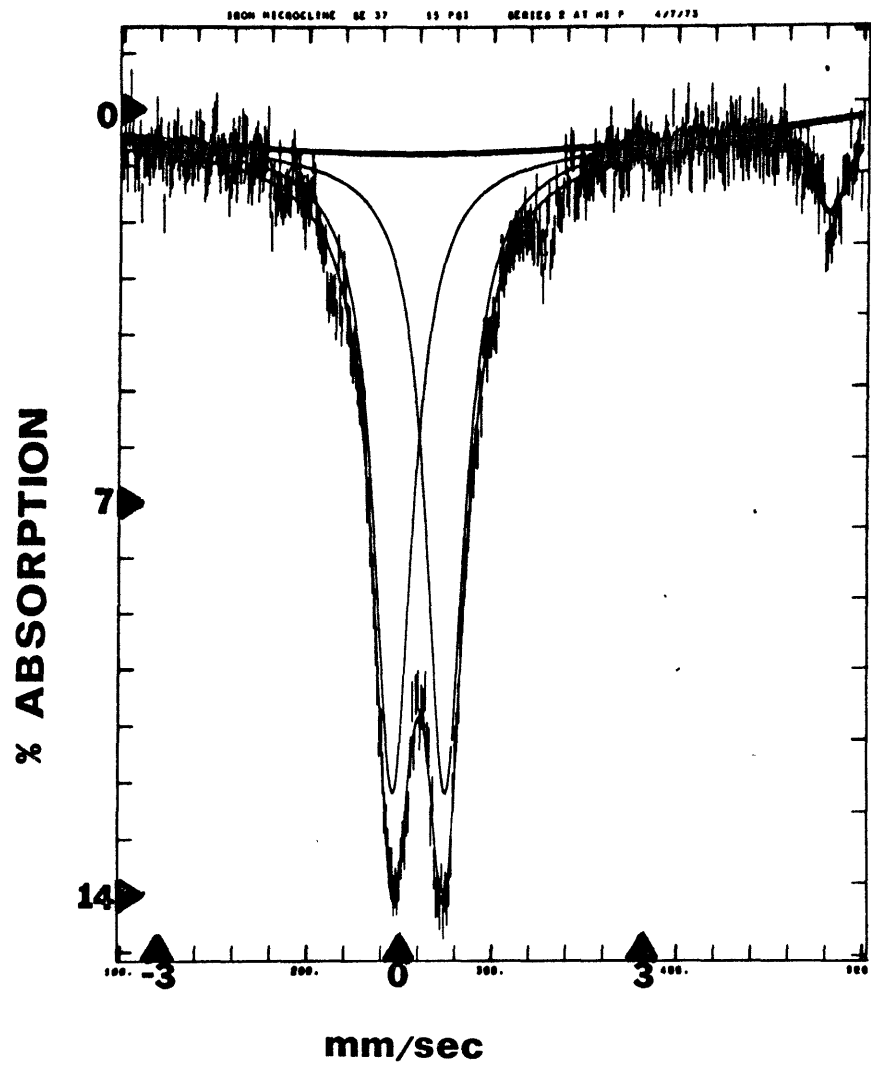
<sup>2</sup>Ratio of the area of the two fitted hematite peaks to the total area under the envelope.

All fits reported at that stage in the computer fitting where the widths and areas of only the hematite peaks were constrained equal.

Figure 4.10

Fitted Mössbauer spectra of iron microcline at 0 kb (left) and at 25 kb (right). The smaller peaks are due to hematite.





which appeared in the Mössbauer spectra as two small peaks on either side of the ferric absorption. The ratio of the area of these peaks to the central absorption is tabulated in table 4.9 and shows a large increase on changing the geometry, which can be attributed to thick absorber properties.

As pressure is increased, the widths of the two peaks of the iron microcline doublets become unequal, which may indicate that there is more than one variety of tetrahedral ferric iron and that they behave differently with pressure. This suggests that ordering of  $\text{Fe}^{3+}$  and Si over the four tetrahedral sites of this feldspar structure may not be complete.

#### 4.2.3 (c) Hematite

A sample of  $^{57}\text{Fe}_2\text{O}_3$  was investigated under pressure by means of the Mössbauer technique. This phase served as a pressure calibrant since the effective quadrupole splitting is highly pressure sensitive and has already been reported as a function of pressure (Vaughan and Drickamer, 1967a). The data are tabulated in table 4.10. The effective quadrupole splitting reported in this study is, in fact,  $eqQ(\cos^2\theta-1)$  where  $\theta$  is the angle between the magnetic axis and the main symmetry axis of the EFG tensor (Wertheim, 1964), since in hematite both magnetic and electric field gradient effects are acting simultaneously on the iron nuclei. This effective quadrupole splitting is simply measured as twice the difference between the effective isomer shift of the outer two peaks and the effective isomer shift of the central four peaks (see figure 4.11).

The isomer shift and hyperfine magnetic splitting data agree closely with those reported by Vaughan and Drickamer (1967a). The ratios of peak intensities, which ideally should be 3:2:1:1:2:3, were not close to these

Table 4.10

MÖSSBAUER DATA FOR HEMATITE AS A FUNCTION OF PRESSURE

	Pressure		Fe <sup>3+</sup> (VI)		
	Psi <sup>2</sup>	Kb <sup>3</sup>	IS	"QS" <sup>1</sup>	H <sub>o</sub> <sup>4</sup>
REGULAR	1 bar		0.39	0.38	509
HIGH	0	0	0.39	0.37	510
PRESSURE	500	30	0.39	-0.04	507
RUN	1000	55	0.38	-0.12	506
	1530	80	0.38	-0.16	506
	1990	110	0.37	-0.23	506
	3000	150	0.37	-0.32	506

<sup>1</sup> "QS" defined in text and figure 4.11.

<sup>2</sup> Pressure in psi as read from the Heise gauge on the hydraulic line.

<sup>3</sup> Pressure in kb determined by cross-comparison of "QS" data between this study and the study of Vaughan and Drickamer (1967a).

<sup>4</sup> H<sub>o</sub> in Kgauss; where 30.97 Kgauss = 1 mm/sec

All fits reported at that stage in the computer fitting where the areas and widths of all paired peaks are held equal. The baseline is constrained straight.

Figure 4.11

Upper: Energy level diagram for phases giving rise to magnetically split Mössbauer spectra. When both magnetic and quadrupole interactions are present, the splittings of the  $I = 3/2$  state are no longer equal resulting in an asymmetric spectrum, similar to that shown in the lower diagram.

Lower: Schematic Mössbauer spectrum of hematite, with the asymmetry exaggerated.

Note the definitions of the magnetic parameters  $a_0$ ,  $b_0$  and  $H_0$  in addition to the definition of the effective quadrupole splitting. These definitions are only exact when the magnetic and electric field gradients are parallel or the latter is zero.

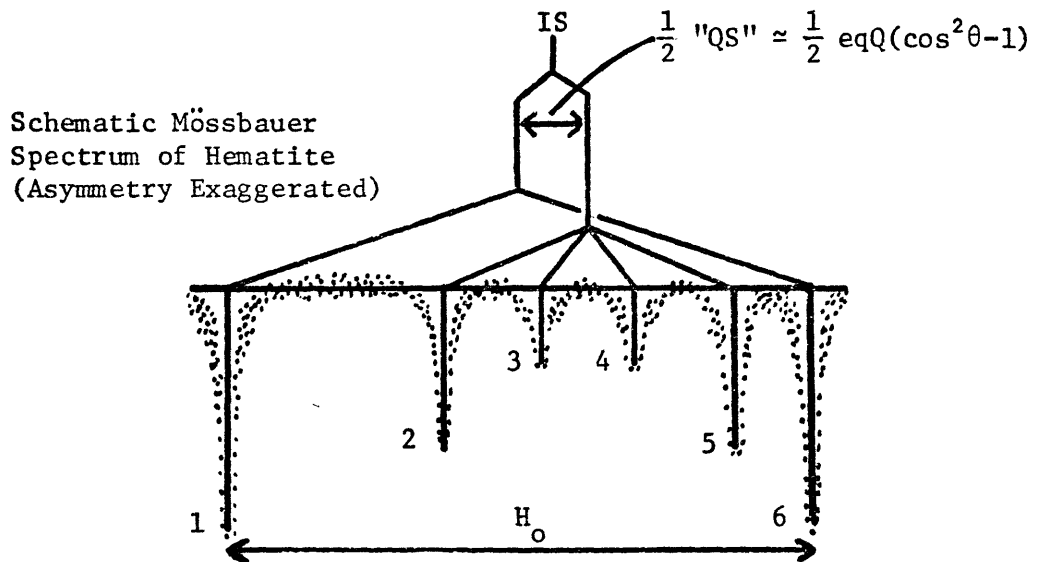
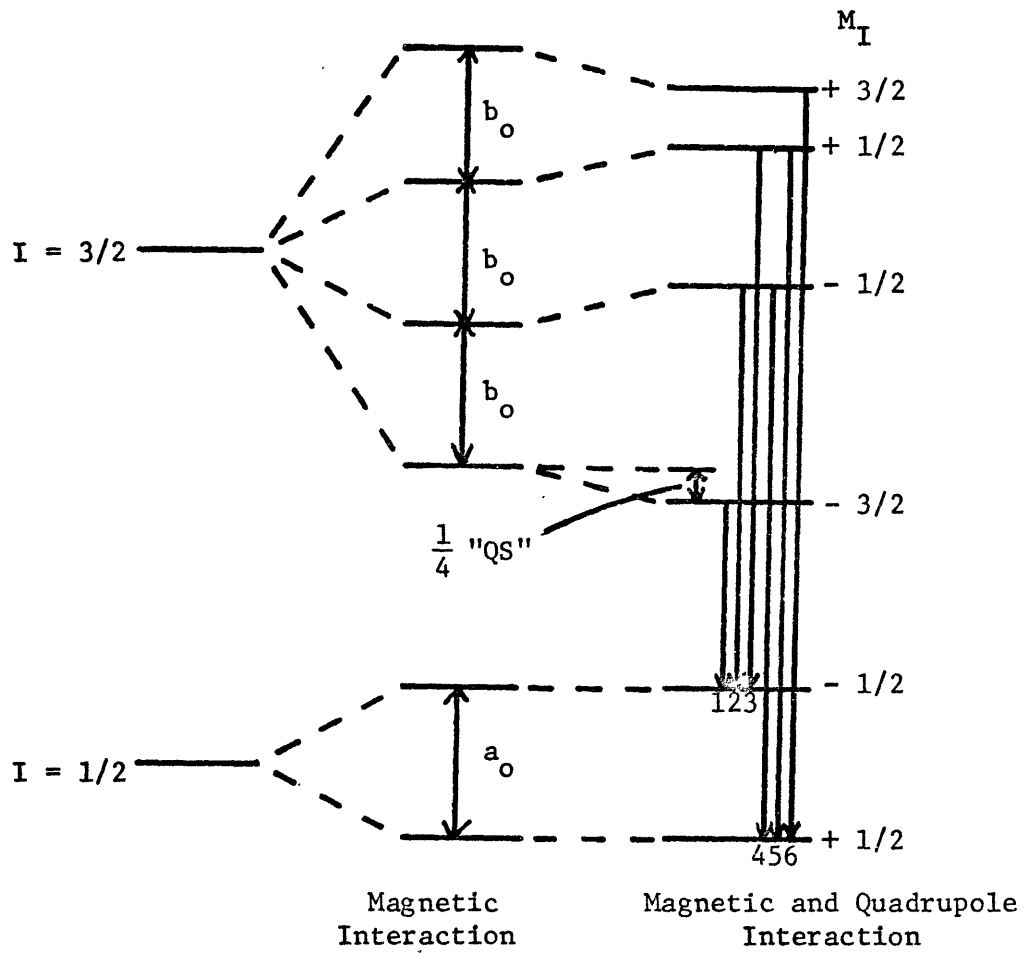
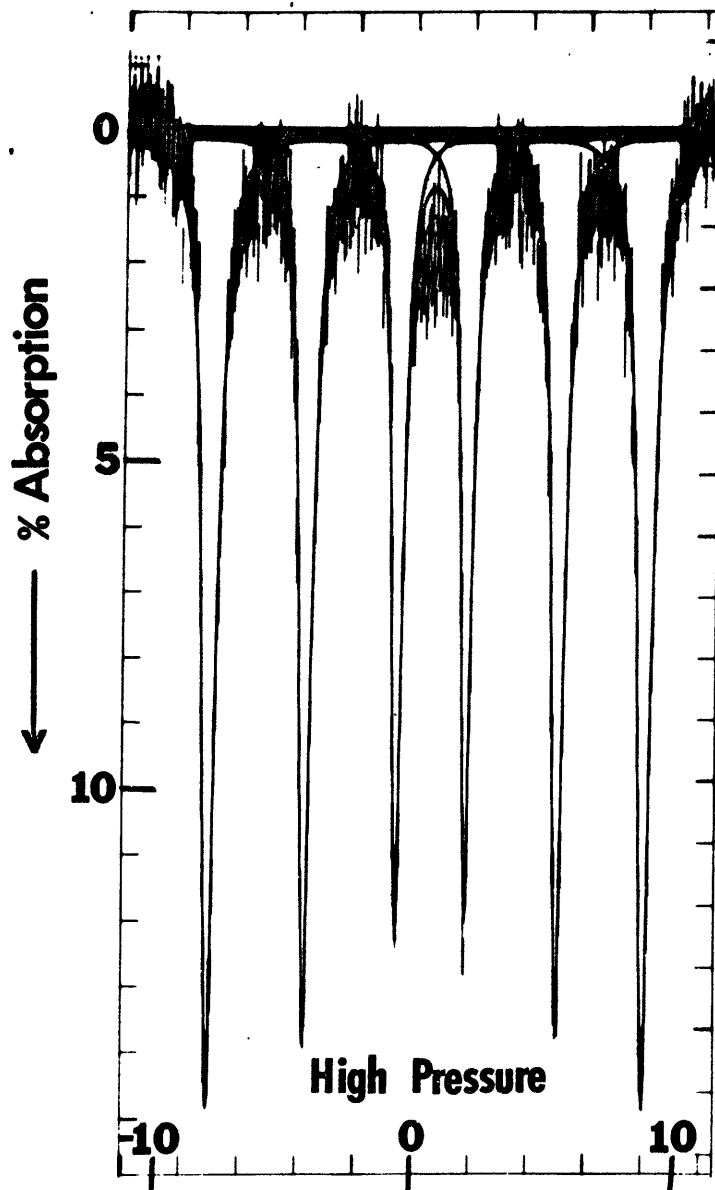
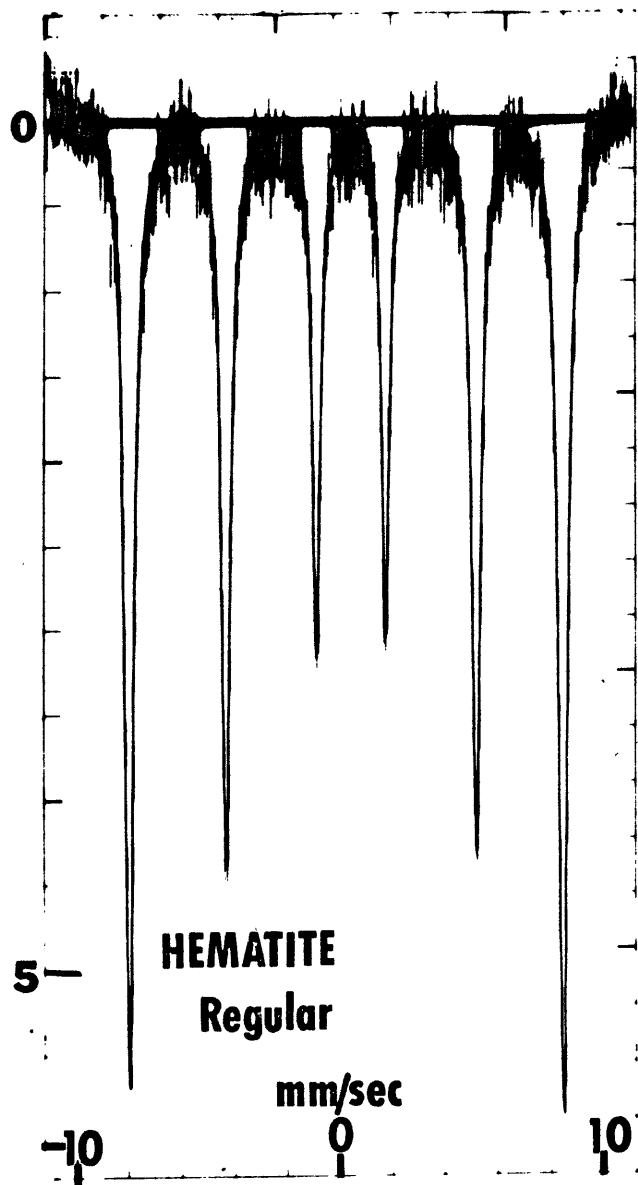


Figure 4.12

Fitted Mössbauer spectra of hematite at 0 kb in the regular geometry (left) and in the high pressure geometry (right). The antiferromagnetism exhibited by hematite is responsible for the observation of six peaks.



ratios in the high pressure geometry, indicating that the sample was probably too thick. This phenomenon is featured in figure 4.12, where the Mössbauer spectrum of hematite is shown in both the regular geometry and the high pressure geometry.

#### 4.2.3 (d) Magnetite

Magnetite exhibits a complex twelve peak Mössbauer spectrum at room temperature. The spectrum may be resolved into two six-peak magnetic subspectra: one subspectra representing  $\text{Fe}^{3+}$  in tetrahedral coordination, the other subspectra representing an averaged  $\text{Fe}^{2+}$ - $\text{Fe}^{3+}$  species in octahedral coordination (Kündig and Hargrove, 1969). The averaged subspectrum arises since electron exchange between the sites is much faster at room temperature than the lifetime of the excited Mössbauer state. At temperatures below 119 °K, this subspectrum does resolve itself into two components as ordering of the  $\text{Fe}^{2+}$  and  $\text{Fe}^{3+}$  cations in the octahedral sites occurs below this temperature.

The presence of twelve peaks presents a formidable problem to computer fitting the spectrum, and very fine counting statistics and resolution are necessary to fit twelve peaks to the envelope. By the judicious choice of constraints a reasonable fit was obtained in the regular geometry run, but for the high pressure geometry run, the statistics and resolution were much worse and fits were not even attempted. Data for the regular geometry run are presented in table 4.11 and the spectrum is shown in figure 4.13.

Visually, the peaks broaden with pressure and wipe out the resolution of the two subspectra patterns. In addition, there may be some coalescing of the two patterns, which also contributes to the loss of resolution.



Table 4.11

MÖSSBAUER DATA FOR MAGNETITE

Regular geometry data:

SPECIES	IS	QS	$a_o^1$	$b_o^1$	$H_o^{1,2}$	%
Fe <sup>3+</sup> (IV)	0.29	0.06	5.77	3.25	485	33
Fe <sup>2.5+</sup> (VI)	0.67	0.02	5.41	3.07	453	67

<sup>1</sup>Defined in figure 4.11.

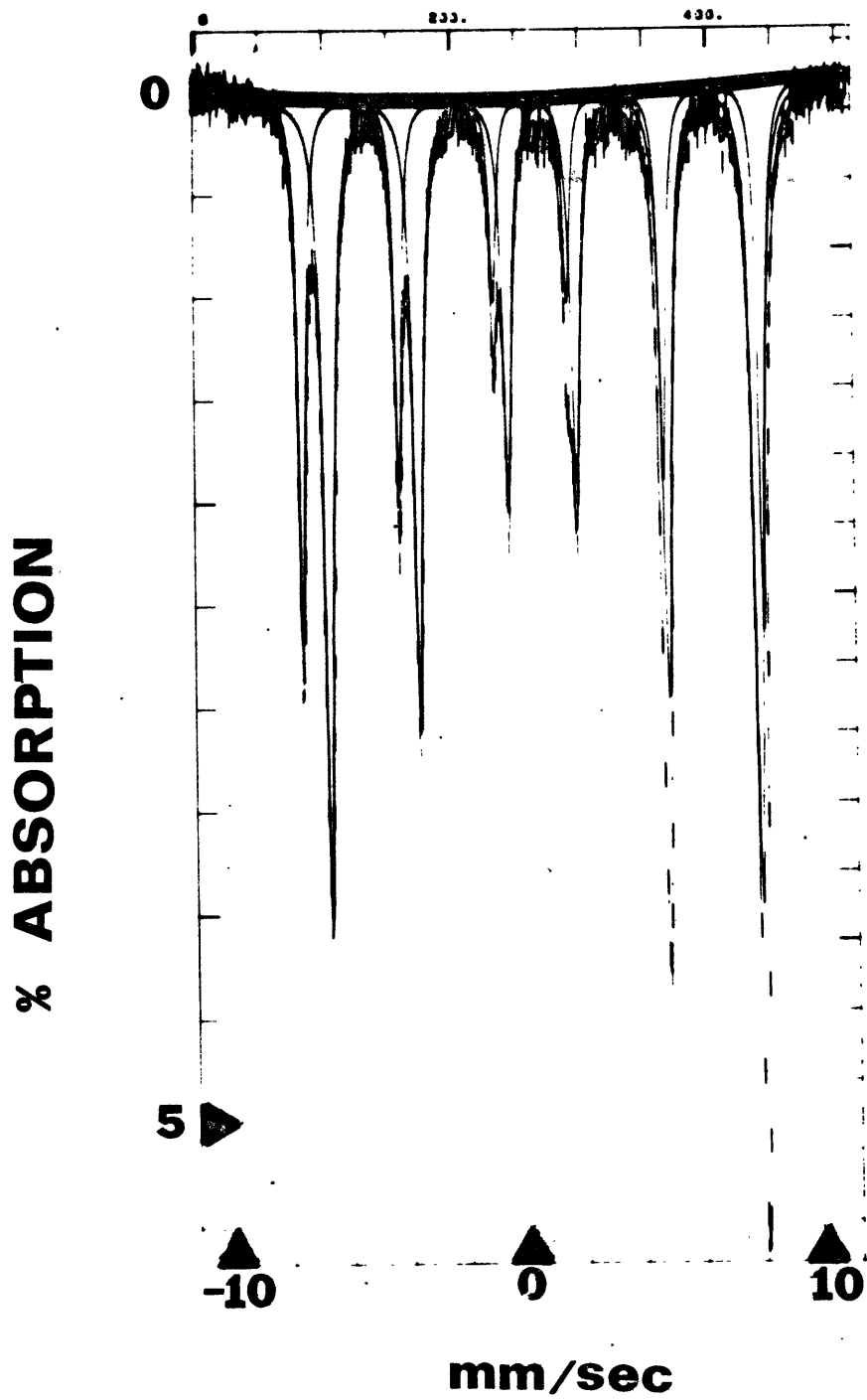
<sup>2</sup>H<sub>o</sub> in Kgauss; where 30.97 Kgauss = 1 mm/sec

High pressure data not fitted.

The fit is reported at that stage in the computer fitting where the widths and areas of all paired peaks are held equal.

Figure 4.13

Fitted Mössbauer spectrum of magnetite in the regular geometry. The ferrimagnetism exhibited by magnetite is responsible for the observation of twelve peaks; the smaller six peaks are assigned to  $\text{Fe}^{3+}$  (IV) and the larger six peaks are assigned to an averaged  $\text{Fe}^{2+}$ - $\text{Fe}^{3+}$  (VI) species.



The magnetic hyperfine splitting does not appear to change significantly with pressure up to 150 kb.

#### 4.2.3 (e) Orthoferrosilite

Mössbauer spectra of a natural orthoferrosilite from Manchuria were recorded at three different pressures and also in the regular geometry. The Mössbauer parameters for the latter spectrum are in good agreement with those found by Bancroft et al. (1967). Four peaks are found in the regular geometry spectrum because the orthopyroxene structure contains two distinct octahedral sites: a fairly regular site, M1, and a highly distorted site, M2. The parameters for all spectra are listed in table 4.12 and two spectra are shown in figure 4.14.

The resolution in the two higher pressure spectra was not very good so that two peak fits were originally fitted for these spectra. However, by constraining the M1:M2 area ratio to that obtained in the zero pressure spectrum, four peak fits were forced for these data. Both two peak and four peak fits are recorded in table 4.12. Both fitting arrangements show relatively large changes in quadrupole splitting between 0 kb and 55 kb, but only a very small change from 55 kb to 110 kb. The M1 isomer shift decreases significantly over the first 55 kb, a trend similar to those shown by other  $\text{Fe}^{2+}$  (VI)-containing phases. The M2 isomer shift, however, remains approximately constant up to 100 kb.

#### 4.2.4 Relative $f^{\#}$ experiments

Two experiments were run to attempt to measure relative changes in  $f^{\#}$ , the recoil-free fraction, with pressure between iron species in different minerals. Mechanical mixtures of fayalite and iron microcline and

Table 4.12

MÖSSBAUER DATA FOR ORTHOFERROSILITE FROM  
MANCHURIA AS A FUNCTION OF PRESSURE

(a) 2 peak fits

	PRESSURE	IS	QS
High	0 kb	1.12	2.19
Pressure	55 kb	1.11	2.33
Run	110 kb	1.11	2.32

All fits reported with no constraints in the computer fitting.

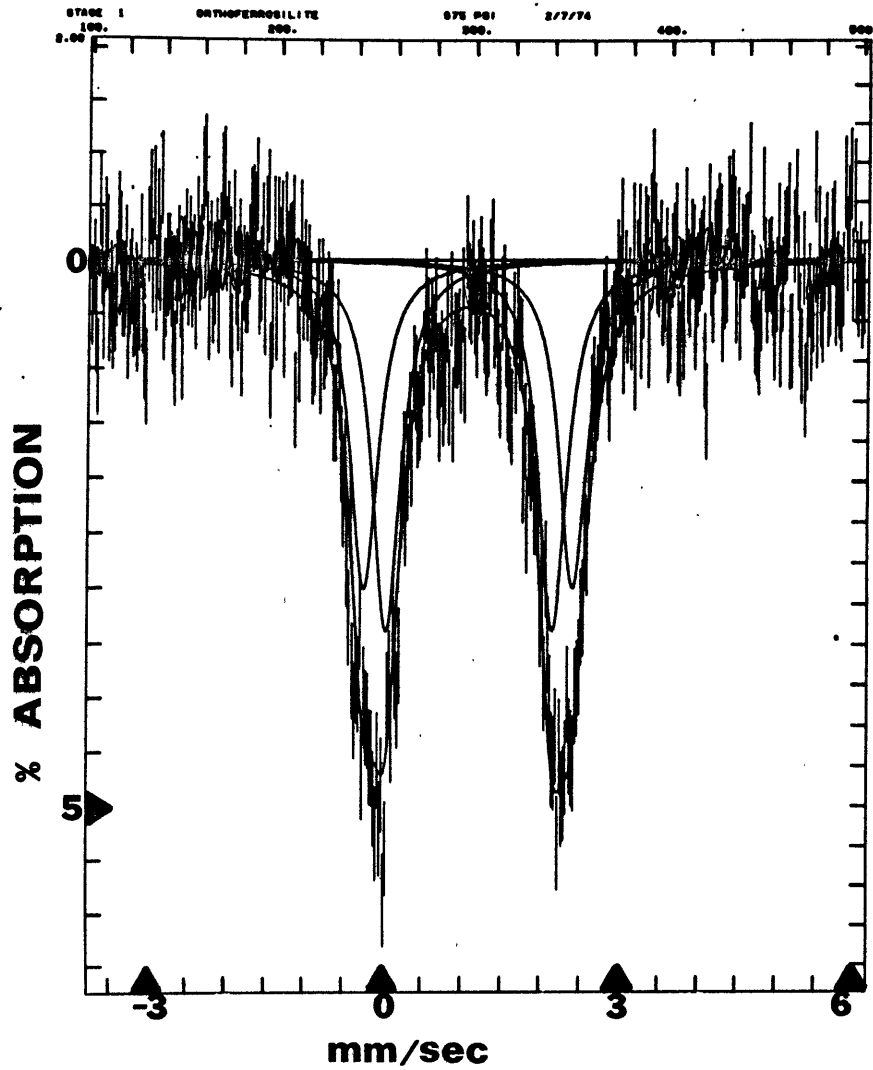
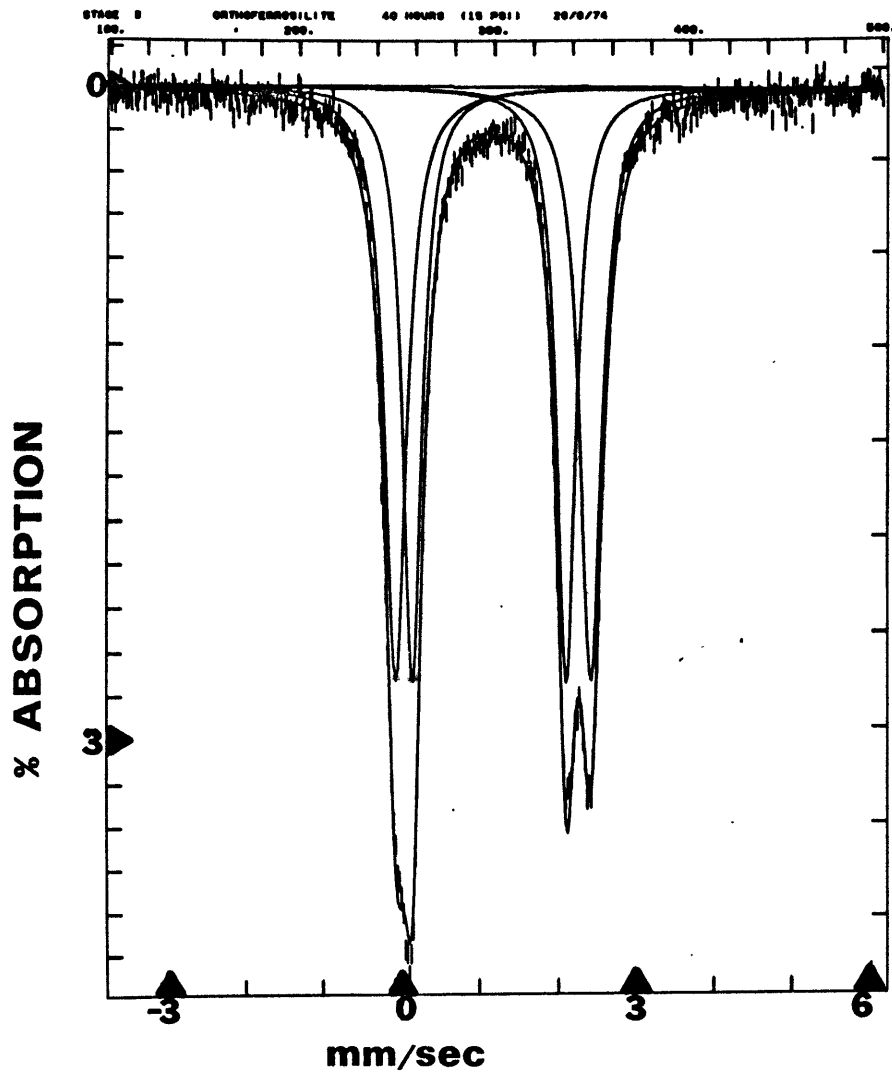
(b) 4 peak fits

	PRESSURE	Fe <sup>2+</sup> (VI) M2			Fe <sup>2+</sup> (VI) M1		
		IS	QS	%	IS	QS	%
Regular	1 bar	1.13	1.97	52	1.18	2.49	48
High	0 kb	1.09	1.95	53	1.16	2.46	47
Pressure	55 kb	1.11	2.09	53	1.10	2.63	47
Run	110 kb	1.11	2.07	53	1.10	2.59	47

All fits reported at that stage in the computer fitting where the widths of the four peaks are all held equal and areas are constrained in pairs. In addition, due to the diminishing resolution with increasing pressure, the areas of the M1 and M2 peaks are constrained in the ratio 47:53 for the spectra at 55 kb and 110 kb.

Figure 4.14

Fitted Mössbauer spectra of orthoferrosilite from Manchuria in the regular geometry (left) and at 55 kb (right). The inner pair of peaks is assigned to  $\text{Fe}^{2+}$  in the M2 sites; the outer pair of peaks is assigned to  $\text{Fe}^{2+}$  in the M1 sites.



of fayalite and acmite were made from samples synthesized using mixes containing 90%  $^{57}\text{Fe}$  compounds. The iron microcline used was SE #37 product while the fayalite and acmite were synthesized by Dr. D.J. Vaughan. In addition, many of the experiments reported above contain two types of iron cations which make them relevant to this topic. These latter experiments are discussed in this respect in sections 4.2.4 (c) and 4.3.5.

#### 4.2.4 (a) Fayalite and iron microcline

The sample pellet prepared was too concentrated in  $^{57}\text{Fe}$  which resulted in unusual additivity of the peaks. The lowest energy peak was formed by overlap of the fayalite and iron microcline low velocity peaks whereas the two high energy peaks of the two phases were well separated. In the regular geometry experiment, the intensity of the lowest energy peak approximated the sum of the two higher energy components, while in the high pressure geometry, no such additivity was obvious because the lowest energy peak had considerably less intensity than the sum of the two higher energy components (figure 4.15). The overall effect of this non-additivity was to reduce the intensity of the microcline component and to force the low energy component of the iron microcline subspectrum at higher energy to overlap the high energy component resulting in anomalous Mössbauer parameters. For this reason, the experiment was adjudged as unlikely to lead to meaningful results, as the changes that were sought were expected to be small.

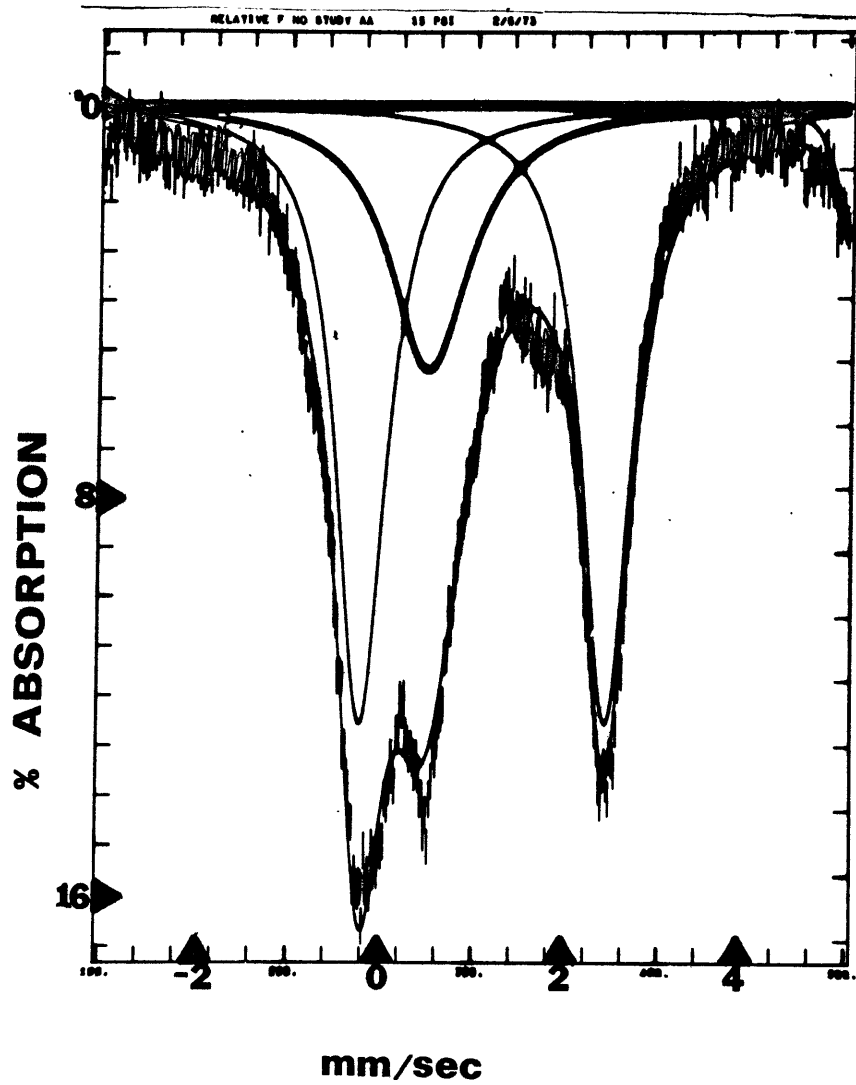
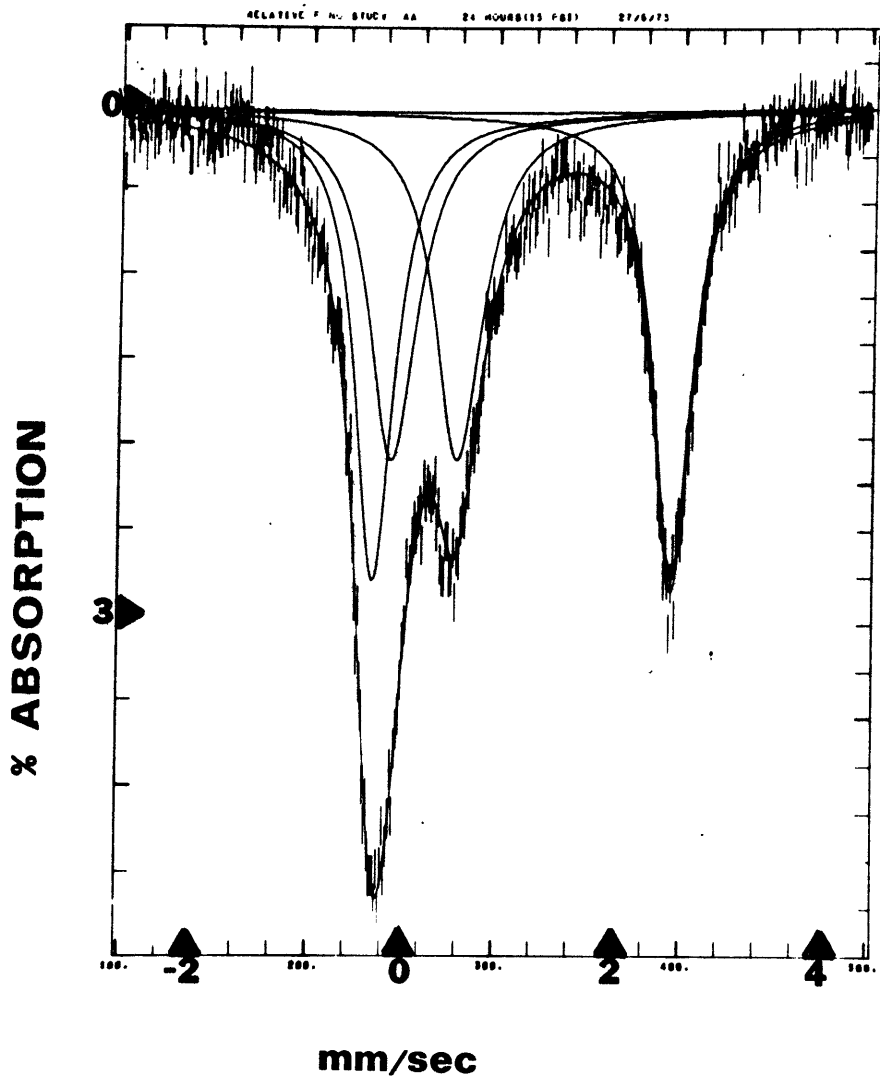
#### 4.2.4 (b) Fayalite and acmite

A similar effect for this mixture of phases was noted on changing the geometry as reported for the study of the mixture of



Figure 4.15

Fitted Mössbauer spectra of a mechanical mixture of fayalite and iron microcline in the regular geometry (left) and in the high pressure geometry (right). The outer, narrow peaks are assigned to fayalite; the inner, broad peaks are assigned to iron microcline. Note the change in position of the microcline peaks on changing the geometry, resulting from thick absorber effects.



fayalite and iron microcline (figure 4.16). However, although the effect was not nearly as large as for the other experiment, it also would appear to preclude obtaining any accurate results.

#### 4.2.4 (c) Other experiments

A number of other experiments would appear to also enable results on relative  $f^{\#}$  for different iron species. These include the iron microcline experiment where hematite was present as a small impurity; and FeAl garnet,  $\text{Ca}_3\text{AlFeSi}_3\text{O}_{12}$ , andradite (Vaughan and Tossell, unpublished), and ferriphlogopite micas which also contained some ferrous due to circumstances of the synthesis experiment. The relative changes in intensities of the two kinds of absorption have already been presented above. Although in these experiments the spectral envelopes change considerably less with changing geometry than those of the two mechanical mixture experiments reported in this section, the changes are large enough to suspect thick absorber phenomena to be present in some of these runs.

The micas and andradite (Vaughan and Tossell, unpublished), in particular, show large changes in  $\text{Fe}^{2+}/\text{Fe}^{3+}$  ratio with pressure while in the high pressure geometry, which may indicate some change in the recoil-free fraction ratio of the two kinds of iron. Further discussion of these changes is presented in section 4.3.5.

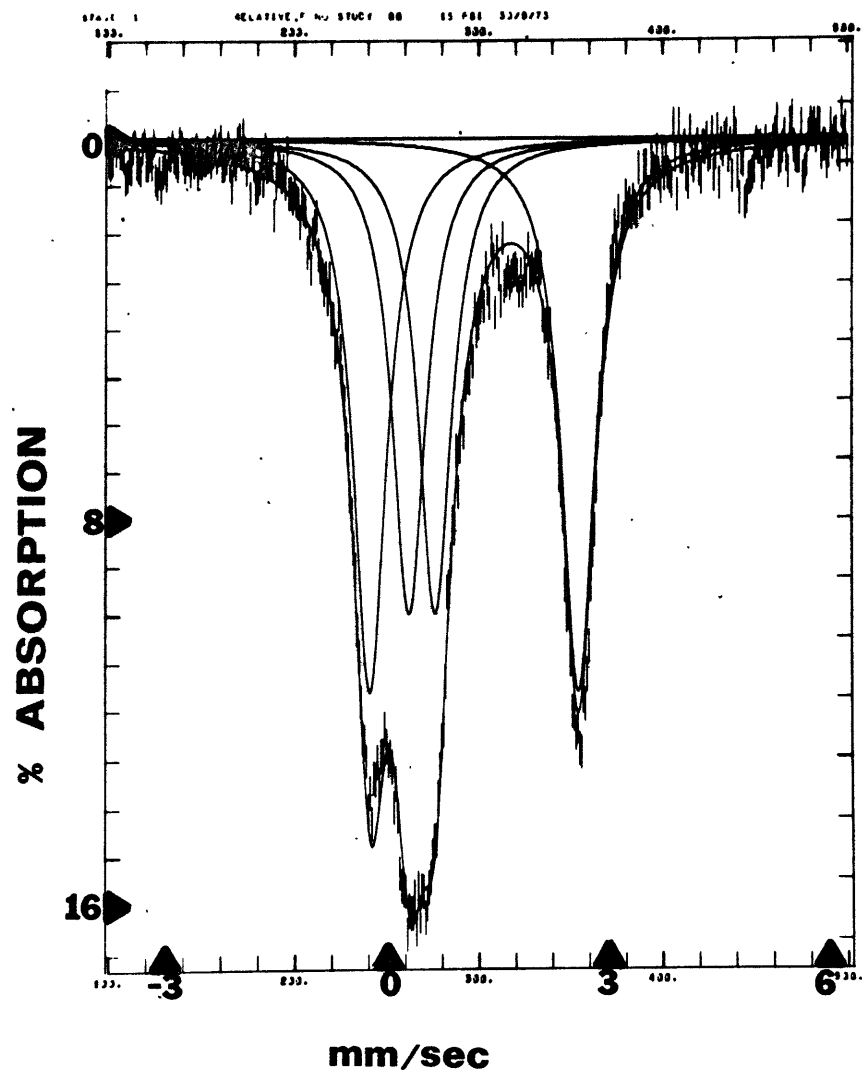
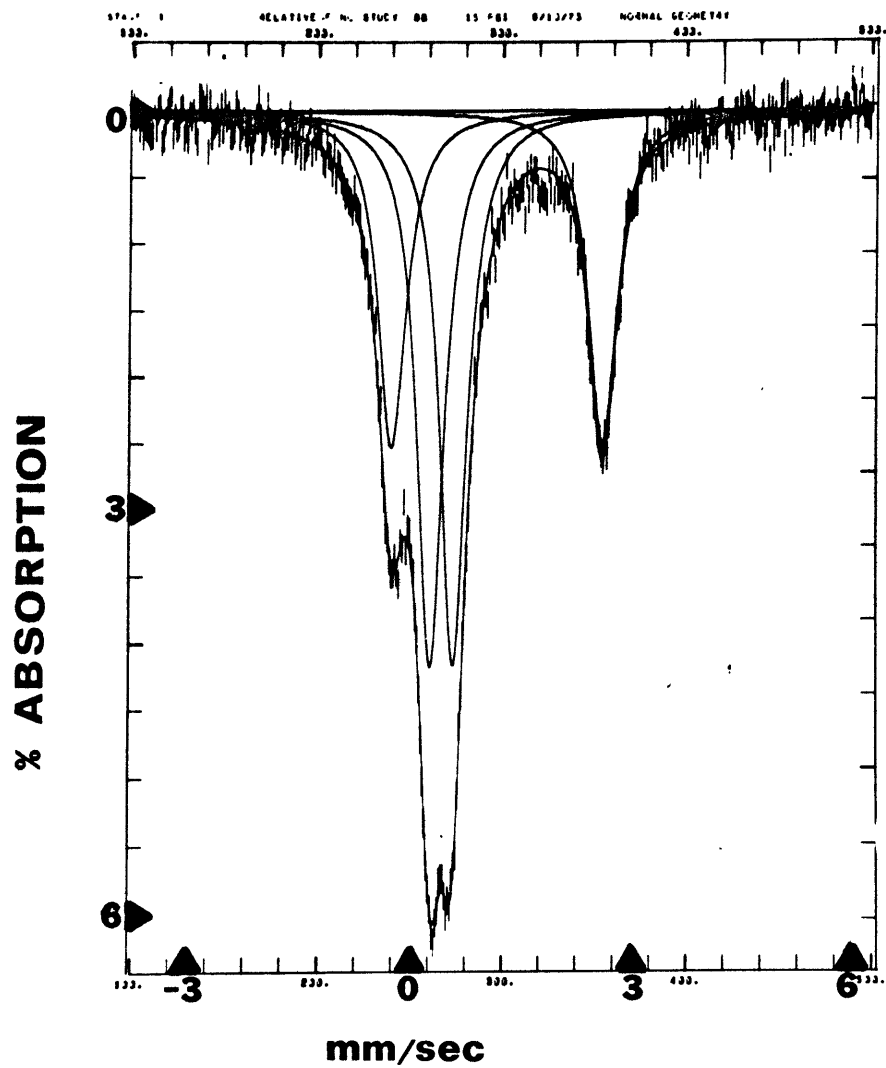
These results could no doubt be improved, if precautions were taken to eliminate thick absorber effects as much as possible.

### 4.3 Discussion of Results

The results are now analyzed and discussed in terms of individual parameters, rather than by individual phase.

Figure 4.16

Fitted Mössbauer spectra of a mechanical mixture of fayalite and acmite in the regular geometry (left) and the high pressure geometry (right). The outer peaks are assigned to fayalite; the inner peaks are assigned to acmite. Note the change in absorption amplitude on changing the geometry, some of which may be due to thick absorber effects and some of which may be due to a difference in fayalite:acmite ratio between the two samples.



#### 4.3.1 Isomer shift changes with pressure

Some of the earliest Mössbauer studies were concerned with interpretations of the isomer shift of iron compounds. Although equation 3.5 was easily derived, actual applications of this equation are limited because it is extremely difficult to calculate accurate values of electron density at the nucleus for iron atoms or cations in solids for calibrating the equation. Also, it would be impossible to quantitatively relate values of electron density at the nucleus to all possible bonding factors. For these reasons, almost all of the work with isomer shift data of minerals has been of a qualitative nature.

According to equation 3.5, the electron density at the nucleus of the sample absorber is the only non-constant parameter in the equation affecting the isomer shift. Since only s electrons have a non-zero probability of being at the nucleus, only these electrons determine the isomer shift value. Therefore, in order to account for the fact that the isomer shift is sensitive to the bonding of the iron to its surrounding ligands, even though iron s electrons are not usually involved in bonding, a number of secondary interactions between the bonding electrons and the iron 3s electrons have been postulated as responsible. This is not unreasonable since the 3s electrons do have significant probability of being in the outer bonding region of the iron atom and of being screened from the nucleus by bonding electrons. The degree of screening of the 3s electrons from the nucleus by the bonding electrons (primarily iron 3d electrons) is determined by the size, spin state and charge of the cation and also by the degree of covalency of the iron-ligand bond. Generally, the smaller the number of 3d electrons,

the greater the s electron density at the nucleus, since, as the number of 3d electrons decreases, the 3s electrons become less screened from the nucleus and increasingly contribute to the total electron density at the nucleus. This increase in electron density at the nucleus is reflected by a decrease in isomer shift as  $\delta R/R$  in equation 3.5 is negative. Therefore, the sequence of isomer shift values for the different oxidation states of iron, when coordinated by oxygen, is as shown in table 4.13. Note that iron metal does not fall into place because the bonding involves 4s electrons which contribute directly to the electron density at the nucleus and effectively lower the isomer shift. The bonding difference between high spin and low spin states of ferrous or ferric iron is reflected by a difference in isomer shift of about the same order as the difference between adjacent oxidation states. An increase in coordination number from 4 to 6 or from 6 to 8 can increase the isomer shift by about 0.20 mm/sec. In addition to these primary factors for determining the coarse value of the isomer shift, the fine details for a given cation type are determined by a number of factors related to the covalency of the cation-ligand bonds. Erickson (1967) discussed these factors in depth and their effect on the value of the isomer shift, and pointed out the usefulness of pressure-induced trends of isomer shifts for interpreting bonding details and determining which factors predominate. The systematic study of Frank and Drickamer (1972) of the effect of pressure on electronic structure of twelve substituted ferric  $\beta$ -diketone complexes used and extended Erickson's approach for interpreting isomer shift trends and the present study also takes this line of approach.

Table 4.13

RANGE OF ISOMER SHIFT VALUES FOR DIFFERENT  
OXIDATION STATES OF IRON COORDINATED BY OXYGENS.

OXIDATION STATE	ISOMER SHIFT (mm/sec)
$\text{Fe}^{6+}$ ( $3d^2$ ) <sup>1,2</sup>	-0.90 - -0.80
$\text{Fe}^{4+}$ ( $3d^4$ ) <sup>1,2</sup>	0.00 - +0.10
$\text{Fe}^{3+}$ ( $3d^5$ ) <sup>3</sup>	+0.15 - +0.40
$\text{Fe}^{2+}$ ( $3d^6$ ) <sup>3</sup>	+0.90 - +1.30
$\text{Fe}^0$ ( $3d^7 4s^1$ ) (metallic)	0.00

<sup>1</sup>Danon (1968)

<sup>2</sup>Panyushkin et al. (1969)

<sup>3</sup>Bancroft (1974) and elsewhere



The trends of isomer shift with pressure for a number of ferrous and ferric minerals are shown in figures 4.17 and 4.18. Except for  $\text{Fe}^{3+}$  in tetrahedral coordination, there is a general decrease in isomer shift, indicating an increase in electron density at the nucleus. The most reasonable explanation for these trends is an increase in the contribution of the 3s electrons to the electron density at the nucleus as a result of increasing delocalization of the 3d electrons towards the anions. This is equivalent to describing an increase in central-field covalency of the iron-oxygen bonds due to increased overlap of the metal 3d and ligand electron clouds with compression. The increased sharing of the bonding 3d electrons between cation and ligands decreases the shielding of cation 3s electrons from the cation nucleus, resulting in the increase in electron density at the nucleus.

Initially, at least, the decrease in isomer shift with pressure (figure 4.19) appears to be in the order:  $\text{Fe}^{3+}(\text{IV}) < \text{Fe}^{3+}(\text{VI}) < \text{Fe}^{2+}(\text{VI}) < \text{Fe}^{2+}(\text{VIII})$  which is, firstly, the order of increasing ionic character of the metal-ligand bonds as indicated by the zero pressure isomer shift values and, secondly, the expected order of increasing site compressibility (see Appendix A2.1). Both of these factors would be expected to play a role in determining isomer shift changes. The levelling-off at high pressure of the ferrous isomer shift trends suggests that some other process may also come into effect which decreases the electron density at the nucleus and counteracts the effect of the spreading d orbitals. One possibility appears to be an increase in the contribution of electron density from the ligand orbitals to the 3d cation orbitals resulting in increased shielding of the 3s electrons. This transfer

Figure 4.17

Summary of isomer shift trends with pressure for ferrous phases investigated in this study. Data for ilmenite from Vaughan and Drickamer (1967a).

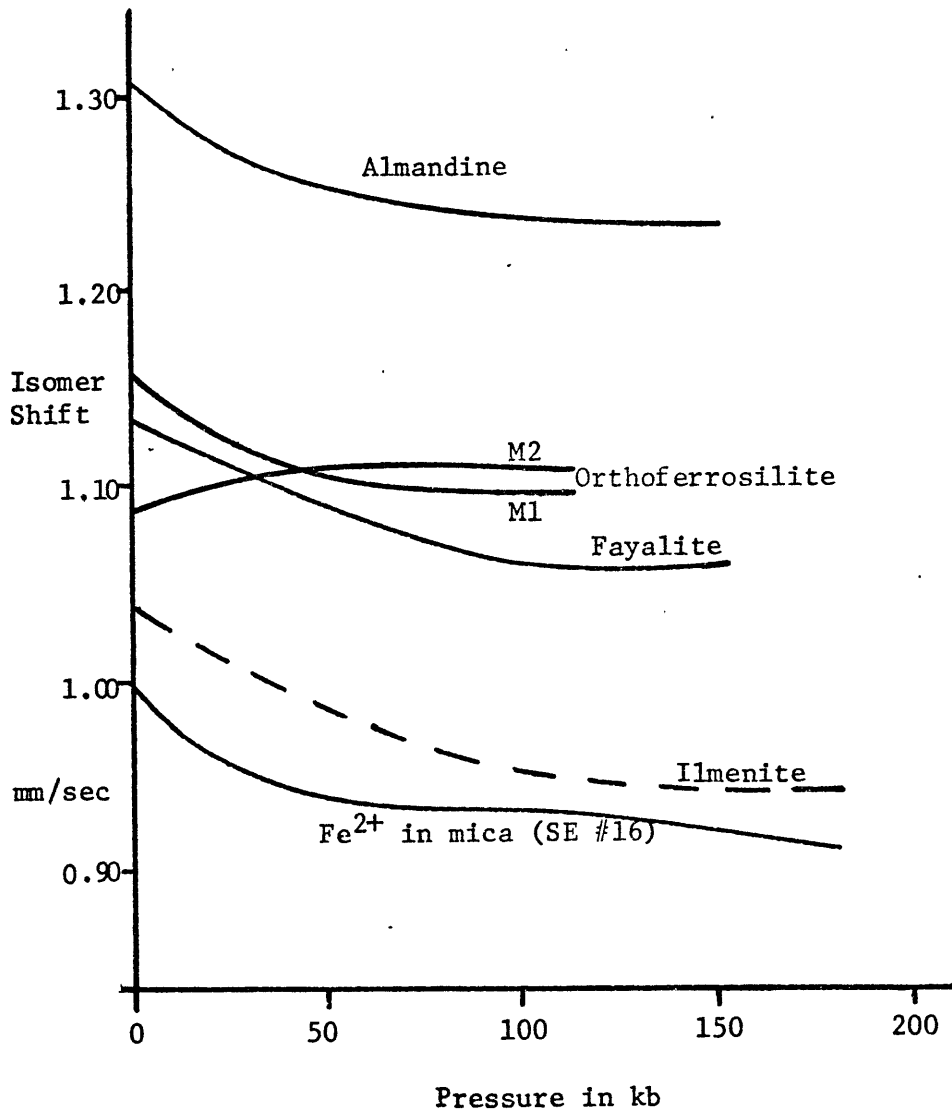


Figure 4.18

Summary of isomer shift trends with pressure for ferric phases investigated in this study. Data for ferric silicate glass from Lewis and Drickamer (1968a).

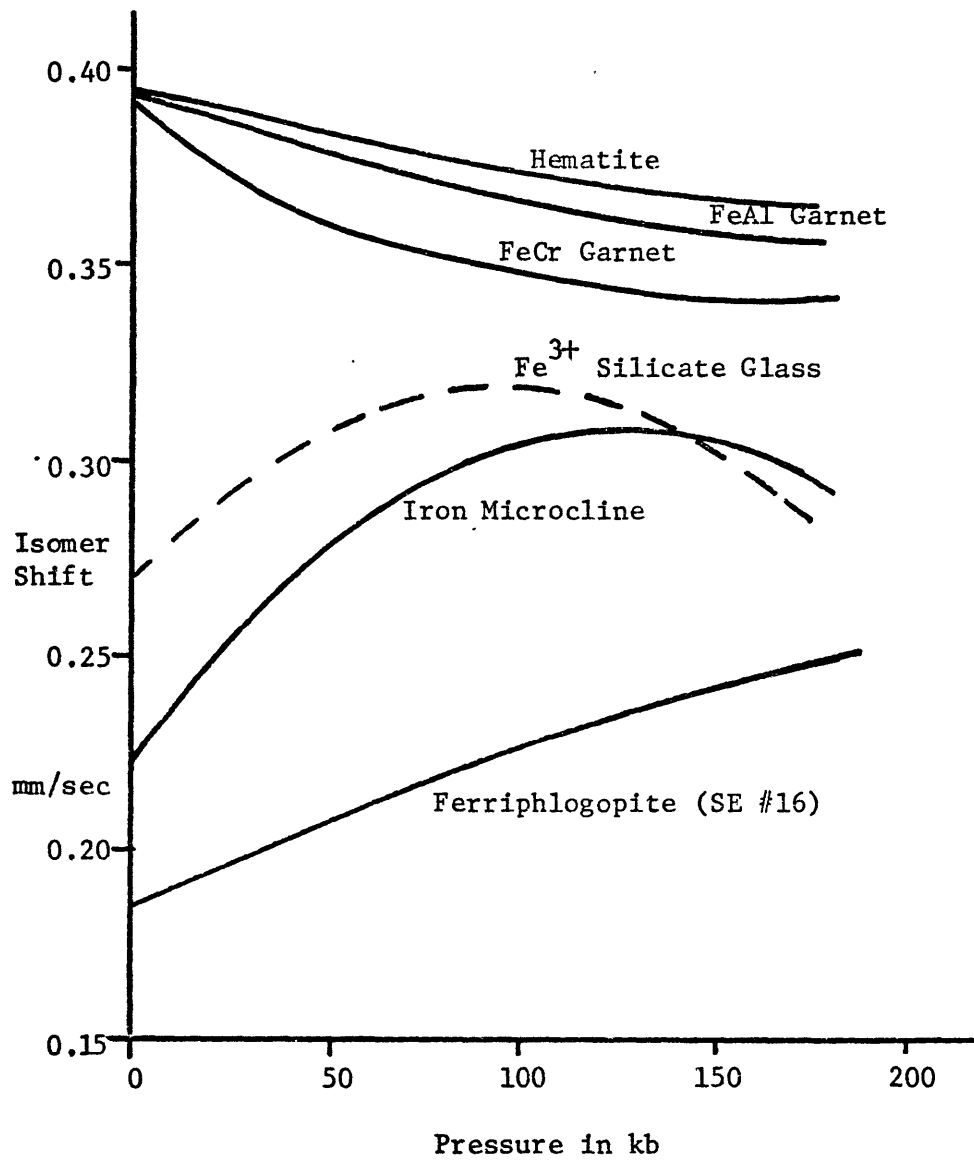
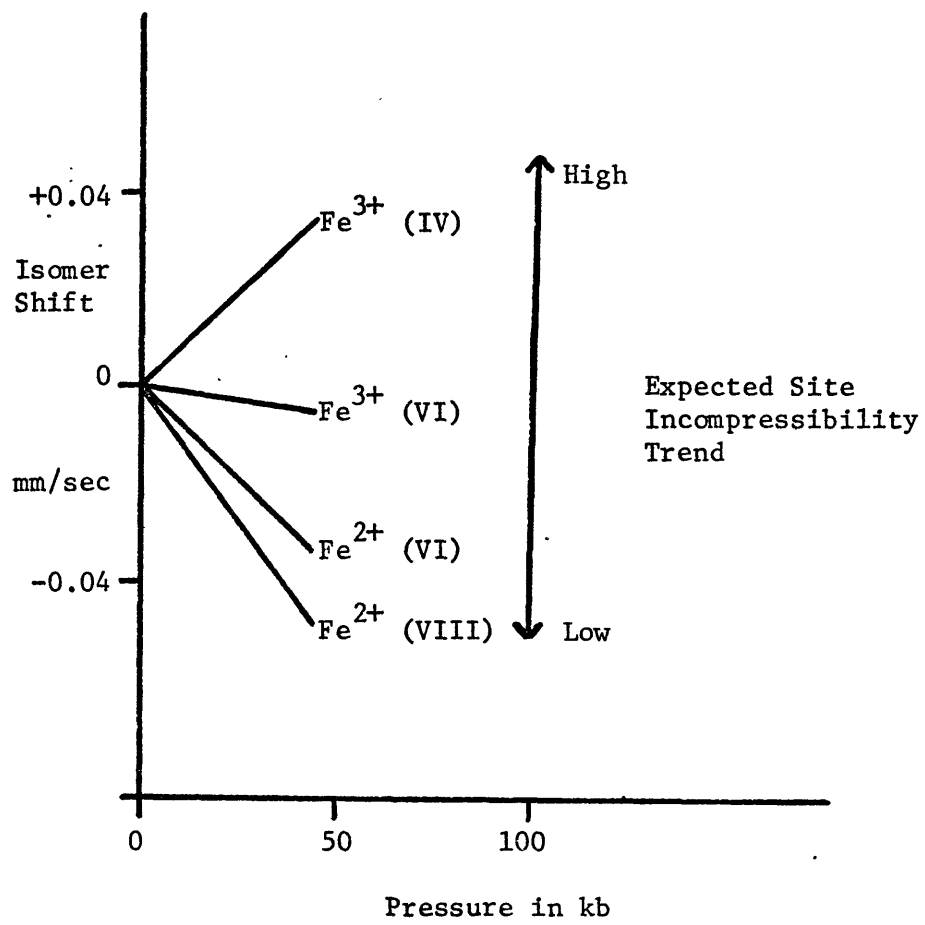


Figure 4.19

Initial isomer shift trends with pressure for the various iron cation and coordination combinations investigated in this study. The data are normalized to a common zero pressure point.



of electrons from ligand to metal orbitals would be consistent with the increase in intensity and red shift of ligand-to-metal charge transfer bands reported by Mao and Bell (1972) and by Mao (1973) in the optical spectra of certain ferrous silicates and oxides.

Ferric iron in tetrahedral sites in silicates is anomalous in that the s electron density at the nucleus decreases significantly with pressure over the first 100 kb. The synthetic CaZrFe garnet, a non-silicate, does not change isomer shift appreciably with pressure and appears to be much more consistent with established trends for the other iron species of different valence state or coordination number, based on expected site compressibility and pressure-induced isomer shift trends. For the ferric silicates, a maximum in the value of the isomer shift in two of the three systems gives credence to the suggestion made by Lewis and Drickamer (1968a) that the trend comes about from two competing factors. These factors are, firstly, a charge transfer process (ligand-to-metal) which increases the 3d electron density at the nucleus and, secondly, a delocalization of the 3d electrons resulting in an increase of 3s electron density at the nucleus. However, because the volume change of this site with pressure is expected to be small, effects involving d electrons, which contribute only in a secondary manner to the electron density at the nucleus, should also be small. Also, because of the large changes in isomer shift with pressure, primary effects involving s electrons would appear to be indicated. This implies that there is considerable cation s electron character in the bonding of the tetrahedral site, which becomes delocalized from the cation with increasing pressure resulting in a decrease in electron density at the nucleus and the



observed increase in isomer shift.

Shannon (personal communication) suggested, by analogy with experiments on the effect of temperature on silicate crystal structures, that this pressure-induced isomer shift trend might arise from an increase in iron-oxygen bond length with pressure. These experiments show that although the structure as a whole expands with increasing temperature, the silicon tetrahedra often remain the same size or even decrease slightly (Brown and Prewitt, 1973; Smyth and Hazen, 1973; Cameron et al., 1973; Smyth, 1973; Sueno et al., 1973; Foit and Peacor, 1973; Peacor, 1973; Pillars and Peacor, 1973). The changes in size of the tetrahedra are small and are often within the experimental error up to 1000 °C. Even if the ferric iron tetrahedra considered here were to expand with pressure by analogy with this behavior, the changes would be so small that it is unlikely that such changes could account for the relatively large changes in isomer shift that have been observed.

Additional evidence for the point of view that the bonding in tetrahedral ferric iron is responsible for the difference in isomer shift trends with pressure compared to the same trends for other iron species comes from the body of isomer shift data for tetrahedral ferric iron. A search through the Mössbauer literature, restricting the data to those phases which are non-magnetic and for which there are data at ambient conditions (1 atm; 295-310 °C or room temperature), resulted in table 4.14. From this table, it is apparent that the more ionic phases have low isomer shifts whereas the more covalent phases have high isomer shift values. This is contrary to trends for  $\text{Fe}^{2+}$  (VI),  $\text{Fe}^{2+}$  (IV) and  $\text{Fe}^{3+}$  (VI), but is consistent with the upward pressure-induced isomer shift trend for  $\text{Fe}^{3+}$  (IV)

Table 4.14  
 COMPILATION OF Fe<sup>3+</sup> (IV) ISOMER SHIFT DATA  
 (RELATIVE TO METALLIC IRON)

PHASE	IS	REF
Bornite, Cu <sub>5</sub> FeS <sub>4</sub>	0.39	Vaughan and Burns (1972)
Germanite, Cu <sub>3</sub> (Fe <sup>3+</sup> ,Ge)(S,As) <sub>4</sub>	0.34	Vaughan and Burns (1972)
KFeCl <sub>4</sub>	0.32	Lewis and Drickamer (1968b)
Sapphirine, Mg <sub>2</sub> (Al,Fe) <sub>4</sub> SiO <sub>10</sub>	0.27-0.30	Bancroft et al. (1968)
Ferric silicate glass	0.25-0.27	Lewis and Drickamer (1968a)
Ca <sub>3</sub> TiFe <sub>2</sub> Si <sub>2</sub> O <sub>12</sub>	0.23	Present Study
NaCa <sub>2</sub> Sb <sub>2</sub> Fe <sub>3</sub> O <sub>12</sub>	0.225	Lyubutin (1971)
KMg <sub>3</sub> (FeAl)Si <sub>3</sub> O <sub>10</sub> (OH) <sub>2</sub>	0.22	Present Study
KFeSi <sub>3</sub> O <sub>8</sub>	0.22	Present Study
Ca <sub>2.5</sub> Th <sub>0.5</sub> Zr <sub>2</sub> Fe <sub>3</sub> O <sub>12</sub>	0.21	Present Study
KFeS <sub>2</sub>	0.19	Fluck et al. (1963)
KMg <sub>3</sub> FeSi <sub>3</sub> O <sub>10</sub> (OH) <sub>2</sub>	0.19	Present Study
YCa <sub>2</sub> Sn <sub>2</sub> Fe <sub>3</sub> O <sub>12</sub>	0.185	Lyubutin (1971)
GdCa <sub>2</sub> Sn <sub>2</sub> Fe <sub>3</sub> O <sub>12</sub>	0.175	Lyubutin (1971)
KFeO <sub>2</sub>	0.17	Fluck et al. (1963)
Ba <sub>2</sub> Fe <sub>2</sub> O <sub>5</sub>	0.165	Gallagher et al. (1965)
Ca <sub>2.5</sub> Zr <sub>2.5</sub> Fe <sub>3</sub> O <sub>12</sub>	0.15	Present Study
Ca(Mg,Fe <sup>3+</sup> )(Fe <sup>3+</sup> ,Si) <sub>2</sub> O <sub>6</sub>	0.14-0.18	Hafner and Huckenholz (1971)

and with the hypothesis that considerable s electron character is involved in the bonding of the iron in tetrahedral site. What form this s electron contribution takes is easy to speculate on, but difficult to substantiate. Assuming a molecular orbital approach to the bonding, the formation of bonding hybrid orbitals by combining s, p and d atomic orbitals of the cation would explain such trends. With increasing covalency these orbitals expand in size and increasingly interact with ligand orbitals. This interaction shields the s electrons from the cation nucleus resulting in a decrease in s electron density at the nucleus and the observed increase in isomer shift with increasing covalency. Presumably in highly ionic species, for example CaZrFe garnet, the orbital overlap between ligand and cation is very small and the expansion of the cation orbitals does not significantly increase the overlap, so that the isomer shift is approximately constant with pressure. On the other hand, the result may indicate that the hybridization scheme is not an adequate explanation for the least covalent situations, and an explanation similar to that used above for other systems is more appropriate.

In effect, the difference between the isomer shift trends for certain  $\text{Fe}^{3+}$  (IV) situations and those of other iron cation and coordination combinations results only from the difference in the degree of s electron participation in the bonding. All isomer shift trends, therefore, appear to be explicable by similar mechanisms, such as cation orbital delocalization and charge transfer effects, regardless of valence state and coordination.

Generally, both the delocalization of cation electron clouds and the transfer of ligand charge to cation orbitals result from increased overlap

of metal and ligand orbitals, or alternatively, from increased covalency of the iron-oxygen bonds and indicate that the ionic model becomes less appropriate at high pressure. Molecular orbital calculations using the method originated by Johnson (1973) and recently applied by Tossell et al. (1973, 1974) to mineralogical systems may enable considerably more quantitative deductions to be made about the change in isomer shift with pressure due to electronic and bonding factors.

Compared to the majority of phases which Drickamer and his co-workers have studied, the isomer shift trends with pressure are relatively small, which is consistent with the expected compressibility differences between the phases of the two areas of study. In addition, this study suggests that the chemical and electronic properties of the oxygen ligands coordinated to the iron cation in silicates (and oxides?) do not vary greatly with structure since no wide range of behavior was observed for the isomer shift trends of a cation of given oxidation state and coordination number. This result should be contrasted with the study of Frank and Drickamer (1972) who found that the isomer shift trends of substituted  $\beta$ -diketone iron complexes with pressure were very sensitive to the perturbation of the electronic structure of the  $\beta$ -diketone caused by the substituting organic functional group.

#### 4.3.2 Quadrupole splitting trends with pressure

The quadrupole splitting arises from the interaction of the electric field gradient at the nucleus and the nuclear quadrupole moment according to equation 3.6. The nuclear quadrupole moment, a nuclear property, will be little affected by pressure and to explain trends of

quadrupole splitting with pressure only the EFG need be considered.

In a site which is only slightly distorted from regular tetrahedral, octahedral or cubic coordination, there is a large distinction between high spin ferrous and ferric iron in terms of valence and lattice contributions to the EFG (see discussion of equation 3.6) and thus to the quadrupole splitting. In high spin ferric iron, each of the five 3d orbitals contains one electron, so that a spherical electron distribution results about the nucleus. Therefore, the net valence contribution to the high spin ferric iron EFG is zero and the quadrupole splitting is only a function of the asymmetry in the ligand positions about the  $^{57}\text{Fe}$  cation. On the other hand, high spin ferrous iron contains an additional electron in the lower set of 3d levels (the  $t_{2g}$  derived levels for octahedral, e derived levels for tetrahedral and  $e_g$  derived levels for eight-fold coordination -- see figure 4.20). This sixth electron permits a large valence contribution to the EFG in slightly distorted sites which completely outweighs the ligand contribution, so that ferrous quadrupole splittings are largely related to the valence electron contribution to the EFG. Due to this difference, ferrous and ferric quadrupole splitting trends with pressure will be treated separately.

#### 4.3.3 Ferric quadrupole splitting trends

Quadrupole splitting trends due to pressure for ferric minerals investigated in this study are summarized in figure 4.21. All samples show a large relative increase over the first 50-100 kb and then level off as pressure is further increased. Only the ligands in ferric phases contribute to the components of the EFG and this contribution is of the form

Figure 4.20

The 3d levels in tetrahedral, cubal and octahedral coordinations are shown. Note the inverse relationship of the levels in octahedral coordination compared to those in the other two coordinations. For this reason, there are two possible lower level splittings,  $\Delta_1$  and  $\Delta_2$ , in octahedral coordination, but only one such splitting,  $\Delta_1$ , for the other two coordinations.

If the different coordinations had the same cation-anion bond distances, then the following relationship would hold:

$$\Delta_o = \frac{9}{4}\Delta_t = \frac{9}{8}\Delta_c$$

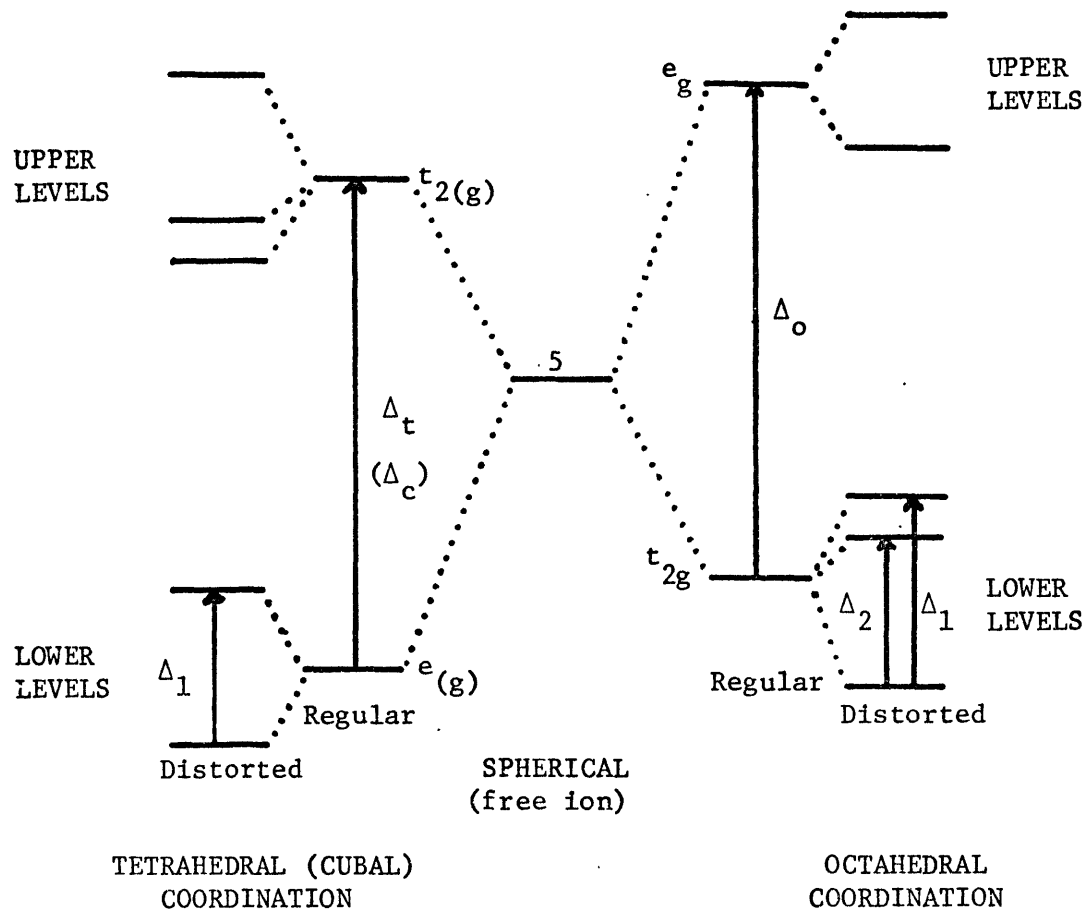
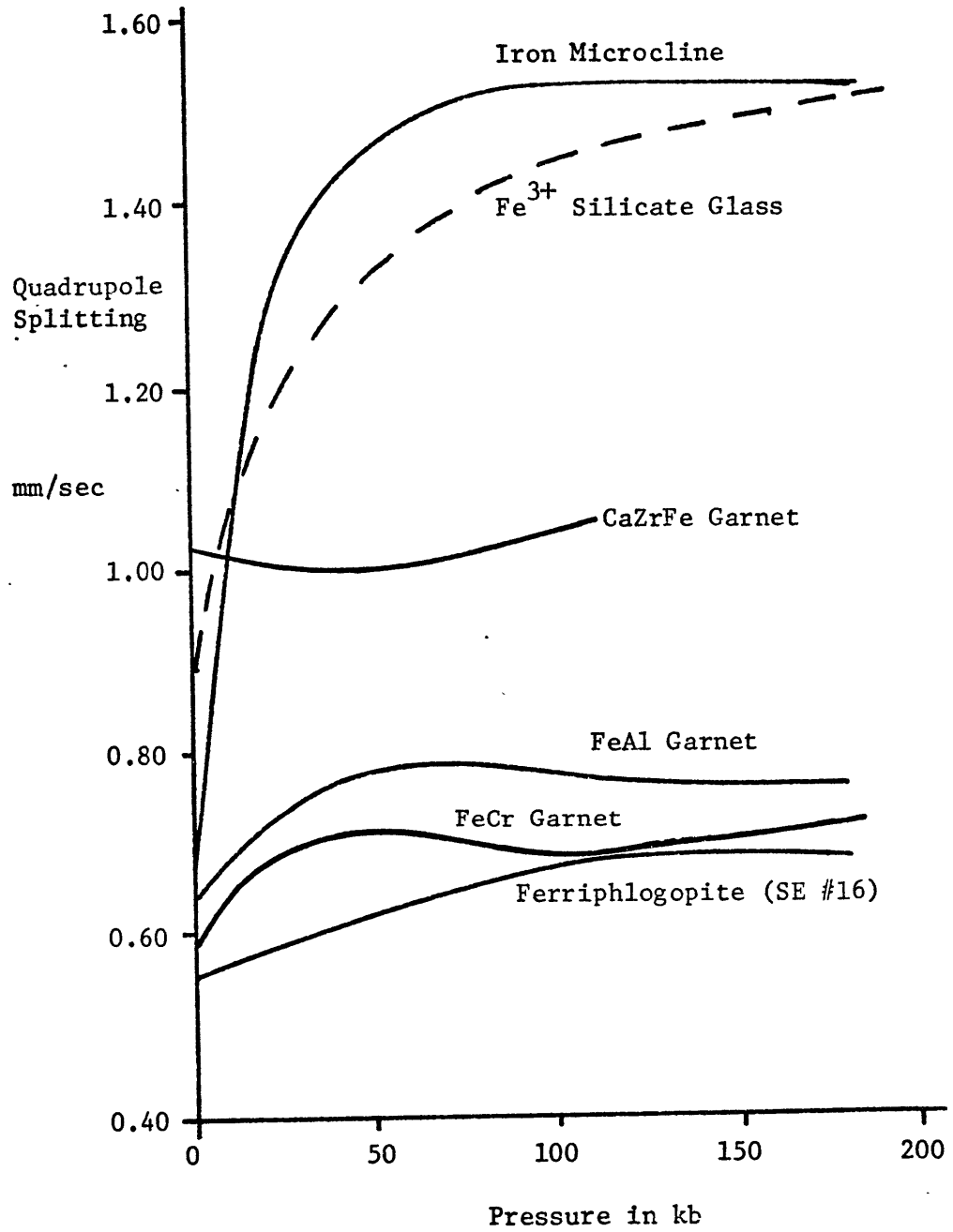


Figure 4.21

Summary of quadrupole splitting trends with pressure for ferric phases investigated in this study. Data for ferric silicate glass from Lewis and Drickamer (1968a).





(Travis, 1971):

$$V_{ij} = \sum_k q_k (3x_{ki}x_{kj} - r_k^2 \delta_{ij}) r_k^{-5} \quad 4.1$$

where  $q_k$  is the charge on the  $k^{\text{th}}$  ligand;  $x_{ki}$  is the  $i^{\text{th}}$  coordinate of the  $k^{\text{th}}$  ligand;  $r_k$  is the distance between the ferric cation and the  $k^{\text{th}}$  ligand; and  $\delta_{ij}$  is Kronecker's delta, which equals unity if  $i$  is equal to  $j$  and equals zero if  $i$  is not equal to  $j$ . To reach convergence, such summations generally have to be performed over spheres of considerable size (up to 100 Å) although more sophisticated methods of computation converge much faster (Artman, 1971). For this reason, except in certain very high symmetry cases, the quadrupole splitting can not be related unambiguously to specific changes in the positions of the ligands. It is possible, however, to estimate the quadrupole splitting trend if the compression were to occur so that the structure remains identical except for a scale factor. Such a change in structure requires that bond angles and ratios of one interatomic distance to another remain unaltered with pressure. If  $\langle r \rangle$  is an average Å distance in the structure, then:

$$\begin{aligned} r_k &= a_k \langle r \rangle \\ x_{ki} &= b_{ki} \langle r \rangle \end{aligned} \quad 4.2$$

and according to this mechanism of compression,  $a_k$  and  $b_{ki}$  are constants independent of pressure, which only changes the value of  $\langle r \rangle$ . Substituting in equation 4.1 leads to:

$$V_{ij} = \sum_k q_k (3b_{ki} b_{kj} - a_k^2 \delta_{ij}) a_k^{-5} \langle r \rangle^{-3} \quad 4.3$$

or, equivalently,

$$V_{ij} = A_{ij} \langle r \rangle^{-3} \quad 4.4$$

where  $A_{ij}$  is also independent of compression. The asymmetry parameter,  $\eta$ , is defined as:

$$\eta = \frac{V_{xx} - V_{yy}}{V_{zz}} = \frac{\langle r \rangle^{-3} A_{xx} - \langle r \rangle^{-3} A_{yy}}{\langle r \rangle^{-3} A_{zz}} \quad 4.5$$

Thus  $\eta = \frac{A_{xx} - A_{yy}}{A_{zz}}$  under compression at constant distortion and is independent of compression. The general equation (3.6) for quadrupole splitting becomes:

$$QS = \frac{eQA_{zz}}{2} (1 + \eta^2/3)^{1/2} \langle r \rangle^{-3} \quad 4.6$$

or, equivalently,

$$QS = k \langle r \rangle^{-3} = k' V^{-1} \quad 4.7$$

where  $k$  ( $k'$ ) is a constant independent of compression; and  $V$  is a characteristic volume of the solid. The pressure dependence of the quadrupole splitting is therefore inversely proportional to the change in volume with pressure.

Putting equation 4.7 in logarithmic form:

$$\ln QS = \ln k' - \ln V \quad 4.8$$

taking derivatives:

$$\left(\frac{\partial \ln QS}{\partial P}\right)_{T, \text{dist}} = - \left(\frac{\partial \ln V}{\partial P}\right)_T \quad 4.9$$

and so

$$\frac{1}{QS} \left(\frac{\partial QS}{\partial P}\right)_{T, \text{dist}} = - \frac{1}{V} \left(\frac{\partial V}{\partial P}\right)_T = \beta \quad 4.10$$

where  $\beta$  is the compressibility of the solid.

Although specific compressibility data are not available for phases of compositions found in this study, approximate values (Voight-Reuss-Hill averages) can be estimated from the compilation of Simmons and Wang (1971). For the ferric garnets, a value for the compressibility of  $0.7 \text{ mb}^{-1}$  can be assigned and the quadrupole splitting would be expected to increase by about 7% in 100 kb. For the octahedral ferric garnets the observed increase is initially much greater, suggesting that the structure distorts on compression in such a way as to increase the EFG at the ferric site. At higher pressures, the quadrupole splitting begins to decrease slightly, indicating perhaps that the structural changes at higher pressures decrease the EFG. On the other hand, for the tetrahedral ferric garnet,  $\text{Ca}_{2.5}\text{Zr}_{2.5}\text{Fe}_3\text{O}_{12}$ , there is virtually no change in quadrupole splitting with pressure, which may, fortuitously perhaps, reflect the predicted incompressible nature of tetrahedral sites (see Appendix A2.1). Therefore, in general, it appears that garnets violate the scheme of compression at constant distortion.

For both ferrimicrocline and ferriphlogopite, the values of compressibility may be estimated from the aluminum analogue data recorded by Simmons and Wang (1971). Values of about  $2.0 \text{ mb}^{-1}$  are appropriate for both

phases, which enables predictions of a 20% increase over 100 kb to be made. The change in ferriphlogopite quadrupole splitting is of this magnitude, whereas the change in ferrimicrocline is considerably greater. The agreement for ferriphlogopite must be fortuitous because it is well known that the linear compressibilities in the mica sheet and perpendicular to the sheet are greatly different, indicating that the constant distortion criterion can not be satisfied.

The quadrupole splitting trend for ferrimicrocline shows a huge increase in the first 50 kb, suggesting an equally impressive rearrangement of the atoms around the ferric cation or possibly a phase change. Whatever the transition may be, the final high pressure state must have a very asymmetric charge distribution around the ferric cation.

Correlations of quadrupole splitting trends with estimated site compressibilities (see Appendix A2.1) are even worse than with bulk compressibilities, since both octahedral and tetrahedral ferric site compressibilities are predicted to be considerably smaller than the bulk compressibilities of the phases considered here. Not only does this result give weight to the idea that, for ferric at least, the EFG at the iron nucleus is sensitive to ions considerably removed from the immediate coordination sphere, but also suggests that attempts to interrelate ferric quadrupole splittings to individual polyhedral distortions would not be a profitable exercise. In addition, it has recently been recognized that this model for the EFG at the nucleus should be modified in order to allow for further small contributions to the EFG arising from ligand electrons in the immediate coordination sphere which perturb the filled metal

orbitals (Artman, 1971 and references therein). The latter addition to the model appears to have cleared up a number of inconsistencies concerning EFG calculations, but it is computationally very complex. The non-inclusion of this factor should neither change the model of compression at constant structure developed in this section, nor the not-too-surprising conclusion that most ferric minerals do not undergo compression in that manner, based on the lack of correlation between compressibilities and ferric quadrupole splitting trends with pressure found in this study.

#### 4.3.4 Ferrous quadrupole splitting trends

The ferrous quadrupole splitting trends with pressure for minerals investigated in this study are summarized in figure 4.22. In order to adequately interpret these trends, it is necessary to understand the temperature dependence of ferrous quadrupole splittings as this is the basis for the most complete model for such parameters.

Ingalls (1964) developed a model for the quadrupole splittings of ferrous phases which depends on the covalency of the bonds ( $\alpha^2$ ), the spin-orbit coupling parameter ( $\lambda_o$ ), temperature (T) and the splittings of the lower 3d energy levels ( $\Delta_1, \Delta_2$ , which are defined in figure 4.20). Parametrically, the equation may be written as:

$$QS = QS_o \alpha^2 F \quad 4.11$$

where  $QS_o$  is the quadrupole splitting at absolute zero for an ideal ionic ferrous site; F is the difference between the lattice and valence contributions and is known as the reduction function:

$$F = F_{val}(\Delta_1, \Delta_2, \alpha^2, \lambda_o, T) - F_{lat} \quad 4.12$$

Figure 4.22

Summary of quadrupole splitting trends with pressure for ferrous phases investigated in this study.

Figure 4.22a. Trends for almandine, fayalite and  $\text{Fe}^{2+}$  in mica (SE #16).

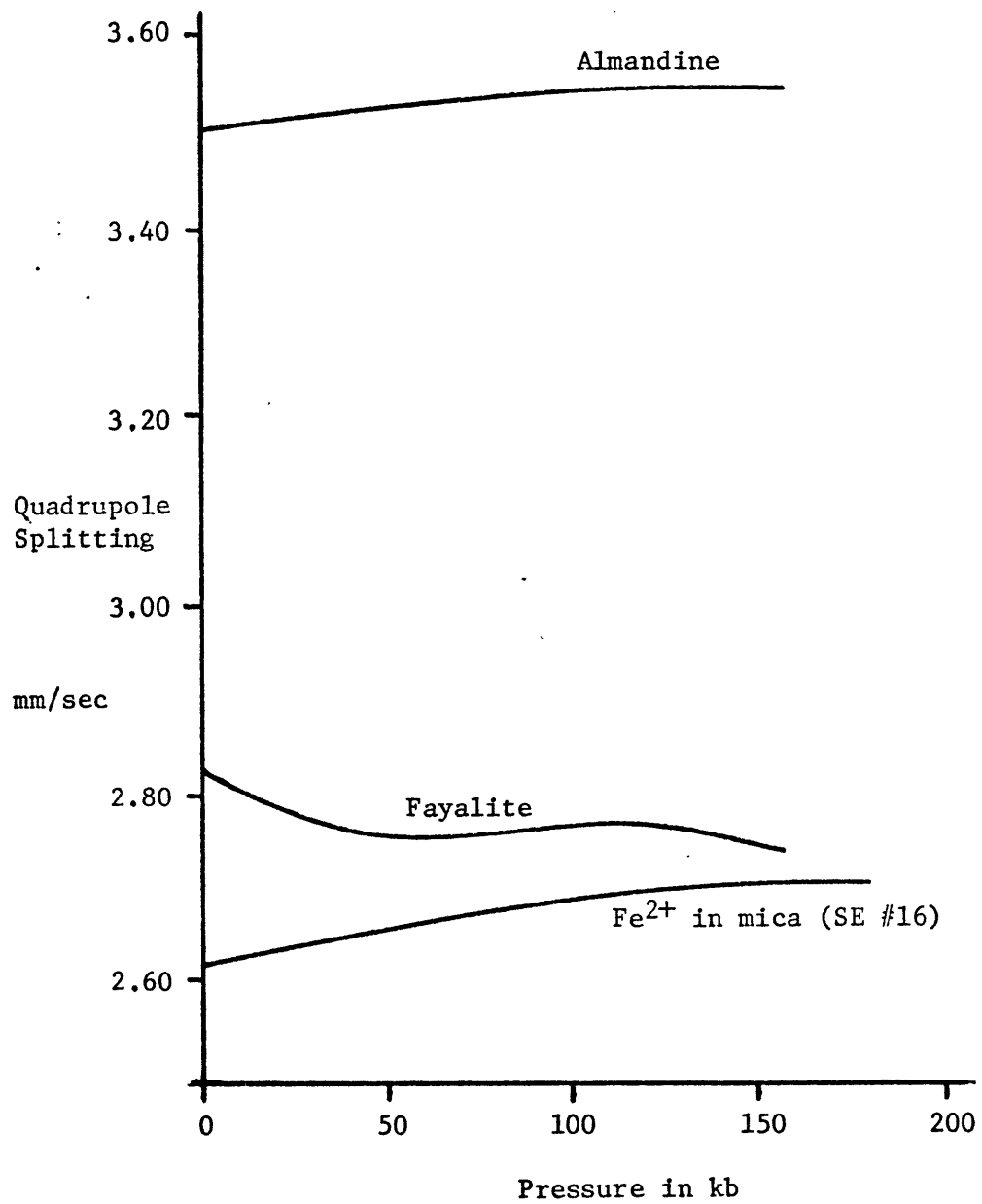
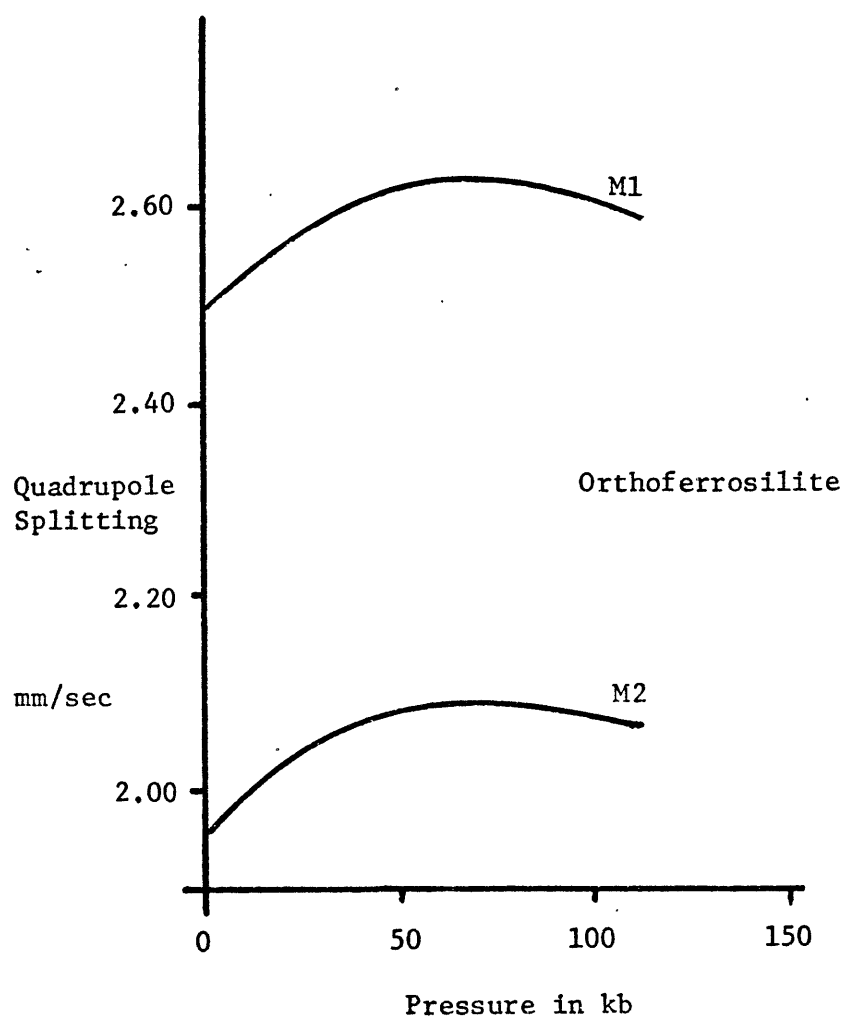




Figure 4.22  
(continued)

Figure 4.22b. Trends for the M1 and M2 sites in orthoferrosilite.



For the purposes of this study:

$$\text{at } 0 \text{ } ^\circ\text{K} \quad \text{QS}_0'' = \text{QS}_0 \alpha^2 \quad 4.13$$

where  $\text{QS}_0' = \text{QS}_0''(1 - F_{\text{lat}})$ ;  $\text{QS}_0'$  is the measured quadrupole splitting at absolute zero,<sup>1</sup> and  $\text{QS}_0''$  is the valence portion of the quadrupole splitting at absolute zero for the ferrous phase in question. Following the suggestion made by Bancroft (1974), the role of  $\alpha^2$  and  $\lambda_0$  in determining the valence contribution to the reduction function will be ignored. These simplifications lead to an easily manipulated form of equation 4.12:

$$\text{QS} = \text{QS}_0''(F_{\text{val}}(\Delta_1, \Delta_2, T) - F_{\text{lat}}) \quad 4.14$$

Since ferric quadrupole splittings are usually independent of temperature, it is a safe assumption that  $F_{\text{lat}}$  will also be independent of temperature. Therefore, the temperature dependence of ferrous quadrupole splittings comes solely from the valence contribution and is due to the Boltzmann

---

<sup>1</sup> $\text{QS}_0'$  differs from  $\text{QS}_0$  by including both the covalency difference and the lattice contribution. The latter contribution for explaining differences between values of  $\text{QS}_0'$  for different ferrous compounds has generally been ignored and such differences have often been attributed only to covalent effects (Shenoy et al., 1969; Hazony, 1971). By ignoring such contributions, which may be quite appreciable (Nozik and Kaplan, 1967), erroneous interpretations can be made concerning the covalency differences between different ferrous iron species. This may well be the case in the study of orthoferrosilite (Shenoy et al., 1969) where there is a large difference in degree of distortion comparing the two ferrous octahedral sites which could easily give rise to a large difference in the lattice contribution of  $\text{QS}_0'$  for the two sites. The conclusion which Shenoy et al. reached, that the M2 site was more covalent than the M1 site on the basis of its lower value of  $\text{QS}_0'$  should be reexamined.

distribution of the sixth 3d electron over the two or three lower energy levels. For tetrahedral or eight-coordinate sites, the explicit expression for the valence contribution is (Ingalls, 1964):

$$F_{\text{val}}(\Delta_1, T) = \frac{1 - \exp(-\Delta_1/kT)}{1 + \exp(-\Delta_1/kT)} \quad 4.15$$

For octahedral sites, the expression is:

$$F_{\text{val}}(\Delta_1, \Delta_2, T) = \frac{[1 + \exp(2x) + \exp(2y) - \exp(x) - \exp(y) - \exp(x+y)]^{1/2}}{1 + \exp(x) + \exp(y)} \quad 4.16$$

where  $x = -\Delta_1/kT$  and  $y = -\Delta_2/kT$ . Various aspects of these equations are plotted in figure 4.23a,b.

Since  $\Delta_1$  and  $\Delta_2$  are not generally expected to change significantly compared to  $T$ , the temperature dependence of the quadrupole splitting is often fitted to equations 4.15 or 4.16 to evaluate the lower level splittings, assuming that these energy level splittings are constant over the complete temperature range. Such an assumption negates, for the most part, any sophistication of this approach by attempting to allow for the small effects of  $\lambda_0$  and  $\alpha^2$  on the valence contribution.

The pressure dependence of ferrous quadrupole splittings at constant temperature comes about from changes in  $\Delta_1$ ,  $\Delta_2$  and  $F_{\text{lat}}$  with pressure:

$$QS(P) = QS(T)[F_{\text{val}}(\Delta_1(P), \Delta_2(P), T) - F_{\text{lat}}(P)] \quad 4.17$$

Depending on the value of  $\Delta_1$  and  $\Delta_2$ , the quadrupole splitting may be very sensitive or insensitive to values of  $\Delta_1$  and  $\Delta_2$ . For instance, at low distortion where  $\Delta_1$  and  $\Delta_2$  are small, the quadrupole splitting should be

Figure 4.23

Two aspects of Ingalls' model for the quadrupole splitting of ferrous phases are shown. In the simplified model developed here, the temperature dependence of the quadrupole splitting is fitted to values of the lower 3d level splittings. The reduction function,  $F$ , is directly proportional to the quadrupole splitting and is the difference between the valence contribution and lattice contribution. Only the valence contribution is dependent on temperature. This dependence is described by equations 4.15 and 4.16.

Figure 4.23a. The effect of distortion on the reduction function at constant temperature.

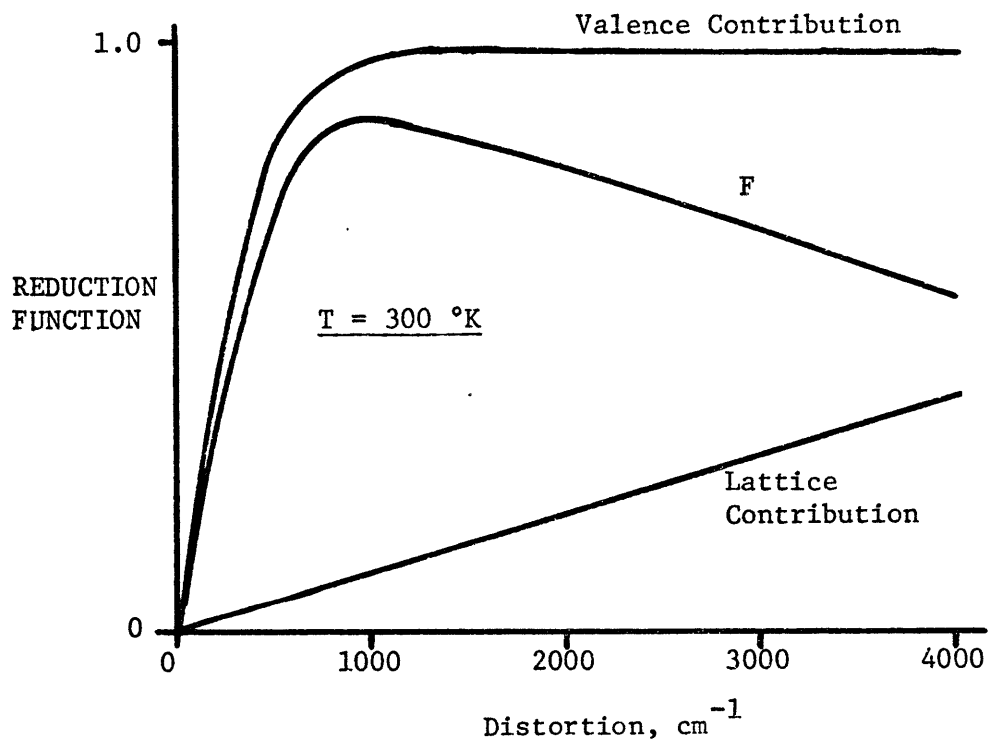
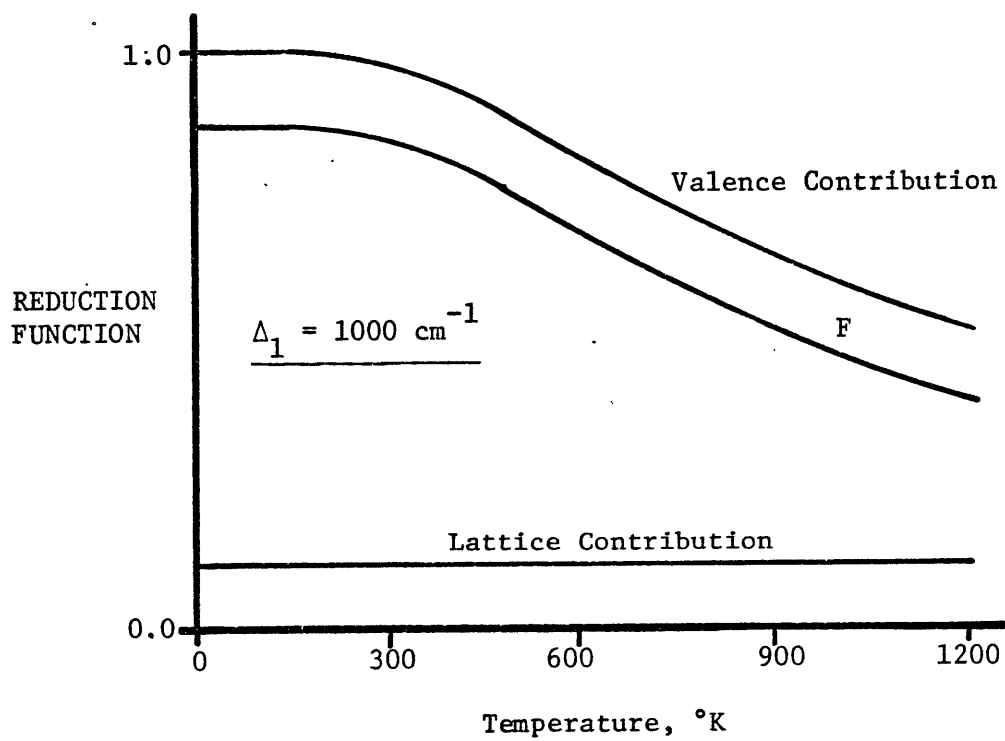


Figure 4.23  
(continued)

Figure 4.23b. The effect of temperature on the reduction function at constant value of the lower level splitting,  $\Delta_1$ .





very sensitive to changes in these parameters, whereas at high distortion the quadrupole splitting should reflect changes in  $F_{1at}$  only since  $F_{val}$  is virtually independent of distortion (see figure 4.23a). Therefore, in order to know which factor is dominant in determining the pressure sensitivity of quadrupole splitting, it is necessary to determine the values of  $\Delta_1$  and  $\Delta_2$  from the temperature dependence of the quadrupole splitting by means of either equation 4.15 or equation 4.16. Some phases of mineralogical interest, the quadrupole splittings of which have been measured as a function of temperature, are listed in table 4.15. In order to calculate values for  $\Delta_1$  and  $\Delta_2$ , where only the data were presented (usually only graphically), the program listed in Appendix A3.2 was used to tabulate values of  $F_{val}$  for values of  $\Delta_1$ ,  $\Delta_2$  and T using equations 4.15 and 4.16. The raw data were normalized by first estimating  $QS'_0$  for the phase from the data and then dividing each datum point by  $QS'_0$  to give  $F_{val}(T)$  values. These values were then compared to the tabulation of calculated  $F_{val}(T)$  values and the best fit to the data gave the values of  $\Delta_1$  and  $\Delta_2$ . The values estimated in this way are accurate to within  $\pm 5\%$ . The largest uncertainty concerns the value of  $F_{1at}$ , which is unknown. Fits, which include this parameter, were achieved by adding  $F_{1at}$  to each quadrupole splitting datum point before normalization to give  $F_{val}(T)$  values. Fortunately, the value of  $F_{1at}$  should usually be no more than about 15% of  $F_{val}$  (Ingalls, 1964; Nozik and Kaplan, 1967) and the values of  $\Delta_1$  and  $\Delta_2$  are generally not greatly influenced by  $F_{1at}$ , as the following discussion of quadrupole splitting trends for individual minerals will show. More sophisticated techniques could be envisaged for analyzing the data, but in the absence of the numerical data,

Table 4.15

VALUES OF LOWER ENERGY LEVEL SPLITTINGS CALCULATED FROM THE TEMPERATURE DEPENDENCE OF THE QUADRUPOLE SPLITTING FOR FERROUS PHASES OF MINERALOGICAL INTEREST

PHASE	T RANGE FOR DATA (°K)	SITE	$\Delta_1$	$\Delta_2$	$F_{lat}$ MM/SEC	REF DATA	REF CALCULATION
Fayalite, $Fe_2SiO_4$	77 - 1200	6A	1500	710	0.45	2	1
		6B	1400	630	0.30		
Almandine	77 - 850	8	1100	--	0.30	3	1, 3
Mica	77 - 370 <sup>1</sup>	6	<500 <sup>2</sup>	<500 <sup>2</sup>	--	4	1
Orthopyroxene, $Fs_{87}En_{13}$	4 - 300 <sup>1</sup>	6 M1	1000	350	0.0	5	1
		6 M2	1200<	1200<	--		
Ilmenite	80, 300, 420	6	200	0	0.0	6	6
$FeF_2$	95 - 700	6	900	800	0.0	7	7
$Fe_2GeO_4$ (Spinel)	77 - 1040	6	1050	1050		8	8
	77 - 1040		1150	1150		9	9

<sup>1</sup>Data insufficient to be highly accurate.

<sup>2</sup>Limited data suggest  $\Delta_1$ ,  $\Delta_2$  decrease markedly with temperature.

Table 4.15  
(continued)

References:

- |                                  |                                 |
|----------------------------------|---------------------------------|
| (1) Present Study                | (6) Bashkirov et al. (1967)     |
| (2) Eibschutz and Ganiel (1967)  | (7) Ganiel and Shtrikman (1969) |
| (3) Lyubutin and Dodokin (1971b) | (8) Sinha and Sinha (1968)      |
| (4) Annersten (1974)             | (9) Eibschutz et al. (1966)     |
| (5) Shenoy et al. (1969)         |                                 |

it was felt that such additional procedures would not be of any great value.

Having obtained values for these lower level energy splittings at zero pressure, the pressure dependence of the quadrupole splittings of the ferrous phases investigated in this study, which are shown in figure 4.22, could now be explained.

For almandine, a value of between 1050 and 1200  $\text{cm}^{-1}$  for  $\Delta_1$  was determined from the data of Lyubutin and Dodokin (1971b). The range of values is to allow for a lattice contribution to the quadrupole splitting of up to 1 mm/sec. However, since the original value of the quadrupole splitting is so large (within 8% of the largest ferrous quadrupole splitting ever recorded), the lattice contribution is, in all probability, quite small ( $< 0.30$  mm/sec) and the value of  $1100 \pm 50 \text{ cm}^{-1}$  was assigned to  $\Delta_1$ . This value plots just to the high distortion side of the maxima in figure 4.23a and suggests that the observed small increase in the quadrupole splitting of almandine with pressure comes about from a slight decrease in the lattice contribution to the EFG, presumably from a decrease in the site distortion.

For fayalite, values of  $620 \pm 20 \text{ cm}^{-1}$  for  $\Delta_2$  and  $1400 \pm 200 \text{ cm}^{-1}$  for  $\Delta_1$  for one octahedral site and  $710 \pm 20 \text{ cm}^{-1}$  for  $\Delta_2$  and  $1500 \pm 200 \text{ cm}^{-1}$  for  $\Delta_1$  for the other site, assuming a small lattice contribution of 0.30-0.45 mm/sec, were estimated from the data of Eibschutz and Ganiel (1967).

Although pressure did not resolve the two contributions any better than the spectrum at ambient conditions, the decrease in separation of the two components of the spectrum suggested that the values of  $\Delta_1$  and  $\Delta_2$  for both sites were decreasing. Since  $\Delta_2$  has more influence on the quadrupole

splitting, the assumption is made that fayalite plots on the low distortion side, but rather close to the maximum. A decrease of about 10% in all three parameters,  $\Delta_1$ ,  $\Delta_2$  and  $F_{1at}$  for both sites over 150 kb would explain the quadrupole splitting trend. However, this is obviously not a unique result, since the three parameters may vary independently and the trend is only sufficiently accurate to require that  $\Delta_2$  decrease by about this amount. As for the changes in value of  $\Delta_1$  and  $F_{1at}$ , which have much less influence on the value of the quadrupole splitting, nothing definitive can be written. Although the data are not conclusive, the decrease in the energy level splittings suggests a change in site distortion towards a more regular site, which is consistent with the results obtained by Abu-Eid (1974) from changes of energies of the absorption spectral peaks of the fayalite M1 site with pressure.

For ferrous in ferriphlogopite, an increase in quadrupole splitting with pressure is observed. The limited data presented by Annersten (1974) suggest that all ferrous splittings of the  $t_{2g}$  levels in phlogopite are less than  $500 \text{ cm}^{-1}$  and that they decrease with increasing temperature. The pressure trend may therefore be explained by an increase in these splittings with pressure resulting from an increase in site distortion. Since micas are much more compressible perpendicular to the sheets in the structure, the octahedral sites, which are already compressed along a pseudo-trigonal axis approximately perpendicular to the sheets (Hazen and Burnham, 1973), would appear to become even more compressed in this direction at high pressure.

For the Manchurian orthoferrosilite, some limited quadrupole splitting

data as a function of temperature are available (Shenoy et al., 1969) which suggest that the values of  $\Delta_1$  and  $\Delta_2$  are  $1000 \pm 100 \text{ cm}^{-1}$  and  $350 \pm 50 \text{ cm}^{-1}$  respectively for the M1 site and that  $\Delta_1$  and  $\Delta_2$  are both greater than  $1250 \text{ cm}^{-1}$  for the M2 site. The M1 site, therefore, falls on the low distortion side of the maximum in plots of quadrupole splitting against distortion, similar to that shown in figure 4.23a. The M2 site, on the other hand, falls on the high distortion side. The abrupt increase in quadrupole splitting for both sites between 0 kb and 55 kb suggests that the M1 site is more distorted whereas the M2 site is less distorted at 55 kb than at 0 kb. A 25% increase in the values of  $\Delta_1$  and  $\Delta_2$  for the M1 site could explain the quadrupole splitting change for this site. As for fayalite, this is not a unique result, however. The M2 quadrupole splitting change over this pressure interval can be explained by a decrease of 0.15 mm/sec in  $F_{1at}$ . However, changes in  $\Delta_1$  and  $\Delta_2$  can not be estimated for this site. These changes suggest that a significant rearrangement of the crystal structure of this pyroxene may have occurred between 0 and 55 kb, possibly involving an increase in the effective coordination number of the M2 site to explain the anomalous isomer shift trend with pressure for this site.

Quadrupole splitting data as a function of pressure have also been reported for the mineral ilmenite,  $\text{FeTiO}_3$  (Vaughan and Drickamer, 1967a). Quadrupole splitting data as a function of temperature are also available for ilmenite (Bashkirov et al., 1967) which indicate that  $\Delta_1 \approx 200 \text{ cm}^{-1}$  and  $\Delta_2 = 0 \text{ cm}^{-1}$ . Ilmenite shows a large increase in the quadrupole splitting with pressure which is best explained by an increase in  $\Delta_1$  from 200 to about  $1000 \text{ cm}^{-1}$  over the pressure range from zero to 75 kb. The ferrous

site in ilmenite is compressed along the trigonal axis and pressure, therefore, must increase the distortion suggesting that the ratio of unit cell axes,  $c/a$ , is decreasing with pressure. X-ray data obtained by Liu et al. (1974) do indeed show a decrease in the  $c/a$  ratio. The mechanism proposed by Liu et al. (1974) to explain the change in  $c/a$  ratio with pressure is neither proven nor disproven by this result. The fact that the quadrupole splitting levels off at high pressure at a value of 1.50 mm/sec, which is the same as  $QS'_O$  for this compound, suggests that the lattice contribution is small and insensitive to the distortion of the site.

Throughout this discussion  $\alpha^2$  has been assumed to be independent of pressure and the justification for this assumption is now presented. Firstly, most ferrous compounds show an increase in quadrupole splitting with pressure and if changes in  $\alpha^2$  with pressure were significant, which would be expected to decrease the quadrupole splitting, most ferrous compounds ought to show the opposite trend. Secondly, the fact that the data for ilmenite can be fitted to the crystal-field model and the quadrupole splitting at high pressure (where  $F_{val} \approx 1$ ) is exactly the same as  $QS'_O$ , suggests that  $\alpha^2$  can not have changed. Note that in ilmenite, the increase in site distortion with pressure should lead to an increase in  $F_{lat}$  which should also decrease the quadrupole splitting. Therefore, changes in  $F_{lat}$  and  $\alpha^2$  can not be compensating, and the only explanation appears to be that such parameters do not change significantly with pressure in ilmenite.  $\alpha^2$  is a crude measure of  $\langle r^{-3} \rangle$ , the radial extent of the 3d orbital occupied by the sixth electron (Hazony, 1971) and these results suggest that  $\langle r^{-3} \rangle$  does not change significantly with pressure. The isomer shift trends with pressure, on the

other hand, do suggest that significant changes are taking place in the bonding and this apparent paradox will be discussed in section 4.3.7. A test of the constancy of  $\alpha^2$  and  $F_{lat}$  with respect to pressure could only be made by carrying out high pressure studies at very low temperatures. No change in the value of  $QS'_0$  with pressure could be taken as evidence that  $\alpha^2$  and  $F_{lat}$  are independent of pressure.

#### 4.3.5 Changes in $Fe^{2+}/Fe^{3+}$ ratio with pressure

The main emphasis of the research carried out by Drickamer and his group at the University of Illinois concerned the changes in the Mössbauer  $Fe^{2+}/Fe^{3+}$  ratio as a result of pressure. Examples of changes in the valence state ratio from zero to 4 or 5 over 200 kb may be found in their studies (Drickamer et al., 1970; Drickamer and Frank, 1973). This phenomenon was discussed in some detail in section 2.3.3 (b) and was explained as resulting from an electron transfer from the ligands to the central ferric cation leading to a new electronic ground state involving ferrous cations and some unspecified radical anion species. Since the iron is monitored by Mössbauer spectroscopy and the formation of ferrous at the expense of ferric is observed directly, the phenomenon has been described as "pressure-induced reduction" although "pressure-induced electron transfer" would be a more accurate description. In one sense, this phenomenon is similar to a disproportionation reaction, since changes of valence state are involved and, apart from pressure and temperature, it appears to be independent of conditions external to the phase (Drickamer and Frank, 1973). However, disproportionation reactions are not true redox reactions, since there is no net loss or gain of electrons, so that pressure-induced



electronic transitions should not be regarded as true redox reactions.

The systematic study of Frank and Drickamer (1972) showed that the extent of this change in electronic ground state with pressure was related to the electron-donor properties of the surrounding ligands. Furthermore, the degree of conversion of ferric to ferrous can be correlated with the change in isomer shift, which also depends on the electron-donating properties of the ligands. More detailed theoretical aspects of this electronic transition have been presented by Slichter and Drickamer (1972) and Drickamer et al. (1972).

The investigations carried out at Illinois were mostly of indirect mineralogical interest and the ferric phases which were of direct interest, such as hematite and ferric-containing silicate glass, showed no signs of the formation of ferrous by the charge transfer process.

Except for magnesioriebeckite (Burns et al., 1972b) and the FeCr garnet (see section 4.2 (b)) only very small increases in  $\text{Fe}^{2+}/\text{Fe}^{3+}$  ratio with pressure have been observed in silicate minerals studied at room temperature. Since most of these silicates already contained a minor amount of ferrous in addition to ferric at ambient conditions, two further factors must be discussed before the changes in valence state ratio can be ascribed to the charge transfer process.

The first of these factors is the possible change in the recoil-free fraction,  $f$ , of the different iron species with pressure. Equations 3.1 and 3.2 are expressions for  $f$  and, since the parameters  $\langle x^2 \rangle$  and  $\theta_D$  depend on the vibrational spectrum of the solid, changes in  $f$  with pressure can be expected which will reflect pressure-induced changes in the vibrational

frequencies of the solid, especially those related to the cation sites. Whipple (1973) has demonstrated that within the same mineral phase, the ferrous recoil-free fraction may be smaller than the ferric recoil-free fraction by as much as 25%. For example, he found that  $f(\text{Fe}^{2+}, \text{VIII})/f(\text{Fe}^{3+}, \text{VI}) \approx 0.77$  for the garnet structure at 25 °C. Other investigators have also shown that the coordination number and valence state determine the recoil-free fraction at 25 °C (Lyubutin et al., 1970, 1971a, 1971b; Sawatzky et al., 1969). With increasing pressure, absolute values of recoil-free fractions increase towards unity since Debye temperatures increase with pressure. For this reason, ratios of recoil-free fractions will also tend to unity, which will lead to an increase in the observed  $\text{Fe}^{2+}/\text{Fe}^{3+}$  ratio with pressure as the ferrous recoil-free fraction can be expected to increase faster. In principle, increases in the valence state ratio of up to 25% might be expected. The micas in particular showed quite large increases of  $\text{Fe}^{2+}/\text{Fe}^{3+}$  ratio with pressure which can probably be attributed to this phenomenon.

The second factor is related to thick absorber phenomena. When the amount of  $^{57}\text{Fe}$  in a Mössbauer sample is too great, the area under the peak no longer bears a linear relationship to the amount of  $^{57}\text{Fe}$  in the phase. Instead, self absorption effects cause the amount of  $^{57}\text{Fe}$  to be underestimated. As the ferrous absorptions are generally small in these studies of the pressure-induced charge transfer process in ferric silicates, they approach thin absorber behavior more closely than the ferric absorptions. Therefore, as the deviation from ideal thin absorber behavior increases, the apparent  $\text{Fe}^{2+}/\text{Fe}^{3+}$  ratio would be expected to increase in these phases

containing small amounts of ferrous iron (figure 4.24).

The combination of both these factors occurring at the same time could lead to significant changes in the Mössbauer  $\text{Fe}^{2+}/\text{Fe}^{3+}$  ratio in these ferric phases containing small amounts of ferrous iron. Except for magnesio-riebeckite and the iron-chromium garnet (which contained virtually no ferrous iron (VI) originally) all changes in  $\text{Fe}^{2+}/\text{Fe}^{3+}$  ratio observed in studies of ferric silicates are smaller than the uncertainties introduced by such factors. Therefore, it is unlikely that pressure-induced reduction occurs at room temperature and at pressures below 200 kb for ferrimicrocline, ferriphlogopite, FeAl garnet, and Ito's CaZrFe garnet. In addition, Vaughan and Tossell (unpublished results) found no signs of reduction in acmite and andradite under the same conditions. Although broadening may result in poor resolution, it is unlikely to obscure emerging ferrous features since at least one peak of the ferrous absorption occurs outside the region of ferric absorption.

The effect of temperature has been shown to assist the charge transfer process and to increase the amount of ferrous formed at the expense of ferric (Drickamer et al., 1970). For this reason, experiments were carried out at a pressure of about 100 kb and at temperatures of 57 °C and 88 °C on FeCr garnet, which showed emerging peaks with increasing pressure. At room temperature, at 100 kb, the emerging absorption constituted only about 10% of the absorption which increased to about 20% at 88 °C. This doublet is obviously neither due to thick absorber complications nor to the change in recoil-free fraction since no appreciable absorption was present originally. The most reasonable explanation appears to be that this

Figure 4.24

The relationship between Mössbauer absorption and iron concentration in the Mössbauer sample is shown schematically.

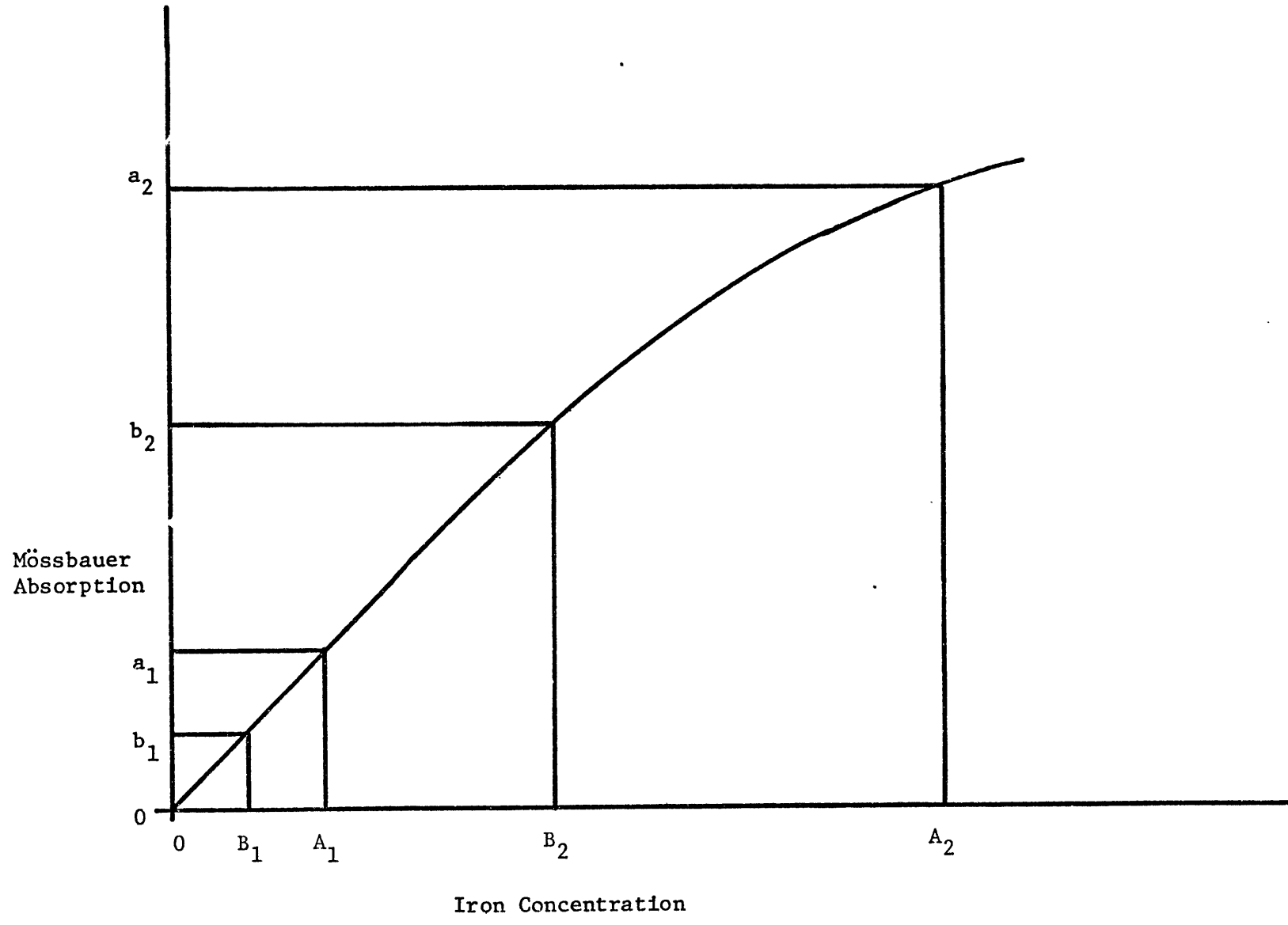
As the concentration of iron increases, the Mössbauer absorption increasingly deviates from a linear relationship with the iron concentration due to self absorption of  $\gamma$ -rays by the iron in the sample. Consequently, the Mössbauer absorption underestimates the iron concentration in the sample, if estimated using a linear relationship. At low iron concentration where there is a linear relationship, the absorber is described as being "thin." At high iron concentration, conversely, the absorber is described as "thick."

Considering the values on the graph, the Mössbauer absorption and iron concentration have the following relationships:

$$\frac{a_1}{A_1} = \frac{b_1}{B_1} \quad (\text{thin absorber})$$

$$\frac{a_2}{A_2} < \frac{b_2}{B_2} \quad (\text{thick absorber})$$

The latter relationship describes the phenomenon most commonly encountered in this study of the augmentation of a small ferrous absorption ( $b_2, B_2$ ) relative to a large ferric absorption ( $a_2, A_2$ ) due to thick absorber effects in the high pressure geometry.



is ferrous (VI) formed by pressure (and temperature) induced electron transfer from the ligands to ferric (VI) as discussed in section 4.2.1 (b).

Temperature appears, therefore, to play a critical role in addition to pressure in controlling the electron transfer process in minerals. Thus at pressures and temperatures appropriate to mantle conditions, the new electronic ground state may be extensive in nominally ferric minerals.

Attempts to use the valence state ratio-isomer shift correlation for ferric silicates, according to the scheme of Frank and Drickamer (1972), are obviously not appropriate, suggesting that such correlations must be restricted to given ligand types. The reasons why the electron transfer occurs in ferric silicates to such a small extent compared to the organoferric compounds must be attributed to differences in site compressibilities and poor electron-donor ability of the oxygen ligands in silicates.

Magnesioriebeckite, which shows the largest pressure-induced change in  $Fe^{2+}/Fe^{3+}$  ratio of any silicate at room temperature, contains some ferric in the hydroxylated site of the amphibole structure. Such sites are expected to be more compressible than the non-hydroxylated ferric sites most commonly found in silicates and may explain why the largest change in valence state ratio is seen with this phase.

The question of why the charge transfer phenomenon occurs with FeCr garnet, but not with other garnets, must also be answered. In section 2.3.3 (b) a survey of the pressure-induced reduction phenomena in the compounds which Drickamer and his co-workers have studied suggested that pressure-induced reduction occurs most easily when, firstly, the ferric concentration is small and, secondly, when the coordination site is large. No

evidence for reduction has yet been observed for ferric in tetrahedral coordination by oxygen in silicates and oxides. When comparing andradite, FeCr garnet and FeAl garnet, pressure-induced reduction may be inhibited in andradite due to a larger ferric concentration relative to FeCr garnet and also in FeAl garnet since the average size of the octahedral site relative to FeCr garnet is smaller. The data for garnets are qualitatively in agreement with the requirements deduced from analysis of all the data on pressure-induced reduction. However, they can not be seriously considered as proving this point and more work is obviously needed on these systems. It is also interesting to point out that the isomer shift decrease with pressure is larger for FeCr garnet than for FeAl garnet or andradite, which is qualitatively in agreement with the results of Frank and Drickamer (1972) who found that the largest decrease in isomer shift also correlated with the largest increase in  $Fe^{2+}/Fe^{3+}$  ratio for the ferric  $\beta$ -diketone complexes.

#### 4.3.6 Changes in magnetism of oxides and silicates with pressure

Only very small changes have so far been observed in the magnetic properties of oxides at pressures up to 200 kb at 25 °C and no pressure-induced magnetic effects have been encountered in similar experiments with iron silicates, which remain paramagnetic.

With hematite, a reduction in the magnetic field strength of 1% over 200 kb and a change in the sign of the quadrupole splitting at about 30 kb have been observed (Vaughan and Drickamer, 1967a). The magnetic field strength in magnetite also does not appear to change much, but the tetrahedral and octahedral magnetic subpatterns may lose some resolution with

increasing pressure.

Compared to the changes in magnetism of iron sulphides with pressure, such changes are minimal. Vaughan and Tossell (1973) reported that the application of 50 kb<sup>1</sup> completely eliminates the magnetism in chalcopyrite and pyrrhotite, while Kasper and Drickamer (1968) reported that application of 36 kb eliminates the magnetism in troilite. These results suggest that sulphides become paramagnetic at high pressure. Work on pyrite (Vaughan and Drickamer, 1967b) up to 200 kb confirms that this phase remains diamagnetic at high pressures as well.

The difference between sulphides and oxides with respect to their magnetic behavior at high pressures must be a function of compressibility and electronic differences, which permit the oxides to retain magnetic coupling between iron sites in oxides while quenching the magnetic coupling between iron sites in sulphides. Except for pyrite, the other three sulphides and the two magnetic oxides mentioned in this discussion all contain high spin cations and a change in spin state of the iron cations was postulated by Vaughan and Tossell (1973) as one possible mechanism to explain the paramagnetism of the sulphides at high pressure. Such spin state transitions should not occur in oxides until considerably higher pressures are attained and the phenomenon would appear to be a good candidate for

---

<sup>1</sup>The pressure given here differs from that given in the paper by Vaughan and Tossell (1973) due to a computational error in their calibration of the pressure scale. Their reported pressures are approximately 3 times too small. The pressure calibration for the paper on magnesioriebeckite, Burns et al. (1972b), is also in error for the same reason.



explaining this difference between oxides and sulphides in their magnetic behavior at high pressure. There are data for the  $\text{Fe}^{2+}$  high spin-low spin transition in  $\text{MnS}_2$  containing 2%  $\text{Fe}^{2+}$ , which show that the low spin state is obtained completely at 130 kb, although only about 10% of the ferrous iron was in the low spin state at zero pressure (Bargeron et al., 1971). Unfortunately,  $\text{MnS}_2$  ( $\text{Fe}^{2+}$ ) is paramagnetic at low pressure and, therefore, the high spin-low spin transition in this phase does not involve a magnetically split spectrum. For this reason, no direct correlation can be made between this spin state change and the disappearance of the magnetically split spectrum found in other sulphides. The changes in isomer shift for both pyrrhotite and troilite are consistent with a spin state change and, in addition, the octahedral coordination of the ferrous ions in these phases is also favorable for spin state changes. However, the isomer shift change with pressure of chalcopyrite would appear to be inconsistent with a spin state change.

In summary, iron silicates remain paramagnetic up to at least 200 kb; iron oxides remain magnetic with very little change in parameters over the same range. For the sulphides, pyrite,  $\text{FeS}_2$ , remains diamagnetic up to 200 kb, while magnetic sulphides become paramagnetic at high pressure. The evidence appears to favor a high spin to low spin change in both troilite and pyrrhotite, while chalcopyrite may undergo some other transition, perhaps a structural change to the  $\text{CuFeO}_2$  structure-type.

#### 4.3.7 Pressure-induced changes in isomer shifts and quadrupole splittings and their relation to the covalency of ferrous-ligand bonds

As was indicated earlier (sections 4.3.1 and 4.3.4) and

elsewhere (Hazony, 1971), the Mössbauer parameters, isomer shift and quadrupole splitting, can both be related to the covalency of the ferrous-ligand bond. However, although the isomer shift values of ferrous phases appear to decrease systematically with pressure, indicating an increase in covalency, no such systematic change is observed for the quadrupole splitting to indicate an increase in covalency. This is somewhat disconcerting and paradoxical at first sight, especially since the quadrupole splitting appears to show a much larger range of value for ferrous compounds than the isomer shift.

The answer to this problem lies in recognizing exactly what each parameter measures in terms of covalent interactions. The ferrous quadrupole splitting is principally determined by the behavior of the sixth 3d electron, which is of opposite spin to the other five. This electron lies in the 3d orbital which has the least interaction with the ligand orbitals or electrons. On the other hand, the isomer shift is principally determined by the screening of s electrons from the nucleus by all six 3d electrons. Therefore, the quadrupole splitting relates only to the covalency of one 3d orbital: that of least interaction with the ligands, whereas the isomer shift relates to the covalency of all five 3d orbitals, including those which interact much more strongly with the ligands.

For an octahedrally coordinated ferrous cation this analysis implies that the quadrupole splitting is sensitive only to the behavior of one of the  $t_{2g}$  levels, whereas the isomer shift is sensitive to both the  $t_{2g}$  levels and the  $e_g$  levels. In most molecular orbital treatments such  $t_{2g}$  levels are regarded as non-bonding (Tossell et al., 1974) which means they are

essentially localized on the cation and have minimal interaction with the ligand orbitals, while the  $e_g$  levels are slightly anti-bonding and interact more strongly with the ligands.

The difference, therefore, between the change in covalency with pressure as indicated by variations of isomer shift and quadrupole splitting must be due to the fact that the  $e_g$  levels become more covalent by overlapping with the ligand orbitals whereas the lowest  $t_{2g}$  level does not overlap significantly differently with the ligand orbitals at high pressure than at zero pressure. In view of the non-bonding nature of the  $t_{2g}$  orbitals in an octahedral complex, the minimal change in interaction with the ligand orbitals would appear to be quite acceptable for these changes in pressure.

This result has a number of interesting ramifications:

1. The energy of non-bonding cation orbitals can be expected to stay approximately constant in energy over 200 kb. The slightly anti-bonding cation orbitals, which interact more strongly with ligands, become less stable (more anti-bonding) in energy with pressure.
2. The compression of a ferrous cation proceeds mostly through the upper 3d orbitals and has a much smaller effect on the lower 3d orbitals. The pressure-induced decreases in isomer shift and also in the Racah parameter, B, which result from an increase in covalency, are due less to an expansion of the d orbitals, but more to an increase in interaction with the ligand orbitals. This fact results from the lack of

expansion of the  $t_{2g}$  orbitals indicated by the quadrupole splitting changes with pressure, and suggests that compression does not increase the size of the 3d orbitals.

3. The isomer shift, as a measure of covalency, bears a resemblance to the Racah parameter,  $\beta_{35}$ , while the quadrupole splitting, as a measure of covalency, bears a resemblance to  $\beta_{55}$  or  $\beta_{33}$ . Lever (1968) describes these different Racah parameters:  $\beta_{35}$  results from electronic transitions between  $e_g$  and  $t_{2g}$  orbitals;  $\beta_{33}$  or  $\beta_{55}$  result from electronic transitions within the  $e_g$  or  $t_{2g}$  orbitals respectively and each is a measure of the covalency of only the  $e_g$  or  $t_{2g}$  orbitals respectively. It is interesting to note that in chromium complexes, for which the distinction between  $\beta_{35}$  and  $\beta_{55}$  can be made,  $\beta_{55}$  is much less sensitive to the changes in the covalent nature of the ligands than  $\beta_{35}$  (Lever, 1968). Unfortunately, these Racah parameters can not be measured at present for ferrous phases, so that extensions of these qualitative analogies between Mössbauer parameters and Racah parameters can not be made.
4. Since the covalency of ferrous-ligand bonds as measured by quadrupole splitting appears insensitive to the cation-anion bond length (from both pressure and temperature measurements), it may well be that all ferrous silicate minerals of a given coordination number have very similar values of  $\alpha^2$ , (the covalency parameter in equation 4.11) and thus very similar

values of  $QS_0''$  (the valence portion of the quadrupole splitting at 0 °K in equation 4.13). If this is the case, then values for the lattice contribution may be estimated for the different ferrous polyhedra once a suitable value for  $QS_0''$  for ferrous silicates is established. This knowledge would be extremely useful for determining the lower level splittings,  $\Delta_1$  and  $\Delta_2$ , from quadrupole splitting data as a function of temperature.

## Chapter 5

### DISCUSSION AND SPECULATION ON TOPICS OF IMPORTANCE FOR EARTH SCIENCES ARISING FROM THIS STUDY

#### 5.1 Speculations on the Pressure-induced Electron Transfer Transition in Ferric Silicates

Direct evidence for the new electronic ground state formed by pressure-induced electron transfer from ligand to cation in ferric silicates is rather meager at present, being limited to two phases. These phases, magnesioriebeckite and FeCr garnet, both contain octahedral ferric cations. No evidence exists for this transition in tetrahedrally coordinated ferric cations in oxides or silicates. However, as both temperature and pressure appear to augment the electron transfer from ligand to metal and as ferric cations in the mantle will most likely be octahedrally coordinated, it is not inconceivable that, by extrapolating to mantle conditions, the new electronic ground state may be extensive for ferric phases deep within the Earth. For this reason, some further discussion of the transition, particularly concerning its possible effects on various aspects of mantle mineralogy, is presented here.

Since oxygen anions usually constitute about 90% by volume of silicate and oxide minerals, any means of reducing the size of oxygen anions will be favored at high pressure and the formation of oxygen radical anions (e.g.,  $O^-$ ) at the expense of  $O^{2-}$  by means of electron transfer from the oxygen anions to the reducible ferric cation satisfies this condition. As long as the decrease in anion volume exceeds the increase in cation volume, the transfer will be favored at high pressure. Taking a most naive approach

and assuming that  $O^-$  has the same ionic radius as  $F^-$ , it will be about  $1.60 \text{ \AA}^3$  smaller in volume than  $O^{2-}$  and this volume change exceeds the increase in volume of the iron cation which is about  $0.90 \text{ \AA}^3$  (based on Shannon and Prewitt (1969) ionic radii data). Evidence for radical anions such as  $O^-$  could, in principle, be investigated by electron spin resonance (ESR) at high pressure, but such experiments would be extremely difficult. ESR experiments at ambient conditions on certain phases have shown the presence of small amounts of radical anions. Vinokurov et al. (1971) showed that  $O^-$  is present in zircon and Low and Zeira (1972) have shown  $CO_2^-$  to be present in  $CaCO_3$ .

The combination of the decrease in charge on ions in ferric minerals at high pressure and the large concomitant increase in radius ratio ( $r_c/r_a$ ) should seriously alter the crystal chemistry of such phases. Cation size has been used to predict stability fields for known and hypothetical phases in the Earth. The change in oxidation state and radius ratio would be expected to invalidate such predictions for ferric phases at very high pressures. Generally, radius ratio can be expected to increase slowly with pressure (Ringwood, 1970), but the charge transfer process should accelerate this increase markedly, so that phase boundaries based on cation radii may be crossed very much sooner than anticipated based on zero pressure crystal chemistry. In this way, ferric phases may exhibit unusual crystal chemical behavior at high pressure if they were originally close to such boundaries so that the charge transfer process could cause them to cross the boundaries.

The charge transfer process at high pressure may also result in unexpected elastic properties for phases. As a general rule, all phase

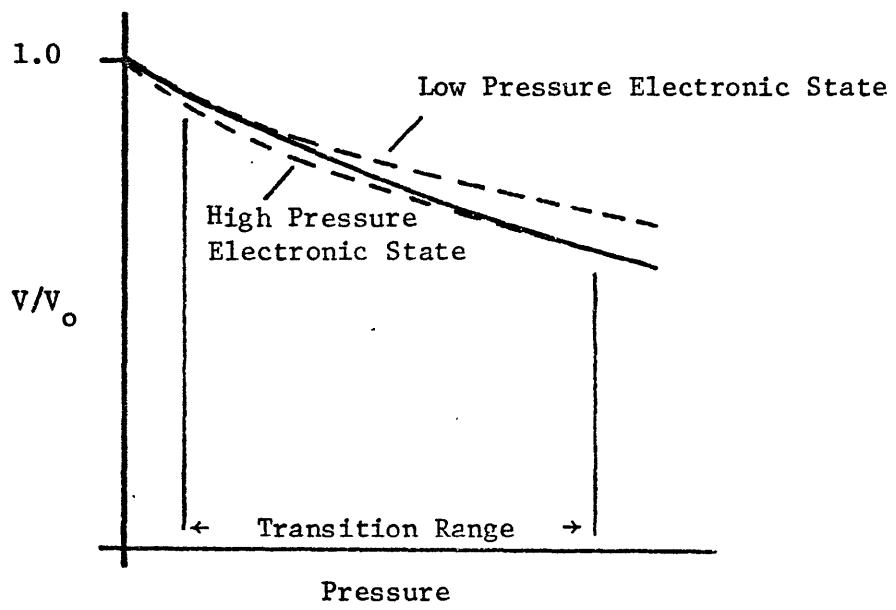
changes in minerals, which occur as the result of increasing pressure, involve an increase in bulk modulus and a decrease in volume for the high pressure phase. The pressure-induced charge transfer transition may well be an exception to this rule. The new phase that results at high pressure due to this transition can be expected to have somewhat different physical properties than the low pressure phase since a less highly charged pair of ions have been formed. Extending the scheme of Anderson and Anderson (1970) suggests that the bulk modulus of the high pressure phase may, in fact, be less than that of the low pressure phase. Therefore, it is conceivable that the change in electronic state may occur with a minimal volume change at the start of the transition and that the decrease in bulk modulus may be responsible for the formation of the new electronic state. Figure 5.1 shows schematically what would happen to the volume if this hypothesis was correct. Such deviations from expected behavior in  $\Delta V/V$  versus pressure might easily be lost within the accuracy of even the most precise PV measurements, especially if the ferric content is small.

The charge transfer process will tend to greatly decrease the amount of ferric iron in the mantle and would appear to invalidate one of the arguments proposed by Ringwood (1966b) concerning non-equilibrium between the core and mantle on the basis of the predicted  $Fe^{2+}/Fe^{3+}$  ratio in the lower mantle. Ringwood argues that for silicates coexisting with an iron core, the  $Fe^{2+}/Fe^{3+}$  ratio should be around 200, whereas the upper mantle ratio based on his pyrolite model is about 15. Ringwood rules out the possibility of strong upward fractionation of ferric relative to ferrous which might cause such enrichment, and states that the core and mantle must be out



Figure 5.1

Predicted change of molar volume with pressure for a ferric phase undergoing the pressure-induced charge transfer transition.



of equilibrium. Pressure-induced reduction, however, could easily be responsible for the change in  $\text{Fe}^{2+}/\text{Fe}^{3+}$  ratio from 15 at the crust-mantle boundary to 200 at the core-mantle boundary and would appear to invalidate the argument. However, the question to be considered now is whether equilibrium is possible between iron metal and the oxygen radical anion, assuming the core to be an iron-nickel-light element alloy. If, however, the core resembles  $\text{Fe}_2\text{O}$  which has been postulated by Bullen (1973), then the oxygen radical anion could well be in equilibrium with such a phase. Strens (1974), on the other hand, discounts the possibility of  $\text{Fe}_2\text{O}$  being a viable core phase. Until static experiments are feasible in the megabar range, the exact nature of the core and core-mantle boundary will remain uncertain. The pressure-induced electronic process being considered here only adds more uncertainty to such speculative arguments at the present time.

Duba (1972), Duba and Nicholls (1973) and Duba et al. (1973) have shown that the electrical conductivities of olivine and other iron-containing phases are very sensitive to the amount of ferric-iron present, which suggests that changes in oxidation state of iron will lead to changes in electrical conductivity. The new electronic ground state for ferric phases under high pressure should therefore also be expected to give rise to different electrical properties. However, such investigations have not been reported for materials in which this transition extensively occurs as the result of pressure. Intuitively, it might be expected that electrical conduction should increase since "holes" are being formed on the anions which could facilitate the charge carrying process. However, it is equally

conceivable that this electron transfer between anion and cation is highly localized, and that no change in electrical conduction occurs.

Certain other physicochemical properties of mantle phases have been shown to be sensitive to the oxidation state of iron. These include viscosity of melts (Cukiermann and Uhlmann, 1974), phase boundaries at the liquidus (Kushiro, 1973), the fugacity of gases in equilibrium with iron-containing phases (Eugster, 1972) and the magnetic properties of Fe-Ti oxides (O'Reilly, 1969; Johnson, 1969). Presumably these factors could also be affected by the pressure-induced charge transfer process, but it is not worthwhile speculating on these effects at this time.

Other than ferric iron, the pressure-induced change in electronic ground state by means of electron transfer from anion to ligand has been observed in the higher oxidation states, Fe (VI) and Fe (IV), of iron in  $\text{BaFeO}_4$  and  $\text{SrFeO}_3$  (Panyushkin et al., 1969), in cupric systems (Wang and Drickamer, 1973) and in certain low-spin Mn (III) systems (Ahsbahr et al., 1974) and the question is raised as to how general this electronic transition may be. The transition requires a fairly oxidizing cation to be reduced to a fairly stable cation and the ligand-to-metal charge transfer band in the optical absorption spectrum to be of relatively low energy. Of the transition metal oxidation states which occur in mantle phases and satisfy this condition, ferric iron is probably the most likely candidate.  $\text{Ti}^{4+}$ , although it is probably more stable to reduction than  $\text{Fe}^{3+}$ , may also exhibit this property to some extent since it, too, has a relatively low energy for the charge transfer with oxygen anions (Loeffler et al., 1974) and the volume change for  $\text{Ti}^{4+} \rightarrow \text{Ti}^{3+}$  should not be as large as for  $\text{Fe}^{3+} \rightarrow \text{Fe}^{2+}$ .

Of the less common oxidation states,  $V^{4+}$  and  $Mn^{3+}$  also appear to have potential in this respect, whereas  $Cr^{3+}$ , due to the reducing nature of  $Cr^{2+}$ , may well be stable with respect to this transition.

Recently Gibbons et al. (1974) have described the effect of shock pressures on rhodonite,  $MnSiO_3$ , containing appreciable  $Mn^{3+}$ . The  $Mn^{3+}$  was effectively reduced to  $Mn^{2+}$  by the application of pressures in excess of 200 kb. Gibbons et al. (1974) favored a reduction mechanism for  $Mn^{3+}$  involving water present in the sample rather than from pressure per se. This result has a couple of interesting ramifications. Firstly, it is unlikely that experiments involving recovered shocked samples will be able to monitor pressure-induced charge transfer effects, since the phenomenon is usually quite reversible and the compaction shock wave will be counter-balanced by the rarefaction shock wave negating the effect of the former. For this reason, Gibbons' et al. (1974) result does not rule out the possibility of pressure-induced reduction occurring in  $Mn^{3+}$  in rhodonite. Secondly, pressure-induced reduction is just one process affecting oxidation states of elements in natural phases and it appears that if there is any water or volatile phase present that competing or side reactions could happen extremely quickly at high pressures and temperatures so as to negate the formation of radical anions. Similarly, structural imperfections and defects involving charge misbalances may also offset the formation of radical anions. For these reasons, the unequivocal detection of pressure-induced charge transfer from recovered samples, either natural from the Earth's interior or synthetic from high pressure (especially shock) experiments, is unlikely. Only static high pressure experiments, with in situ

monitoring of oxidation states, can be expected to be successful in delineating this charge transfer process.

In summary, pressure-induced charge transfer is likely to affect the elastic properties, electrical properties and crystal chemistry of ferric minerals under the pressure and temperature conditions found in the mantle. Although at present there is no direct evidence to suggest that pressure-induced charge transfer occurs in minerals containing cations other than ferric iron, there is also no reason to suggest that ferric iron should be unique in this respect, especially as reduction of  $Mn^{3+}$  and  $Cu^{2+}$  ions at high pressures has been observed in organo-metallic phases.

## 5.2 Covalency Changes in the Earth

The covalent character of iron-oxygen bonds in minerals is closely allied with structural details, particularly bond lengths and coordination number (Shannon, 1974). In general, due to compression, shorter bond lengths and increases in radius ratio ( $r_c/r_a$ ) result if the structure remains the same. In addition, phase changes occur with increasing pressure, resulting in more efficient packing and longer bond lengths if the coordination number increases. Since at constant temperature covalency appears to correlate inversely with bond lengths, compression without a structural change usually increases bond covalency, as is indicated by the Mössbauer experiments carried out in this study. However, such increases are offset by phase changes to structures containing higher coordination numbers and longer bond lengths. The general effect of temperature is to expand the structure leading to longer bond lengths. However, the increase in ionic character due to longer bond lengths is more than offset by increasing

overlap of metal and ligand orbitals as the electron clouds expand. Evidence for increasing covalency with rising temperature comes from the shift of the charge transfer edge of olivine and other ferrous minerals towards low energy as the temperature is increased (Balchan and Drickamer, 1959; Fukao et al., 1968; Pitt and Tozer, 1970a,b). Alternatively, changes in spin state from high spin to low spin in the transition cations due to compression will result in shorter bond lengths and increased covalency. The pressure-induced electron transfer phenomenon, on the other hand, by decreasing the effective nuclear charge on neighboring ions, will result in a decrease in covalency and an increase in radius ratio.

Similar arguments can be advanced for the effect of changes in coordination number, spin state and oxidation state with depth on bulk modulus. Table 5.1 summarizes such arguments. Schematic examples of these changes are also shown in figure 5.2. From such trends, it appears that although covalency generally increases with pressure, there are a number of factors which will decrease the covalency of metal-oxygen bonds, the most important of these being phase changes involving increases in coordination number with depth. From table 5.1 and figure 5.2 it is apparent that covalency parallels neither bulk modulus nor radius ratio.

A manifestation of the covalency of ferrous-oxygen bonds in silicates is the pressure-induced shifts and increase in intensity of the ligand→metal charge transfer bands in  $(\text{Mg,Fe})_2\text{SiO}_4$  polymorphs, and in ferropericlase (Mao and Bell, 1972; Mao, 1973). Such changes are consistent with increasing overlap of cation and anion electron clouds or increasing covalency with compression. It is these features rather than the crystal

Table 5.1

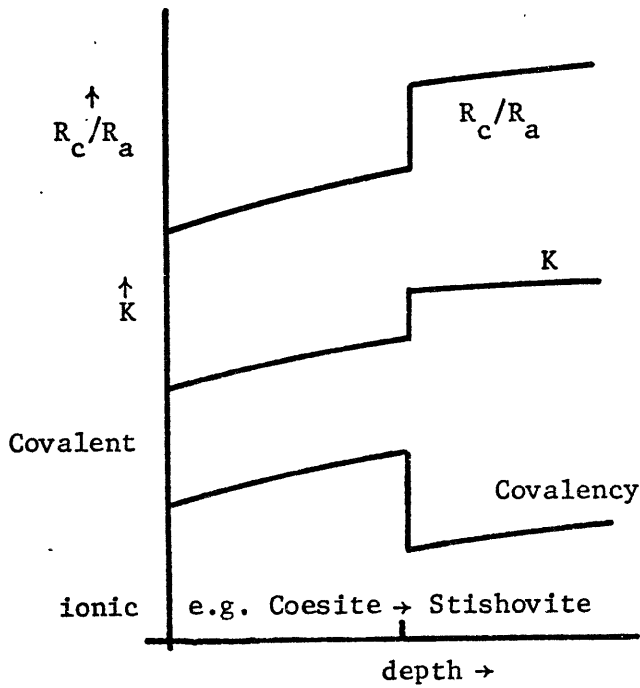
EFFECT OF CHANGES IN PRESSURE, TEMPERATURE, COORDINATION NUMBER, SPIN MULTIPLICITY AND CATION OXIDATION STATE ON RADIUS RATIO, COVALENCY OF METAL-OXYGEN BONDS AND BULK MODULUS.

Expected change in property with increasing depth in Earth		Effect of change in property with depth on		
Property	Change	Radius Ratio	Bond Covalency	Bulk Modulus
Pressure	Increase	Increase	Increase	Increase
Temperature	Increase	Decrease	Increase	Decrease
Coordination No.	Increase	Increase	Decrease	Increase
Spin Multiplicity	Decrease	Decrease	Increase	Increase
Cation Oxidation State	Decrease	Increase	Decrease	Decrease ?

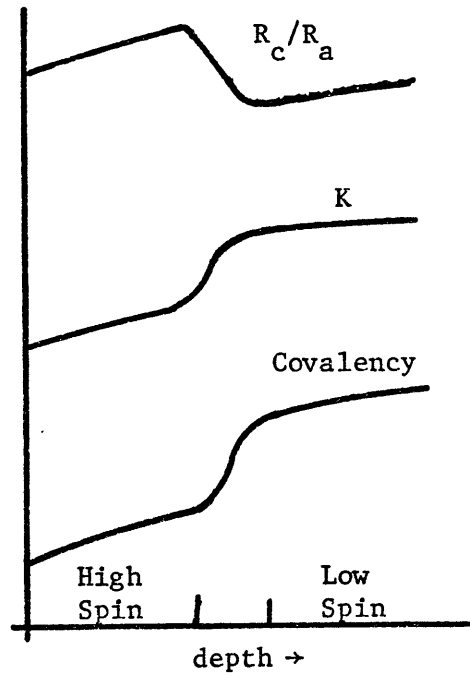


Figure 5.2

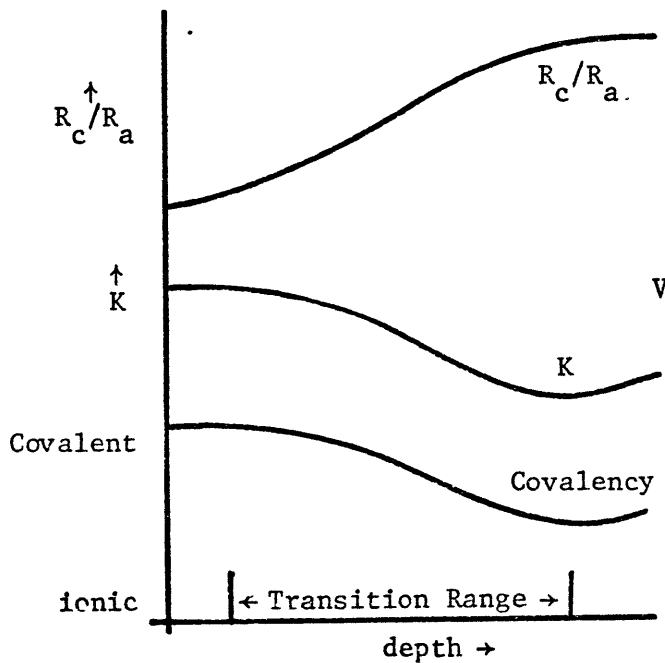
Expected changes with depth of radius ratio  $R_c/R_a$ , bulk modulus,  $K$ , and bond covalency due to: (a) coordination number change; (b) spin state change; and (c) ferric electronic ground state change. (d) Expected changes in volume,  $V$ , with depth caused by (a), (b) and (c).



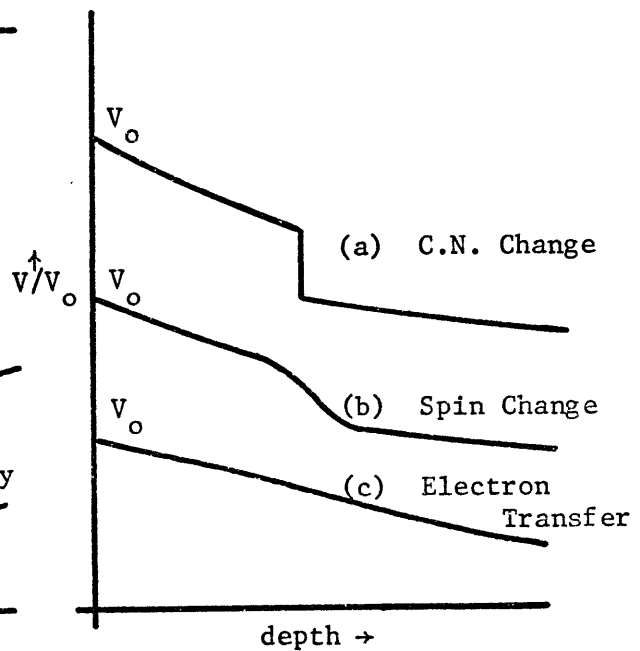
(a) Coordination Number Change



(b) Spin State Change



(c) Change in Electronic Ground State by L→M Electron Transfer



(d) Effect of Changes on Volume

field absorptions which play a dominant role in determining radiative transfer in minerals under mantle conditions. Accompanying and related to this shift is a large increase in electrical conductivity with pressure which precludes the accurate inversion of Earth conductivity data to give temperature data within the Earth (Mao, 1973). This phenomenon is equivalent to describing a decrease in the gap between valence and conduction bands and may represent the beginning of the predicted change towards metallic-like behavior at very high pressure (Drickamer, 1965).

The ionic model becomes less appropriate with depth in the Earth since the emerging ligand-metal charge transfer features can not be treated adequately by crystal-field theory and the structures postulated for high pressure phases (Ringwood, 1970) increasingly violate Pauling's rules as the coordination number increases. Indeed, it is a necessary condition that as the coordination numbers of the cations increase, intimate contact between polyhedra also increases.<sup>1</sup> One consequence of increased polyhedral contact is that the distance between neighboring cations in the structure decreases. This would suggest that metal-metal charge transfer phenomenon should also become increasingly prevalent with depth as the coordination number increases, as well as metal-ligand intervalence effects.

The ionic model in the guise of the Born-Mayer potential is often used to rationalize elastic property-volume systematics (Anderson and Anderson,

---

<sup>1</sup>For instance, all possible structures for  $\text{MO}_2$  containing four-coordinate cations only involve corner sharing between polyhedra, whereas the rutile  $\text{MO}_2$  structure containing six-coordinate cations involves some edge sharing of polyhedra and the fluorite  $\text{MO}_2$  structure containing eight-coordinate cations requires that all polyhedral edges be shared.

1970; Shankland, 1972; Shankland and Chung, 1974). However, such interrelationships hold for phases with considerable covalency where the charges on the ions should be much less than their formal valence charge. The explanation for this extension of the systematics to fairly covalent phases must be that the sum of the actual ionic plus covalent contributions to the lattice energy must be approximately equal to the lattice energy based on the formal valence charge only. A satisfactory description of the lattice energy of covalent crystals has not been written, so that it must be assumed that except for its dependence on ionic charges, it has similar parametric dependences as the Born-Mayer potential in order for the systematics to appear independent of the degree of covalency. For this reason, elastic property-volume systematics should differ little at depths in the Earth from those at ambient conditions despite the expected increases in covalency. Only drastic electronic rearrangements such as the pressure-induced electron transfer reaction referred to above or a change from insulating to metallic behavior may be expected to significantly upset these systematics. However, as covalency increases, the rationalization of elastic property-volume systematics by use of the Born-Mayer potential becomes increasingly tenuous.

Even though such systematics may well be self-compensating for changes in the degree of covalency, the augmentation with pressure of charge transfer effects relative to crystal-field effects requires that more sophisticated theories be developed to allow for changes in covalency with increasing depth in the Earth so that such changes and their effect on heat and electrical transfer within the Earth may be better understood. Two

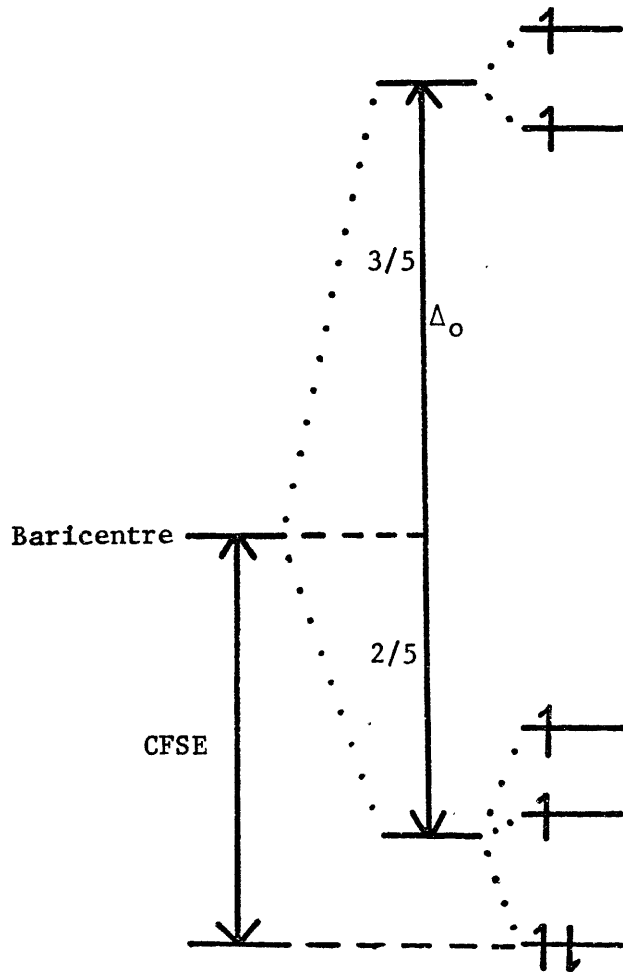
more complex theories which have been but little applied to questions of the electronic properties of mantle materials are molecular orbital theory and band theory. The more quantitative aspects of band theory appear, at the present, to be inapplicable to even the simplest of silicate structures, whereas molecular orbital theory still retains aspects of the localized treatment, in that for the most part, only one site of the structure is considered. If some compromise could be made between these two theories, such as molecular orbital theory being extended to include all atoms in a unit cell or band theory being adapted to include some description of localized phenomena, then progress in the theoretical treatment of the electronic states in silicates may be possible. Until such time, the increase in covalency of phases with increasing pressure can be only qualitatively understood.

### 5.3 Discussion on the Effect of Pressure and Temperature on Ferrous Crystal-field Stabilization Energies

The ferrous crystal-field stabilization energy arises from the difference in energy of the 3d level which is occupied by the sixth ferrous 3d electron (of opposite spin to the other five 3d electrons) and that of the baricentre of energy of all five 3d electron energy levels (figure 5.3). Such values are of interest because they are important energy and entropy factors in considering the ordering of ferrous cations over the different sites in a crystal structure or the distribution of ferrous cations between minerals. For example, Burns (1969b) attempted to rationalize cation distributions in minerals on the basis of crystal-field stabilization energies and site size only. Agreement between the predicted and observed

Figure 5.3

Example of the interrelationship of CFSE,  $\Delta_o$ , and the five 3d levels for ferrous iron in an octahedral site. (For eight-coordinate or tetrahedral sites see figure 5.4.)



Fe-Mg distribution was quite satisfactory.

In the course of this study, it has been shown that Mössbauer studies, as a function of temperature, can lead to estimates of the relative energy of the lower 3d levels which contain the extra electron. Therefore, if such measurements are coupled with optical absorption measurements which, for ferrous iron, lead to estimates of the relative energy of the very lowest level and the upper energy levels, then values may be obtained for the relative energies of all five 3d levels, for the crystal-field parameter,  $\Delta$ , and for the crystal-field stabilization energy, CFSE. Such measurements can also be extended as a function of pressure, although with less certainty, to yield values of  $\Delta$  and CFSE at elevated pressures. Due to differences in site compressibility and changes of site distortion with pressure, the variation of  $\Delta$  and CFSE for different ferrous sites in minerals may not be similar, so that the distribution of ferrous between such sites may therefore be quite pressure sensitive.

As an example of the application of this Mössbauer method of obtaining the lower level splitting, the mineral almandine will be chosen. Burns (1970) presents the absorption spectrum of almandine and shows that there are bands at 7650, 5820 and 4450  $\text{cm}^{-1}$ . He then uses erroneous data of Clark (1957b) to fix the lower level splitting at about 3000  $\text{cm}^{-1}$  and calculates  $\Delta_c$  to be 4520  $\text{cm}^{-1}$  and the CFSE to be 4160  $\text{cm}^{-1}$ . White and Moore (1972) reassessed these data and showed that the data are inconsistent. They predicted that the lower level splitting must be less than 2000  $\text{cm}^{-1}$ . As was shown above, the lower level splitting is about 1100  $\text{cm}^{-1}$ . Therefore, using the data presented by White and Moore (1972) for the sample of



composition closest to the almandine studied above leads to the energy level scheme in figure 5.4. The CFSE is calculated to be  $3800 \text{ cm}^{-1}$  (10.86 Kcal/mole) and  $\Delta_c$  is  $5425 \text{ cm}^{-1}$ . The errors in these figures are  $\pm 50 \text{ cm}^{-1}$  as opposed to  $\pm 300 \text{ cm}^{-1}$  error for the data of White and Moore (1972) who ignored this splitting in their calculations and therefore obtained values which were in error.

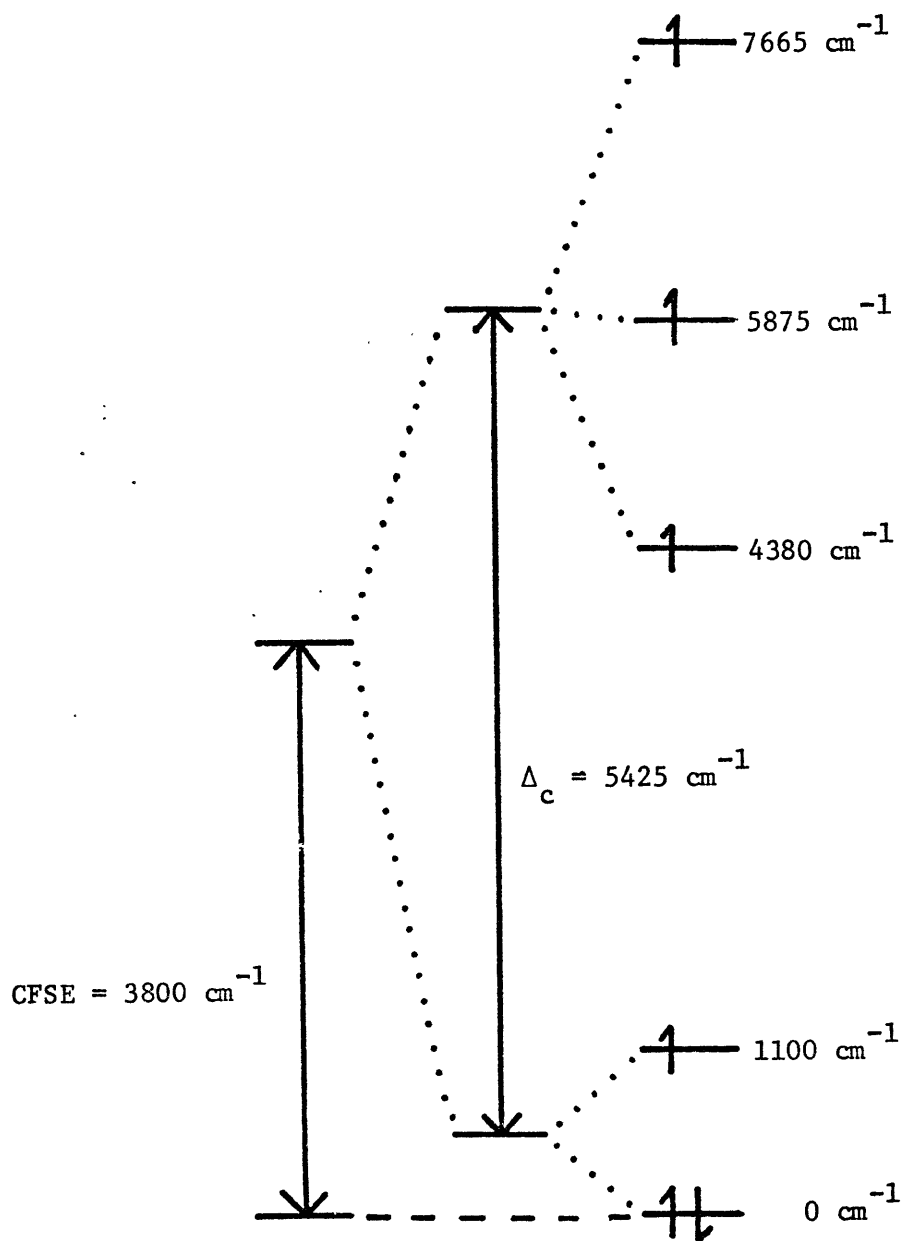
Recently, Runciman and Sengupta (1974) have criticized the model of White and Moore (1972) claiming that it is inconsistent with selection rules because the band at about  $4500 \text{ cm}^{-1}$  should be forbidden in this model. On the basis of a new point charge model, Runciman and Sengupta (1974) claim that the lowest energy transition is, in fact, the  $4500 \text{ cm}^{-1}$  band and that a further transition at about  $7000 \text{ cm}^{-1}$  is not observed as it is forbidden by the selection rules. Although a simpler model based only on the first coordination sphere about the  $\text{Fe}^{2+}$  cation was evaluated by Runciman and Sengupta (1974) and gave results agreeing with White and Moore (1972), it was rejected in favor of a more complex model which included two silicon atoms of the second coordination sphere as well.

This latter model results in an unreasonably large splitting of the lower 3d levels ( $4500 \text{ cm}^{-1}$ ) and a value for  $\Delta_c$  of about  $4700 \text{ cm}^{-1}$ , which is rather small. The model is also inconsistent with the Mössbauer results on almandine. As discussed above, the Mössbauer data require an electronic level at about  $1100 \text{ cm}^{-1}$ , which is consistent with White and Moore's model but not with Runciman and Sengupta's model.

The addition of silicon atoms from the second coordination sphere in the model of Runciman and Sengupta (1974) must be suspect and one wonders

Figure 5.4

Five 3d energy levels, CFSE and  $\Delta_c$  for ferrous iron in almandine.



why only these two atoms and not all the atoms of the second coordination sphere were included in their calculations. These authors themselves admit that the first coordination sphere is sufficient to generate the model of White and Moore (1972) and other models of crystal-field spectra (Wood and Strens, 1972; Gaffney, 1972) based only on the first coordination sphere have also proved adequate.

Finally, the original criticism of White and Moore's (1972) model for the  $\text{Fe}^{2+}$  site in almandine was based on intensity predictions and as Burns (1974) has shown, theoretical understanding of selection rules and intensities of bands arising from cations in solids is nowhere near adequate and can be very misleading. It appears that the approach taken by Runciman and Sengupta (1974) is incorrect and the model of White and Moore (1972) is the better description of  $\text{Fe}^{2+}$  in almandine.

The Mössbauer method for obtaining the lower level splittings is now applied to fayalite in order to calculate values for  $\Delta_o$  and CFSE for ferrous iron in this mineral. Some earlier calculations were made for this phase by Burns (1970), who took some limited data on the splitting of the  $t_{2g}$  derived levels in fayalite and, making the best of such data, predicted that  $\Delta_o$  is  $8940 \text{ cm}^{-1}$  and  $8050 \text{ cm}^{-1}$  and the CFSE is  $4200 \text{ cm}^{-1}$  and  $4460 \text{ cm}^{-1}$  for the M1 and M2 sites respectively. The analysis of the fayalite Mössbauer data suggests that the splittings of the  $t_{2g}$  level for one site is  $630 \text{ cm}^{-1}$  and  $1400 \text{ cm}^{-1}$  and  $710 \text{ cm}^{-1}$  and  $1500 \text{ cm}^{-1}$  for the other. The larger splitting of the levels is consistent with the band at  $1650 \text{ cm}^{-1}$  reported by White and Keester (1967) for an olivine of unspecified composition and with the bands reported by Runciman et al. (1973) at  $1775 \text{ cm}^{-1}$

and  $1668 \text{ cm}^{-1}$  for a forsteritic olivine ( $\text{Fo}_{89}$ ).<sup>1</sup> Taking the Mössbauer data for the lower level splittings and the more complete data of Gaffey (1974) for the optical absorption bands of fayalite values of  $\Delta_0$  and CFSE were calculated. Since the assignment of the Mössbauer data to a given site remains ambiguous and since the values for the two sites do not differ greatly, averaged values of  $670 \text{ cm}^{-1}$  and  $1450 \text{ cm}^{-1}$  were used for the lower level splittings of both sites. This assumption only introduces a  $\pm 20 \text{ cm}^{-1}$  error. For the M1 and M2 sites respectively,  $\Delta_0$  values are calculated to be  $8340 \text{ cm}^{-1}$  and  $8510 \text{ cm}^{-1}$  while CFSE values are  $4045 \text{ cm}^{-1}$  (11.56 Kcal/mole) and  $4110 \text{ cm}^{-1}$  (11.75 Kcal/mole). These values are estimated to be accurate to  $\pm 200 \text{ cm}^{-1}$  and  $\pm 150 \text{ cm}^{-1}$  respectively, considering errors in both Mössbauer and absorption spectral measurements and the fact that some of the errors cancel out in the calculation of CFSE. Therefore, it is possible that both  $\Delta_0$  and CFSE for the two olivine sites are equal within experimental error. If such close agreement between the two sites persists over the whole range of compositions for Mg-Fe olivines, which, judging from the similarity of both optical absorption spectra and Mössbauer spectra across the series, is quite possible, then it is not surprising that Mg-Fe olivines behave closely to an ideal solid solution. The similarity of CFSE

---

<sup>1</sup>Exact agreement is not expected due to the large uncertainty in the larger of the two values derived from Mössbauer spectra ( $\pm 200 \text{ cm}^{-1}$ ), the unknown effect of composition on the value of the splitting, and also because the Mössbauer effect measures the energy of the lowest vibrational states of the excited electronic states relative to the ground state, whereas the optical effect, due to the Franck-Condon principle, probably measures the energy difference between a higher vibrational state of the excited electronic state and the ground state. The difference is therefore not considered significant.

values for the two sites suggests that they do not determine the ordering of iron in Mg-Fe olivines. In fact, there appears to be no appreciable ordering of magnesium and  $\text{Fe}^{2+}$  in olivines, so that there must be cancellation of other energy factors that would be important in determining site preferences of ferrous iron relative to magnesium. Since the only other factor commonly considered in determining site preferences is ionic radius, this result would suggest that the difference in ionic radius between  $\text{Fe}^{2+}$  and  $\text{Mg}^{2+}$  also does not play a role in determining site preferences of these ions in olivine. Alternatively, the result may suggest that there are further unconsidered energy factors which contribute to the total site preference energy in order to offset the ionic radius difference.

The trend of CFSE and  $\Delta$ , or more basically the five 3d orbital energies, with pressure can lead to an understanding of the effect of pressure on Mg-Fe distribution between sites within a mineral structure and between different mineral phases. In principle, the combination of absorption spectral and Mössbauer data can provide all the necessary information, but at the time of writing, such data are not available or are inadequately correlated, so that the following analysis will not be complete. Table 5.2 shows the change in lower level splittings over the range zero to 100 kb estimated from the Mössbauer data for fayalite, orthoferrosilite, almandine and ilmenite. Except for ilmenite, the changes are small, and if values of the crystal-field splitting parameter for all phases change by about the same amount, then pressure can be expected to have a minimal effect on Mg-Fe distribution. The pressure-induced increase of distortion in ilmenite leads to a CFSE for  $\text{Fe}^{2+}$  which increases fairly rapidly with pressure

Table 5.2

ESTIMATED CHANGES OVER 100 KB IN THE SPLITTINGS OF  
LOWER 3d LEVELS,  $\Delta_1$  AND  $\Delta_2$ , FOR SOME FERROUS MINERALS

(Units are  $\text{cm}^{-1}$ )

PHASE	SITE	$\Delta_1$ (100-0)	$\Delta_2$ (100-0)
Fayalite	M1	-150?	- 70
	M2	-150?	- 70
Orthoferrosilite	M1	+250	+100
	M2	?	?
Almandine	8	<-50	--
Ilmenite	6	+800	0

compared to other phases. If other energy factors do not offset this change, the results suggest that geikielite,  $(\text{Mg,Fe})\text{TiO}_3$ , might be expected to become increasingly iron-rich with respect to mantle silicates with depth.

Obviously, the assumption that other energy factors remain the same is not justified and one important example must be mentioned. The high pressure absorption spectral data obtained by Abu-Eid (1974) for almandine and for olivine, coupled with Mössbauer data obtained in this study, indicate that  $\Delta_c$  for almandine increases more rapidly with pressure than does  $\Delta_o$  for olivine. Similarly, the CFSE for  $\text{Fe}^{2+}$  in almandine increases more rapidly with pressure compared to fayalite. This trend suggests that due to pressure alone the  $\text{Fe}^{2+}/\text{Mg}$  ratio should increase in almandine relative to olivine. On the other hand, temperature tends to randomize cation distributions so that considering a depth profile through the Earth, the effects of increasing temperature and pressure tend to be compensating. An average Earth geotherm shows a very rapidly increasing temperature with rising pressure at shallow depths into the Earth while at much greater depths, temperature increases more slowly with pressure. For the purposes of the Mg-Fe distribution between almandine and other mantle phases along an average mantle geotherm, the temperature dependence at shallow depths of the geotherm will result in increasingly random Mg-Fe distributions between the phases while at greater depths, the pressure effect on the Mg-Fe distributions may dominate and cause the Fe/Mg ratio to increase in almandine relative to other mantle phases. Such conclusions are entirely consistent with the model for Fe-Mg distribution between almandine and



other phases developed by Ahrens (1972) on the basis of thermodynamic data, and suggest that such qualitative arguments based on CFSE may indeed be quite valid.

So far, CFSEs have been discussed as if they are invariant with respect to temperature, which can not be the case. The Mössbauer technique gives information on the averaged thermal occupation of levels higher than the lowest 3d energy level and indicates that such occupations may be considerable depending on the energy of the level relative to the lowest level and the temperature. Any occupation of the levels higher than the lowest level decreases the CFSE. For this reason, previous calculations and use of CFSE, which are based solely on the assumption of 100% occupation of the lowest electron level (which is only true at absolute zero), may well be in error when applied to high temperature phenomena.

Assuming a Boltzmann-type distribution for the sixth electron over the 3d energy levels, the relative averaged occupancy of the levels at temperature,  $T$ , under equilibrium conditions is proportional to  $e^{-E_i/kT}$  where  $E_i$  is the energy of the  $i^{\text{th}}$  level relative to the lowest level. At absolute zero, the electron is located in the lowest level only (assuming non-degeneracy) and the CFSE is then the difference between the energy of the lowest level ( $E = 0$ ) and the baricentre of energy of all five levels:

$$\text{CFSE}(0) = \sum_i^5 E_i / 5 \quad 5.1$$

At temperature,  $T$ , the CFSE is reduced from this amount by the product of the relative probability of finding the electron in the  $i^{\text{th}}$  level and the energy,  $E_i$ , of the  $i^{\text{th}}$  level relative to the lowest level:

$$\text{CFSE} = \text{CFSE}(T) - \frac{1}{Z} \sum_i E_i e^{-E_i/kT} \quad 5.2$$

where Z is the partition function:

$$Z = \sum_i e^{-E_i/kT} \quad 5.3$$

and CFSE(T) differs from CFSE(0) due to the change in  $\Delta$  with temperature. Equation 5.2 describes the temperature dependence of CFSE. For temperatures less than 1500-2000 °K, splittings greater than 6000  $\text{cm}^{-1}$  do not contribute appreciably to the change from CFSE(T). For the most part, only the lower 3d levels need be of interest for octahedral complexes. If these two energy level splittings are small ( $< 500 \text{ cm}^{-1}$ ) there will only be a small temperature perturbation of CFSE. Similarly, if the energy level splittings are very large ( $> 3000 \text{ cm}^{-1}$ ), the temperature perturbation will again be small at temperatures less than 2000 °C, due to the low thermal occupation of such levels. In between this range, the effect of temperature could be sizable (maximum expected reduction of CFSE due to this effect is about 10-15% at 1500 °K). Therefore, by using absolute zero values for CFSE erroneous deductions could be made if high temperature phenomena were being considered. Figure 5.5 attempts to demonstrate this for an idealized system using calculations based on equation 5.2. The regular site shows a decrease of only about 120  $\text{cm}^{-1}$  over 1500 °K whereas the distorted site<sup>1</sup> shows a decrease of about 500  $\text{cm}^{-1}$  over the same temperature range. Therefore, if the two sites have CFSE(0) which were about the same value, at

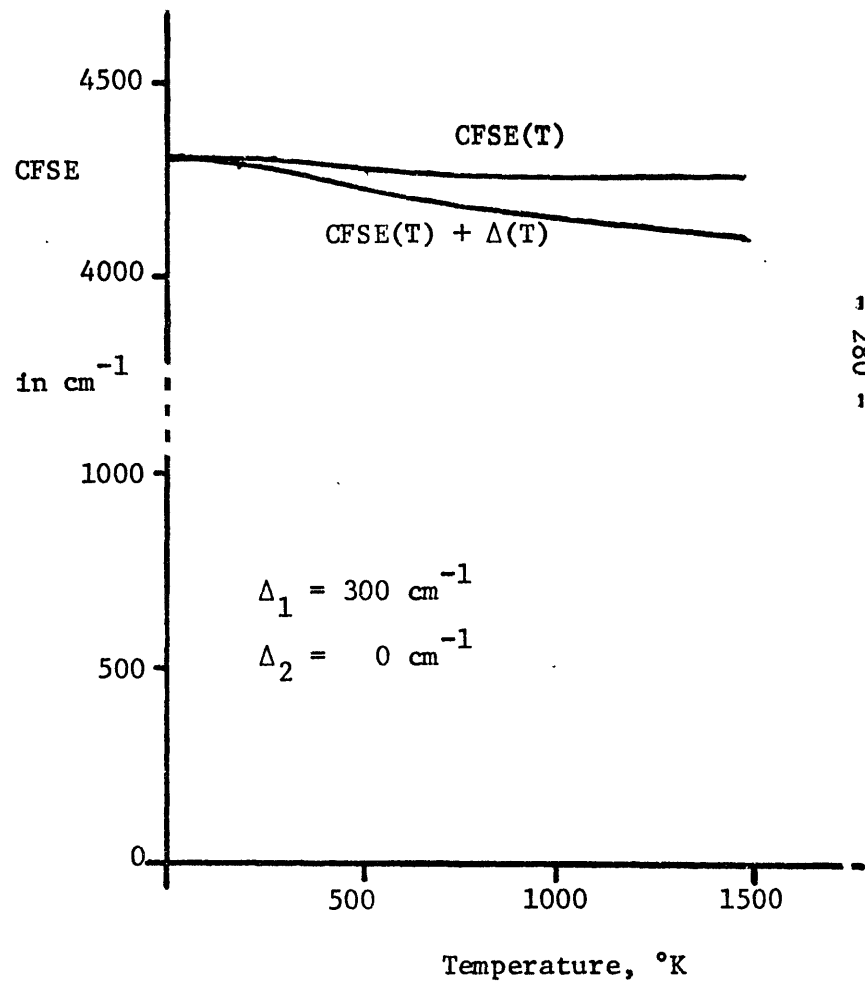
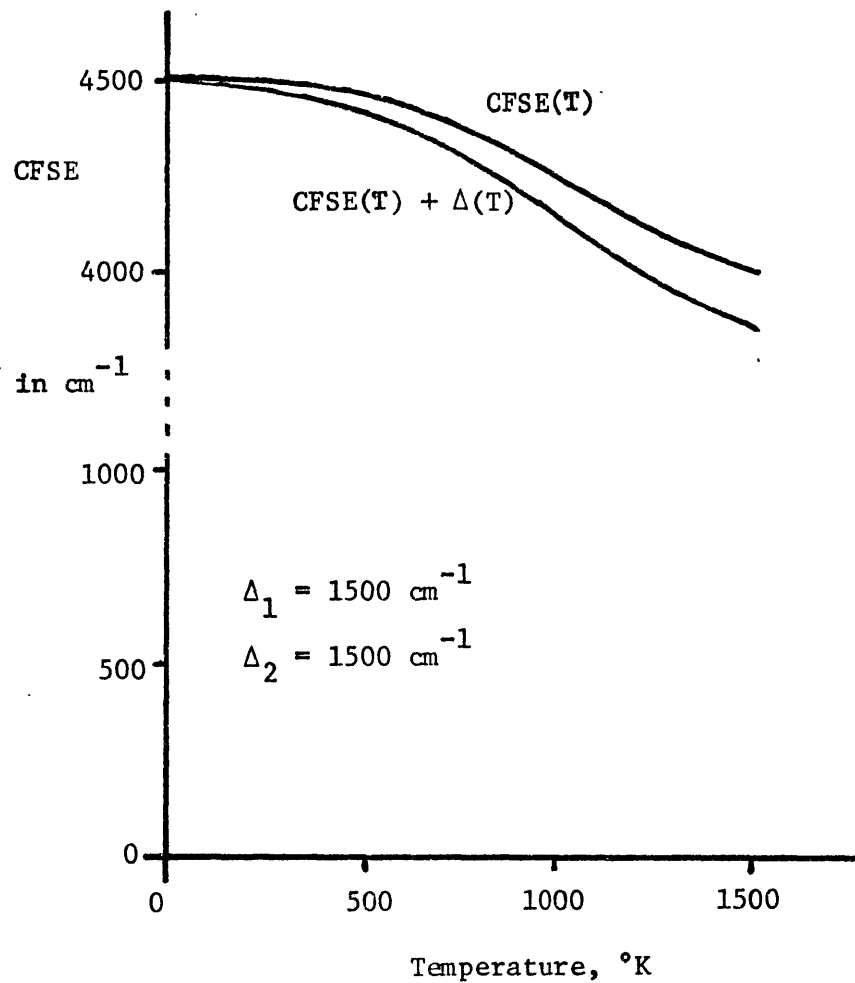
---

<sup>1</sup>Degree of distortion of a site is defined here pragmatically according to the splitting of the lower 3d energy levels.

Figure 5.5

CFSE as a function of temperature for a highly distorted site (diagram on left) and for a slightly distorted site (diagram on right). Upper curves: change in CFSE without allowance for change in  $\Delta$  with temperature. Lower curves: change in CFSE with allowance for change in  $\Delta$  with temperature.

Note that the slightly distorted site has the smaller CFSE at 0 °K, but has the larger CFSE at geologically important temperatures.



higher temperatures the CFSE difference between the two sites of about 1 Kcal/mole would cause ferrous cations to favor the regular site. In the same way, since the electron distribution would be more nearly random over the three lower  $t_{2g}$  levels in the regular site, entropy considerations would also favor ferrous cations to be enriched in the more regular site at high temperatures. On this basis, as a general rule one would expect to find ferrous favoring the most regular site at high temperature or, conversely, on cooling to find ferrous migrating increasingly towards the more distorted site, as long as equilibrium was maintained. This result suggests that both  $\Delta H_{mix}$  and  $\Delta S_{mix}$  for the distribution of  $Fe^{2+}$  between two or more sites are usually temperature dependent whenever the cation can gain additional stabilization energy due to site distortions. On this basis, the pyroxene Mg-Fe solid solution series can not be ideal solid solutions since the M1 and M2 structural sites are so different in distortion, whereas the olivine Mg-Fe solid solution series may be treated as ideal because the site distortions are so similar in terms of the splitting of the lower 3d energy levels of each site. However, in the case of orthopyroxene factors may very well compensate so that relative changes in CFSE with temperature over the geologically important temperature range, 750 °K-1250 °K, are small, causing the (Mg,Fe) orthopyroxene series to show only very small deviations from ideal solid solution behavior as postulated by Navrotsky (1971).

In summary, the Mössbauer measurements have enabled considerably more precise estimates of  $\Delta$  and CFSE to be made. The increased precision has lead to an investigation of the effect of temperature on CFSE, which has

hitherto been ignored. The effect of pressure on CFSEs indicate that geikielites,  $(\text{Mg,Fe})\text{TiO}_3$ , and almandines  $(\text{Mg,Fe})_3\text{Al}_2\text{Si}_3\text{O}_{12}$ , should both become more iron-rich relative to olivines,  $(\text{Mg,Fe})_2\text{SiO}_4$ , in the absence of other changes with pressure. Finally, it should be noted that CFSEs are relatively small energies compared to lattice energies, and that to be able to ascribe effects due solely to relative changes in CFSEs requires the rather large assumption that other relative effects are smaller still or cancel out.

## Chapter 6

### CONCLUSIONS AND SUGGESTIONS FOR FUTURE WORK

#### 6.1 Conclusions and Summary of High Pressure Mössbauer Results

In this study, a broad range of iron-containing oxide and silicate phases of direct mineralogical interest has been investigated by means of Mössbauer spectroscopy while the phases were under pressures of up to 200 kb. In a sense, this study is a survey of possible effects that pressure may have on the Mössbauer spectra of iron minerals. Compared to earlier investigations on inorganic and organoiron compounds, the observed electronic changes are small, which is due, firstly, to the relatively incompressible nature of oxides and silicates and, secondly, to the fairly ionic nature of such phases that allows for little electronic interaction between the iron cations and their surrounding oxygen anions. No changes in spin state were encountered in this study and only the FeCr garnet showed positive signs of pressure-induced reduction. This phase and magnesioriebeckite, which also shows evidence of this phenomenon (Burns et al., 1972b), suggest that larger and more compressible octahedral sites do facilitate the electron transfer from ligands to cation. No changes in oxidation state were observed for ferric iron tetrahedrally coordinated by oxygen anions in silicates or oxides. Both pressure-induced reduction in ferric minerals and spin-state transitions in iron minerals should occur by analogy with phases investigated by Drickamer and his co-workers. This study indicates that considerably greater pressures are required. However, the effect of temperature facilitates the pressure-induced charge transfer process, so that higher

temperatures could make this phenomenon extensive in ferric silicates and oxides at relatively low and easily attainable pressures.

The magnetic properties of iron silicates and oxides at 200 kb are very similar to those at zero pressure. Iron silicates remain paramagnetic, while hematite and magnetite show only small changes in their hyperfine magnetic splittings.

Except for  $\text{Fe}^{3+}$  (IV) in silicates, isomer shifts decrease with pressure, although not very rapidly, and such trends appear to correlate well with expected site compressibilities. A more detailed inspection of the  $\text{Fe}^{3+}$  (IV) isomer shift data and the pressure trends of isomer shifts of silicates containing  $\text{Fe}^{3+}$  (IV) suggest that the interrelationship between covalency and isomer shift is opposite to that of other coordination number and valence state combinations of iron. Therefore, increasing  $s$  electron densities at the nucleus or, equivalently, decreasing isomer shift values for  $\text{Fe}^{3+}$  (IV) do not reflect increases but rather decreases in the degree of covalency of the iron-ligand bond. As far as is known, this is the first time that this effect has been fully recognized, and it would suggest that the bonding in  $\text{Fe}^{3+}$  (IV) must have considerable cation  $s$  electron character.

Crystallographic changes with pressure are indicated by changes in the Mössbauer quadrupole splittings of ferric phases with pressure. The data show that the crystal structures of the ferric minerals studied here do not undergo compression by simply uniformly shortening bond lengths in the unit cell. More complex rearrangement of atomic positions must be involved.



Ferrous quadrupole splitting trends with pressure depend on the degree of distortion of the site, the temperature and the value of the quadrupole splitting at 0 °K. At low distortion, changes in the lower 3d orbital level splittings determine the trend, whereas at high distortion, lattice effects dominate. By combining optical absorption spectral data with Mössbauer data complete details of the relative energies of all five 3d orbital levels can be obtained for ferrous phases. This leads to more precise estimates of the values of crystal-field splitting parameters and stabilization energies than were obtained previously. These parameters can be obtained as a function of pressure, although for minerals containing octahedral ferrous iron, a non-unique result will usually be obtained. High pressure/high temperature Mössbauer measurements could, in principle, resolve this problem.

To be able to fully utilize these data on the pressure-induced electronic changes of minerals for studies of the Earth, the effects of both temperature and pressure should be investigated, since the pressure-induced charge transfer phenomenon, magnetic effects and ferrous quadrupole splittings are as sensitive to temperature as to pressure. The effect of pressure alone on the electronic properties of minerals is relatively small, resulting in only slight increases in covalency and minimal additional electronic effects. This increase in covalency is consistent with predictions made by Drickamer (1965) and correlates well with the broadening and shift to lower energy with increasing pressure of the ligand-metal charge transfer bands of ferrous minerals observed by Mao and Bell (1972) and by Mao (1973).

The high pressure Mössbauer experimentation evolved in quality as the thesis progressed as practical factors regarding the elimination of thick absorber problems were realized. At the present time, spectra can be obtained routinely if the phase contains in excess of 1/2 wt %  $^{57}\text{Fe}$ /site, which is somewhat restrictive for natural minerals, but is easy to circumvent with a source of  $^{57}\text{Fe}$  and the necessary synthesis equipment.

The high pressure Mössbauer technique can lead to useful information on the electronic properties of minerals as a function of pressure, but the main conclusion from this study is that pressures of up to 200 kb have very little effect on the electronic properties of silicates and oxides at room temperature. Except for those mineral properties such as the electrical conductivity and charge transfer phenomena which are very sensitive to changes in covalency, the models proposed for the properties of silicate and oxide minerals at zero pressure would appear to be appropriate at least to 200 kb. In particular, the small changes in covalency probably have no serious effect in converting seismic velocity data from earthquake studies to mineralogic information about the Earth's mantle.

## 6.2 Suggestions for Future Work

### 6.2.1 High pressure Mössbauer experiments

The most obvious extension of this study would appear to be in the direction of simultaneous high pressure/high temperature Mössbauer studies. For this work, temperatures of up to 500 °C should be contemplated. This will almost certainly necessitate redesign of the high pressure cell, since the heating experiments attempted in this study are not at all suitable for very high temperatures given the present press design.

The use of the diamond cell for Mössbauer studies at high pressures/high temperatures should be investigated since local heating of the sample to 500 °C is rather easily achieved. The diamond cell appears capable of enabling Mössbauer experiments to be carried out on samples under quasi-hydrostatic pressures of up to about 100 kb. The gasketing technique, which appears to be a necessary feature of the diamond cell Mössbauer technique, is used to apply near-hydrostatic pressures to the sample by filling the gasket with liquid. Some criticism of the pressure-induced charge transfer process has been made on the grounds that it could be a shear effect rather than a pressure effect (Gardiner et al., 1970). Hydrostatic experiments with the diamond cell could resolve this issue, although convincing arguments have been presented against the shear hypothesis (Drickamer and Frank, 1973).

Topics to concentrate on in the future should include the pressure-induced charge transfer phenomenon, magnetic effects and ferrous quadrupole splitting data. Judicious selecting of pressure and temperature conditions and of the phases based on the present work should give rise to extremely interesting experiments.

#### 6.2.2 Related experiments

Pressure-induced reduction of ferric to ferrous in minerals still remains to be demonstrated to be highly significant for studies of mantle mineralogy although the high pressure/high temperature Mössbauer experiments should delineate it further. Experiments on electrical conductivity at high pressures and high temperatures or very precise PV measurements should also be examined to see if such techniques can be used to give

information on the change in electronic ground state for ferric phases.

High pressure crystallographic studies, which could confirm some of the conclusions reached in this study by use of the Mössbauer effect alone, would also appear to be a profitable area for research. Also, the molecular orbital calculations of the type performed by Tossell et al. (1973, 1974) should find the isomer shift trends with pressure most interesting to interpret since direct calculation of the electron density at the nucleus appears possible with this computational technique.

More data on the lower level splittings of the 3d orbital levels of ferrous iron in minerals are definitely required and more Mössbauer experiments as a function of temperature should be attempted. The values of  $\Delta$  and CFSE for ferrous minerals, which can be obtained from such experiments when combined with optical absorption experiments, will be of use for the study of order/disorder phenomena in minerals and for questions concerning the non-ideality of (Mg,Fe) solid solution series in silicates.

### 6.2.3 Unrelated topic

The Mössbauer effect has shown itself to be an extremely useful analytical tool in experimental petrologic studies in the present study and elsewhere (Semet, 1973; Virgo, 1972). Since the Mössbauer technique is so specific for the oxidation state and coordination number of iron cations, hydrothermal studies of iron minerals, especially of hydroxyl-containing phases, should always use the Mössbauer effect to identify and elucidate the role of iron cations in minerals. This combination of Mössbauer studies and experimental petrology should be a highly profitable area of research.

REFERENCES

- Abu-Eid, R.M. (1974) Unpublished Ph.D. thesis, Massachusetts Institute of Technology, Cambridge, MA. (in preparation)
- Ahrens, T.J. (1972) The mineralogic distribution of iron in the upper mantle. Phys. Earth Planet. Ints. 5, 267-281.
- Ahrens, T.J. (1973) Petrologic properties of the upper 670 km of the Earth's mantle; geophysical implications. Phys. Earth Planet. Ints. 7, 167-186.
- Ahsbahs, H., Dehnicke, G., Dehnicke, K. and Hellner, E. (1974) IR-spectra of different transition metal complexes under high pressure (abstract), p. 26, Conference on High Pressure Research, Marburg, Germany.
- Allen, G.C. and Hush, N.S. (1967) Intervalence-transfer absorption, Part 1. Qualitative evidence for intervalence-transfer absorption in inorganic systems in solution and in the solid state. Prog. Inorg. Chem. 8, 357-389.
- Anderson, D.L. and Anderson, O.L. (1970) The bulk modulus-volume relationship for oxides. J. Geophys. Res. 75, 3494-3500.
- Anderson, D.L., Sammis, C. and Jordan, T. (1971) Composition and evolution of the mantle and core. Science. 171, 1103-1112.
- Annersten, H. (1974) Mössbauer studies of natural biotites. Amer. Mineral. 59, 143-151.
- Annersten, H., Devanarayanan, S., Haggström, L. and Wäppling, R. (1971) Mössbauer study of synthetic ferriphlogopite,  $\text{KMg}_3\text{Fe}^{3+}\text{Si}_3\text{O}_{10}(\text{OH})_2$ .

- Phys. Stat. Sol. (b) 48, K137-K138.
- Artman, J.O. (1971) Electric-field gradient calculations in ionic crystals, pp. 187-211 in Mössbauer Effect Methodology, Vol. 7, ed. I.J. Gruverman, Plenum Press, New York.
- Babb, S.E. and Robertson, Jr., W.W. (1963) High pressure spectroscopy of solids, Chapter 5.vi, pp. 375-409 in High Pressure Physics and Chemistry, Vol. 1, ed. R.S. Bradley, Academic Press, London.
- Balchan, A.S. and Drickamer, H.G. (1959) Effect of pressure on the spectra of olivine and garnet. J. Appl. Phys. 30, 1446-1447.
- Bancroft, G.M. (1974) Mössbauer Spectroscopy: An Introduction for Inorganic Chemists and Geochemists. McGraw-Hill, Maidenhead, England.
- Bancroft, G.M., Burns, R.G. and Stone, A.J. (1968) Applications of the Mössbauer effect to silicate mineralogy - II. Iron silicates of unknown and complex crystal structures. Geochim. Cosmochim. Acta. 32, 547-559.
- Bancroft, G.M., Maddock, A.G. and Burns, R.G. (1967) Applications of the Mössbauer effect to silicate mineralogy - I. Iron silicates of known crystal structure. Geochim. Cosmochim. Acta. 31, 2219-2246.
- Bargeron, C.B., Avinor, M. and Drickamer, H.G. (1971) The effect of pressure on the Mössbauer resonance for  $^{57}\text{Fe}$  in  $\text{MnS}_2$ . Inorg. Chem. 10, 1338-1341.
- Bashkirov, Sh. Sh., Kurbatov, G.D., Manopov, R.A., Penkov, I.N., Sadykov, E.K. and Chistiakov, V.A. (1967) Ilmenite ( $\text{FeTiO}_3$ ) examined with the aid of the nuclear gamma-resonance method. Doklady, Earth Sciences Sections (trans.). 173, 89-91.

- Bassett, W.A. (1974) The application of the diamond anvil cell to geophysical and geochemical problems. Crosby Lecture Series, Department of Earth and Planetary Sciences, Massachusetts Institute of Technology, February-April, 1974.
- Bell, P.M. and Mao, H.K. (1972) Apparatus for the measurement of crystal-field spectra of single crystals. Ann. Rep. Dir. Geophys. Lab. 608-611.
- Birch, F. (1952) Elasticity and constitution of the Earth's interior. J. Geophys. Res. 57, 227-286.
- Böwen, L.H., Weed, S.B. and Stevens, J.G. (1969) Mössbauer study of micas and their potassium-depleted products. Amer. Mineral. 54, 72-84.
- Bradley, R.S., Jamil, A.K. and Munro, D.C. (1964) The electrical conductivity of olivine at high temperatures and pressures. Geochim. Cosmochim. Acta. 28, 1669-1678.
- Bradley, R.S., Milnes, G.J. and Munro, D.C. (1973) The electrical conductivities at elevated temperatures and pressures of polycrystalline manganese, cobalt and nickel orthosilicates. Geochim. Cosmochim. Acta. 37, 2379-2394.
- Brown, G.M. and Prewitt, C.T. (1973) High temperature crystal chemistry of hortonolite. Amer. Mineral. 58, 577-587.
- Bullen, K.E. (1973) Cores of terrestrial planets. Nature. 243, 68-70.
- Burns, R.G. (1969a) Optical absorption in silicates, pp. 191-211 in The Application of Modern Physics to the Earth and Planetary Interiors, ed. S.K. Runcorn, J. Wiley and Sons, London.
- Burns, R.G. (1969b) Site preferences of transition metal ions in silicate crystal structures. Chem. Geol. 5, 275-283.

- Burns, R.G. (1970) Mineralogical Applications of Crystal-field Theory.  
Cambridge University Press, Cambridge, England.
- Burns, R.G. (1972) Mixed valencies and site occupancies of iron in silicate minerals from Mössbauer spectroscopy. Canad. J. Spectrosc. 17, 51-59.
- Burns, R.G. (1974) The polarized spectra of iron in silicates: Olivine. A discussion of neglected contributions from  $Fe^{2+}$  ions in M(1) sites. Amer. Mineral. 59, 625-629.
- Burns, R.G. and Huggins, F.E. (1972) Cation determinative curves for Mg-Fe-Mn olivines from vibrational spectra. Amer. Mineral. 57, 967-985.
- Burns, R.G., Huggins, F.E. and Drickamer, H.G. (1972a) Applications of high pressure Mössbauer spectroscopy to mantle mineralogy. XXIV<sup>th</sup> Intern. Geol. Congress, Section Reports. 14, 113-123.
- Burns, R.G., Tossell, J.A. and Vaughan, D.J. (1972b) Pressure-induced reduction of a ferric amphibole. Nature Phys. Sci. 240, 33-35.
- Cameron, M., Sueno, S., Prewitt, C.T. and Papike, J.J. (1973) High temperature crystal chemistry of acmite, diopside, hedenbergite, jadeite, spodumene and ureyite. Amer. Mineral. 58, 594-618.
- Carmichael, I.S.E., Fyfe, W.S. and Machin, D.J. (1966) Low spin ferrous iron in the iron silicate deerite. Nature. 211, 1389.
- Champion, A.R. and Drickamer, H.G. (1967) The effect of pressure on the Mössbauer resonance in hemin and iron phthalocyanine. Proc. Nat. Acad. Sci. 58, 876-883.
- Champion, A.R., Vaughan, R.W. and Drickamer, H.G. (1967) Effect of pressure on the Mössbauer resonance in ionic compounds of iron. J. Chem.



- Phys. 47, 2583-2590.
- Christoe, C.W. and Drickamer, H.G. (1970) Effect of pressure on the quadrupole interaction in iron-fluorine compounds. Phys. Rev. B3, 1813-1822.
- Christophe-Michel-Levy, M. (1956) Reproduction artificielle des grenats calciques: grossulaire et andradite. Bull. Soc. franc. Min. Crist. 79, 124-128.
- Clark, Jr., S.P. (1957a) Radiative transfer in the Earth's mantle. Trans. Amer. Geophys. Union. 38, 931-937.
- Clark, Jr., S.P. (1957b) Absorption spectra of some silicates in the visible and near infrared. Amer. Mineral. 42, 732-742.
- Coes, L. (1955) High-pressure minerals. J. Amer. Ceram. Soc. 38, 298.
- Cohen, J.A. and Drickamer, H.G. (1973) The effect of pressure on  $^{57}\text{Fe}$  hyperfine fields in ferromagnetic PdCo alloys. Phys. Rev. B7, 960-975.
- Cotton, F.A. (1971) Chemical Applications of Group Theory. 2nd edition, Wiley-Interscience, New York.
- Crowley, M.S. and Roy, R. (1964) Crystalline solubility in the muscovite and phlogopite groups. Amer. Mineral. 49, 348-362.
- Cukiermann, M. and Uhlmann, D.R. (1974) Effects of iron oxidation state on viscosity, lunar composition, 15555. J. Geophys. Res. 79, 1594-1598.
- Danon, J. (1966) Lectures on the Mössbauer Effect. Gordon and Breach, Inc., New York.
- Debrunner, P., Vaughan, R.W., Champion, A.R., Cohen, J., Moyzis, J. and Drickamer, H.G. (1966) Versatile high pressure Mössbauer apparatus.

Rev. Sci. Instrs. 37, 1310-1315.

Deer, W.A., Howie, R.S. and Zussman, J. (1963) Chain Silicates, Vol. 2, Rock-forming Minerals. Longmans, London.

Drickamer, H.G. (1965) The effects of high pressure on the electronic structure of solids. Solid State Physics. 17, 1-133.

Drickamer, H.G., Bastron, V.C., Fisher, D.C. and Grenoble, D.C. (1970) The high pressure chemistry of iron. J. Sol. State Chem. 2, 94-104.

Drickamer, H.G. and Frank, C.W. (1973) Electronic Transitions and the High Pressure Chemistry and Physics of Solids. Chapman and Hall, London.

Drickamer, H.G., Frank, C.W. and Slichter, C.P. (1972) Optical vs. thermal transitions in solids at high pressures. Proc. Nat. Acad. Sci. 69, 933-937.

Drickamer, H.G., Lewis, Jr., G.K. and Fung, S.C. (1969a) The oxidation state of iron at high pressure. Science. 163, 885-890.

Drickamer, H.G., Vaughan, R.W. and Lewis, Jr., G.K. (1969b) The effect of high pressure on the oxidation state of iron. Comm. Sol. State Phys. 1, 163-167.

Duba, A. (1972) Electrical conductivity of olivine. J. Geophys. Res. 77, 2483-2495.

Duba, A., Heard, H.C. and Schock, R.N. (1974) Electrical conductivity of olivine at high pressure and under controlled oxygen fugacity. J. Geophys. Res. 79, 1667-1673.

Duba, A., Ito, J. and Jamieson, J.C. (1973) The effect of ferric iron on the electrical conductivity of olivine. Earth Planet. Sci. Lett. 18, 279-284.

- Duba, A. and Nicholls, I.A. (1973) The influence of oxidation state on the electrical conductivity of olivine. Earth Planet. Sci. Lett. 18, 59-64.
- Eibschutz, M. and Ganiel, U. (1967) Mössbauer studies of  $\text{Fe}^{2+}$  in paramagnetic fayalite. Sol. State Comm. 5, 267-270.
- Eibschutz, M., Ganiel, U. and Shtrikman, S. (1966) Measurement of trigonal field splitting of  $\text{Fe}^{2+}$  in  $\text{GeFe}_2\text{O}_4$  by the Mössbauer effect. Phys. Rev. 151, 245-247.
- Erickson, N.E. (1967) Mössbauer spectroscopy of iron compounds, Chapter 6, pp. 86-104 in The Mössbauer Effect and Its Application in Chemistry, Vol. 68, Advances in Chemistry Series, ed. R.F. Gould, American Chemical Society, Washington, D.C.
- Ernst, W.G. and Wai, C.M. (1970) Mössbauer, infrared, X-ray and optical study of cation ordering and dehydrogenation in natural and heat-treated sodic amphiboles. Amer. Mineral. 55, 1226-1258.
- Eugster, H.P. (1972) Reduction and oxidation in metamorphism. XXIV<sup>th</sup> Intern. Geol. Congress, Section Reports. 10, 3-11.
- Figgis, B.N. (1968) Introduction to Ligand Fields. Interscience, J. Wiley and Sons, New York.
- Fisher, D.C. and Drickamer, H.G. (1971) The effect of pressure on the spin-state of iron in ferrous phenanthroline compounds. J. Chem. Phys. 54, 4825-4837.
- Fluck, E., Kerler, W. and Neuwirth, W. (1963) The Mössbauer effect and its significance in chemistry. Angew. Chem. (Intern. Ed.). 2, 277-287.
- Foit, Jr., F.F. and Peacor, D.R. (1973) The anorthite crystal structure at

- 410 and 830 °C. Amer. Mineral. 58, 665-675.
- Frank, C.W. and Drickamer, H.G. (1972) The effect of pressure on the electronic structure of twelve  $\beta$ -diketone complexes. J. Chem. Phys. 56, 3551-3565.
- Fukao, Y., Mizutani, H. and Uyeda, S. (1968) Optical absorption spectra at high temperatures and radiative thermal conductivity of olivines. Phys. Earth Planet. Ints. 1, 57-62.
- Fyfe, W.S. (1960) The possibility of d electron coupling in olivine at high pressures. Geochim. Cosmochim. Acta. 19, 141-143.
- Gaffey, M.J. (1974) Unpublished Ph.D. thesis, Massachusetts Institute of Technology, Cambridge, MA.
- Gaffney, E.S. (1972) Crystal-field effects in mantle minerals. Phys. Earth Planet. Ints. 6, 385-390.
- Gaffney, E.S. and Anderson, D.L. (1973) Effect of low spin  $\text{Fe}^{2+}$  on the composition of the lower mantle. J. Geophys. Res. 78, 7005-7014.
- Gallagher, P.K., MacChesney, J.B. and Buchanan, D.N.E. (1965) Mössbauer effect in the system  $\text{BaFeO}_{2.5-3.0}$ . J. Chem. Phys. 43, 516-520.
- Ganiel, U. and Shtrikman, S. (1969) Crystal-field studies of  $\text{Fe}^{2+}$  by the Mössbauer effect:  $\text{FeF}_2$ . Phys. Rev. 177, 503-508.
- Gardiner, R.G., Hamaan, S.D. and Linton, M. (1970) Oxidation state of ferric salts at high pressures. Aust. J. Chem. 23, 2369-2373.
- Geller, S., Williams, H.J., Sherwood, R.C. and Espinosa, G.P. (1962) Substitutions of divalent transition metal ions in yttrium iron garnet. J. Appl. Phys. 33, 1195-1196.
- Gibbons, R.V., Ahrens, T.J. and Rossman, G.R. (1974) A spectrographic

- interpretation of the shock produced color change in rhodonite ( $\text{MnSiO}_3$ ): The shock-induced reduction of Mn(III) to Mn(II). Amer. Mineral. 59, 177-182.
- Grant, R.W. (1967) Study of magnetic properties of minerals using the Mössbauer effect, Chapter 3, pp. 34-51 in The Mössbauer Effect and Its Application in Chemistry, Vol. 68, Advances in Chemistry Series, ed. R.F. Gould, American Chemical Society, Washington, D.C.
- Greenwood, N.N. (1970) Mössbauer spectroscopy, Chapter 12, pp. 633-707 in Physical Chemistry: An Advanced Treatise, Vol. 4, ed. D. Henderson, Academic Press, New York.
- Grenoble, D.C. and Drickamer, H.G. (1971) Effect of pressure on the electronic structure of ferric hydroxamates and ferrichrome A. Proc. Nat. Acad. Sci. 68, 549-553.
- Hafner, S.S. and Huckenholz, H.G. (1971) Mössbauer spectrum of synthetic ferridiopside. Nature. 233, 9-11.
- Hara, Y., Shirotani, I., Sakai, N., Nagakura, S. and Minomura, S. (1974) Pressure effect on the absorption spectra of iron compounds. Bull. Chem. Soc. Japan. 47, 434-437.
- Hazen, R.M. (1972) Unpublished M.Sc. thesis, Massachusetts Institute of Technology, Cambridge, MA.
- Hazen, R.M. and Abu-Eid, R.M. (1974) Crystallography of the displacive high pressure gillespite phase transformation (abstract). Trans. Amer. Geophys. Union. 55, 463.
- Hazen, R.M. and Burnham, C.W. (1973) The crystal structures of one-layer phlogopite and annite. Amer. Mineral. 58, 889-900.

- Hazen, R.M. and Wones, D.R. (1972) The effect of cation substitutions on the physical properties of trioctahedral micas. Amer. Mineral. 57, 103-129.
- Hazon, Y. (1971)  $H_c$ -QS-IS correlations in octahedral iron compounds, pp. 147-166 in Mössbauer Effect Methodology, Vol. 7, ed. I.J. Gruverman, Plenum Press, New York.
- Herber, R.H. (1967) The Mössbauer effect and its application in chemistry, Chapter 1, pp. 1-20 in The Mössbauer Effect and Its Application in Chemistry, Vol. 68, Advances in Chemistry Series, ed. R.F. Gould, American Chemical Society, Washington, D.C.
- Holzappel, W. (1970) Mössbauer studies on solids under high pressures: A review. High Temp. High Press. 2, 241-258.
- Holzappel, W. and Drickamer, H.G. (1969) Effect of pressure on the oxidation state of iron in  $FeCl_3 \cdot 6H_2O$ ,  $FeCl_3 \cdot 6NH_3$ , and  $FeF_3 \cdot 3H_2O$ . J. Chem. Phys. 50, 1480-1481.
- Hsu, L.C. (1968) Selected phase relationships in the system Al-Mn-Fe-Si-O-H: A model for garnet equilibria. J. Petrol. 9, 40-83.
- Huckenholz, H.G. (1969) Synthesis and stability of titanium andradite. Amer. J. Sci. (Schairer Vol.). 267, 209-232.
- Huckenholz, H.G. and Yoder, Jr., H.S. (1971) Andradite stability relations in the  $CaSiO_3$ - $Fe_2O_3$  join up to 30 kl. N. Jb. Miner. Abh. 114, 246-280.
- Huebner, J.S. (1971) Buffering techniques for hydrostatic systems at elevated pressures, Chapter 5, pp. 123-177 in Research Techniques for

- High Pressure and High Temperature, ed. G.C. Ulmer, Springer-Verlag, New York.
- Hush, N.S. (1967) Intervalence-transfer absorption, Part 2. Theoretical considerations and spectroscopic data. Prog. Inorg. Chem. 8, 391-444.
- Ingalls, R. (1964) Electric-field gradient tensor in ferrous compounds, Phys. Rev. 133A, 787-795.
- Ito, J. (1967) A new yttrium magnesium silicate garnet,  $Y_6Mg_5Si_5O_{24}$ , and its rare earth and nickel analogues. Mater. Res. Bull. 2, 1093-1098.
- Ito, J. and Frondel, C. (1967) Synthetic zirconium and titanium garnets. Amer. Mineral. 52, 773-781.
- Jagitsch, R. (1956) The synthesis of some Skarn minerals from the powdered components. Arkiv Kemi. 9, 319-325. (in German)
- Johnson, C.E. (1969) Mössbauer effect studies of magnetic minerals, pp. 485-496 in The Application of Modern Physics to the Earth and Planetary Interiors, ed. S.K. Runcorn, J. Wiley and Sons, London.
- Johnson, K.H. (1973) Scattered wave theory of the chemical bond. Adv. Quant. Chem. 7, 143-185.
- Kalvius, G.M. and Kankeleit, E. (1972) Recent improvements in instrumentation and methods of Mössbauer spectroscopy, pp. 9-88 in Mössbauer Spectroscopy and Its Applications, I.A.E.A., Vienna.
- Kasper, H. and Drickamer, H.G. (1968) High pressure Mössbauer resonance studies of compounds of iron with group V and VI elements. Proc. Nat. Acad. Sci. 60, 773-775.
- Kittel, C. (1966) Introduction to Solid-state Physics. 3rd edition, J. Wiley and Sons, New York.

- Kündig, W. and Hargrove, R.S. (1969) Electron hopping in magnetite. Solid State Comm. 7, 223-227.
- Kushiro, I. (1973) Regularities in the shift of liquidus boundaries in silicate systems and their significance in magma genesis. Ann. Rep. Dir. Geophys. Lab. 497-502.
- Lever, A.B.P. (1968) Inorganic Electronic Spectroscopy. Elsevier Publishing Company, Amsterdam.
- Lewis, Jr., G.K. and Drickamer, H.G. (1968a) High-pressure Mössbauer studies of  $^{57}\text{Fe}$  in silicate and phosphate glasses. J. Chem. Phys. 49, 3785-3789.
- Lewis, Jr., G.K. and Drickamer, H.G. (1968b) High-pressure Mössbauer resonance studies of the conversion of Fe(III) to Fe(II) in ferric halides. Proc. Nat. Acad. Sci. 61, 414-421.
- Lindqvist, B. (1966) Hydrothermal synthesis studies of potash-bearing sesquioxide-silica systems. Geol. Fören. Stockholm Förhandl. 88, 133-178.
- Liu, L.G., Bassett, W.A. and Takahashi, T. (1974) Isothermal compressions of a spinel phase of  $\text{Co}_2\text{SiO}_4$  and magnesian ilmenite. J. Geophys. Res. 79, 1171-1174.
- Loeffler, B.M., Burns, R.G., Tossell, J.A., Vaughan, D.J. and Johnson, K.H. (1974) Charge transfer in lunar materials. Interpretation of UV-visible spectral properties of the moon. Submitted to Proc. Fifth Lunar Sci. Conf., Geochim. Cosmochim. Acta. Suppl. 5, Vol. 3.
- Low, W. and Zeira, S. (1972) E.S.R. spectra of  $\text{Mn}^{2+}$  in heat-treated aragonite. Amer. Mineral. 57, 1115-1124.



- Lyubutin, I.S. (1971) Magnetism and crystal chemistry of garnets studied by Mössbauer spectroscopy, pp. 467-489 in Proceedings of the Conference on the Application of the Mössbauer Effect, ed. I. Dezsi, Akademiai Kiado, Budapest.
- Lyubutin, I.S. and Dodokin, A.P. (1971a) Temperature dependence of the Mössbauer effect for tetrahedral iron atoms in garnets. Sov. Phys. Cryst. (trans.). 15, 936-938.
- Lyubutin, I.S. and Dodokin, A.P. (1971b) Temperature dependence of the Mössbauer effect for  $\text{Fe}^{2+}$  in dodecahedral coordination in garnet. Sov. Phys. Cryst. (trans.). 15, 1091-1092.
- Lyubutin, I.S., Dodokin, A.P. and Belyaev, L.M. (1970) Temperature dependence of the Mössbauer effect for octahedral iron atoms in garnets. Sov. Phys. Sol. State. (trans.). 12, 1100-1102.
- Maddock, A.G. (1972) Mössbauer spectroscopy in mineralogy, pp. 329-347 in Mössbauer Spectroscopy and Its Applications, I.A.E.A., Vienna.
- Mao, H.K. (1973) Electrical and optical properties of the olivine series at high pressure. Observations of optical absorption and electrical conductivity in magnesiowüstite at high pressures. Thermal and electrical properties of the Earth's mantle. Ann. Rep. Dir. Geophys. Lab. 552-564.
- Mao, H.K. and Bell, P.M. (1972) Electrical conductivity and the red shift of absorption in olivine and spinel at high pressure. Science. 176, 403-406.
- Mason, B.H. (1966) Principles of Geochemistry. 3rd edition, J. Wiley and Sons, New York.

Mössbauer, R.L. (1958) Kernresonanzfluoreszenz von gammastrahlung in  $^{191}\text{Ir}$ .

Z. Physik. 151, 124-143.

Navrotsky, A. (1971) The intracrystalline cation distribution and the thermodynamics of solid solution formation in the system  $\text{FeSiO}_3\text{-MgSiO}_3$ .

Amer. Mineral. 56, 201-211.

Novak, G.A. and Gibbs, G.V. (1971) The crystal chemistry of the silicate garnets. Amer. Mineral. 56, 791-825.

Nozik, A.J. and Kaplan, M. (1967) Significance of the lattice contribution to Mössbauer quadrupole splitting. Phys. Rev. 159, 273-276.

O'Reilly, W. (1969) Application of neutron diffraction and Mössbauer effect to rock magnetism, pp. 479-484 in The Application of Modern Physics to the Earth and Planetary Interiors, ed. S.K. Runcorn, J. Wiley and Sons, London.

Panyushkin, V.N., De Pasquali, G. and Drickamer, H.G. (1969) Effect of pressure on the oxidation state of ferrates. J. Chem. Phys. 51, 3305-3308.

Peacor, D.R. (1973) High temperature single crystal study of natrolite. Amer. Mineral. 58, 676-680.

Pillars, W.W. and Peacor, D.R. (1973) The crystal structure of beta eucryptite as a function of temperature. Amer. Mineral. 58, 681-690.

Pipkorn, D.N., Edge, C.K., Debrunner, P., De Pasquali, G., Drickamer, H.G. and Frauenfelder, H. (1964) Mössbauer effect in iron under very high pressure. Phys. Rev. 135A, 1604-1612.

Pitt, G.D. and Tozer, D.C. (1970a) Optical absorption measurements on natural and synthetic ferromagnesian minerals subjected to high

- pressures. Phys. Earth Planet. Ints. 2, 179-188.
- Pitt, G.D. and Tozer, D.C. (1970b) Radiative heat transfer in dense media and its magnitude in olivines and some other ferromagnesian minerals under typical upper mantle conditions. Phys. Earth Planet. Ints. 2, 189-199.
- Press, F. (1970) Earth models consistent with geophysical data. Phys. Earth Planet. Ints. 3, 3-22.
- Ringwood, A.E. (1966a) The chemical composition and origins of the Earth, pp. 287-356 in Advances in Earth Sciences, ed. P.M. Hurley, M.I.T. Press, Cambridge, MA.
- Ringwood, A.E. (1966b) Chemical evolution of the terrestrial planets. Geochim. Cosmochim. Acta. 30, 41-104.
- Ringwood, A.E. (1970) Phase transformations and the constitution of the mantle. Phys. Earth Planet. Ints. 3, 109-155.
- Roy, D.M. and Roy, R. (1957) System  $\text{CaO-Al}_2\text{O}_3\text{-SiO}_2\text{-H}_2\text{O}$  VI. The grossularite- $3\text{CaO}\cdot\text{Al}_2\text{O}_3\cdot 6\text{H}_2\text{O}$  join (abstract). Bull. Geol. Soc. Amer. 68, 1788-1789.
- Runciman, W.A. and Sengupta, D. (1974) The spectrum of  $\text{Fe}^{2+}$  in silicate garnets. Amer. Mineral. 59, 567-572.
- Runciman, W.A., Sengupta, D. and Gourley, J.T. (1973) The polarized spectra of iron in silicates. II. Olivine. Amer. Mineral. 58, 451-456.
- Sawatzky, G.A., Van der Woude, F. and Morrish, A.M. (1969) Recoilless-fraction ratios for  $^{57}\text{Fe}$  in octahedral and tetrahedral sites of a spinel and garnet. Phys. Rev. 183, 383-386.
- Schairer, J.F. and Bowen, N.L. (1955) The system  $\text{K}_2\text{O-Al}_2\text{O}_3\text{-SiO}_2$ . Amer. J.

Sci. 253, 681-746.

- Schmidtke, H.H. (1968) Electronic absorption spectroscopy, pp. 107-166 in Physical Methods in Advanced Inorganic Chemistry, eds. H.A.O. Hill and P. Day, Interscience, J. Wiley and Sons, London.
- Seifert, F. and Schreyer, W. (1971) Synthesis and stability of micas in the system  $K_2O-MgO-SiO_2-H_2O$  and their relations to phlogopite. Contr. Mineral. Petrol. 30, 196-215.
- Semet, M.P. (1973) A crystal-chemical study of synthetic magnesiohastingsite. Amer. Mineral. 58, 480-494.
- Shankland, T.J. (1969) Transport properties of olivine, pp. 175-190 in The Application of Modern Physics to the Earth and Planetary Interiors, ed. S.K. Runcorn, J. Wiley and Sons, London.
- Shankland, T.J. (1972) Velocity-density systematics: Derivation from Debye theory and the effect of ionic size. J. Geophys. Res. 77, 3750-3758.
- Shankland, T.J. and Chung, D.H. (1974) General relationships among sound speeds. II. Theory and discussion. Phys. Earth Planet. Ints. 8, 121-129.
- Shankland, T.J., Duba, A.G. and Woronow, A. (1974) Pressure shifts of optical absorption bands in iron-bearing garnet, spinel, olivine, pyroxene and periclase. J. Geophys. Res. 79, (in press).
- Shannon, R.D. (1974) Systematic studies of interatomic distances of oxides (abstract), p. 45, Abstracts, Petrophysics: The Physics and Chemistry of Minerals and Rocks, NATO Advanced Study Institute, Newcastle-Upon-Tyne, England.
- Shannon, R.D. and Prewitt, C.T. (1969) Effective ionic radii in oxides and

- fluorides. Acta Cryst. B25, 925-946.
- Shenoy, G.K., Kalvius, G.M. and Hafner, S.S. (1969) Magnetic behavior of the  $\text{FeSiO}_3$ - $\text{MgSiO}_3$  orthopyroxene system from NGR in  $^{57}\text{Fe}$ . J. Appl. Phys. 40, 1314-1316.
- Simmons, G. and Wang, H. (1971) Single Crystal Elastic Constants and Calculated Aggregate Properties. M.I.T. Press, Cambridge, MA.
- Sinha, K.P. and Sinha, A.P.B. (1968) On the quadrupole splitting of Mössbauer spectra in ferros spinels. Indian J. Pure Appl. Phys. 6, 105-108.
- Slichter, C.P. and Drickamer, H.G. (1972) Pressure induced electronic changes in compounds of iron. J. Chem. Phys. 56, 2142-2160.
- Smyth, J.R. (1973) An orthopyroxene structure up to 850 °C. Amer. Mineral. 58, 636-648.
- Smyth, J.R. and Hazen, R.M. (1973) The crystal structures of forsterite and hortonolite at several temperatures up to 900 °C. Amer. Mineral. 58, 588-593.
- Stone, A.J. (1967) Appendix to Bancroft et al. J. Chem. Soc. A, 1966-1971.
- Strens, R.G.J. (1966) Pressure-induced spin pairing in gillespite,  $\text{BaFe(II)Si}_4\text{O}_{10}$ . Chem. Comm. 777.
- Strens, R.G.J. (1969) The nature and geophysical importance of spin-pairing in minerals of iron (II), pp. 213-220 in Applications of Modern Physics to the Earth and Planetary Interiors, ed. S.K. Runcorn, J. Wiley and Sons, London.
- Strens, R.G.J. (1974) The stability of  $\text{Fe}_2\text{O}$  at high pressure (abstract), p. 54, Abstracts, Petrophysics: The Physics and Chemistry of Minerals and Rocks, NATO Advanced Study Institute, Newcastle-Upon-

Tyne, England.

- Sueno, S., Cameron, M., Papike, J.J. and Prewitt, C.T. (1973) The high temperature crystal chemistry of tremolite. Amer. Mineral. 58, 649-664.
- Syassen, K. and Holzapfel, W.B. (1973) Effect of pressure and temperature on the magnetic hyperfine interaction of Fe(II) in CoO. Phys. Rev. B8, 1799-1805.
- Tossell, J.A., Vaughan, D.J., Burns, R.G. and Huggins F.E. (1972) Do ferric ions occur in the mantle? (abstract). Trans. Amer. Geophys. Union. 53, 1130.
- Tossell, J.A., Vaughan, D.J. and Johnson, K.H. (1973) Electronic structure of ferric iron octahedrally coordinated to oxygen. Nature Phys. Sci. 244, 42-45.
- Tossell, J.A., Vaughan, D.J. and Johnson, K.H. (1974) The electronic structure of rutile, wüstite and hematite from molecular orbital calculations. Amer. Mineral. 59, 319-334.
- Travis, J.C. (1971) The electric field gradient tensor, Chapter 4, pp. 75-103 in An Introduction to Mössbauer Spectroscopy, ed. L. May, Plenum Press, New York.
- Vaughan, D.J. and Burns, R.G. (1972) Mössbauer spectroscopy and bonding in sulphide minerals containing four-coordinated iron. XXIV<sup>th</sup> Intern. Geol. Congress, Section Reports. 14, 158-170.
- Vaughan, D.J. and Tossell, J.A. (1973) Magnetic transitions observed in sulphide minerals at elevated pressures and their geophysical significance. Science. 179, 375-377.

- Vaughan, R.W. and Drickamer, H.G. (1967a) High pressure Mössbauer studies on  $\alpha\text{Fe}_2\text{O}_3$ ,  $\text{FeTiO}_3$  and  $\text{FeO}$ . J. Chem. Phys. 47, 1530-1536.
- Vaughan, R.W. and Drickamer, H.G. (1967b) Effect of pressure on the Mössbauer resonance in ferrocene and pyrite. J. Chem. Phys. 47, 468-472.
- Vinokurov, V.M., Gainullina, N.M., Evgrafova, L.A., Nizamutdinov, N.M. and Suslina, A.N. (1971)  $\text{Zr}^{4+} \rightarrow \text{Y}^{3+}$  isomorphism in zircon and the associated charge balance. Sov. Phys. Cryst. (trans.). 16, 262-265.
- Virgo, D. (1972) Preliminary fitting of  $^{57}\text{Fe}$  Mössbauer spectra of synthetic Mg-Fe richterites. Ann. Rep. Dir. Geophys. Lab. 513-516.
- Virgo, D. and Hafner, S.S. (1972) Temperature-dependent Mg,Fe distribution in lunar olivines. Earth Planet. Sci. Lett. 14, 305-312.
- Walker, L.R., Wertheim, G.K. and Jaccarino, V. (1961) Interpretation of the  $^{57}\text{Fe}$  isomer shift. Phys. Rev. Lett. 6, 98-101.
- Wang, P.J. and Drickamer, H.G. (1974) The reduction of Cu(II) at high pressure. J. Chem. Phys. 59, 713-717.
- Wäppling, R., Häggström, L. and Devanarayanan, S. (1972) Mössbauer investigation of iron in boron. Physica Scripta. 5, 97-98.
- Wertheim, G.K. (1964) Mössbauer Effect: Principles and Applications. Academic Press, Inc., New York.
- Whipple, E.R. (1973) Unpublished Ph.D. thesis, Massachusetts Institute of Technology, Cambridge, MA.
- White, W.B. and Keester, K.L. (1967) Selection rules and assignments for the spectra of ferrous iron in pyroxenes. Amer. Mineral. 52,

1508-1514.

White, W.B. and Moore, R.K. (1972) Interpretation of the spin-allowed bands of  $\text{Fe}^{2+}$  in silicate garnets. Amer. Mineral. 57, 1692-1710.

Wise, W.S. and Eugster, H.P. (1964) Celadonite: Synthesis, thermal stability and occurrence. Amer. Mineral. 49, 1031-1083.

Wones, D.R. (1963) Phase equilibria of ferriannite,  $\text{KFe}_3^{2+}\text{Fe}^{3+}\text{Si}_3\text{O}_{10}(\text{OH})_2$ . Amer. J. Sci. 261, 581-596.

Wood, B.J. and Strens, R.G.J. (1972) Calculation of crystal-field splittings in distorted coordination polyhedra: Spectra and thermodynamic properties of minerals. Mineral. Mag. 38, 909-917.

Yoder, Jr., H.S. (1950) Stability relations of grossularite. J. Geol. 58, 221-253.

Yoder, Jr., H.S. and Eugster, H.P. (1955) Synthetic and natural muscovites. Geochim. Cosmochim. Acta. 8, 225-280.



APPENDICES

Appendix A1: RESULTS FROM SYNTHESIS EXPERIMENTS

Appendix A2: SITE COMPRESSIBILITIES

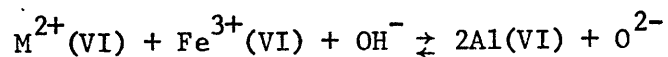
Appendix A3: COMPUTER ROUTINES

Appendix A1

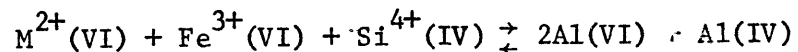
RESULTS FROM SYNTHESIS EXPERIMENTS

A1.1 The Substitution of Octahedral Aluminum by Ferric Iron in Muscovite

Natural muscovite analyses, as listed by Foster (1964) and Deer et al. (1963) rarely show more than 20% ferric iron substituting for aluminum in the octahedral sites, and as figure A1.1.1 attempts to show, the substitution of divalent cations for aluminum is usually more substantial. In fact, except for one analysis (#13, table 5, Deer et al. 1963), all ferric iron in muscovite could be accounted for by  $M^{2+}-Fe^{3+}$  coupled substitutions of the type:



or

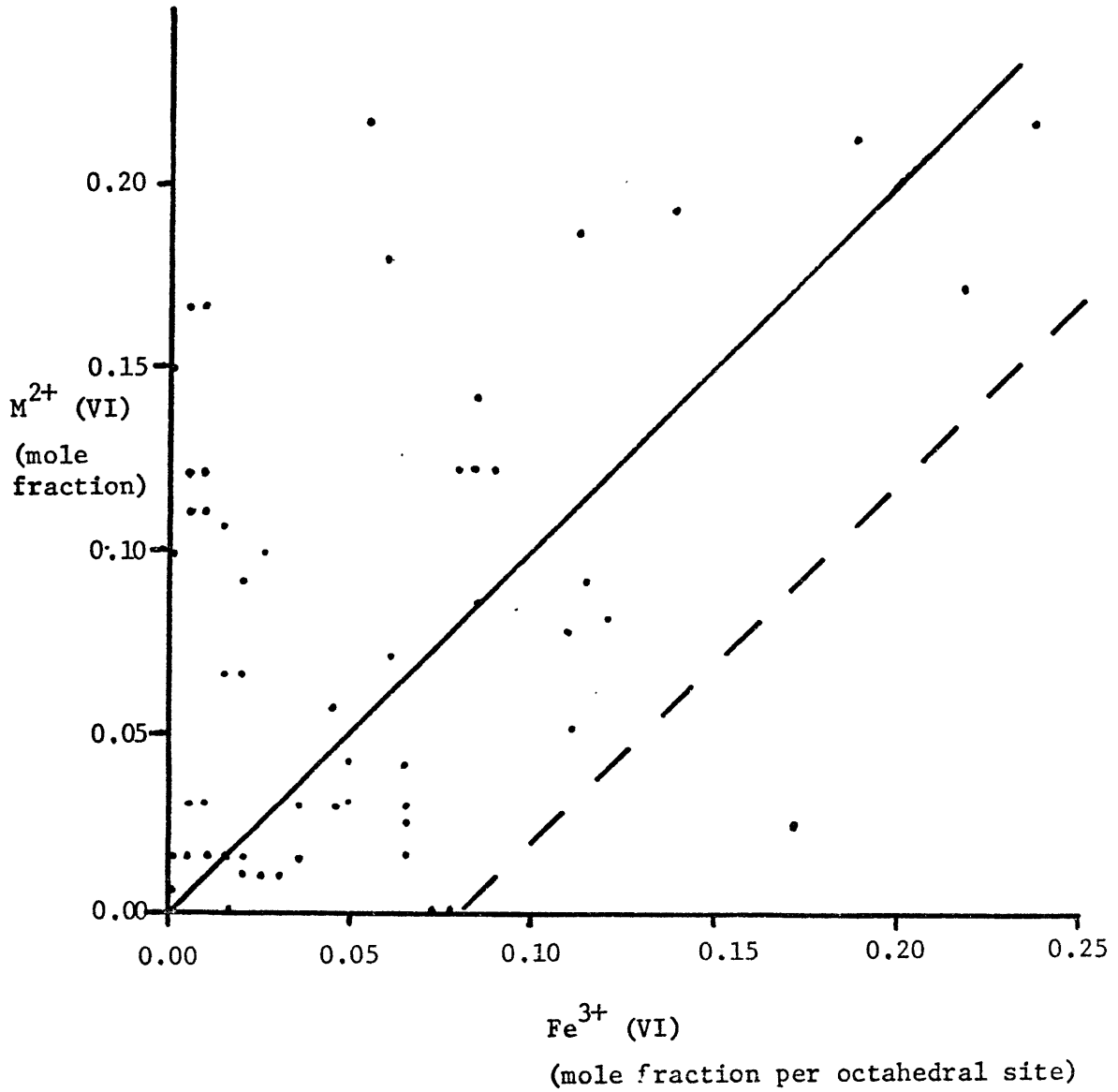


along with, at most, only 8% of the direct substitution of  $Fe^{3+}$  for  $Al^{3+}(VI)$ . The dashed line in figure A1.1.1 represents the limit of  $Fe^{3+}$  substitution according to this scheme. Excess  $M^{2+}$  content (above the full line in figure A1.1.1) can be explained by any combination of three possible substitutions:

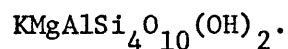
- (i)  $M^{2+} + OH^{-} \rightleftharpoons Al^{3+} + O^{2-}$ . This requires excess hydroxyls over 2 per formula unit, if all other factors are stoichiometric.
- (ii)  $M^{2+} + Si^{4+} \rightleftharpoons Al(VI) + Al(IV)$ . This requires excess Si over 3 per formula unit, if all other factors are stoichiometric.

Figure A1.1.1

Plot of octahedral divalent cations ( $M^{2+}$ ) against octahedral ferric iron for muscovite analyses listed by Foster (1964) and Deer et al. (1963). The full line at  $45^\circ$  to the axes represents the celadonite  $M^{2+}:Fe^{3+}$  ratio. The dashed line is the same ratio offset by 8% along the ferric iron axis.



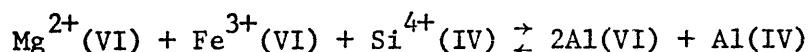
The composition tends towards phengite type compositions,



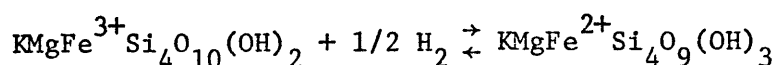
(iii)  $3\text{M}^{2+} \rightleftharpoons 2\text{Al}^{3+} + \text{Vac}$ . This substitution introduces a trioctahedral component and requires that the sum of the octahedral cations exceeds 2 per formula unit, if all other factors are stoichiometric.

Unfortunately, the considerable scope of the many coupled substitutions possible in a complex structure and composition such as that of muscovite, precludes any further analysis of the chemical component data of these micas. Both Foster (1964) and Forbes (1972) have documented just how sensitive is the hydroxyl content for maintaining overall charge balance between anions and cations, and Forbes (1972) suggested seven possible coupled substitutions involving  $\text{OH}^-$  and cations alone, without considering any coupled substitutions among just the cations. For this reason, studies of synthetic phases of controlled compositions are more informative regarding the substitution of  $\text{Fe}^{3+}$  for  $\text{Al(VI)}$  in muscovites.

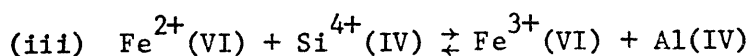
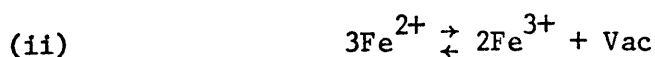
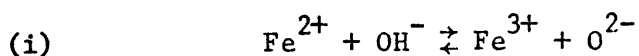
Crowley and Roy (1964) and Lindqvist (1966) have attempted to synthesize ferric-containing dioctahedral micas and both indicate that the limit of substitution of iron cations in the dioctahedral structure is about 30% of the aluminum in octahedral coordination. The experimental results (table 3.3(b)) found in the course of this study are also compatible with this limit. Wise and Eugster (1964) were able to substitute up to 50% of the  $\text{Al}^{3+}(\text{VI})$  by iron, by means of synthesizing celadonite,  $\text{KMgFe}^{3+}\text{Si}_4\text{O}_{10}(\text{OH})_2$ , which requires the coupled substitution:



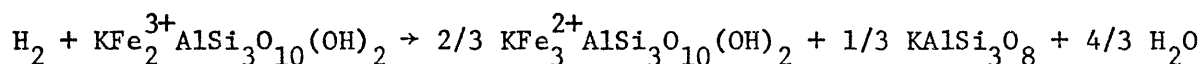
to relate it to muscovite. Other tetrasilicic dioctahedral micas which Wise and Eugster (1964) attempted to synthesize were unsuccessful except for  $\text{K}(\text{Mg}, \text{Fe}^{2+})\text{Fe}^{3+}\text{Si}_4\text{O}_{10}(\text{OH})_2$  compositions. These investigators also controlled oxygen fugacities, which neither Lindqvist (1966) nor Crowley and Roy (1964) reported in their studies, and suggested that the variation of d spacings and mean refractive index with oxygen fugacity can be best explained by the reaction:



The ferric contents in the micas synthesized in this study were towards either celadonite or ferrimuscovite end-member compositions from muscovite. Unlike previous studies,  $\text{Fe}^{2+}/\text{Fe}^{3+}$  ratios were directly measured by means of Mössbauer spectroscopy, which showed that up to 50% of the iron was present as ferrous in some of these synthetic micas. In most of these syntheses, the run product contained potassium feldspar and the intensity of the X-ray diffraction peaks of the feldspar relative to those of the mica appeared to be directly proportional to the  $\text{Fe}^{2+}/\text{Fe}^{3+}$  ratio measured by Mössbauer spectroscopy. There are three possible ways of accommodating  $\text{Fe}^{2+}$  as well as  $\text{Fe}^{3+}$  in muscovite:



Possibility (iii) may be ignored since the only product other than mica is  $\text{KAlSi}_3\text{O}_8$  which requires that an excess of Al be present in the mica contrary to the coupled substitution. Of the other two substitutions, (ii) can allow for the formation of  $\text{KAlSi}_3\text{O}_8$  along with the mica according to the hypothetical reaction for the ferrimuscovite component:



Experiments using  $\text{PtO}_2$  as an internal buffer (SE #38, 55) for high oxygen fugacity conditions suggest that all the iron in muscovite up to a limit of about 15% could be present as  $\text{Fe}^{\text{3+}}$ , but that any iron in muscovite above this amount would be present as  $\text{Fe}^{\text{2+}}$  in the form of a trioctahedral component for the most part. Since oxygen fugacities as high as those determined by the HM buffer are rare in nature, the limit of 8% direct substitution of  $\text{Fe}^{\text{3+}}$  for  $\text{Al}^{\text{3+}}$  suggested by the analyses of natural muscovites may be appropriate for more commonly encountered values of oxygen fugacity.

Ferric contents in dioctahedral micas in excess of 8% must therefore be stabilized by means of a coupled substitution with  $\text{M}^{\text{2+}}$ , especially  $\text{Mg}^{\text{2+}}$ , as discussed above. The exception referred to above (#13, table 5, Deer et al., 1963) may be explained as a muscovite formed in a highly oxidizing environment, since its ferric content is consistent with the limit found at very high oxygen fugacity.

This revision of the maximum amount of ferric iron substituting for octahedral aluminum to around 10% is consistent with the contents of  $\text{Mn}^{\text{3+}}$  and  $\text{Cr}^{\text{3+}}$  found in naturally occurring muscovites as well (Deer et al., 1963). This similarity suggests that size may be the determining factor,

since the sizes of these three trivalent cations are similar and about 0.10 Å larger than  $\text{Al}^{3+}$  (Shannon and Prewitt, 1969). However,  $\text{V}^{3+}$  also has a similar ionic radius, but  $\text{V}^{3+}$ -containing micas (roscoelites) with up to 70%  $\text{KV}_2\text{AlSi}_3\text{O}_{10}(\text{OH})_2$  component have been found in nature and the end member composition has also been synthesized, albeit with some  $\text{V}^{4+}$  present (Ito, 1965). To explain this, it is necessary to resort to a crystal field argument.

The Al site in muscovite has a cis configuration of the two  $\text{OH}^-$  anions (Güven, 1971) and would be expected to give rise to the d electron energy level diagram shown in figure A1.1.2 assuming an otherwise perfect octahedron. In this case, cations containing 1, 2, 4, 6, 7 and 9 3d electrons would be stabilized in such a site and 1 and 6 3d electron systems especially so. Thus, the small extra crystal field stabilization energy (CFSE) obtained by  $\text{V}^{3+}(\text{d}^2)$  must offset the unfavorable ionic radius and make the solid solution of  $\text{V}^{3+}$  for  $\text{Al}^{3+}$  extensive. This also explains why  $\text{V}^{4+}(\text{d}^1)$  might be stabilized in muscovite as well, since the energy level diagram strongly favors  $\text{d}^1$  systems.  $\text{Cr}^{3+}$ ,  $\text{Fe}^{3+}$  do not gain any CFSE over any other kind of octahedral site and ionic radii discriminates against incorporation of these trivalent cations into muscovite.  $\text{Mn}^{3+}(\text{d}^4)$  might be stabilized in this site, but depends on the splitting of the  $e_g$  levels.

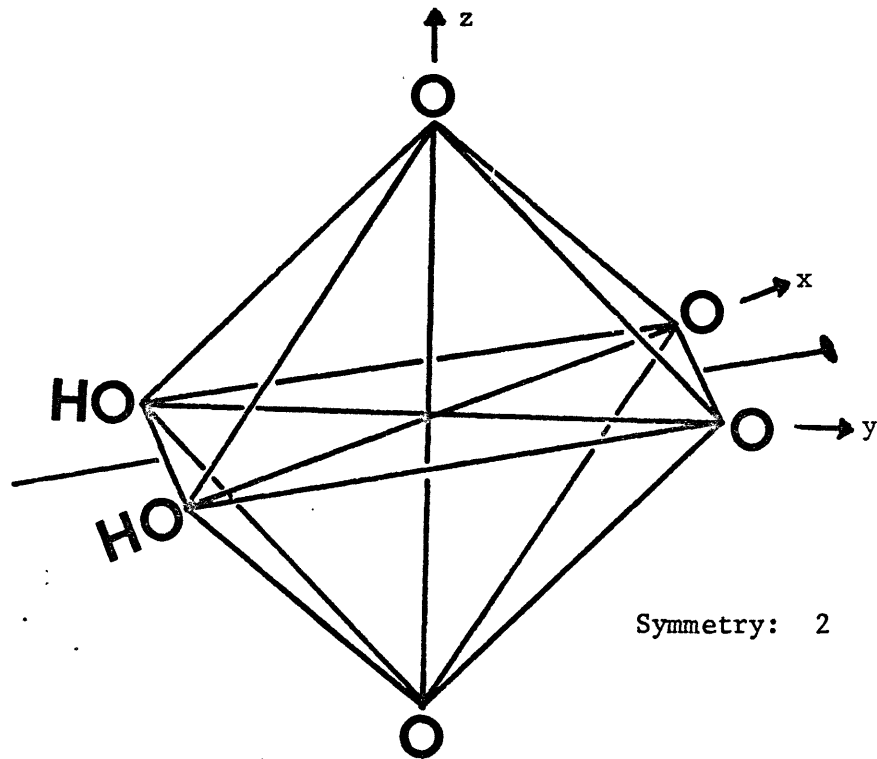
The layer stacking polymorphism and stability of muscovite are affected by the substitution of iron and magnesium for aluminum. Substitution of iron reduces the temperature of breakdown to  $\text{KAlSi}_3\text{O}_8$  and  $\text{Al}_2\text{O}_3$  at 2 kb. Both magnesium and iron substitution eliminate the metastable field found by Yoder and Eugster (1955) for  $\text{KAlSi}_3\text{O}_8 + \text{Al}_2\text{O}_3$  at end member



Figure A1.1.2

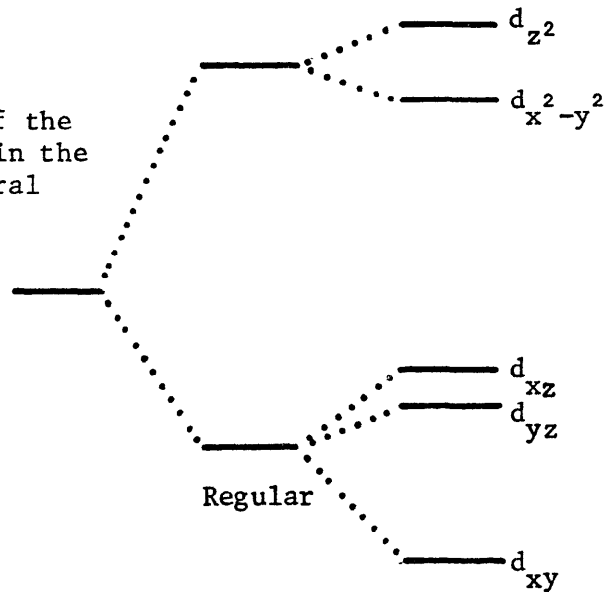
Upper: The octahedral site in muscovite showing the hydroxyl groups in the cis configuration.

Lower: Predicted order of the 3d energy levels in the muscovite octahedral site based on the site geometry.



The Octahedral Site in Muscovite

Predicted order of the 3d energy levels in the muscovite octahedral site.



Muscovite Site

muscovite compositions when the starting material was an oxide mix. The observed layer stacking polymorph of muscovite synthesized at about 600 °C is 1M (Yoder and Eugster, 1955) and the addition of iron cations does not appear to affect the polymorphism along the join toward ferrimuscovite. However, along the join toward celadonite which involves the substitution of both magnesium and iron cations, the observed layer stacking polymorph is 1Md, the disordered stacking scheme.

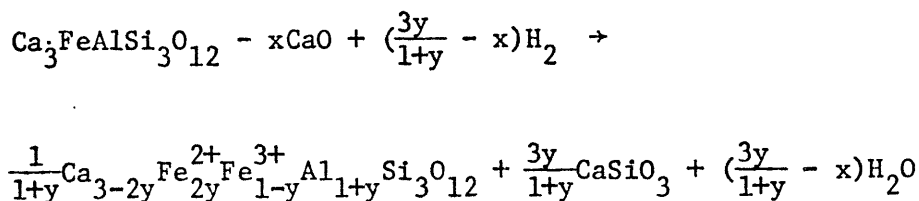
Conclusions:

1. At very high  $fO_2$  ( $\geq H/M$ ) the limit of direct substitution of  $Fe^{3+}$  for octahedral  $Al^{3+}$  in muscovite is about 15%. At commonly occurring  $fO_2$  values, the limit may be nearer 8%.
2. Ferric contents in dioctahedral micas greater than the above limits are stabilized by coupled substitution with  $M^{2+}$ , especially towards celadonite compositions.
3. The limit of 30% ferric substitution for  $Al^{3+}$ (VI) in muscovite proposed by both Crowley and Roy (1964) and by Lindqvist (1966) represents the limit of  $Fe^{3+}$  and  $Fe^{2+}$  substitution in muscovite;  $Fe^{2+}$  substitution for  $Al^{3+}$  accounts for at least half of the iron content at this limiting value.
4. If this analysis is correct, then the explanation why  $V^{3+}$  is so stable in the dioctahedral structure is probably due to CFSE. If the 5d orbitals are split as shown in figure A1.1.2, which is not unreasonable given the site geometry, then  $V^{3+}(d^2)$  will be stabilized and the other trivalent transition metals will not be.

We expect the substitution order  $V^{3+} \gg Cr^{3+} \gtrsim Mn^{3+} > Fe^{3+}$   
on this basis, ionic size having a small effect.

Al.2 Calculation of the Formula of the Garnet Formed in Synthesis Experiment #41

Synthesis experiment #41 was supposed to be the synthesis of the garnet phase of formula  $\text{Ca}_3\text{FeAlSi}_3\text{O}_{12}$ , the components of which were weighed out to correspond exactly to that formula. However, the XRD pattern of the run product showed the presence of small amounts of  $\text{CaCO}_3$  and  $\text{CaSiO}_3$  in addition to garnet and the Mössbauer spectrum of the run product showed that the garnet contained  $\text{Fe}^{2+}$  in the cubic or eight coordinate site which amounted to 8% of the total iron. Subsequently, an XRD pattern of the calcium hydroxide used in the synthesis mix showed the presence of  $\text{CaCO}_3$  and indicated that the synthesis mix for this garnet was, in fact, calcium deficient since  $\text{CaCO}_3$  has a formula weight of 100 compared to 74 for  $\text{Ca(OH)}_2$ . Using these facts and the following assumptions, it is the purpose of this section to calculate the composition of the garnet and the amount of  $\text{CaCO}_3$  present in the  $\text{Ca(OH)}_2$ . The assumptions that must be made are that the impurity  $\text{CaCO}_3$  is effectively inert during the synthesis run, that the other oxides were weighed out correctly and that no phases are present other than garnet,  $\text{CaSiO}_3$  and  $\text{CaCO}_3$ . If  $x\text{CaO}$  represents the calcium oxide deficiency due to the presence of  $\text{CaCO}_3$  in  $\text{Ca(OH)}_2$ , then the following equation can be written which preserves the stoichiometry of the other elements in this hydrothermal synthesis:



Balancing Ca:

$$3 - x = \frac{3-2y}{1+y} + \frac{3y}{1+y}$$

$$x = 3 - \frac{3+y}{1+y}$$

$$x = \frac{2y}{1+y} \tag{A1.2.1}$$

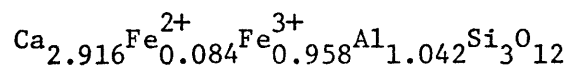
The Mössbauer spectrum gives an approximate  $\text{Fe}^{2+}/\text{Fe}^{3+}$  ratio. For the garnet phase formed in SE #41:

$$\frac{\text{Fe}^{2+}}{\text{Fe}^{2+} + \text{Fe}^{3+}} = \frac{2y}{1-y+2y} = \frac{2y}{1+y}$$

And so

$$x = \frac{\text{Fe}^{2+}}{\text{Fe}^{2+} + \text{Fe}^{3+}}$$

For this particular case, the  $\text{Fe}^{2+}$ /total iron ratio as measured by Mössbauer spectroscopy is directly comparable to the CaO deficiency and so  $x = 0.08$ . From equation A1.2.1,  $y$  is calculated to be 0.042 and so the correct composition of this garnet is:



or by component garnets:

- 2.8% almandine,  $\text{Fe}_3\text{Al}_2\text{Si}_3\text{O}_{12}$
- 49.3% grossular,  $\text{Ca}_3\text{Al}_2\text{Si}_3\text{O}_{12}$
- 47.9% andradite,  $\text{Ca}_3\text{Fe}_2\text{Si}_3\text{O}_{12}$

Assuming the CaO used in the synthesis is equivalent to the CaO produced from all the  $\text{Ca(OH)}_2$  present in the starting mix then:

$$\begin{aligned}\text{actual CaO in synthesis} &= (\text{required CaO} - \text{CaO deficiency}) \\ &= 3 - 0.08 \\ &= 2.92 \\ &= 97.33\% \text{ of required CaO}\end{aligned}$$

Balancing weights:

$$\begin{aligned}100 \text{ mole\% Ca(OH)}_2 &= 97.33\% \text{ mole\% Ca(OH)}_2 + Z \text{ mole\% CaCO}_3 \\ \text{required} &= \text{actual} + \text{deficiency} \\ 100 \times 74 &= (97.33 \times 74) + (Z \times 100) \\ Z &= \frac{2.67 \times 74}{100} \\ &= 1.98 \text{ mole\%}\end{aligned}$$

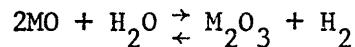
Therefore, 1.98 mole% of the CaO in  $\text{Ca(OH)}_2$  used for SE #41 is in the form of  $\text{CaCO}_3$ , which is inert for the purposes of the synthesis and a further 0.69 mole% of the CaO is absent due to weighing out  $\text{CaCO}_3$  as  $\text{Ca(OH)}_2$ . By weight,  $\text{CaCO}_3$  makes up 2.67% of the hydroxide.

This calculation is a powerful example of the importance of performing Mössbauer experiments on the products of iron-containing hydrothermal synthesis runs. The small almandine component in the garnet would not have been suspected by either X-ray diffraction or by optical observations.

### Al.3 Control of Oxidation State in Oxides and Silicate Minerals

Only a handful of elements have been shown to exist in more than one oxidation state in naturally occurring oxide and silicate minerals. These elements include Ti, V, Cr, Mn, Fe, Cu, Eu and U, and examples of the different valence states are given in Table Al.3.1. Of these elements, only Fe is a major element. Ti, Cr and Mn are minor elements and the rest are trace elements. It is the purpose of this appendix to examine the factors controlling oxidation state in oxides and silicates in minerals.

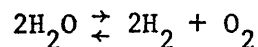
Of primary importance in controlling oxidation state is the oxygen fugacity at the time of the mineral's formation. As a general rule, higher oxidation states are favored by high oxygen fugacities as will now be shown. In a hydrothermal situation which approximates most geological situations, control of an element's oxidation state is achieved by reactions of the type:



At equilibrium:

$$K_1 = \frac{[a_{M_2O_3}]f_{H_2}}{[a_{MO}]^2 f_{H_2O}} \quad \text{Al.3.1}$$

The fugacities of  $H_2O$  and  $H_2$  may be related to the oxygen fugacity since:



At equilibrium:

$$K_D = \frac{f_{H_2}^2 \cdot f_{O_2}}{f_{H_2O}^2} \quad \text{Al.3.2}$$



Table A1.3.1

## EXAMPLES OF MULTIVALENT ELEMENTS IN OXIDES AND SILICATES

ELEMENT	+1	+2	+3	+4	+5	+6
Ti			NaTiSi <sub>2</sub> O <sub>6</sub> Allende	Perovskite Rutile Pyroxene		
V			Goldmanite	Haradaite Roscoelite	Vanadates	
Cr		Lunar olivine (?)	Uvarovite Fuchsite			Chromates
Mn		Tephroite	Piemontite	MnO <sub>2</sub> phases		
Fe		Fayalite Almandine Amphiboles	Andradite			
Cu	Cu <sub>2</sub> O	Diopside				
Eu		Eu <sub>2</sub> Al <sub>2</sub> SiO <sub>7</sub>	Zircon, (Ca,RE)TiO <sub>3</sub>			
U				USiO <sub>4</sub>		U <sub>3</sub> O <sub>8</sub>

Thus, rearranging and combining equations 2 and 1:

$$fO_2 = \frac{[a_{M_2O_3}]^2 K_D}{[a_{MO}]^4 K_1^2} \quad A1.3.3$$

Under conditions of constant temperature and pressure (i.e., both  $K_1$  and  $K_D$  constant) an increase in oxygen fugacity favors the higher oxidation state at the expense of the lower oxidation state as evidenced by the form of equation A1.3.3. At a constant  $fO_2$  value, however, there is no general rule for predicting which oxidation state will be favored by changes in temperature or pressure since the relative dependence of  $K_1$  and  $K_D$  on temperature and pressure can not be predicted without thermodynamic data.

Although oxygen fugacity controls the gross features of redox equilibria in minerals, crystallographic considerations must play an important part in determining the fine details of the redox behavior of an element in a mineral. Two separate crystallographic effects can be distinguished: firstly, structural control, a term which is coined to describe situations where the mineral crystal structure imposes constraints on the redox behavior of an element and, secondly, coordination control, which describes situations in which only the size and coordination number of the cation site appear to affect the  $fO_2$ -valence state relationship.

Structural control of situations will generally only occur when the variable valence state element is a major element. Examples of this phenomenon are the behavior of iron in annite, ideally  $KFe_3^{2+}AlSi_3O_{10}(OH)_2$ . Hazen and Wones (1972) and Wones and Burns (unpublished data) have shown that the trioctahedral mica structure for this composition requires that

some of the ferrous iron be ferric. According to Hazen and Wones (1972), there is an upper limit of  $0.76 \text{ \AA}$  (Shannon and Prewitt (1969) ionic radii) for the average ionic radii of the octahedral cations above which a match in size of the octahedral layers and the Si-Al tetrahedral layers is not possible. Accordingly,  $\text{Fe}^{2+}$  cations, which have an ionic radius of  $0.78 \text{ \AA}$  are, in fact, just slightly too large to be accommodated in the mica structure and some of the ferrous cations are oxidized to ferric (ionic radius  $0.64 \text{ \AA}$ ) in order to reduce the average ionic radius to a more comfortable fit. If this is the case, then a certain percentage of the iron in annite should always be ferric regardless of the external  $f\text{O}_2$  conditions. Mössbauer studies (Wones and Burns, unpublished) do indeed confirm that some of the iron is ferric even under the most reducing conditions of formation. Similarly, the existence of  $\text{Mn}^{3+}$  in trioctahedral micas (Hazen and Wones, 1972; Burns, 1970) may also result from similar structural constraints.

A further example of structural control is the behavior of iron in tourmalines. According to Donnay and Barton (1973) and Hermon et al. (1973), the distribution of both ferrous and ferric over both the Y and Z octahedral sites when chemistry and cation size do not warrant it, occurs because of redox reactions involving iron and possibly other variable valency elements. These reactions take place so as to preserve a match in size of the edge-sharing polyhedra and allow solid solution between the tourmalines, dravite-schorl and schorl-elbaite.

Coordination control is more general than structural control and concerns the interrelationship between oxygen fugacity, oxidation state, cation size and coordination number. Cations of low oxidation state and

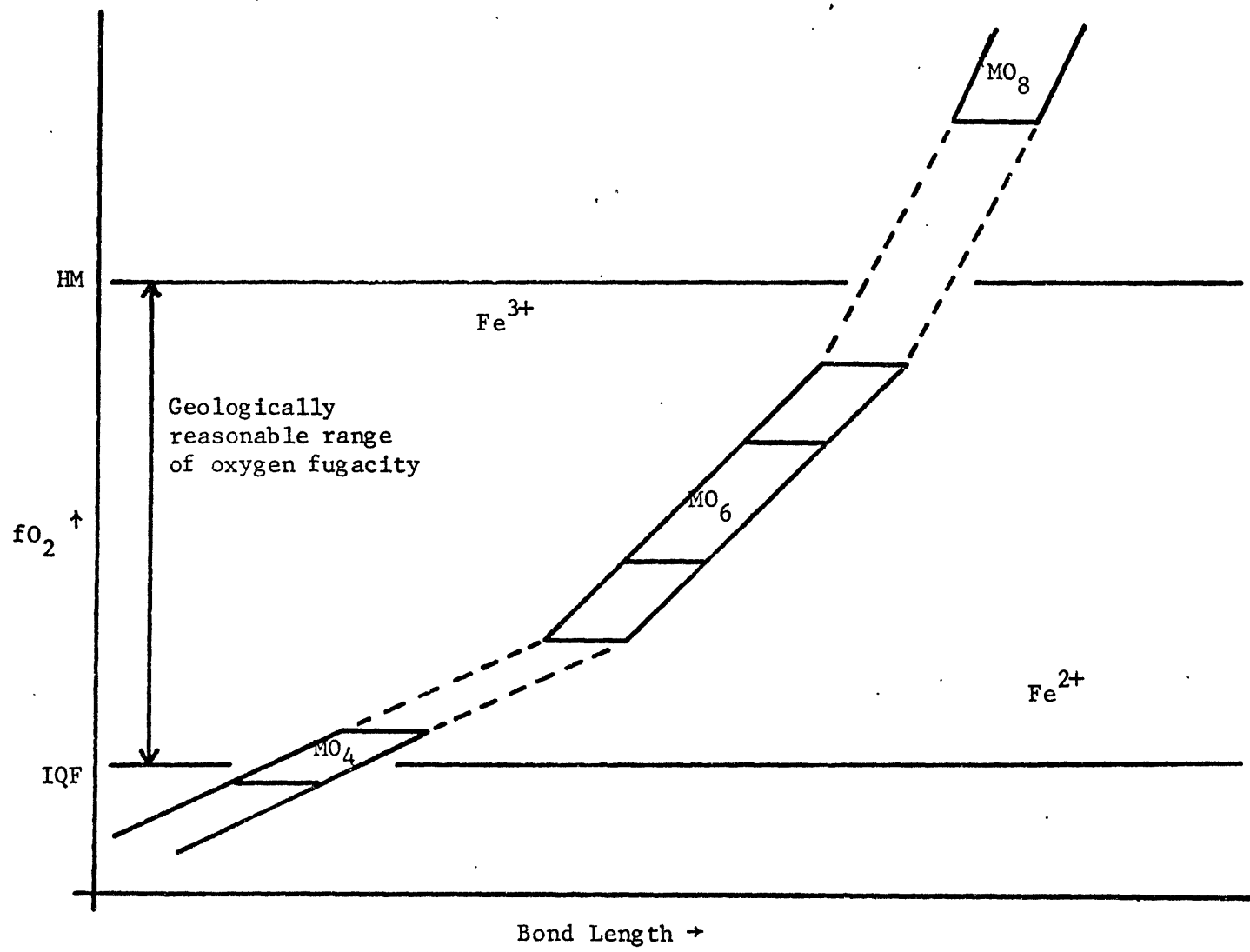
large size are usually accommodated in high coordination number sites whereas cations of high oxidation state and small size are generally found in small coordination number sites. In the case of iron, ferric cations are found either in four coordination or six coordination whereas ferrous cations are usually found in six coordination, although examples of ferrous in four coordination (staurolite, gillespite and certain normal ferrous spinels) and in eight coordination (almandine) are known. No example of eight coordinated ferric iron is known in minerals. The presence of a small amount of ferrous iron in eight coordination in synthetic calcium garnets persists even when synthesized with  $\text{PtO}_2$  as a source of oxygen inside the gold synthesis capsule (SE #41, table 3.4 (a)). These experiments were at much higher oxygen fugacity conditions than the stability limit established by Hsu (1968) for almandine,  $\text{Fe}_3\text{Al}_2\text{Si}_3\text{O}_{12}$ . Thus, in minor or trace element situations, ferrous iron appears capable of existing under high  $f\text{O}_2$  conditions in eight coordination. Similarly, ferric iron in four coordination has been documented to be present at very low oxygen fugacity conditions. For example, ferriannite,  $\text{KFe}_3^{2+}\text{Fe}^{3+}\text{Si}_3\text{O}_{10}(\text{OH})_2$ , has been synthesized on the IW buffer (Wones, 1963b) and probably exists at lower oxygen fugacities as well. For six-fold coordination there appears to be an approximate boundary at about the QFM or NNO buffer above which ferric is found in octahedral coordination and below which ferrous is found. Often there is a range of coexistence especially with hydroxylated minerals such as amphiboles and micas as evidenced by Mössbauer studies (Semet, 1973) and by changes in physical properties such as color, refractive index and cell parameters over a range of oxygen fugacity (for

example, Wones, 1963a; Ernst, 1962). Mössbauer results on synthetic magnesiohastingsite (Semet, 1973) and ferrorichterite (Charles, 1974; Virgo, 1972) indicate that  $\text{Fe}^{3+}$  exists in the smaller non-hydroxylated M2 site at much lower oxygen fugacities than in the larger hydroxylated M1 or M3 site in these amphiboles; however, the possibility that there may be some structural control here too can not be ruled out. Summarizing these results leads to the schematic diagram in figure A1.3.1, which attempts to relate oxygen fugacity, size, coordination number and iron valence state. It should be emphasized that figure A1.3.1 is strictly applicable to situations where structural control and thermodynamic considerations, which would cause other factors to be considered, are not important.

Similar relationships between oxygen fugacity, site size, coordination number and valence state should be found for other elements as well. For the sake of argument, the case for  $\text{Ti}^{3+}$  in garnets will be considered. Titanium is generally found as  $\text{Ti}^{4+}$  in minerals and only in a few cases is the existence of  $\text{Ti}^{3+}$  documented or suspected. The existence of  $\text{Ti}^{3+}$  is proven in the Allende pyroxene phase (Dowty and Clark, 1973) and in the synthetic pyroxene  $\text{NaTiSi}_2\text{O}_6$  (Prewitt et al., 1972).  $\text{Ti}^{3+}$  is suspected to exist in the orange lunar glass (Mao et al., 1973), in lunar subcalcic pyroxenes (Burns et al., 1972; Sung et al., 1974), in certain other lunar phases and also in certain titanium-rich andradites (Manning and Harris, 1970; Burns, 1972), where Mössbauer and wet chemical  $\text{Fe}^{2+}/\text{Fe}^{3+}$  determinations are grossly different. The available evidence from the documented examples suggest that  $\text{Ti}^{3+}$  exists only under very low oxygen fugacity conditions. The Allende phase was formed at well below IW conditions since

Figure A1.3.1

Schematic diagram showing the expected interrelationship between oxygen fugacity, bond length, coordination and oxidation state of iron.



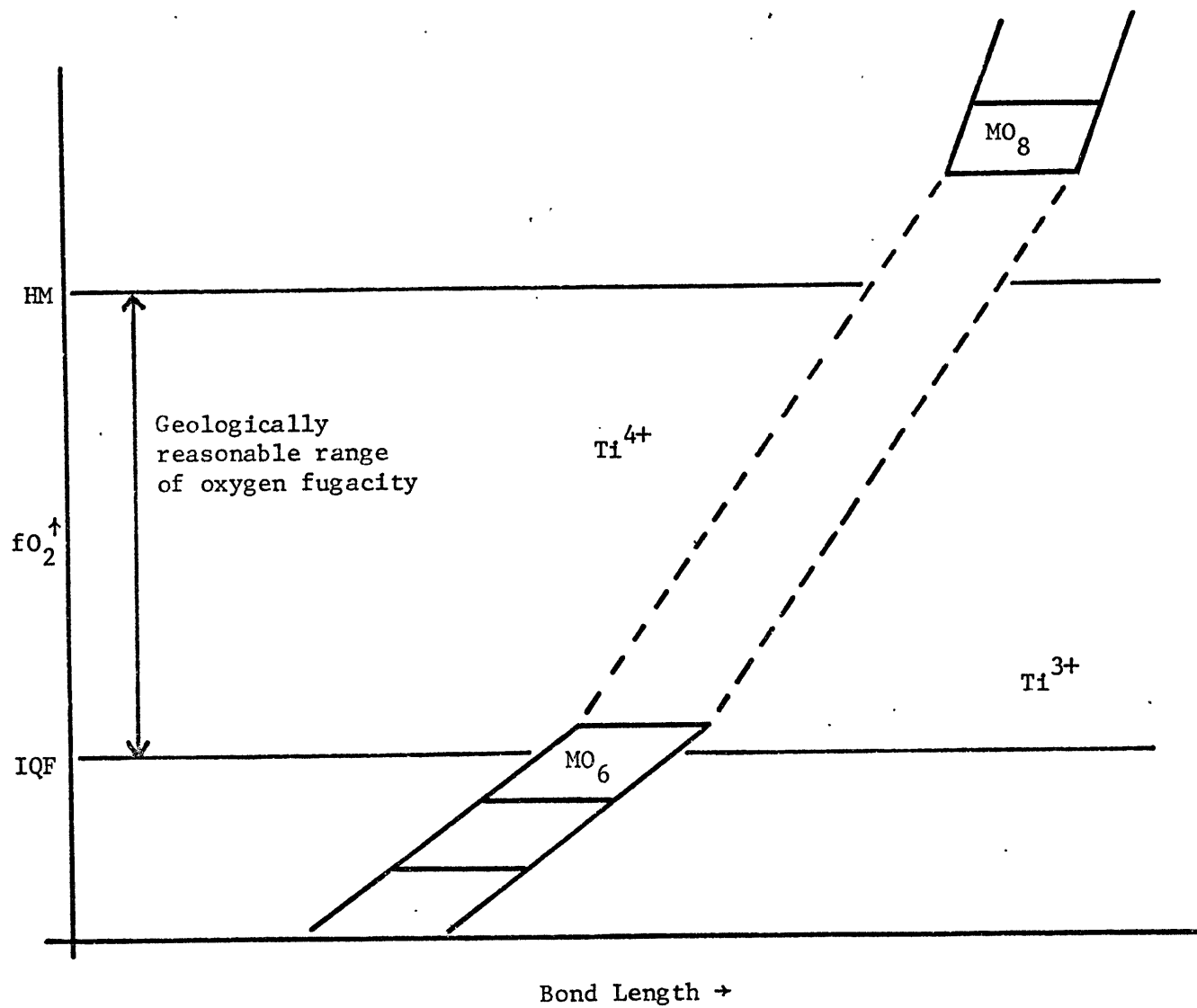
iron is only present as metal. On the other hand, the results of Mao et al. (1973) have shown that as  $fO_2$  is lowered  $Ti^{3+}$  is formed in the lunar silicate glass before iron metal. However, the site of Ti is unknown in the silicate glass. From the work of Ito and Frondel (1967), the amount of  $Ti^{4+}$  in tetrahedral sites in garnet is likely to be small since only  $Zr^{4+}$  forces  $Ti^{4+}$  into these sites.  $Ti^{4+}$  is probably almost exclusively in octahedral sites in natural garnets and  $Fe^{3+}$ , and perhaps  $Al^{3+}$ , substitute for  $Si^{4+}$ . The study by Ito and Frondel (1967) also showed that  $Ti^{4+}$  does not go into the calcium site either. In the problem garnets, where ferrous iron by Mössbauer is much less than by wet chemistry, some other reducing species appears to be required and  $Ti^{3+}$  is the obvious choice. Since  $Ti^{4+}$  favors octahedral sites in garnets,  $Ti^{3+}$  should be found in an equal or higher coordination number site in order to be present.  $Ti^{3+}$  in eight coordination would appear to satisfy these requirements and would also offer an explanation of the band at  $\sim 16,500\text{ cm}^{-1}$  which Manning and Harris (1970) found in certain of these garnets. The work of Ito and Frondel (1967) showed that the eight coordinate site could accept large trivalent and tetravalent cations along with concomitant replacement of  $Si^{4+}$  by  $Fe^{3+}$  or  $Al^{3+}$ . The scheme in figure A1.3.2 summarizes the above arguments for  $Ti^{3+}$  in garnets. Similarly, with the subcalcic augites found on the moon,  $Ti^{3+}$  may be stabilized in the larger Ca-deficient M2 site.

The europium anomaly also results from redox equilibria at the time of a mineral's formation. The anomaly arises because of strong preferential incorporation of  $Eu^{2+}$  into a mineral relative to another phase when compared to  $Eu^{3+}$  and other rare earth elements. The anomaly is most



Figure A1.3.2

Schematic diagram showing the expected interrelationship between oxygen fugacity, bond length, coordination and oxidation state of titanium.



pronounced with feldspars and plagioclase in particular and is accentuated when the oxygen fugacity is low. The calcium site in plagioclase is small for that particular site in feldspar and the larger  $\text{Eu}^{2+}$  cation is readily accepted into feldspars. On the other hand, the calcium sites in pyroxenes and garnets are the largest which can be accepted by these silicates and the larger  $\text{Eu}^{2+}$  ion is not so readily taken into the structure. In order to get more  $\text{Eu}^{2+}$  than  $\text{Eu}^{3+}$  in clinopyroxene or garnet, lower  $f\text{O}_2$  conditions are necessary since the europium site will be smaller. Even at lower  $f\text{O}_2$  conditions, a europium anomaly may not be observed with these phases since the difference in distribution coefficient between  $\text{Eu}^{2+}$  and other trivalent lanthanides may not be marked. In fact, a negative anomaly may be observed if  $\text{Eu}^{2+}$  is preferentially rejected by the structure.

Conclusions:

1. Oxygen fugacity controls gross features of redox phenomena in minerals.
2. Crystallographic constraints on oxidation state have been described as either structural controls, where individual mineral structures can dictate aspects of the redox behavior of major elements, or coordination controls, where the interrelationship between coordination number, site size,  $f\text{O}_2$  and valence state can be considered as independent of crystal structure. In certain cases this distinction may be very blurry, e.g., redox phenomena of iron at amphibole M2 sites.
3. Both increases in coordination and in site size tend to stabilize low oxidation state cations.

Appendix A1

REFERENCES

- Burns, R.G. (1970) Mineralogical Applications of Crystal Field Theory.  
Cambridge University Press, Cambridge, England.
- Burns, R.G. (1972) Mixed valencies and site occupancies of iron in silicate minerals from Mössbauer spectroscopy. Canad. J. Spect. 17, 51-59.
- Burns, R.G., Huggins, F.E. and Abu-Eid, R.M. (1972) Polarized absorption spectra of single crystals of lunar pyroxenes and olivines.  
The Moon. 4, 93-102.
- Charles, R.W. (1974) The physical properties of the Mg-Fe richterites.  
Amer. Mineral. 59, 518-528.
- Crowley, M.S. and Roy, R. (1964) Crystalline solubility in the muscovite and phlogopite groups, Amer. Mineral. 49, 348-362.
- Déer, W.A., Howie, R.S. and Zussman, J. (1963) Sheet Silicates, Vol. 3,  
Rock-Forming Minerals. Longmans, London.
- Donnay, G. and Barton, Jr., R. (1972) Refinement of the crystal structure of elbaite and the mechanism of tourmaline solid solution.  
Tschermaks. Min. Petr. Mitt. 18, 273-286.
- Dowty, E. and Clark, J.R. (1973) Crystal structure refinement and optical properties of a  $Ti^{3+}$  fassaite from the Allende meteorite.  
Amer. Mineral. 58, 230-242.
- Ernst, W.G. (1962) Synthesis, stability relations and occurrence of riebeckite and riebeckite-arfvedsonite solid solutions. J. Geol. 70, 689-736.

- Forbes, W.C. (1972) An interpretation of the hydroxyl contents of biotites and muscovites. Mineral. Mag. 38, 712-720.
- Foster, M.D. (1964) Water content of micas and chlorites. U.S. Geol. Survey, Prof. Paper. 474F, 15 pp.
- Güven, N. (1971) The crystal structures of  $2M_1$  phengite and  $2M_1$  muscovite. Z. Krist. 134, 196-212.
- Hazen, R.M. and Wones, D.R. (1972) The effect of cation substitutions on the physical properties of trioctahedral micas. Amer. Mineral. 57, 103-129.
- Hermon, E., Simkin, D.J., Donnay, G. and Muir, W.B. (1973) The distribution of  $Fe^{2+}$  and  $Fe^{3+}$  in iron-bearing tourmalines: A Mössbauer study. Tschermaks. Min. Petr. Mitt. 19, 124-132.
- Hsu, L.C. (1968) Selected phase relationships in the system Al-Mn-Fe-Si-O-H: A model for garnet equilibrium. J. Petrol. 9, 40-83.
- Ito, J. (1965) Synthesis of vanadium silicates: Haradaite, goldmanite and roscoelite. Mineral. Journ. (Japan) 4, 299-316.
- Ito, J. and Frondel, C. (1967) Synthetic zirconium and titanium garnets. Amer. Mineral. 52, 773-781.
- Lindqvist, B. (1966) Hydrothermal synthesis studies of potash-bearing sesquioxide-silica systems. Geol. Fören. Stockholm Förhandl. 88, 133-178.
- Manning, P.G. and Harris, D.C. (1970) Optical absorption and EMP studies of some high Ti andradites. Canad. Mineral. 10, 260-271.
- Mao, H.K., Virgo, D. and Bell, P.M. (1973) Analytical study of the orange lunar soil returned by the Apollo 17 astronauts. Ann. Rep. Dir.

Geophys. Lab. 631-638.

Prewitt, C.T., Shannon, R.D. and White, W.B. (1972) Synthesis of a pyroxene containing trivalent titanium. Contr. Min. Pet. 35, 77-82.

Semet, M.P. (1973) A crystal-chemistry study of synthetic magnesiohastingsite. Amer. Mineral. 58, 480-494.

Shannon, R.D. and Prewitt, C.T. (1969) Effective ionic radii in oxides and fluorides. Acta Cryst. B25, 925-946.

Sung, C.M., Abu-Eid, R.M. and Burns, R.G. (1974)  $Ti^{3+}/Ti^{4+}$  ratios in lunar pyroxenes: Implications to depth of origin of more basalt magma. Submitted to Proc. Fifth Lunar Sci. Conf., Geochim. Cosmochim. Acta, Suppl. 5, Vol. 1.

Virgo, D. (1972) Preliminary fitting of  $^{57}Fe$  Mössbauer spectra of synthetic Mg-Fe richterites. Ann. Rep. Dir. Geophys. Lab. 513-516.

Wise, W.S. and Eugster, H.P. (1964) Celadonite: Synthesis, thermal stability and occurrence. Amer. Mineral. 49, 1031-1083.

Wones, D.R. (1963a) Physical properties of synthetic biotites on the join phlogopite-annite. Amer. Mineral. 48, 1300-1321.

Wones, D.R. (1963b) Phase equilibria of ferriannite,  $KFe_3^{2+}Fe^{3+}Si_3O_{10}(OH)_2$ . Amer. J. Sci. 261, 581-596.

Yoder, Jr., H.S. and Eugster, H.P. (1955) Synthetic and natural muscovites. Geochim. Cosmochim. Acta 8, 225-280.

Appendix A2

SITE COMPRESSIBILITIES

A2.1 Considerations on the Compressibilities of Individual Polyhedral Sites Within a Crystal Structure

In this study and other high pressure spectral studies (Drickamer, 1965; Shankland et al., 1974; Abu-Eid, 1974) some considerable importance has been attached to the compressibilities of individual polyhedral sites and this appendix discusses such quantities.

There are two methods of experimentally estimating site compressibilities which are currently feasible. Both methods involve estimating or measuring the volume of the site as a function of pressure; the first of these methods is single crystal X-ray studies which give structural details, including site volumes, as a function of pressure; and the second of these methods is high pressure absorption spectral measurements based on measured values of  $\Delta$  and its relationship to site volume as described in section 2.3.2 and in Shankland et al. (1974). Of the two methods, the former is potentially the most accurate and widely applicable; however, much more work has been carried out with the latter method, which is much easier experimentally, but less accurate and restricted to polyhedra of high symmetry containing certain transition metal cations for which  $\Delta$  can be estimated.

Site compressibilities are generally not expected to be equal to bulk mineral compressibilities by analogy with recent single crystal X-ray studies as a function of temperature. Such experiments have shown that different polyhedra within a complex mineral structure can be expected to have different thermal expansions, so that it is not unreasonable to expect different compressibilities for the different polyhedra within a structure.

The estimation of polyhedral compressibilities from the bulk mineral compressibility can be attempted based on the findings of Anderson and Anderson (1970). These investigators found that the product of the bulk modulus or incompressibility,  $K$ , and the molar volume,  $V_o$ , is a constant for isomorphous phases:

$$KV = \text{const} \quad \text{A2.1.1}$$

Anderson and Anderson (1970) were able to rationalize this equation by using the Born-Mayer potential to derive an expression for the product of the bulk modulus and volume:

$$KV_o = \frac{AZ_c Z_a e^2 (n-1)}{9r_o} \quad \text{A2.1.2}$$

where  $Z_c$  and  $Z_a$  are the cation and anion charges respectively;  $A$  is the Madelung constant for the structure;  $e$  is the electronic charge;  $n$  is the repulsive exponent in the Born-Mayer potential, and  $r_o$  is a distance characteristic of the structure.

By combining equations A2.1.1 and A2.1.2:

$$\text{const} = \frac{AZ_c Z_a e^2 (n-1)}{9r_o} \quad \text{A2.1.3}$$

Anderson and Anderson (1970) showed that  $A(n-1)/9r_o$  was approximately  $0.157 \pm 0.005$  for virtually all oxides regardless of structure type. Therefore, for any oxide:

$$KV_o = 0.157 Z_c Z_a e^2 \quad \text{A2.1.4}$$

If it is now assumed that the individual polyhedra themselves follow an



interrelationship similar to equation A2.1.4, then for oxides where

$Z_a = -2$ , this assumption leads to:

$$K_{pol} = \frac{kZ_c}{V_{pol}} \quad A2.1.5$$

where  $k$  is a constant. This equation suggests that cations of high charge which generally have small polyhedral volumes can be expected to be much less compressible than cation polyhedra of low charge and large volume. Therefore, the following order of site compressibilities,  $\beta_{pol}$ , may be predicted for iron polyhedra:

$$\beta_{Fe^{3+}(IV)} < \beta_{Fe^{3+}(VI)} < \beta_{Fe^{2+}(VI)} < \beta_{Fe^{2+}(VIII)}$$

where  $\beta_{pol}$  is equal to  $1/K_{pol}$ .

Equation A2.1.5 can be used to partition the bulk incompressibility of a mineral into polyhedral component incompressibilities. There are two ways of doing this partitioning by analogy with the problem of estimating the bulk incompressibilities of rocks from the bulk incompressibilities of their component minerals. Firstly, after Voight:

$$K = \frac{\sum_i n_i V_i K_i}{\sum_i n_i V_i} \quad A2.1.6$$

where  $K$  is the bulk modulus or incompressibility of the mineral phase; and where  $n_i$ ,  $V_i$ ,  $K_i$  refer to the  $i^{th}$  type of polyhedron in the mineral;  $n_i$  is the number of polyhedra of type  $i$  per formula unit;  $V_i$  is the volume; and  $K_i$  is the incompressibility. Secondly, after Reuss:

$$1/K_{\text{meas}} = \frac{\sum_i n_i V_i / K_i}{\sum_i n_i V_i} \quad \text{A2.1.7}$$

These two averaging schemes lead to upper and lower bounds on the polyhedral incompressibilities.

Based on equation A2.1.5:

$$K_i = \frac{kZ_i}{V_i} \quad \text{A2.1.8}$$

Now for a polyhedron of type 1:

$$K_1 = \frac{kZ_1}{V_1} \quad \text{A2.1.9}$$

so that combining equations A2.1.8 and A2.1.9 leads to:

$$K_i = \frac{K_1 V_1}{Z_1} \frac{Z_i}{V_i} \quad \text{A2.1.10}$$

Substituting this expression into the equations A2.1.6 and A2.1.7 leads to new expressions for the two averaging schemes:

$$\text{After Voigt:} \quad K = \frac{K_1 V_1}{Z_1} \frac{\sum_i n_i Z_i}{\sum_i n_i V_i} \quad \text{A2.1.11}$$

$$\text{After Reuss:} \quad K = \frac{K_1 V_1}{Z_1} \frac{\sum_i n_i V_i}{\sum_i n_i V_i / Z_i} \quad \text{A2.1.12}$$

In this way, from a knowledge of  $n_i$ ,  $V_i$  and  $Z_i$  for each polyhedral component of a mineral and  $K$  for the bulk phase, a value can be estimated for  $K_1$  by both the Voigt and Reuss averaging schemes. By use of equation A2.1.10, values of  $K_i$  can be obtained for the other polyhedra. A

Voight-Reuss-Hill type average can be defined for calculation purposes:

$$K_i(\text{VRH}) = \frac{K_i(\text{V}) + K_i(\text{R})}{2} \quad \text{A2.1.13}$$

The polyhedral compressibilities of andradite were calculated in this manner and are given in table A2.1.1 as an example. The results are given in terms of  $K$ , the bulk modulus of andradite, which, to date, has not been measured. However, it will probably be around 1.50 mb, based on data reported for other garnets (Simmons and Wang, 1971), so that absolute values can be estimated for the polyhedra:

$$K_{\text{Ca}(\text{VRH})} \approx 0.7 \text{ mb}$$

$$K_{\text{Fe}(\text{VRH})} \approx 2.4 \text{ mb}$$

$$K_{\text{Si}(\text{VRH})} \approx 13.9 \text{ mb}$$

This result suggests that the calcium polyhedra will be, by far, the most compressible and will be responsible for most of the change in volume with increasing pressure. The silicon polyhedra, on the other hand, will hardly be affected at all by pressure. Si-O bond lengths can be expected to change by less than 0.3% in 100 kb based on this value for the incompressibility.

Obviously this approach for calculating polyhedral compressibilities is a gross simplification of the actual physical compression of a solid. For instance, many structures contain unfilled octahedral or tetrahedral holes surrounded by filled polyhedra. These empty sites have not been explicitly considered in this analysis. However, their sizes are generally

Table A2.1.1

POLYHEDRAL COMPRESSIBILITIES FOR ANDRADITE,  $\text{Ca}_3\text{Fe}_2\text{Si}_3\text{O}_{12}$

(a) Data:

i	$n_i$	$Z_i$	$V_i (\text{\AA}^3)$
Ca	3	2	21.28
Fe	2	3	9.15
Si	3	4	2.10

$V_i$  data were calculated from Novak and Gibbs (1971).

(b) Results:

i	$K_i(V)$	$K_i(R)$	$K_i(VRH)$
Ca	0.35 K	0.57 K	0.46 K
Fe	1.21 K	2.00 K	1.60 K
Si	7.02 K	11.50 K	9.26 K

where K is the bulk modulus of andradite.

determined by edges of filled polyhedra in close-packed oxides, so that their contribution to the change in volume with pressure may, in fact, be taken into account. However, if the solid is not close-packed so that unfilled polyhedra are not adequately defined by the edges of filled polyhedra, then there is no way that this approach can be adequate.

It can be argued that there ought to be some fundamental underlying principle on the atomic scale that explains the existing KV systematics for bulk phases. Both the Born-Mayer theory utilized by Anderson and Anderson (1970) and the more general approach based on the Debye theory of lattice vibrations taken by Shankland (1972) have been quite successfully applied to such systematics. Although neither approach is strictly an atomistic type approach, both explanations do involve estimating average force constants or bond strengths between atoms which are then extended to the solid as a whole. The fact that most oxides can be approximated in such a way virtually demands that there be some simple underlying principle on an atomic scale rather than only on a bulk scale.

Suitable high pressure crystallographic studies will have to be carried out to test the feasibility of this approach and also to see if there is indeed a principle on the atomic scale for extending KV systematics to individual polyhedra. If KV systematics can be extended to polyhedra, such systematics will enable detailed predictions of crystal structures to be made at any pressure and may provide valuable insight into crystallochemical criteria for the stability of structures and into the reasons for phase changes. However, if it turns out that there is no apparent relationship such as equation A2.1.1 for polyhedra, then the need for high pressure crystallographic studies will become even more acute.

Appendix A2

REFERENCES

- Abu-Eid, R.M. (1974) Unpublished Ph.D. thesis, Massachusetts Institute of Technology, Cambridge, MA. (in preparation)
- Anderson, D.L. and Anderson, O.L. (1970) The bulk modulus-volume relationship for oxides. J. Geophys. Res. 75, 3494-3500.
- Drickamer, H.G. (1965) The effects of high pressure on the electronic structure of solids. Solid State Physics. 17, 1-137.
- Novak, G.A. and Gibbs, G.V. (1971) The crystal chemistry of the silicate garnets. Amer. Mineral. 56, 791-825.
- Shankland, T.J. (1972) Velocity-density systematics: Derivation from Debye theory and the effect of ionic size. J. Geophys. Res. 77, 3750-3758.
- Shankland, T.J., Duba, A.G. and Woronow, A. (1974) Pressure shifts of optical absorption bands in iron-bearing garnet, spinel, olivine, pyroxene and periclase. J. Geophys. Res. 79. (in press)
- Simmons, G. and Wang, H. (1971) Single Crystal Elastic Constants and Calculated Aggregate Properties. M.I.T. Press, Cambridge, MA.

## Appendix A3

### COMPUTER ROUTINES

#### A3.1 Modification of Stone's Original Program

A number of additions were made to the original Mössbauer program prepared by Dr. A.J. Stone of Cambridge University, England. This program is described briefly by Stone (1967) and Bancroft (1974) and in more detail in Stone et al. (1969). The reader is assumed to have some knowledge of Stone's program.

For general fitting of Mössbauer spectra this program is very good. However, for a number of reasons, especially since our usage is restricted to iron Mössbauer studies, some additions were felt to be required. The two most important of these changes are, firstly, the calculation and print out of iron Mössbauer parametric data from the computed peak positions and areas; and, secondly, the computation of calibration parameters by means of a least squares method from computer-fitted peak positions of standard iron foil spectra.

##### A3.1.1 Calculation of iron Mössbauer parametric data from the fit

This procedure involves taking specified pairs of peaks or groups of six peaks and calculating Mössbauer data for quadrupole doublets or magnetically split spectra respectively. The computer subroutines for achieving this are as follows:

A3.1.1 (a) Modifying read in of initial estimates and number of peaks

		0114 <sup>1</sup>
	NSUB=0	
	MSUB=0	
212	READ (5,284) N, NSUB, MSUB	
284	FORMAT (3I2)	
	V=3*N+4	0116
	V1=5	0117
	READ (5,283) (B(I), I=1,4)	
283	FORMAT (4F10.0)	
	IF (N .EQ. 0) GO TO 2833	
	DO 2831 J=1,N	
	KJ=3*J+2	
	LJ=3*J+3	
	MJ=3*J+4	
	READ (5,2832) B(KJ), B(LJ), B(MJ), NS(J), MS(J)	
2832	FORMAT (3F10.0,2I2)	
2831	CONTINUE	
2833	CONTINUE	0121

NSUB is the number of quadrupole doublets in the spectrum; each peak of the same doublet is given the same value of NS(J), where  $1 \leq NS(J) \leq NSUB$ . Similarly, MSUB is the number of magnetic subspectra of six peaks in the spectrum; each peak of the magnetic subspectrum is given the same value of MS(J), where  $1 \leq MS(J) \leq MSUB$ . To set up a deck to carry out this calculation only the cards with the number of peaks and initial estimates of the peak parameters are affected.

---

<sup>1</sup>The numbers on the right hand side refer to card numbers in Stone's original program, and show where these additions are located in the program.



A3.1.1 (b) Calculation of Mössbauer parameters and print out of such data

0542

```
IF (NSUB .LE. 0) GO TO 3320
  FACTR1=FACTOR
  WRITE (6,3301)
3301 FORMAT (1H0 /31H0      SUBSPECTRA MOSSBAUER DATA /
           54H0 PEAKS      ISOMER SHIFT      QUADRUPOLE SPLITTING)
  IF (ORIGIN .NE. 0.) GO TO 3303
  FACTR1=1.0
  WRITE (6,3302)
3302 FORMAT (48H           CHANNELS           CHANNELS )
  GO TO 3305
3303 WRITE (6,3304)
3304 FORMAT (46H           MM/SEC           MM/SEC)
3305 DO 3310 J=1,NSUB
  VIS=0.
  VQS=0.
  NW2=0
  NM=0
  DO 3308 L=1,N
  NS1=0
  I=3*L+2
  IF (NS(L)-J) 3307,3306,3307
3306 NS1=1
  NM=NM+1
  IF (NM .EQ. 1) NW1=L
  IF (NM .EQ. 2) NW2=L
3307 VIS=VIS+(B(I)-ORIGIN)*FACTR1*NS1/2
3308 VQS=VQS+((-1)**NM)*(B(I)-ORIGIN)*FACTR1*NS1
  IF (NM .EQ. 1) VQS=0.0
  WRITE (6,3309) NW1, NW2, VIS, VQS
3309 FORMAT (1H0 ,2I3,2F20.4)
3310 CONTINUE
3320 IF (MSUB .LE. 0) GO TO 3340
  FACTR2=FACTOR
  WRITE (6,3321)
3321 FORMAT (1H0 /31H0      MAGNETIC SUBSPECTRA DATA /
  1      47H0      PEAKS      I.S.      Q.S.      A,
  2      30H      B      HO      HO)
  IF (ORIGIN .NE. 0.) GO TO 3323
  FACTR2=1.0
  WRITE (6,3322)
3322 FORMAT (50H           CHANNELS  CHANNELS  CHANNELS,
  1      36H  CHANNELS  CHANNELS  NOT CALCULATED)
  GO TO 3325
3323 WRITE (6,3324)
3324 FORMAT (51H           MM/SEC  MM/SEC  MM/SEC ,
```

```

1          28H MM/SEC   MM/SEC   KGAUSS)
3325 DO 3329 J=1,MSUB
      SUMM=0
      MM=0
      DO 3328 L=1,N
      I=3*L+2
      IF (MS(L)-J) 3327,3326,3327
3326 MM=MM+1
      SMG(MM)=B(I)
      MW(MM)=L
      SUMM=SUMM+SMG(MM)
3327 CONTINUE
3328 CONTINUE
      VIS1=(SMG(1)+SMG(6)+SUMM-8*ORIGIN)*FACTR2/8
      VQS1=((SMG(5)+SMG(2))*3-SUMM)*FACTR2/2
      AO=(SMG(5)+SMG(4)-SMG(3)-SMG(2))*FACTR2/2
      BO=(SMG(5)-SMG(4)+SMG(3)-SMG(2))*FACTR2/2
      HO1=(SMG(6)-SMG(1))*FACTR2
      HO2=0.0
      IF (ORIGIN .NE. 0.0) HO2=HO1*30.97
      WRITE (6,3331) (MW(MM), MM=1,6),VIS1, VQS1,AO,BO,HO1,HO2
3331 FORMAT (1H0 ,6I3,5F10.4,F10.3)
3329 CONTINUE
      WRITE (6,3330)
3330 FORMAT (52HONOTE: THE ABOVE MAGNETIC PARAMETERS ARE ONLY EXACT ,
1          47H WHEN THE MAGNETIC AND ELECTRIC FIELD GRADIENTS /
2          19H ARE PARALLEL / 1H0 )
3340 IF (TRACE) 9650,9650,9651

```

0543

For each pair of peaks assigned a value of NS(J), the isomer shift and quadrupole splitting are calculated and printed out; while for each set of six peaks assigned the same value of MS(J) the isomer shift and magnetic hyperfine splitting ( $H_0$ ) are calculated and, given the proviso that the magnetic and electric field gradient should be parallel for such calculations to be exact, values for the quadrupole splitting, the splitting of the  $I=1/2$  state ( $a_0$ ) and the splittings of the  $I=3/2$  state ( $b_0$ ) are also calculated. The data are printed out in either channels or, if conversion parameters have been specified, in mm/sec.

### A3.1.2 Calculation of conversion parameters from iron foil spectra

If a card with FOIL punched on it in columns 1-4 is placed at the end of a constraint set for a given stage in a Mössbauer fit of an iron foil spectrum, the computer takes the fitted peak positions in channels and relates them to the standard peak positions in mm/sec of iron foil at room temperatures as given by Stevens and Stevens (1970) by means of a least squares analysis in order to compute the conversion factors, GR and PM. PM is zero velocity point of the calibration (equivalent to the isomer shift of iron foil) and GR is the gradient of the conversion in mm/sec/channel. Some statistical parameters, such as the standard deviations for each conversion factor and sigma, which is the uncertainty in peak position resulting from use of calibration curve in converting channels to mm/sec, are also given.

0495

```
2200 WRITE (6,2201) TITLE, STAGE
2201 FORMAT (1H1, 20A4 / 6H0STAGE,I2 /
1      38HOIRON FOIL LEAST SQUARES DATA ANALYSIS)
C      USING KNOWN IRON FOIL MOSSBAUER PARAMETERS, A LEAST SQUARES FIT
C      OF THE DATA NOW FOLLOWS.
      IF (TEST .GT. 0.001) GO TO 2210
      XY=0.
      X2=0.
      X1=0.
      DO 2202 I=1,V
2202   YH(I)=0.
      IF (N .NE. 6) GO TO 2203
      YH(5)=-5.3133
      YH(8)=-3.077
      YH(11)= 0.8407
      YH(14)=0.8407
      YH(17)=3.077
      YH(20)=5.3133
      GO TO 2204
2203   IF (N .NE. 4) GO TO 2212
      YH(5)=-3.077
      YH(8)=-0.8407
```

```
      YH(11)=0.8407
      YH(14)=3.077
2204 DO 2205 I=V1,V,3
      XY=XY+B(I)*YH(I)
      X2=X2+B(I)*B(I)
2205 X1=X1+B(I)
C     CALCULATE GRADIENT (GR) AND MIDPOINT (PM) OF IRON FOIL SPECTRUM
      GR=N*XY/(N*X2-X1*X1)
      PM=X1/N
C     CALCULATE STANDARD DEVIATIONS IN GR 'AL' AND IN PM 'BT'
C     'SM' IS THE ERROR IN READING A POINT FROM THE COMPUTED LINE
C     'DX' IS THE SUM OF SQUARES OF RESIDUALS
C     'AM' IS 'AL' CONVERTED TO MAGNETIC UNITS
      DX=0.
      DO 2206 I=V1,V,3
2206  DX=DX+(YH(I)-GR*(B(I)-PM))**2
      SD=DSQRT(DX/(N-1))
      XN=N
      IF (N .EQ. 4) GO TO 2207
      AL=1.41421*SD/((B(20)-B(5))*DSQRT(XN))
      GO TO 2208
2207  AL=SD/((B(14)-B(5))*1.41421)
2208  AM=30.97*GR
      BT=SD/(GR*DSQRT(XN))
      SM=SD/DSQRT(XN)
C     WRITE RESULTS FOR THIS DATA
      WRITE (6,2209) N, GR, AL, PM, BT, SM, AM
2209 FORMAT (26H0EQUATIONS IS OF THE FORM:
1       34H Y(MM/SEC) = GRAD(X(CH) - MPT(CH)) /
2       10H0BASED ON ,I2,15H PEAK POSITIONS /
3       33H0      GRAD      S.D.      MPT,
4       37H      S.D.      SIGMA      MAG GRAD /
5       32H      MM/SEC/CH      CH,
6       38H      MM/SEC      KGAUSS/CH /
7       1H0, 2F11.6, 4F11.4 /
8       53H0SIGMA IS THE UNCERTAINTY IN PEAK POSITION RESULTING ,
9       36H FROM THE ABOVE CALIBRATION EQUATION)
      GO TO 2214
2210 WRITE (6,2211)
2211 FORMAT (42H0DATA TOO FAR FROM CONVERGENCE TO WARRANT ,
1       23H LEAST SQUARES ANALYSIS)
      GO TO 2214
2212 WRITE (6,2213) N
2213 FORMAT (38H0LEAST SQUARES FIT NOT PERFORMED WITH ,I2,6H PEAKS)
2214 GO TO 5001
```

The parameters, GR and PM, are related to the calibration factors, ORIGIN and FACTOR, already in Stone's original program by means of the following cards:

```
      READ (5,581)  F, CONSTR, I, J, ORIGIN, FACTOR           0170
581   FORMAT (A4, I2, 2I4, 2F10.0)                          0171
      IF (ORIGIN .NE. -1.0) GO TO 5003
      ORIGIN=PM
      FACTOR=GR
      GO TO 5002
5003  PM=ORIGIN
      GR=FACTOR
      GO TO 5002
5001  SW=-1
      ASSIGN 82 TO MESS1
      READ (5,5811) F, CONSTR, I, J
5811  FORMAT (A4, I2, 2I4)
5002  IF (F .EQ. EXIT) GO TO 1                               0172
      IF (F .EQ. FOIL) GO TO 2200                            0173
```

This ensures that both ORIGIN and PM and both FACTOR and GR have the same values for a given spectrum. Note that the value of -1.0 for ORIGIN in columns 14-23 on the first card after the data deck enables the present spectrum to have the same calibration parameters as the previous spectrum, as GR and PM retain their values between spectra. ORIGIN and FACTOR do not retain their values between spectra, being set to 0.0 and 1.0, if they are not specified and ORIGIN is not equal to -1.0. GR and PM can either be defined by an iron foil spectrum or by specified values of ORIGIN and FACTOR on the first card after the data deck for a previous spectrum.

#### A3.1.3 Other changes

Some other minor changes and additions were also made to the program. Since these changes are small, no details will be given.

Such changes included:

1. printing of the stage number on the SC4020 plots;
2. restricting the print-out of the covariance-variance matrix to those runs where the card FULL is used;
3. printing the value of the TEST parameter with the results summary, if the Mössbauer fitting procedure should fail to converge, to indicate how close the fit is to meeting the convergence criterion ( $TEST < 10^{-6}$ );
4. printing of the Mössbauer peak positions and widths in mm/sec as well as in channels;
5. expressing the peak areas as percentages of the total area under the envelope;
6. printing of the calibration parameters in the results summary.

A3.2 Calculation of  $F_{val}$  for Ferrous Minerals as a Function of Temperature, T, and the Lower Level Splittings,  $\Delta_1$  and  $\Delta_2$

In order to fit the temperature dependence of the ferrous quadrupole splitting, using the model of Ingalls (1964), to specific values of  $\Delta_1$  and  $\Delta_2$ , a computer routine was devised to tabulate values of  $F_{val}$ . The program was built around equations 4.15 and 4.16. The fitting of QS(T) data to give  $\Delta_1$  and  $\Delta_2$  values was then possible by inspection after allowance for  $F_{lat}$  and normalization of the data.

The program is now listed:

```

IMPLICIT REAL*8(A-H,O-Z), INTEGER*4(I-N)
DIMENSION DEL(11), F(11), X(11), Y(11), Z(11)
C = 0.6948
DO 100 I = 1,22
IF (I .LE. 10) DEL1 = 100.*I
IF (I .GT. 10 .AND. I .LE. 14) DEL1 = 250.*(I-6)
IF (I .GT. 14) DEL1 = 500.*(I-10)
WRITE (6,99) DEL1
99 FORMAT(1H1, F5.0, 43X, 'CALCULATION OF QUADRUPOLE SPLITTINGS' /
1 1H0, 57X, 'FOR FERROUS CATIONS' )
DO 101 J = 1,11
101 DEL(J) = DEL1*(J-1)/10.
WRITE (6,102) DEL1, (DEL(J), J = 1,11), DEL1
102 FORMAT(1H0, 45X, 'OCTAHEDRAL', 58X, 'TETRAHEDRAL' /
1 1H0, 15X, 'LARGEST SPLITTING OF T2G LEVEL IS ', F5.0,
2 ' CM-1', 54X, 'AND CUBAL' /
3 1H0, 15X, 'SPLITTING OF LOWEST TWO LEVELS IN CM-1', 64X,
4 'E SPLITTING' /
5 1H , 2X, 'T', 4X, 11F9.0, 7X, 'T', F8.0, ' CM-1' /1H0)
DO 103 K = 1,72
IF (K .LE. 40) T = 10.*K
IF (K .GT. 40) T = 25.*(K-24)
W = -1.*DEL1/(C*T)
IF (DABS(W) .GT. 39) W = -39.
V = (1-DEXP(W))/(1+DEXP(W))
DO 104 J = 1,11
X(J) = -1.*DEL(J)/(C*T)
IF (DABS(X(J)) .GT. 39) X(J) = -39.
Y(J) = 1+DEXP(2.*W)+DEXP(2.*X(J))-DEXP(W)-DEXP(X(J))-DEXP(W+X(J))

```

```
Z(J) = 1+DEXP(W)+DEXP(X(J))
104 F(J) = DSQRT(Y(J))/Z(J)
    IF (K .GT. 40) GO TO 106
    WRITE (6,105) T, (F(J), J = 1,11), T, V
105 FORMAT(1H ,F5.0, 2X, 11F9.3, 5X, F5.0, F9.3)
    GO TO 108
106 WRITE (6,107) T, (F(J), J = 1,11), T, V
107 FORMAT(1H0,F5.0, 2X, 11F9.3, 5X, F5.0, F9.3)
108 CONTINUE
103 CONTINUE
100 CONTINUE
    STOP
    END
```



Appendix A3

REFERENCES

- Bancroft, G.M. (1974) Mössbauer Spectroscopy: An Introduction for Inorganic Chemists and Geochemists. McGraw-Hill, Maidenhead, England.
- Ingalls, R. (1964) Electric-field gradient tensor in ferrous compounds. Phys. Rev. 133A 787-795.
- Stevens, J.G. and Stevens, V.E. (1970) Mössbauer Effect Data Index Covering the 1969 Literature. Plenum Publishing Corporation, New York.
- Stone, A.J. (1967) Appendix to Bancroft et al. J. Chem. Soc. A 1966-1971.
- Stone, A.J., Aagard, H.J. and Fenger, J. (1969) General constrained non-linear regression for Mössbauer spectra. Publ. Danish Atomic Energy Comm. RISO-M-1348.

VITA

Frank Edward Huggins was born on 13th of April, 1947, in the village of Kintbury, Berkshire, England. In 1957, he won a scholarship to attend Christ's Hospital, Sussex, where he remained until 1966. In that year, he was awarded an Open Exhibition at Pembroke College, Oxford University and received the B.A. degree with 2nd Class Honors in Chemistry in 1970. During the final year at Oxford, he wrote a thesis on the infra-red spectra of olivines, which proved to be his introduction to Earth Sciences.

In August 1970, he was wedded to Michelle Jane Kaveny of San Lorenzo, California and the following month began postgraduate studies in the Department of Earth and Planetary Sciences at Massachusetts Institute of Technology, where, supported by research and teaching assistantships, he remained until August 1974. On completing this Ph.D. thesis, he moved to Washington, D.C., where he had accepted a joint appointment as Postdoctoral Fellow and Research Associate at the Geophysical Laboratory of the Carnegie Institution of Washington.